UNIVERSITÀ DI PISA

Facoltà di Ingegneria
Corso di Laurea in Ingegneria Aerospaziale

Controller Design for the Acquisition Phase of the LISA Mission using a Kalman Filter

Tesi di Laurea

Anno Accademico 2006-2007
27 Luglio 2007

Relatori:

Prof. G. MENGALI

Prof. A. SALVETTI

Dr. P. GATH

Allievo:

FRANCESCA CIRILLO

Ai miei nonni

Muovesi l'amante per la cosa amata
come il senso alla sensibile,
e con seco s'unisce e fassi una cosa medesima.
L'opera è la prima cosa che nasce dall'unione.
Se la cosa amata è vile, l'amante si fa vile.
Quando la cosa unita è conveniente al suo unitore,
li seguita dilettazione e piacere e sadisfazione.
Quando l'amante è giunto all'amato, lì si riposa.
Quando il peso è posato, lì si riposa.
La cosa conosciuta col nostro intelletto.

Leonardo da Vinci, *Codice Trivulziano*

Abstract

LISA, the Laser Interferometer Space Antenna, and its technology-demonstrating precursor LISA Pathfinder form an ESA/NASA collaborative project, selected as an ESA Cornerstone and included in NASA's 'Beyond Einstein' initiative.

The primary objective of the LISA mission is to detect and observe gravitational waves emitted from massive black holes and galactic binaries in the low-frequency band which ranges from 0.1 mHz up to 1 Hz with a goal of extending the measurements down to 30 μHz. The underlying measurement principle is a laser interferometry system built up with three satellites that are flying in a triangular constellation with an edge length of 5 million km. Each of the three identical spacecraft carries a V-shaped payload which is a measurement system consisting of two free-flying test masses, associated laser interferometer measurement systems and electronics. The two branches of the V-shaped payload at one corner of the triangle, together with the corresponding single arms of the other two spacecraft, constitute one of three Michelson-Type interferometers. These will detect low frequency gravitational waves through the measurement of changes in the length of the optical path between the two reflective proof masses of one arm of the interferometer relative to the other arm. In order to ensure that the test masses are flying in a disturbance-free motion along their geodesics, so that an extremely small displacement due to the passage of gravitational waves is detectable, challenging performance requirements with respect to internal and external disturbance rejection must be satisfied by an overall Drag-Free-System. Detailed simulations are needed in order to ensure mission success and an End-to-End simulator is currently under development aiming at verifying the on-orbit performance.

Nevertheless, the interferometric measurements of LISA are only possible once the three laser links between the three spacecraft of the LISA constellation are established. This phase is addressed as the constellation acquisition for LISA. LISA constellation acquisition is challenging, given the 5 million km distance between the spacecraft, inherent limits of the attitude sensors accuracy, orbit determination accuracy issues and the time required to phase-lock the incoming and outgoing laser signals. In order to counteract all these adverse constraints and make the LISA constellation acquisition possible, the laser pointing must satisfy challenging performance requirements during the whole duration of the acquisition phase.

This thesis proposes a strategy for the acquisition control of the LISA formation based on the use of a Kalman filter: it pre-processes the measurement data providing enhanced signals for the controller, which has the very same structure used in the science mode. The Kalman filter is designed such that it realizes a continuous blend of the sensors data, providing a massive disturbance rejection. Simulations and sensitivity analysis are performed in order to demonstrate the feasibility of the proposed approach.

LISA, acronimo per *Laser Interferometer Space Antenna* e LISA Pathfinder, la missione test che verificherà le tecnologie necessarie alla realizzazione di LISA, costituiscono un progetto in collaborazione tra ESA, che lo ha selezionato come *'ESA Cornerstone'* e NASA, che lo ha incluso nell'iniziativa *'Beyond Einstein'*.

L'obiettivo primario della missione LISA è il rilevamento e l'osservazione di onde gravitazionali nella banda di bassa frequenza compresa tra 0.1 mHz e 1 Hz (con il proposito di estendere le misurazioni fino a 30 μHz), emesse da sistemi di stelle binarie presenti nella nostra galassia e da buchi neri massicci. Il principio utilizzato per la misurazione è rappresentato da un sistema di interferometria laser realizzato mediante tre satelliti identici che formano una costellazione triangolare con lato di lunghezza pari a 5 milioni di km. Ognuno dei tre satelliti contiene un carico pagante a forma di V, ovvero un sistema di misurazione costituito da due masse test in moto di caduta libera, il sistema di misurazione ad interferometria laser e l'elettronica associata. I due rami del carico pagante a forma di V ad un vertice del triangolo e i due corrispondenti bracci appartenenti agli altri due satelliti della costellazione costituiscono uno dei tre interferometri di tipo Michelson. Questi ultimi rileveranno onde gravitazionali di bassa frequenza mediante la misurazione dei cambiamenti nella lunghezza del percorso ottico tra le 2 masse test riflettenti di un braccio dell'interferometro relativamente all'altro braccio. Allo scopo di assicurare che le masse test compiano un volo di quasi perfetta caduta libera lungo le geodetiche, cosicché anche un impercettibile spostamento dovuto al passaggio di onde gravitazionali possa essere rilevato, è necessario che stringenti requisiti di riduzione di effetti di perturbazione siano soddisfatti da un *Drag-Free-System*. Simulazioni dettagliate sono necessarie per garantire il successo della missione e, a questo fine, un simulatore End-to-End è attualmente in fase di sviluppo.

Tuttavia, le misurazioni interferometriche di LISA sono possibili solo una volta che siano stati stabiliti i tre collegamenti laser tra i tre satelliti della costellazione. Questa fase è denominata come fase di acquisizione della costellazione. L'acquisizione della costellazione di LISA è estremamente complessa e delicata data la distanza di 5 milioni di km che separa i satelliti, gli inerenti limiti di accuratezza dei sensori d'assetto e di precisione nella determinazione dell'orbita, nonché il tempo necessario per mettere in fase i segnali laser in ingresso e in uscita. Allo scopo di contrastare tutte queste circostanze avverse e rendere possibile l'acquisizione della costellazione, il puntamento laser deve soddisfare stringenti requisiti durante l'intera durata dell'acquisizione.

Il presente lavoro di tesi propone una strategia per il controllo durante l'acquisizione basato sull'utilizzo di un filtro di Kalman che pre-processi le misurazioni fornendo un segnale migliorato al controllore, il quale ha la stessa struttura usata durante lo *science mode*. Il filtro di Kalman è progettato in modo che esso realizzi una continua fusione tra i dati forniti dai sensori, garantendo una massiccia riduzione del rumore e dei disturbi. Simulazioni e analisi di sensibilità sono stati condotti allo scopo di dimostrare la fattibilità dell'approccio proposto.

Acknowledgments

The present thesis has been carried out during a seven month stage at EADS Astrium Gmbh, Future Mission and Instruments division, Friedrichshafen, Germany.

It was an extremely challenging and formative experience, and I am deeply grateful to my Prof. Giovanni Mengali and to Stefano Lucarelli, who not only paved the way to this work experience, but who have patiently followed, advised and encouraged me, always with great sensitiveness.

My warm thanks to my advisor Dr. Peter Gath, for having offered me the opportunity of collaborating with his team, for his suggestions, for his care in my future and for his attitude in the work which spurred me to give always my best. My sincere thanks to Dr. Jens Levenhagen, for his precious technical support during the developing of my thesis.

In the timeframe of these long, hard, wonderful University years, the most important lesson I learnt is that the great achievements, also the apparently more individual ones, are nearly always the result of the work and the care of several people. This is certainly my case.

My thought runs to my father and my mother which, patiently and with endless devotion, shared successes and difficult periods with me; to my little sister Giuditta, for being an irreplaceable piece of my heart, my alter ego and my model; to my aunt Sandra, for her incommensurable maternal love and for having taught me to never mistrust oneself; to all my beloved family.

To Francesco, for having always listened, encouraged and supported me, even renouncing to his personal happiness; and to his family, which I feel almost as it is mine as well.

To Luca, the most altruist friend one can desire and with who I have shared much more than all the University period.

To all the friends of the German adventure and, particularly, to Marianna, Domenico and Danilo, for our nightly talks and for the mutual support we found in each other so far from home.

To all my friends, whose names cannot find place in these few lines, but who always occupy a special space in my mind and in my heart.

My everlasting gratitude goes to all of you, since, in spite of my dark periods and my being sometimes lunatic, I have never stopped to feel your affection and your attentions. I have never been able to reach my target without you. You were my inspiration and my determination, my steadfastness and my willpower. You taught me that everyone does not worth that much by himself. In this day, your love is my biggest satisfaction.

La presente tesi è frutto di uno stage di sette mesi svolto presso EADS Astrium Gmbh, dipartimento di Future Mission and Instruments, Friedrichshafen, Germania.

È stata una esperienza estremamente stimolante e formativa, e sono profondamente grata al Prof. Giovanni Mengali e a Stefano Lucarelli, che non solo hanno reso possibile lo svolgimento di questo lavoro, ma che con grande sensibilità mi hanno pazientemente seguita, consigliata e incoraggiata.

Un caloroso ringraziamento al mio advisor Dr. Peter Gath, per avermi offerto la possibilità di collaborare con il suo team, per i suoi consigli, per il suo interessamento nei confronti del mio futuro e per il suo approccio nel lavoro che mi ha stimolato a dare sempre il meglio di me. Un sincero ringraziamento al Dr. Jens Levenhagen, per il suo prezioso supporto tecnico durante lo svolgimento del mio lavoro di tesi.

Nel corso di questi lunghi, duri, meravigliosi anni di Università, la lezione più importante che ho appreso è che le grandi conquiste, anche quelle di carattere apparentemente più individuale, sono quasi sempre il risultato del lavoro e dell'impegno di molte persone. Questo è indubbiamente il mio caso.

Il mio pensiero corre a mio padre e a mia madre che, pazientemente e con infinita devozione, hanno condiviso con me successi e momenti difficili; alla mia sorellina Giuditta, per essere un insostituibile pezzo del mio cuore, il mio alter ego e il mio modello; a zia Sandra, per il suo incommensurabile amore materno e per avermi insegnato a non dubitare mai; e alla mia adorata famiglia tutta.

A Francesco per avermi sempre ascoltata, incoraggiata e sostenuta anche a spese della sua personale felicità; e alla sua famiglia, che ormai sento un po' anche come mia.

A Luca, l'amico più altruista che si possa desiderare e con il quale ho condiviso molto di più che tutto il periodo universitario.

Agli amici dell'avventura tedesca ed, in particolare, a Marianna, Domenico e Danilo, per le nostre chiacchierate fino a notte fonda, per il conforto che trovavamo l'uno nell'altro nell'essere lontani da casa.

Agli amici tutti, i cui nomi non possono trovare spazio tra queste poche righe, ma che occupano da sempre un posto speciale nella mia mente e nel mio cuore.

A tutti voi va la mia riconoscenza, perché, nonostante i miei periodi bui e il mio essere a volte scostante, non ho mai smesso di avvertire il vostro affetto e le vostre attenzioni. Senza di voi non ce l'avrei fatta. Voi siete stati la mia inspirazione e la mia determinazione, la mia costanza e la mia forza di volontà. Mi avete insegnato che da soli non si vale un granchè. In questo giorno, il vostro amore è la mia soddisfazione più grande.

Pisa, 27 Luglio 2007

Francesca Cirillo

Contents

List of Figures

List of Tables

Acronyms

AST	Autonomous Star Tracker
AU	Astronomical Unit
CCD	Acquisition Sensor
CoM	Center of Mass
DFACS	Drag-Free Attitude Control System
DoF	Degree of Freedom
DSN	Deep Space Network
EoM	Equation of Motion
ESA	European Space Agency
E2E	End-to-End
FEEP	Field Emission Electric Propulsion
FOV	Field-Of-View
IS	Inertial Sensor
IWS	Inertial Wavefront Sensing
KF	Kalman Filter
LIGO	Laser Interferometer Gravitational Wave Observatory
LISA	Laser Interferometer Space Antenna
LOS	Line-Of-Sight
LTI	Linear Time Invariant
MIMO	Multiple Inputs Multiple Outputs
MOA	Movable Optical Assembly
MoI	Moment of Inertia
NASA	National Aeronautics and Space Administration
OATM	Optical Assembly Tracking Mechanism

OBC	On-Board Computer
OMS	Optical Metrology System
PAA	Point-Ahead Angle
PSD	Power Spectral Density
QPD	Quadrant Photodiode
RMS	Root Mean Square
RSS	Root Square Sum
SC	Spacecraft
SISO	Single Input Single Output
STR	Star Tracker
TBC	To Be Confirmed
TBD	To Be Determined
T/M	Test Mass

Part I

System-Level Introduction

Chapter 1

Introduction

This chapter aims to provide a brief introduction to the LISA Mission in order to depict the scientific and technical framework this thesis is included in.

1.1 Gravitational Waves

The experimental verification and analysis of gravitational waves are among the most important challenges of modern physics. According to Einstein's Theory of General Relativity, time and space are woven together, forming a four-dimensional fabric called "space-time". Gravitation can be thought of as the motion of objects following the curved lines, the geodesics, of the space-time caused by the presence of matter and energy; consequently, the wave associated with gravitation can be regarded as a dynamic oscillation in this curvature of space-time. In other words, if a mass distribution moves in an asymmetric way it produces "indentantions" in the space-time fabric which travel outwards as ripples in space-time called gravitational waves.

Gravitational waves stretch and compress space as they move through it, changing the distance between macroscopic bodies that are floating freely in space (i.e. isolated from all forces other than gravity). For this reason, one powerful technique to detect gravitational waves is to measure the distances between free floating masses using laser interferometry. Since the relative length change caused by the passage of a gravitational wave is exceedingly small, gravitational waves have not yet been directly detected. The weakness of the interaction of the gravitational waves with matter is not due to the fact

that they carry little energy, but rather to the fact that space-time is an extremely stiff elastic medium so that it takes extremely large energies to produce even minute distortions. Although the weakness of interaction makes the gravitational waves hard to detect, it implies also that they do not scattered or get absorbed by any other matter they may encounter on the way from their source; thus, to detect a gravitational wave means to see the behavior of the gravitational wave source with perfect clarity. Since electromagnetic waves do not have this property, gravitational waves can help to map the space-time geometry of the universe for the first time.

Detection of gravitational waves requires strain sensitivities in the range 10^{-21}-10^{-23} over time scales 10^{-3}-10^{+4} s and several detectors are needed on Earth and in space in order to cover the whole spectrum of possible sources (Figure 1.1-1).

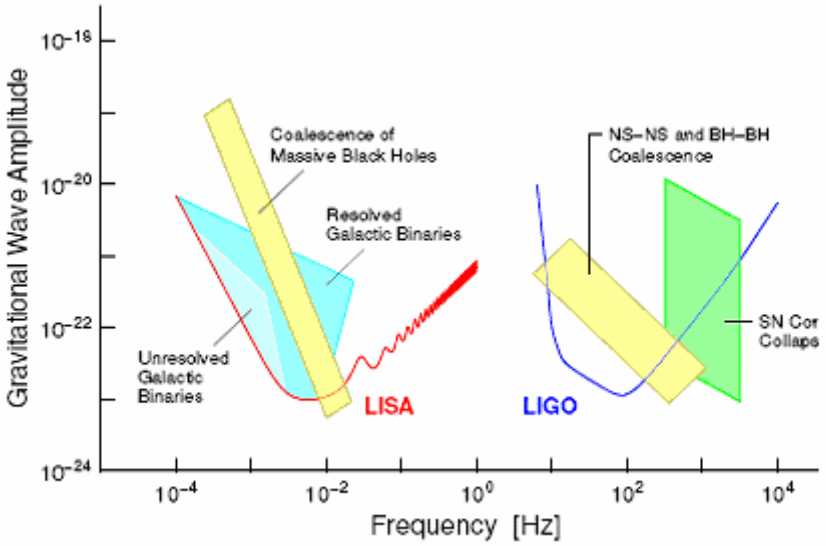

Figure 1.1-1: Comparison of frequency range of sources for ground-based and space-based gravitational wave detectors, Ref. [17]

The current status of the search for gravitational waves is that four first generation ground-based interferometric detectors (LIGO, VIRGO, TAMA 300 and GEO 600) are on-line and plans are at advanced stages for further generations. They will observe gravitational waves over the higher frequency regime (10-1000 Hz), which are produced in astronomical events that last only one second or less. They include supernova explosions and collisions of black holes that were formed from stars in earlier supernova explosions.

At low frequencies (below a few Hz), where lot of the most interesting gravitational wave sources are emitted, such as massive black holes and galactic binaries, the performance of ground-based detectors is limited by gravitational gradient noise, caused for instance by motions inside the Earth's crust. Measurement and subtraction of this disturbance can only work to a certain extent, therefore, in order to enter this very interesting frequency range, it is necessary to go into space as is planned with the Laser Interferometer Space Antenna (LISA) mission.

1.2 The Laser Interferometer Space Antenna Project

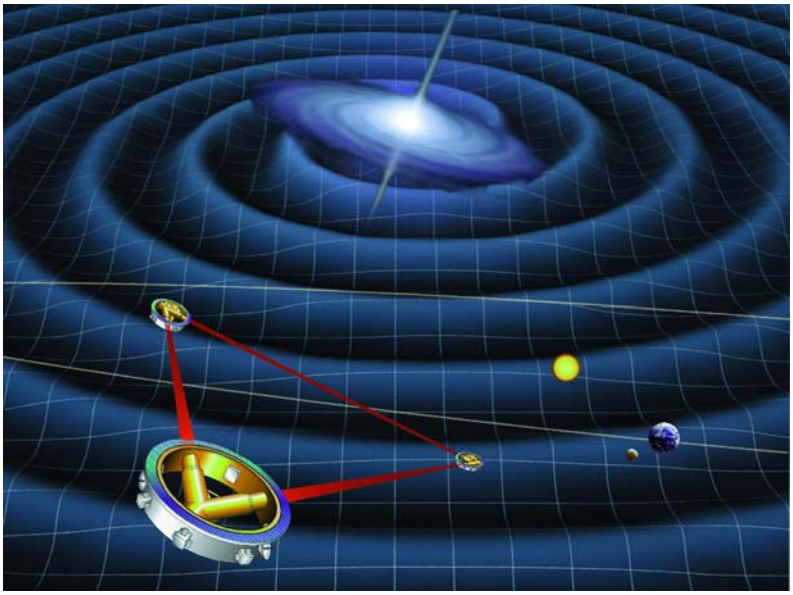

Figure 1.2-1: Artistic conception of LISA, Ref. [17]

Approved as an ESA "Cornerstone Mission" and a NASA "Beyond Einstein Great Observatory Mission", LISA consists of a cluster of three identical spacecraft, flying in a quasi-equilateral triangular formation with an edge length of 5 million km in a heliocentric orbit with a semi-major axis of 1 AU. The LISA constellation is trailing the Earth at a distance of approximately 60 millions Km or around 20° Constellation-Sun-Earth angle. The position of the formation, 20° behind the Earth, is a result of a trade-off between minimising the gravitational disturbances from the Earth-Moon system and the communications needs (Figure 1.2-2).

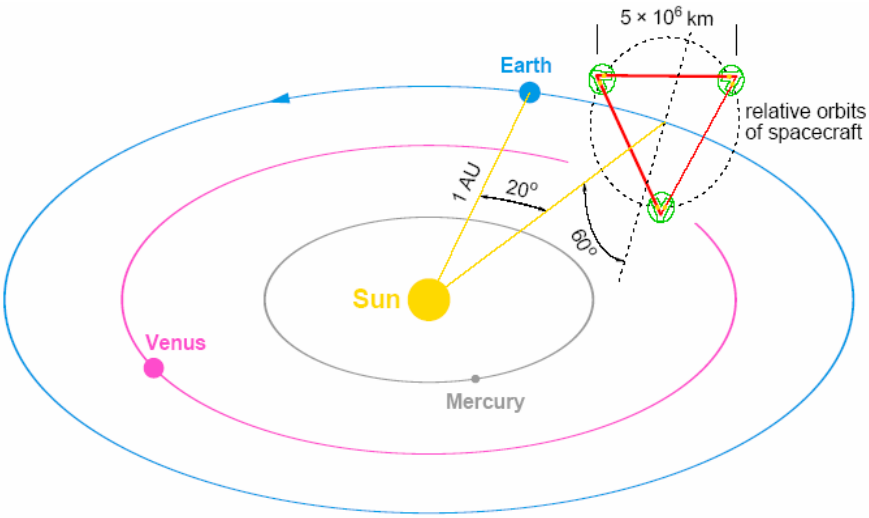

Figure 1.2-2: LISA orbital constellation geometry, Ref. [11]

The plane of the triangle is tilted by 60° with respect to the ecliptic plane which means that the triangular formation of the spacecraft is maintained throughout the year, with the triangle appearing to counter-rotate about the centre of the formation once per year (Figure 1.2-3). This annual motion enables the LISA system to provide angular information about gravitational wave sources.

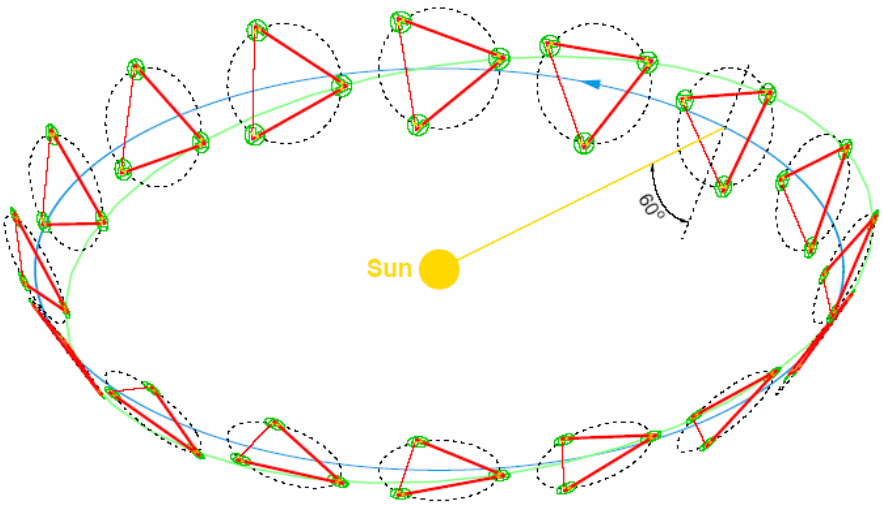

Figure 1.2-3: Annular Motion of the LISA Constellation, Ref. [11]

The current baseline is to launch all three LISA spacecraft at once in 2015. In order to reach the final operational orbit, each science spacecraft is equipped with an additional propulsion module which is separated when the target orbit is obtained after approximately 14 months. The mission will make continuous observation for up to 8

years after that. Figure 1.2-4 depicts the launch stack configuration and the composite spacecraft (science spacecraft and the propulsion module) with the propulsion module cylinder removed.

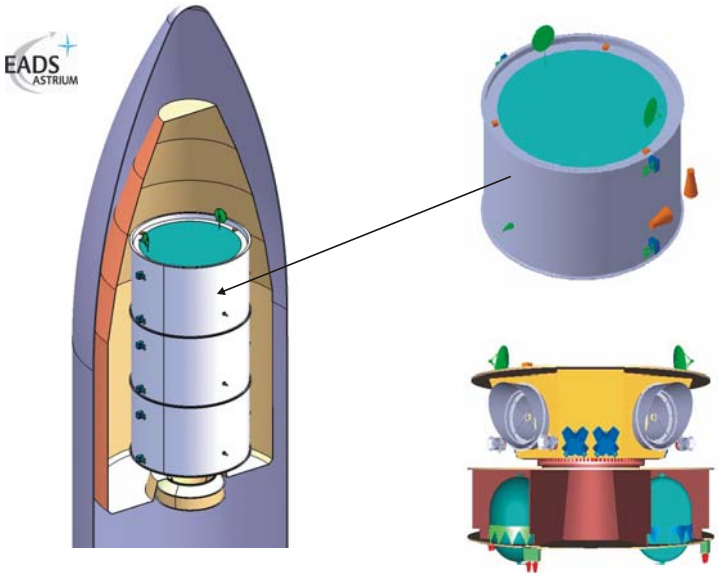

Figure 1.2-4: LISA launch stack under Atlas V short fairing on the B1198 launch adapter (left) and composite spacecraft with propulsion module cylinder removed (right) , Ref. [11]

Each of the three identical spacecraft carries a V-shaped payload which is a measurement system consisting of two steerable telescopes each containing a free-flying test mass, associated laser interferometer measurement systems and electronics (Figure 1.2-5).

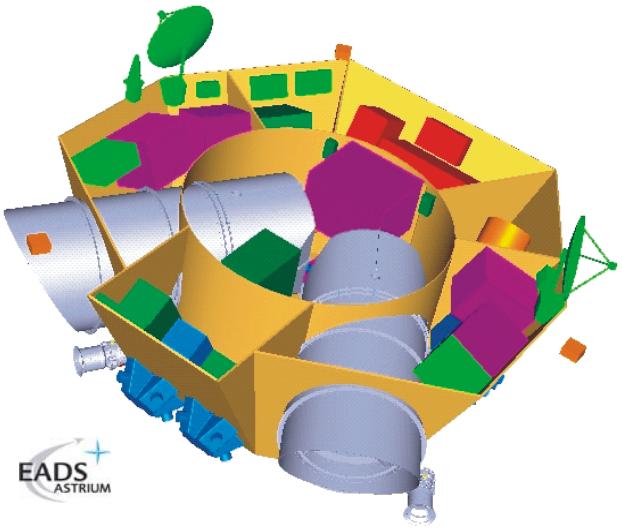

Figure 1.2-5: Inside of a LISA science spacecraft, showing all required units for the V-shaped payload and for the sciencecraft bus, Ref. [11]

The two branches of the V-shaped payload at one corner of the triangle, together with the corresponding single arms of the other two spacecraft, constitute one of three giant Michelson-Type interferometers. The third arm is necessary to give independent information on the two polarisations of gravitational waves and for redundancy. These interferometers will detect low frequency gravitational waves through measurement of changes in the length of the optical path between the two reflective test masses of one arm of the interferometer relative to the other arm.

While LISA can be described as a Michelson interferometer, the actual implementation is somewhat different from a classical interferometer that relies on the 'round-trip' of a beam of reflected laser light. The distances involved are simply too great to use reflection, especially when compared to the available power for the laser. In other words, the laser light transmitted from the centre spacecraft would be much too faint upon reflection and return from the other spacecraft; thus, in an analogy to a radiofrequency transponder scheme, the laser on the receiving spacecraft is instead phase-locked to the incoming light, generating a return beam of full intensity. The transponded light from the far 'reflector' spacecraft is received by the centre spacecraft and superposed with the onboard laser light that serves as the local oscillator in a heterodyne detection. As this entwines laser frequency noise with a potential gravitational wave signal, the signal from the other arm together with a software algorithm for data post-processing, called time-delay interferometry, are used to take out the laser frequency noise and obtain the pure gravitational wave signal.

In order to ensure that the two test masses of each spacecraft are flying in a disturbance-free motion along their geodesics, such that an extremely small displacement due to the passage of gravitational waves is detectable, challenging performance requirements with respect to internal and external disturbance rejection must be satisfied by an overall Drag-Free-System consisting of:

- Inertial sensors (IS, Electrostatic Suspension Actuation and Capacitative Sensing)
- Optical Metrology System (OMS, Laser Interferometry)
- Field Emission Electric Propulsion (FEEP, System of Micro-Propulsion Thrusters)

- Inertial Wavefront Sensing (IWS, Science Interferometer)
- Optical Assembly Tracking Mechanism (OATM)
- On-board computer (OBC , Drag-Free Control Software)

LISA works according to several operating modes during its lifetime; the one during which the science operations are performed is addressed in this work as *science mode*.

1.2.1 Science Requirements

The top level science requirement for LISA is given in terms of strain sensitivity. The strain sensitivity h is a measure for the gravitational wave amplitude and is proportional to the arm-length change such that

$$\frac{\delta L}{L} \approx h \tag{1.1}$$

where L is the arm-length expressed in m and δL is the arm-length variation expressed in m/√Hz due to the passage of a gravitational wave of 'amplitude' h.

LISA sensitivity objective is a strain linear spectral density of $4 \cdot 10^{-21}$ 1/√Hz around 3 mHz. Since the useful measurement bandwidth ranges between 0.1 mHz and 1 Hz with a goal of extending the measurements down to 30 μHz, more detailed LISA measurement strain sensitivity requirements are listed in Table 1.2.1-1.

Frequency (mHz)	Strain sensitivity with 35% system margin (1/√Hz)	Strain sensitivity excluding system margin (1/√Hz)
0.03	*2.6×10^{-16}*	*1.69×10^{-16}*
0.1	3.9×10^{-17} (7.8×10^{-17})	2.54×10^{-17}
1	3.2×10^{-19} (7.9×10^{-19})	2.08×10^{-19}
5	1.1×10^{-20} (1.1×10^{-19})	7.15×10^{-21}
10	1.3×10^{-20}	8.45×10^{-21}
100	7.5×10^{-20}	4.87×10^{-20}
1000	7.5×10^{-19}	4.87×10^{-19}

Table 1.2.1-1: Required LISA Measurement Sensitivity (values in brackets are the minimum science requirements) , Ref. [11]

Sources of gravitational waves that can thereby be detected are e.g. galactic binaries (neutron stars, white dwarfs), extra-galactic targets like super-massive black hole binaries, super-massive black hole formations and cosmic background gravitational waves.

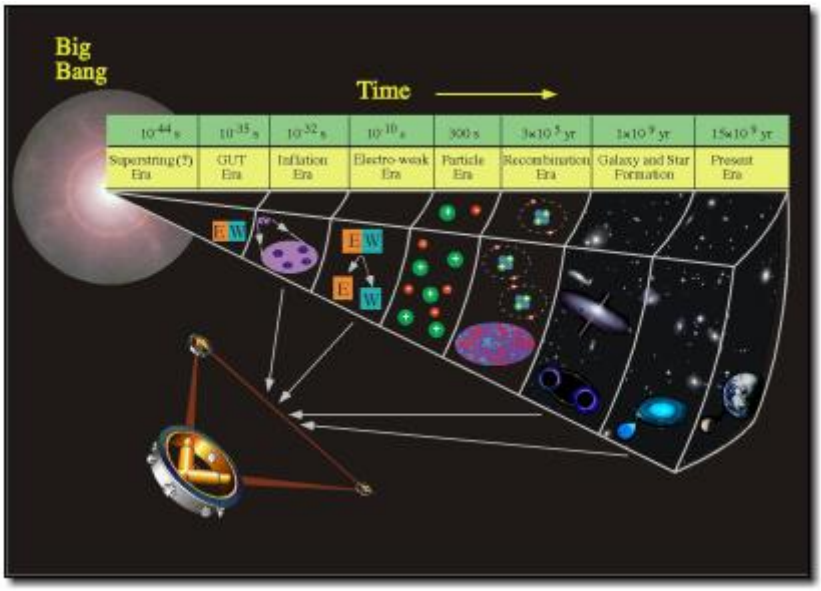

Figure 1.2.1-1: Gravitational waves sources detectable by LISA, Ref. [17]

1.2.2 Science Performances

The sensitivity that can be achieved by LISA is determined by a wide variety of noise sources and by the degree to which their effects can be kept small. There are two main categories of such sensitivity-limiting noise effects:

- Disturbance Acceleration Noise

  The disturbance acceleration noise is due to forces or accelerations acting on the test masses, causing displacements of them which fake the extremely small displacement due to the passage of gravitational waves. The sources contributing to the acceleration environment of the test mass arise from both direct effects on it and the effects on the spacecraft that are coupled to the test mass through the electrostatic suspension system. These are:

  - External forces on the spacecraft, among them:
    - Thruster forces and thruster noises

  - Telescope counter-force actuation and noise
  - Difference in gravitational acceleration between test mass and spacecraft centre of mass
  - Solar radiation pressure
- Internal forces acting on the test mass and the spacecraft, including:
  - Thermal noise
  - Pressure fluctuations
  - Electrostatic actuation
  - Spacecraft self gravity
- Forces that arise from sensor noise feeding into commands

- Optical Path-Length Measurement Noise
  The optical path-length measurement noise fakes fluctuations in the lengths of the optical paths. This category of disturbances includes different types of noise, the most prominent of which are expected to be shot noise, beam pointing instabilities and thermal distortions.

Therefore, in order to meet the sensitivity goal, two key technologies are required for LISA:

- A disturbance reduction mechanism must shield the test mass from the outside environment in such a way that only gravity waves will cause measurable displacements.
- A laser interferometer for precise measurement of the variation in the distance between the test masses is needed: LISA is expected to detect path length changes of a few picometers within the measurement bandwidth.

1.2.3 The Disturbance Reduction Mechanism Requirement

It can be proved that the science requirement is achieved only if the test mass falls under the effect of the large scale gravitational field within an acceleration noise, relative to a free falling frame, whose linear spectral density is

$$S_a^{1/2}(f) \le 3 \cdot 10^{-15} \frac{m}{s^2} \frac{1}{\sqrt{Hz}} \cdot \sqrt{1 + \left(\frac{f}{8\ mHz}\right)^4 + \left(\frac{0.03\ mHz}{f}\right)^4} \qquad (1.2)$$

in the measurement bandwidth of

$$0.1\ mHz < f < 1\ Hz \text{ (goal } 30\ \mu Hz \text{ as lower end)}$$

This requirement holds for the sensitive axis (nominal line of connection between the two test masses of one arm of the constellation) of each test mass hosted on board of each spacecraft.

1.2.4 Optical Metrology System Requirement

Given the strain sensitivity requirements, LISA is expected to detect path length changes of a few picometers within the measurement bandwidth. Therefore, the interferometer sensing must be able to monitor the test mass position along the sensitive axis with a displacement noise level of

$$S_n^{1/2} \le 12 \frac{pm}{\sqrt{Hz}} \cdot \sqrt{1 + \left(\frac{2.8\ mHz}{f}\right)^4} \qquad (1.3)$$

in the frequency range

$$0.1\ mHz < f < 1\ Hz \text{ (goal } 30\ \mu Hz \text{ as lower end)}$$

1.2.5 Measurement Sensitivity

The overall LISA measurement sensitivity is shown in Figure 1.2.5-1. It illustrates the resulting LISA performance curve and compares it to the original science requirements data points. The most critical points in terms of meeting the overall performance are the 5 mHz requirement and the goal of meeting the 30 μHz requirement. At 5 mHz, the contribution from the acceleration noise and from the optical metrology noise are balanced such that the requirement is just met (with 35% system margin). At very low frequencies, the major disturbance contribution comes

from fluctuating charges on the test-mass which must be controlled with the charge measurement and discharge strategy.

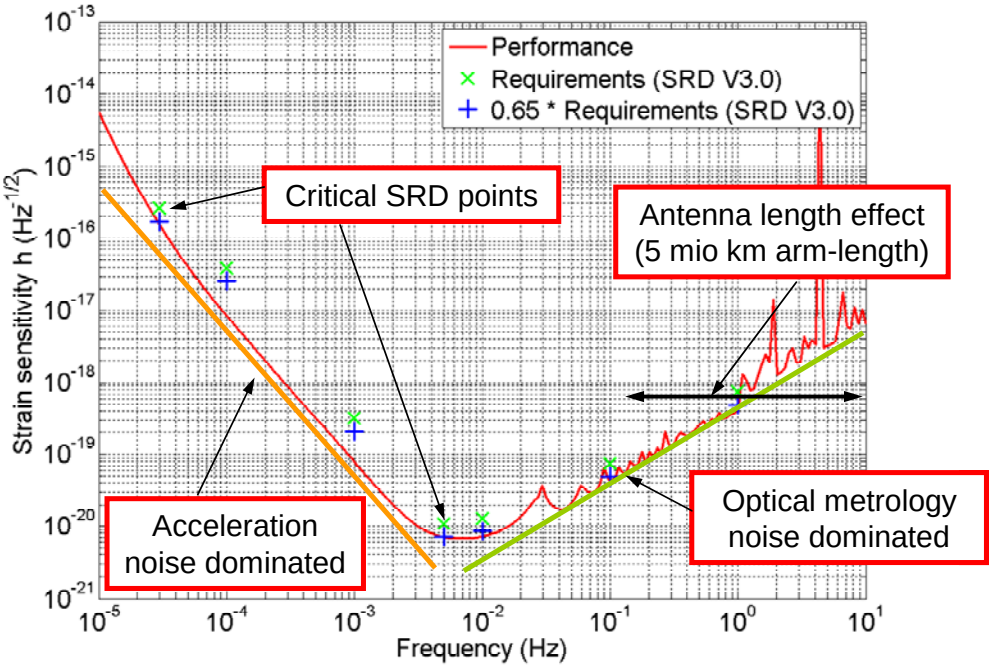

Figure 1.2.5-1: LISA sensitivity performance compared to science requirements, Ref. [11]

1.3 End-to-End simulator

Since LISA relies on technologies that have never been tested before and cannot be properly verified on ground, highly detailed performance simulations are required in order to ensure mission success. An End-to-End (E2E) simulator is currently under development. It aims at verifying the on-orbit performance of a strongly coupled satellite and payload system. Modelling work goes far beyond what is typically done for conventional satellite system simulators and involves a wide spectrum of competencies relating to different scientific and technical areas; the aim is to provide an accurate and integrated tool for performance analysis.

Figure 1.3-1 shows the top-level architecture of the E2E simulator. The simulator is implemented in the Matlab/Simulink® environment (some models are written in C/C++ in order to speed up simulation run-time).

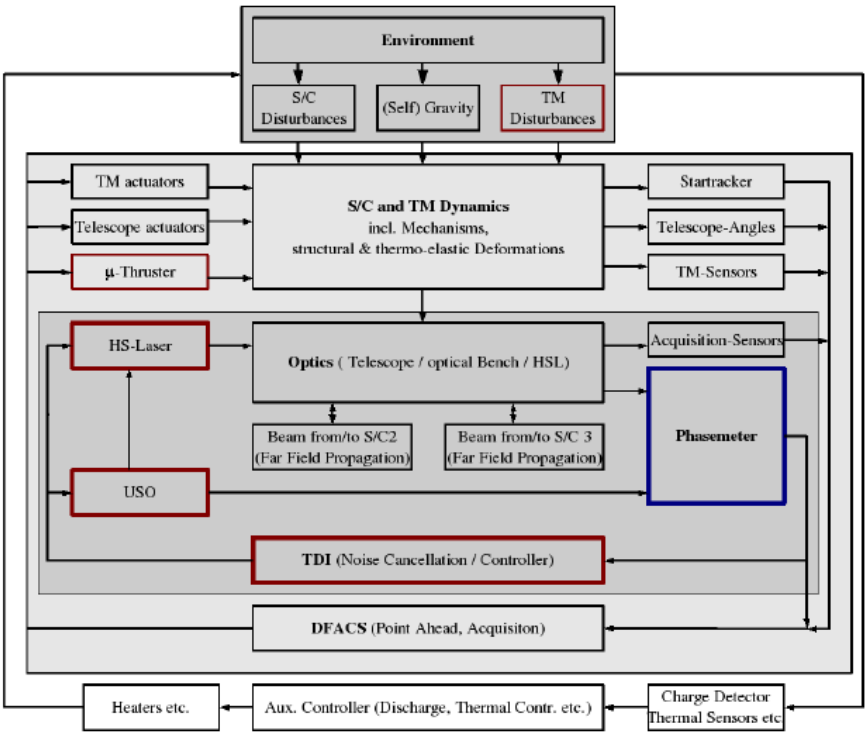

Figure 1.3-1: E2E simulator top-level architecture, Ref. [13]

This thesis aims at providing a control system model for the acquisition phase of LISA that will be included in the LISA E2E simulator. The programming work has been realized in the Matlab/Simulink® environment (version 7.2.0.232 (R2006a)).

1.4 Acquisition Phase

The interferometric measurements of LISA are only possible once the three optical links between the three spacecraft of the LISA constellation are established. More specifically, before LISA science measurements can commence the laser signal transmitted from each arm of each spacecraft has to be acquired by the quadrant photodiode of the receiving spacecraft so that it can be phase-locked with the local laser. This is the process of the constellation acquisition for LISA.

The quadrant photodiode (QPD) is an optical device whose main tasks are to provide the measurement of the arm-length for the science experiment and an accurate spacecraft inertial attitude determination in the *science mode*. The QPD is not available as an attitude sensor until the laser link is established, therefore, two auxiliary less-

accurate inertial attitude sensors are used: a star tracker (STR) and an acquisition sensor (CCD).

LISA constellation acquisition is challenging given the 5 million km distance between the spacecraft, inherent limits of the auxiliary attitude sensors accuracy, orbit determination accuracy issues and the time required to phase-lock the incoming and outgoing laser signals.

In order to counteract all these adverse constraints and make the LISA constellation acquisition possible, the perturbations on the laser pointing must be reduced under stringent limits by means of a highly competitive control system design. A scheme of the control system design is depicted in Figure 1.4-1. It is divided in three parts:

- Guidance law design: it consists in the design of the mathematical algorithm that drives the laser pointing during the whole duration of the acquisition
- Measurement processor design: it consists in the design of a mathematical algorithm that processes the measurements provided by the different sensor devices in order to produce an enhanced estimation of the measurement data for the controller
- Controller design: it consists in the design of the control algorithm that provides the actuation commands which force the laser to follow its pointing guidance law

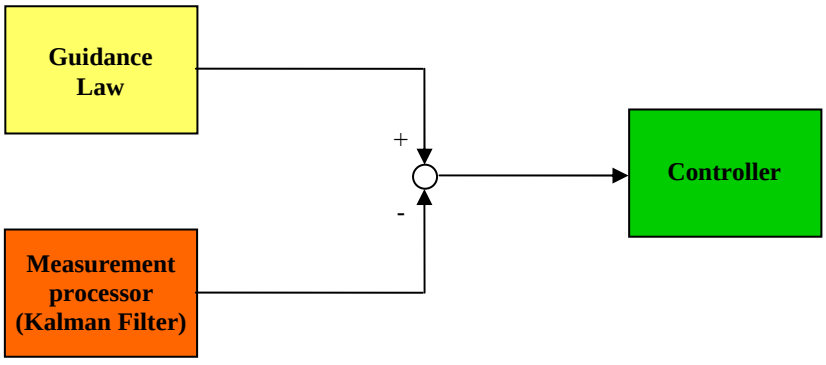

1.4-1: LISA constellation acquisition control system structure

The measurement processing is the essential key to reduce the perturbations on the laser pointing. In fact if the measurement data are not cleaned up from the noise introduced by the poor attitude sensor available, the controller is not able by itself to

fulfill the necessary perturbation reduction and the acquisition phase cannot be completed.

This thesis deals with the design of the measurement processing device: a Kalman filter is chosen to this end.

1.5 Contributions of This Work

- A fully compliant custom tool for the implementation and performance analysis of several Kalman filter algorithms has been developed in the Matlab/Simulink® environment. An extensive research to reduce sources of numerical errors has been performed.
- The application of the Kalman filtering technique to the LISA satellite model in the operative conditions of the acquisition has been performed. An extensive modeling and tuning research has been realized in order to improve the performance of the filter. A sensitivity analysis of the filter performance towards the Kalman filter algorithm, the acquisition phase duration and the sensor noise levels has been realized.
- A sensitivity analysis tool based on the Monte Carlo technique has been developed and used to qualify the performance sensitivity of different Kalman filter algorithms towards model errors. To this end, an error budget of the model parameters has been derived.
- The effect of constant parasitic forces and torques over the acquisition controller has been investigated and a drift compensation strategy has been developed.
- The results achieved have been used to derive requirements for the sensor systems and for the acquisition controller.

1.6 Outline of the Thesis

The current report has been divided in two parts: the first provides a system-level introduction to the following design part.

In chapter 2, the constellation acquisition control for LISA is described in detail and the requirements for the control system are recollected from [7]. In chapter 3, the equations of motion and the measurement equations of the drag-free satellite are derived. In chapter 4, the controller design strategy is presented, while the controller design performances are analyzed in chapter 5 proving the necessity of a Kalman filter for the reduction of the perturbation effect due to the attitude sensor noise level. To this end, an overall model of the closed-loop LISA satellite dynamics is implemented in both Matlab® and Simulink® environments.

The following chapters constitute the second part, concerning the Kalman filter design.

In chapter 6, the main theoretical concepts for the Kalman filter design are introduced with particular attention to the methods to limit numerical errors. In chapter 7, the Kalman filter for the LISA acquisition phase is designed and a Matlab® and a Simulink® tools for its implementation and its performance analysis are developed. The sensitivity analysis toward model errors, based on the use of the Monte Carlo technique, is developed in chapter 8. In chapter 9, DC parasitic forces and torques are introduced in the model: their effect is evaluated and a drift compensation strategy is proposed.

Finally, chapter 10 proposes a summary of the performed work and suggests useful guidelines for further improvements.

Chapter 2

Constellation Acquisition Control for LISA

A system-level introduction to the constellation acquisition control for LISA is provided in this chapter.

2.1 Introduction

As already mentioned in section 1.4, the objective of the acquisition phase is to bring the whole constellation to a *science mode* configuration which is only lacking some of the calibrations before the science measurements can commence. Thus, during the acquisition phase, all the three laser links between the three spacecraft need to be established (Figure 2.1-1).

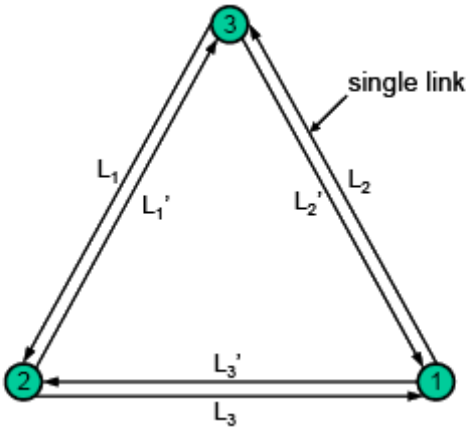

Figure 2.1-1: LISA laser links, Ref. [10]

More specifically, the scope of the acquisition is to obtain the laser signal on the quadrant photodiode (QPD) of each arm of all the three spacecraft of the constellation such that the science interferometer can start to operate continuously measuring the arm-lengths for the science experiment, data transmission between the spacecraft can be established and the QPD can start to be used as a highly accurate inertial wavefront sensing (IWS) for the attitude control of each spacecraft. Because of several sources of uncertainties, that are exhaustively described in the following, the acquisition of the laser signal on the QPD cannot be performed directly by just switching on the laser of one spacecraft and shooting in the direction of the other. Therefore, the acquisition results in a complex ensemble of operations to achieve the signal on the QPD.

Since the QPD is not available as an attitude sensor until it receives a continuous laser signal, two auxiliary inertial attitude sensors are needed during the acquisition phase: a star tracker (STR) and an acquisition sensor (CCD). Although the CCD has better performances than the STR, especially in terms of the measurement noise introduced, it cannot be used as an attitude sensor from the beginning of the acquisition phase. In fact, the CCD does not work as a ‘super star tracker’, but rather as a ‘reduced QPD’ in the sense that it must receive the laser signal from the other spacecraft of the same arm and, moreover, the local laser must be switched off, because the CCD is blinded by the local laser stray light. Thus, the STR is used as an attitude sensor during all the phases of the acquisition in which the laser link between two spacecraft is not yet established and/or the local laser is turned on.

The strategy adopted for the constellation acquisition is sequential in the sense that it establishes one laser link at time. It stands to reason that, after one laser link is performed on one arm, the signal acquisition process on the second and third arm will be in principle the same, except for the fact that high-accuracy attitude knowledge is already available for one direction. Therefore, in this work, just the signal acquisition of the first arm is taken into account, although the feasibility of the whole constellation acquisition should be verified through simulation at a later stage.

2.2 Acquisition Sequence

The process for the single-link acquisition is initiated and then accomplished autonomously. It is divided into four main phases:

- Calibration phase
- Signal acquisition on the acquisition sensor
- Signal fine acquisition on the acquisition sensor
- Signal acquisition on the quadrant photodiode

2.2.1 Calibration Phase

The purpose of this phase is to perform a calibration of the telescope line-of-sight (LOS) by referencing it to the star tracker heads, eliminating in this way the constant bias which causes a deviation from the nominal 30° angle between the star tracker and the telescope acquisition sensor (CCD) lines-of-sight.

During the calibration phase, the spacecraft is rotated around the sun vector (Figure 2.2.1-1). Rotations around other axis are allowed on the condition that they are small in order to maintain the same thermal environment. Providing that the star tracker and the acquisition sensor field-of-view (FOV) are large enough to find stars with sufficient magnitude, first a guide star can be identified by the STR allowing the complete knowledge of the spacecraft attitude. Then, a second guide star is found on the CCD and, together with the known spacecraft attitude, is used to compute and remove the offset angles between the expected and the real telescope line-of-sight.

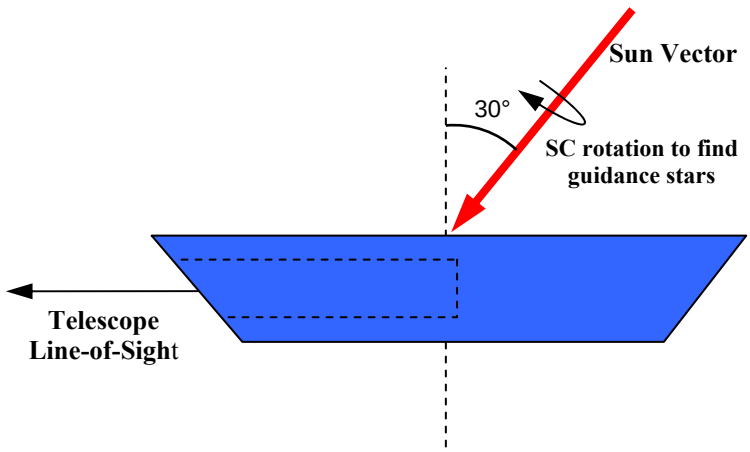

Figure 2.2.1-1: Telescope line-of-sight calibration process, Ref. [7]

For the reasons explained in section 2.1, during the calibration only the STR can be used as attitude sensor.

2.2.2 Signal Acquisition on the Acquisition Sensor

The goal of this acquisition step is to find the laser signal on the acquisition sensor (CCD) of both the spacecraft of one arm of the constellation.

During this phase, one spacecraft, which is addressed as SC 1 or as sending spacecraft in the following, turns on its laser and performs a scanning maneuver to cover the *uncertainty cone* which represents the size of the sky where the target spacecraft (SC 2) is expected to be sited (Figure 2.2.2-1) The scanning is performed by using a given *scanning law*, e.g. by describing a spiral from the center, where it is more likely to find SC 2, to the outer boundary of the uncertainty cone. The laser is switched off between one *scanning position* and the other. Obviously, to be sure that the CCD of SC 2 could be intercepted by the SC 1 laser beam, the sending spacecraft must cover the whole uncertainty cone during the scanning procedure with a sufficient amount of superimposition between the *scanning cones*, each of which represents the size of the laser beam at the receiving spacecraft (Figure 2.2.2-1).

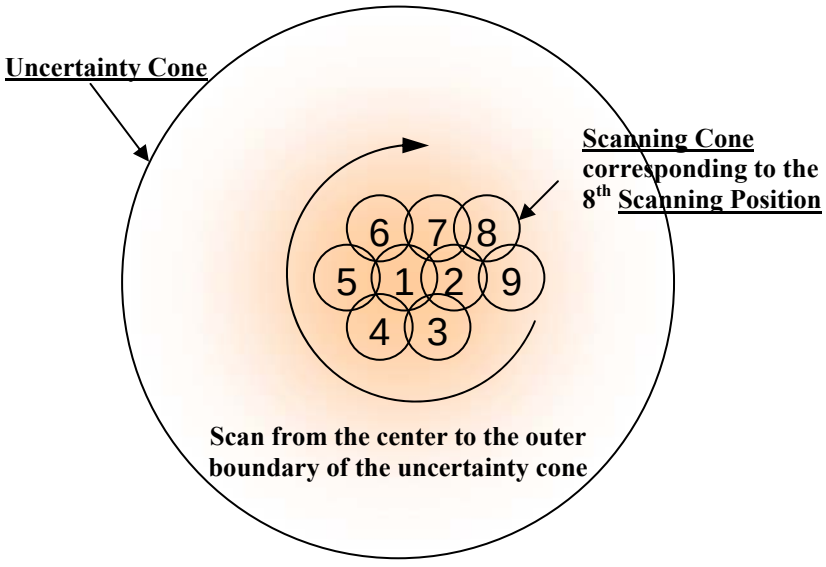

Figure 2.2.2-1: Scanning procedure, Ref. [7]

While SC 1 is actively scanning, the target spacecraft remains in its reference attitude and stares into the corresponding reference direction which is based on ground-

provided navigation data (Figure 2.2.2-2 left side).

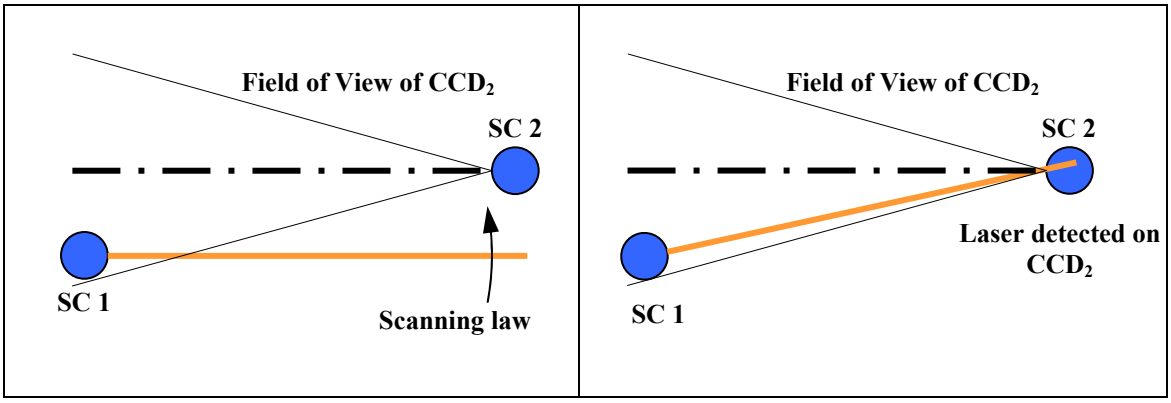

Figure 2.2.2-2: Spacecraft 1 scanning, spacecraft 2 is waiting for a signal (on the left); spacecraft 1 scanning, spacecraft 2 detects a signal (on the right); CCD_2 stands for CCD of SC 2, Ref. [7]

At a certain time during the scanning, SC 2 will detect a signal on its acquisition sensor (Figure 2.2.2-2 right side).

Because of the errors in the ground-provided reference attitude, there will be an offset between the expected (ground-provided) reference position and the real position of the incoming laser signal. Hence this offset, which is expected to be linear, must be computed, using as reference the real position of the laser signal on the acquisition sensor, and the attitude guidance law of SC 2 must be corrected including the computed attitude offset angles (Figure 2.2.2-3).

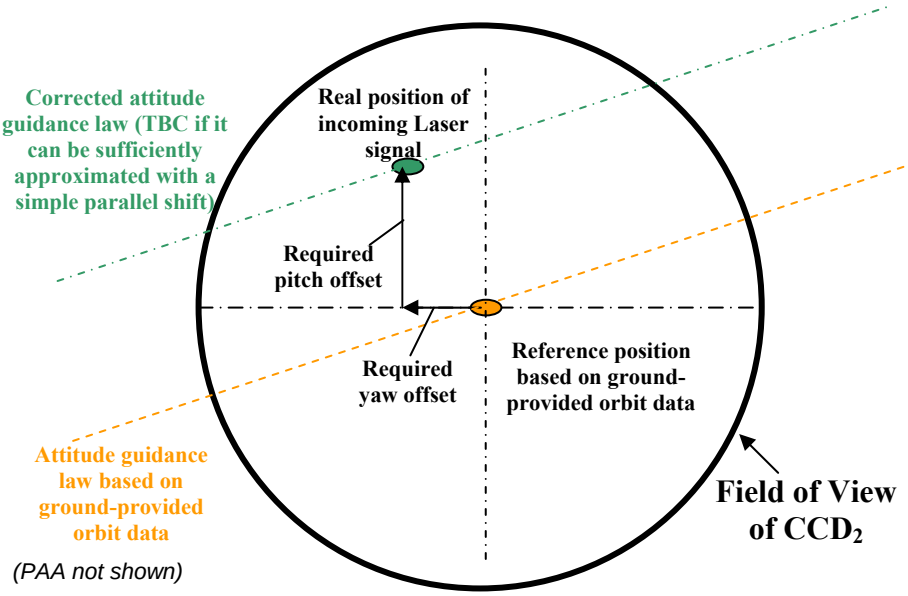

Figure 2.2.2-3: Signal detection on the CCD of spacecraft 2 (CCD_2), Ref. [7]

While SC 2 is accomplishing the attitude correction, SC 1 still performs the scanning producing SC 2 to lose the signal from SC 1 on its acquisition sensor (Figure 2.2.2-4)

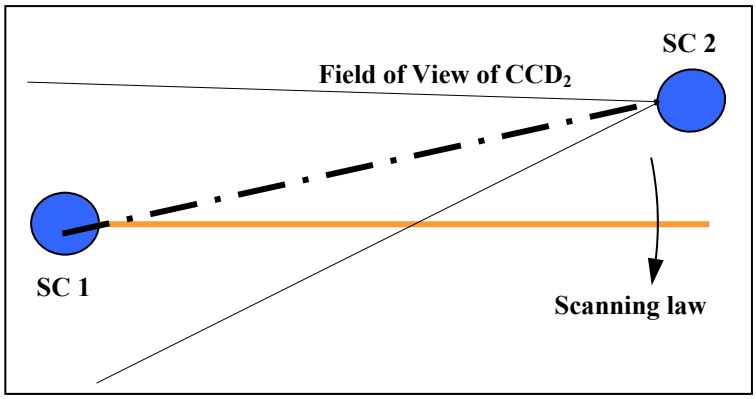

Figure 2.2.2-4: Spacecraft 1 scanning, spacecraft 2 has performed the attitude correction (CCD_2 stands for CCD of SC 2), Ref. [7]

After having obtain the correct attitude, SC 2 can send back a laser signal to the scanning spacecraft. In order that SC 1 can detect the incoming laser signal on its acquisition sensor, two circumstances must occur:

- The laser of SC 1 must be turned off. This condition is satisfied periodically between one scanning position and the next.
- SC 2 must still be in the field-of-view of SC 1. This will be the case if the attitude correction of SC 2 does not take too long, since the scanning pattern ensures that a particular scanning location remains in the FOV of the scanning spacecraft for several minutes (Figure 2.2.2-5)

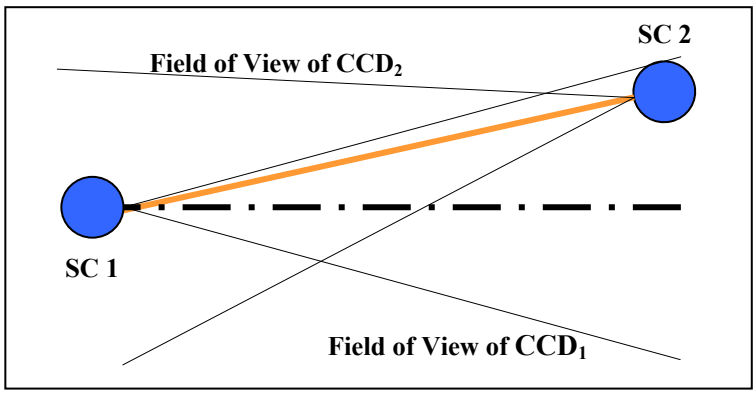

Figure 2.2.2-5: Spacecraft 1 detects signal of spacecraft 2 (CCD_2 stands for CCD of SC 2) , Ref. [7]

Upon detection of the laser signal, SC 1 must perform an attitude correction since it suffers from similar errors in the ground-provided attitude guidance law as SC 2.

For the reasons explained in section 2.1, during the whole duration of this phase only the STR can be used as an inertial attitude sensor.

2.2.3 Signal Fine Acquisition on the Acquisition Sensor

Once both spacecraft have successfully received a laser signal on their acquisition sensor, a fine attitude correction can be performed. The objective of this acquisition step is to bring the incoming laser signal to a reference position of the CCD with high accuracy such that the incoming laser is within the FOV of the QPD. This ensures that a frequency search can be done on the QPD in the next acquisition step (Figure 2.2.3-1)

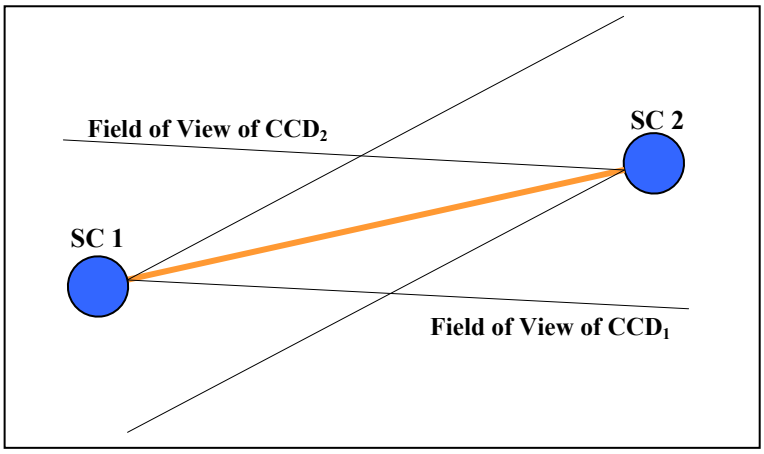

Figure 2.2.3-1: Attitude fine acquisition (CCD_2 stands for CCD of SC 2) , Ref. [7]

In order to perform a fine acquisition of the signal on the acquisition sensor, it is necessary that both spacecraft (SC 1 and SC 2) perform their attitude control based on the read-out of the acquisition sensor itself. Since this sensor is blinded when the local laser is turned on, a laser on/off pattern must be implemented such that it is ensured that SC 1 and SC 2 have the frequent opportunity to detect the laser signal of the other spacecraft.

2.2.4 Signal Acquisition on the Quadrant Photodiode

The goal of this acquisition step is to obtain the laser signal on the QPD of both spacecraft such that both lasers can be turned on in the steady state, allowing data

transmission between the two spacecraft, and the QPD can be used as an highly accurate inertial wavefront sensing for the attitude control in the *science mode*.

In order to detect a signal on its quadrant photodiode, SC 2 performs a frequency scan by changing the frequency of its local laser in order to reveal a beat signal on the quadrant photodiode. This can only be done when the local laser is turned on and light from SC 1 is received. As soon as the beat signal is detected, the QPD can be used as an attitude sensor. However, the local laser must still be turned on/off until spacecraft 1 has successfully found a signal on its QPD as well and, therefore, the attitude control is based on the read-out of the acquisition sensor.

Since the Doppler shift, due to the relative velocities between the two spacecraft, is fairly accurately known in the framework of the ground-provided navigation data and can thus be removed by onboard data processing, SC 1 should be able to detect a signal on the QPD as soon as SC 2 has found the correct frequency as well.

2.3 Uncertainty Cones and Requirements

The reason for this complex strategy of acquisition stands in the fact that the laser link between the two spacecraft of one arm cannot be obtained just by turning on the laser of SC 1 and shooting in the direction of SC 2. This happens because there are several sources of uncertainty that require to be limited as far as possible through a highly demanding overall-system-design, while the not eliminable amount of remaining uncertainty must instead be covered by such an acquisition strategy.

In this section, the constraints (on the spacecraft and payload system side and on the operational side) which cause the mentioned uncertainty will be described in detail for each phase of the acquisition, aiming at deriving requirements for them. A close examination can be found in [7].

In particular, since the objective of this work is to design the control system for the acquisition phase, all those constrains that influence directly (i.e. desired performances) and indirectly (i.e. available sensing and actuation systems) the control system design will be highlighted with special attention and specific requirements will be derived for them.

2.3.1 Preliminary Definitions

The requirements on the spacecraft attitude and the telescope in-plane pointing angle refer to the error signal which represents the deviation of the real signal from the corresponding guidance law

$$\text{Error} = \text{Guidance Signal} - \text{Real Plant Signal}$$

Therefore, the long-term drift is a deviation from the guidance law which represents a perturbation that influences the CCD field-of-view position and it is spread over the whole duration of each acquisition sub-phase.

The short-term jitter is a deviation from the guidance law that perturbs the laser beam position at the receiving spacecraft in the timeframe of the permanency in such position.

The spacecraft attitude requirement involves the spacecraft inertial attitude (Θ_B, H_B, Φ_B) expressed as the three rotation angles around the three body axis of the spacecraft reference frame Σ_B defined in chapter 3. One-axis attitude requirement means that the same requirement is used for each one of the attitude angles.

The telescope in-plane pointing angle requirement refers to the telescope angular deviation (α) from its nominal position around the orthogonal axis to the constellation plane expressed in the spacecraft frame. This requirement involves the articulated telescope (section 2.4.3)

In-plane and out-of-plane qualify the angles that lie or not lie in the constellation plane defined by the three LISA satellites.

For the definitions of the statistical variables (i.e. mean, variance, standard deviation (σ), root mean square (RMS), root square sum (RSS), power spectral density (PSD)) and their relationship refer to Appendix B.

2.3.2 Uncertainty cones

Calibration

As already pointed out in section 2.2.1, sensors (CCD and STR) field-of-view and sensitivity are the main constraints for the calibration to be performed.

In particular, the STR is characterized by a large field-of-view, but also by a small aperture which causes the STR optics sensitivity to be the limiting factor for the magnitude and, consequently, the number of stars that can be seen. In other words, even if the STR field-of-view allows to see a large portion of sky, a reduced aperture causes that only few, very bright stars can be effectively detected. Thus, the main requirement coming from the calibration for the STR is that it must be able to use stars with enough magnitude.

On the other hand, the CCD has a better sensitivity, but a poor field-of-view. Consequently the star that the STR has to point must be chosen such that the CCD, whose LOS is nominally rotated of 30° in the constellation plane from the STR's one, could find another star with enough magnitude in his field-of-view. Moreover, it is necessary to define an uncertainty cone that need to be covered by CCD field-of-view during the calibration to be sure that the selected calibration star is effectively in the CCD field-of-view. Its main contributions are listed in Table 2.3.2-1.

Contribution	**Error in plane (µrad)**	**Error out of plane (µrad)**
Alignment Error between Star Tracker and Spacecraft	50	50
Alignment Error between Spacecraft and Telescope Assembly	50	50
Alignment Error between Telescope Assembly and Telescope Pointing Actuator	25	25
Absolute Position Knowledge of Telescope Pointing Actuator	0.5	0
Spacecraft Attitude (one axis) Long-term Drift (RMS 3σ)	30	30
Telescope in-plane Pointing Angle Long-term Drift w.r.t. Spacecraft (RMS 3σ)	0.01	0
Total (linear sum)	**155.5**	**150**

Table 2.3.2-1: Calibration uncertainty cone budget, Ref. [7]

All the numeric values have to be confirmed, but it seems evident that the telescope field-of-view must be large enough to compensate especially the on-ground alignment error between the star tracker and the telescope line-of-sight.

The spacecraft attitude long-term drift and the telescope in-plane pointing angle long-term drift requirements during the calibration are instead dominated by the quality of the star tracker read-out signal, by the DC (constant) solar forces and torques disturbances acting on the SC, by the DC parasitic forces and torques acting on the T/M and by the telescope pointing actuator and read-out noise. Therefore, it is evident that all these contributions influence directly the control strategy that has to be adopted in this phase in order to achieve the desired performances in term of spacecraft attitude and telescope pointing drift.

Signal Acquisition on the Acquisition Sensor

The uncertainty cone represents the size of sky that must be scanned by the sending spacecraft in order to intercept the CCD of the receiving spacecraft and also the size of sky that must be covered by the CCD field-of-view of the receiving spacecraft during the whole duration of the scanning phase in order to detect a signal from the sending spacecraft (Figure 2.2.2-1). Since it is larger than the scanning cone, which represent the size of the laser beam at the receiving spacecraft, the acquisition cannot be direct. However, the acquisition on CCD can be performed more quickly and more efficiently when the uncertainty cone is kept small and the size of the scanning cone is large.

The size of the acquisition uncertainty half-cone angle is estimated to be around 8.9 μrad RSS. It has contributions from uncertainties in the relative position knowledge of the spacecraft (inertial navigation error), spacecraft attitude long-term drift and the telescope in-plane pointing angle long-term drift, star tracker/telescope line-of-sight alignment knowledge accuracy after calibration and line-of-sight versus outgoing laser beam offset knowledge accuracy. Table 2.3.2-2 captures the breakdown of the uncertainty cone budget. Since it is very small when compared with the calibration uncertainty cone budget, this cone is not the leading factor for the choice of the CCD field-of-view.

Contribution	**Error (μrad)**
Navigation Error	7.2
Star-Tracker/Telescope Line-of-Sight Alignment Knowledge Accuracy after Calibration	1
Point-Ahead Angle Error (mainly due to navigation error)	negligible
Line-of-Sight versus Outgoing Laser Beam	1
Spacecraft Attitude (one axis) Long-term Drift	5 (TBC)
Telescope in-plane Pointing Angle Long-term Drift w.r.t. Spacecraft	1 (TBC)
Total (linear sum)	**15.2**
Total (RSS)	**8.9**

Table 2.3.2-2: Uncertainty cone budget (RMS 3σ) during acquisition on CCD (half-cone angle), Ref. [7]

The uncertainty cone contribution ε_{nav} from the inertial navigation error is given by the trigonometric equation:

$$\varepsilon_{nav} = \arcsin\left(\frac{\sqrt{2}\delta_x}{L_{\min} - 2\delta_x}\right) \approx \frac{\sqrt{2}\delta_x}{L_{\min}} \tag{2.1}$$

where δ_x is the maximum relative navigation error along a coordinate axis of the inertial heliocentric frame provided by the DSN (estimated as 25 km RMS 3σ) and $L_{\min}$ is the minimum arm length assuming an uncertainty of ±1% on the nominal value. Eq. (2.1) represents the worst-case navigation error and it is illustrated in Figure 2.3.2-1.

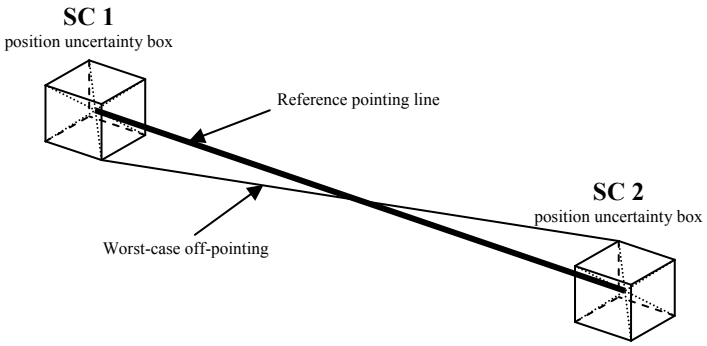

Figure 2.3.2-1: Worst-case navigation error, Ref. [7]

The point-ahead angle α_{pa} (PAA) is the difference between the laser incoming and outgoing direction due to the relative velocity between the two spacecraft and can be computed using the relative position and the relative velocity which are ground-provided (figure 2.3.2-2). The out-of-plane point-ahead angle can be compensated by using a point-ahead angle mechanism. The point-ahead angle error is the offset between the expected PAA and the real one due to navigation error in the relative position and velocity knowledge. Being less than 1 nrad, this error is negligible with respect to the others.

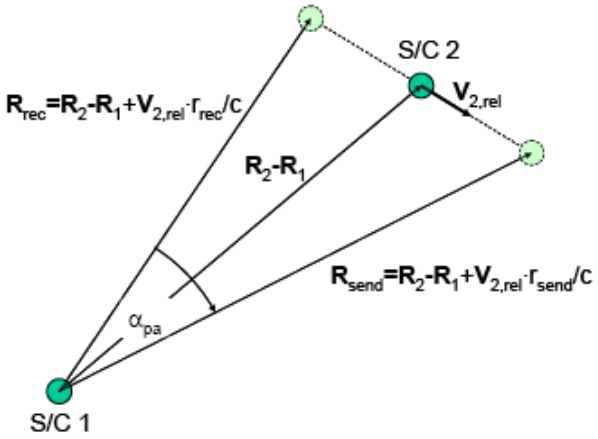

Figure 2.3.2-2: Illustration of the point-ahead angle definition, Ref. [7]

The line-of-sight versus outgoing laser beam error is due to a number of factors, such as launch disturbances, thermal loading, on-ground calibration accuracies and the lateral stability of the fiber launcher. It must be ensured that this angle is sufficiently small such that a signal can be correctly sent back to the sending spacecraft when its real position is detected on the acquisition sensor. Potentially, the CCD acquisition sensor may be used to calibrate out a part of this uncertainty.

The spacecraft attitude long-term drift and the telescope in-plane pointing angle long-term drift requirements during the acquisition on CCD have the same meaning of the correspondent calibration long-term drifts. However, in this context, the drift requirements are more demanding in order to reduce the size of the uncertainty cone and thus their influence on the control design will be greater.

The size of the scanning cone is given by the ideal full-width of the emitted beam

reduced by the local spacecraft attitude jitter and the telescope pointing jitter (Table 2.3.2-3)

Contribution	**Error (µrad)**
Laser Beam Divergence	1.58
Spacecraft Attitude (one-axis) Short-term Jitter (RMS 1σ)	0.1
Telescope Pointing Short-term Jitter w.r.t. Spacecraft (RMS 1σ)	0.05
Total (linear algebraic sum)	**1.43**

Table 2.3.2-3: Scanning cone budget during acquisition on CCD (half-cone angle), Ref. [7]

All the numeric values have to be confirmed. The half-size of the emitted laser beam at the receiving spacecraft for a 1064 nm laser wavelength out of a 40 cm primary mirror must be computed at the smallest possible distance between the two spacecraft in order to represent the worst case condition (Figure 2.3.2-3).

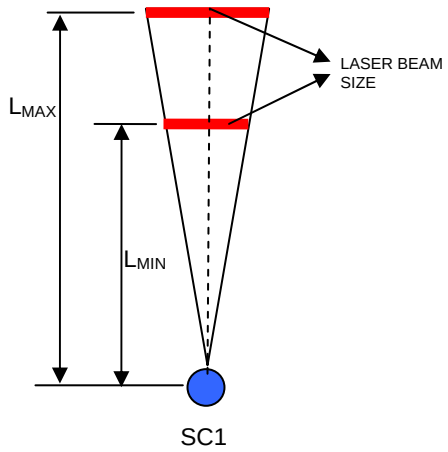

Figure 2.3.2-3: Worst-case and better-case laser beam divergence

The spacecraft attitude and the telescope in-plane pointing angle short-term jitter requirements for the size of the scanning cone are dominated by the quality of the star tracker read-out signal and by the telescope pointing actuator and read-out noise. Therefore, it is evident that also these contributions, together with the long-term drift requirements, influence directly the control strategy that has to be adopted in the acquisition on CCD phase.

Since a sufficient overlap between scanning positions must be provided, the required maximum number of scan positions can be estimated as

$$N_{scan} = \frac{\varepsilon_{uncertainty}^2}{\alpha_{scan}^2} \tag{2.2}$$

where:

- $\varepsilon_{uncertainty}$: half cone angle of uncertainty cone
- α_{scan}: half cone angle of scanning cone

which yields approximately 113 scan positions. Therefore, the scan rate provided by the telescope pointing actuator must be sufficiently high in order to perform the scanning in a reasonable short duration.

Signal Fine Acquisition on the Acquisition Sensor and Signal Acquisition on the Quadrant Photodiode

The level of precision by which the incoming signal can be steered to a reference position on the CCD depends strictly on the resolution of CCD itself. In order to perform the acquisition on the QPD, the mentioned reference position must be seen by the QPD. Therefore, it is necessary that the field-of-view of the QPD is sufficiently large to comply with the resolution of the acquisition sensor and to cope with any misalignments (Table 2.3.3-4).

Contribution	**Error (µrad)**
CCD Resolution (including centroiding)	0.06
Spacecraft Attitude (one axis) and Telescope in-plane Pointing Angle Short-term (w.r.t. Spacecraft) Jitter (RMS 1σ)	0.1
Absolute Pointing Accuracy of the Point-Ahead Angle Mechanism	8
Misalignment between QPD and CCD	1
Total (linear sum)	**9.6**
Total (RSS)	**8.1**

Table 2.3.2-4: Uncertainty cone budget during acquisition on QPD (half-cone angle), Ref. [7]
All the numeric values have to be confirmed.

To be noted is that the navigation error is not part of the list anymore since an on-board measurement of the correct attitude is now provided by the acquisition sensor. Also remarkable is that the spacecraft attitude and telescope in-plane pointing angle control requirements have the same meaning of the correspondent scanning cone short-term jitter contributions, but here they are dominated by the quality of the CCD read-out signal and by the telescope pointing actuator and read-out noise. Therefore, they can be significantly relaxed in the required axes thanks to the availability of acquisition sensor signal which is much less noisy than the STR sensor signal.

Remark

From this discussion can be concluded that, in order to perform the whole acquisition, a switching from one attitude sensor to another must be ensured. This is translated in strict requirements on the field-of-view, the resolution and noise of the sensors. The current baseline for sensors equipment is shown in Table 2.3.2-5.

	STR	**CCD**	**QPD**
Field-of-View	0.3 rad	155 μrad	10 μrad
Resolution	255 μrad/pixel	0.4 μrad/pixel	1 nrad/pixel
Read-Out Noise	29 μrad (RMS 3σ)	60 nrad (RMS 3σ)	750 prad/√Hz

Table 2.3.2-5: Performance requirements for STR, CCD and QPD; all the numeric values are TBC

As can be noted, in order to enhance the field-of-view and the resolution required to realize the measurement chain from one sensor to another, also an increase in the read-out noise is produced.

2.3.3 Requirements for the acquisition controller design

From the analysis performed in the previous sections, it can be concluded that the desired performances in terms of spacecraft inertial attitude control and telescope in-plane pointing angle control change considerably from one acquisition step to another, especially as a consequence of the different inertial attitude sensors available. Specifically, the acquisition on CCD phase results to be the most demanding because:

- There are two types of required performances (long-term drift and short-term jitter) which must be achieved at the same time for the laser beam pointing of the scanning spacecraft, while, in the other phases, the requirements just belong to one category or to the other;
- The requirements on the long-term drifts are more demanding than the correspondent requirements in the calibration phase where the same attitude sensor (STR) is available.
- The requirements on the short-term jitters are of the same order of magnitude of the correspondent requirements for the acquisition on QPD phase where, however, the less noisy CCD is available as an attitude sensor.

Therefore, it is convenient to design a controller that could be used in all the acquisition phases and to test it in the framework of the acquisition on CCD phase since it is the most demanding in terms of desired performances and available sensors. The performance goals to be demonstrated through the controller design for a successful acquisition are summarized in Tables 2.3.3-1 and 2.3.3-2.

States	**Required error (μrad) RMS 1σ**
Spacecraft Attitude (one-axis) Short-Term Jitter	0.1 (TBC)
Telescope in-plane Pointing Angle (w.r.t. Spacecraft) Short-Term Jitter	0.05 (TBC)

Table 2.3.3-1: Requirements on the short-term jitters from the scanning cone budget

States	**Required error (μrad) RMS 3σ**
Spacecraft Attitude (one-axis) Long-Term Drift	5 (TBC)
Telescope in-plane Pointing Angle (w.r.t. Spacecraft) Long-Term Drift	1 (TBC)

Table 2.3.3-2: Requirements on the long-term drift from the uncertainty cone budget during acquisition on CCD

Note that the acquisition controller must guarantee that the laser beam along the arm of the constellation where the acquisition is first performed follows the pointing guidance law determined by the acquisition sequence previously described. The laser beam pointing direction coincides with the telescope line-of-sight direction. The telescope line-of-sight direction can be univocally determined, with reference to the inertial frame, by the in-plane and the out-of-plane angular deviation from its nominal position (H_i, Φ_i where i = 1,2 indicates the i-th telescope of the spacecraft). The roll angle Θ_i, that defines the rotation of the telescope around its line-of-sight direction, can be also considered. Obviously this angle does not influence the laser pointing and does not need a requirement. In the following, the angles (Θ_i, H_i, Φ_i) are referred as telescope line-of-sight inertial attitude. Therefore, the task of the controller system is to allow the telescope line-of-sight inertial attitude to follow its guidance law reducing the perturbations caused by the spacecraft attitude and telescope in-plane pointing angle fluctuations and keeping them within the limits stated in the several budgets presented above.

Consequently, the requirements of Tables 2.3.3-1 and 2.3.3-2 must be translated in the reference frame of each telescope that is involved in the acquisition process (Table 2.3.3-3) in order to be used for the controller performance verification.

Telescope	**Short-Term Jitter (µrad)**		**Long-Term Drift (µrad)**	
	$\mathbf{H_i}$	$\mathbf{\Phi_i}$	$\mathbf{H_i}$	$\mathbf{\Phi_i}$
fixed	0.1	0.1	5	5
actuated	0.1	$\sqrt{0.1^2 + 0.05^2} \approx 0.118$	5	$\sqrt{1^2 + 5^2} \approx 5.099$

Table 2.3.3-3: Requirements on the telescope line-of-sight inertial attitude

Since the duration of the acquisition on CCD phase has to be defined (the expected duration is about 15 minutes providing an adequate scan rate to the scanning spacecraft), the following statistical analysis is performed in order to verify the fulfilment of the requirements of Table 2.3.3-3:

- Time-series of 30000 s of the inertial attitude of each telescope line-of-sight are obtained through simulation and their errors in following the guidance law[1] are computed.
- It is defined a time interval (time-window) representing the duration of the acquisition on CCD phase (long-term) and, conservatively, the permanency of each scanning position (short-term). A time-window of 1000 s is taken as baseline where not explicitly mentioned otherwise.
- The time-window is moved continuously along the time-series (moving time-window) and, on each selected interval, the following statistic variables are computed after having detrended the constant bias:
  - RMS 1σ as a measure of the short-term jitter
  - Slope of the interpolating line as a measure of the long-term drift
- Between all the statistics achieved over each time-series (2 for each moving time-window) the maximums are selected and compared to the corresponding requirements (Table 2.3.3-3)

2.4 Actuators for Acquisition Control

The actuation systems used for the acquisition control are the same that are involved in the *science mode* control since it is not useful to design dedicated systems for the acquisition. They are:

- micro-propulsion system
- electrostatic suspension system
- telescope pointing actuator system

The sampling rates at which actuation commands are considered available are limited to ~ 10 Hz. This limit is dictated by:

[1] As mentioned before (section 1.4), the guidance of the spacecraft and the telescope states is not within the purpose of this work. Therefore, the correspondent reference signals are set to zero if not explicitly mentioned otherwise. The designed acquisition controller should be tested over the correct guidance law at a later stage.

- micro-propulsion system command update rate
- available on-board computer power

2.4.1 Micro-Propulsion System

The micro-propulsion system must provide force and torque actuation capability of all 6 degree of freedom (3 linear and 3 angular coordinates) of the spacecraft.

In order to minimize the noise at the gravitational reference sensors, the drag-free attitude control system (DFACS) on the LISA spacecraft requires an extremely fine level of actuation essentially vibration free. This will be provided by a propulsion system capable of attitude and position control with thrust at micro-Newton level. Field emission electric propulsion thrusters (FEEP), although unqualified, are currently the best placed technology for supplying this function. Figure 2.4.1-1 shows the power spectral density of the noise shape filter used to simulate the FEEP actuation noise in the most conservative way and Figure 2.4.1-2 compares it to the experimental data available.

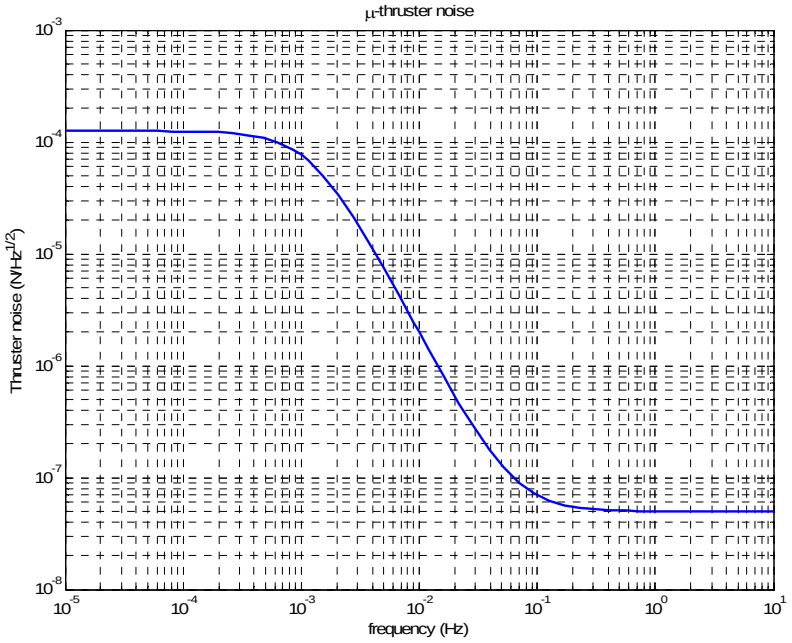

Figure 2.4.1-1: FEEP noise shape filter (bilogarithmic scale)

A field emission thruster is a device that uses an electric field to extract atomic ions from the surface of a metal. For propulsion applications, the most common source of

ions is a metallic liquid. In these sources, a strong electric field is established with a pair of closely spaced electrodes. The free surface of liquid metal exposed to this field is distorted into a series of conical protrusions in which the radius of curvature at the apex becomes smaller as the field increases. When the field reaches a threshold value, atoms on the surface of the tip are ionized and eventually removed. They are then accelerated to a high velocity by the same electric field which produced them. Expelled ions are replenished by the flow of liquid propellant in the capillary feed system. A separate neutralizer is required to maintain charge neutrality of the system (Figure 2.4.1-3).

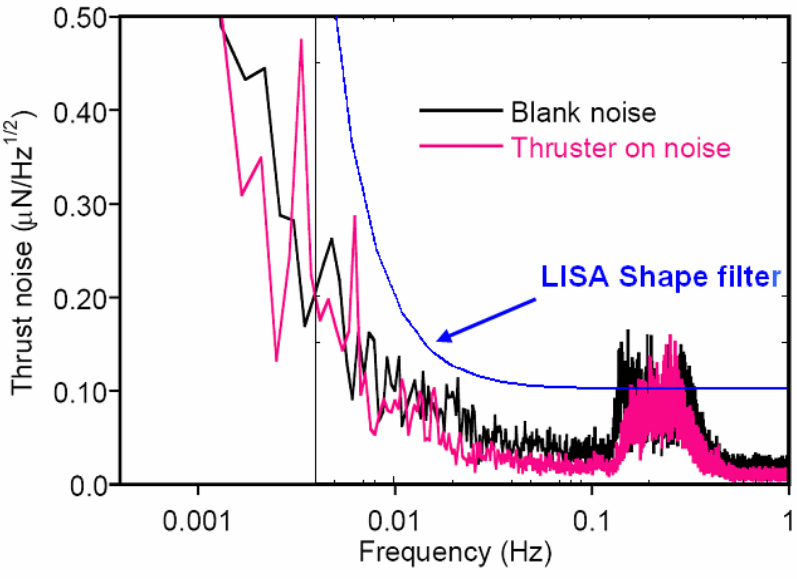

Figure 2.4.1-2: Comparison between LISA noise shape filter for he FEEP and experimental data (linear scale), Ref. [8]

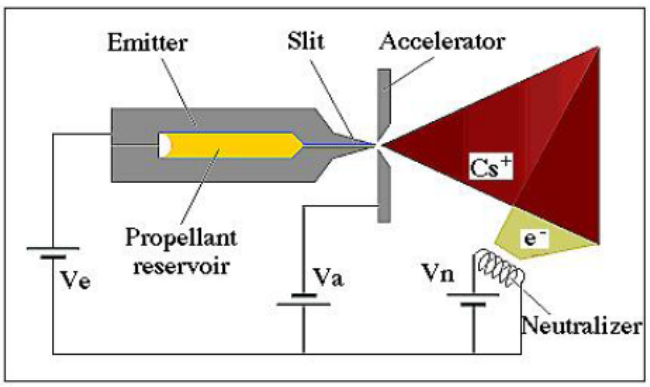

Figure 2.4.1-3: Operation scheme of Caesium FEEP, Ref.[17]

The main advantage of FEEP with respect to other µ-propulsion technology is that their specific impulse is high, which in turn means an increase of possible mission duration. Besides, the small amount of propellant required is contained in a very compact reservoir in the emitter module and the mass flow rate is so small that the gravity field variations are negligible.

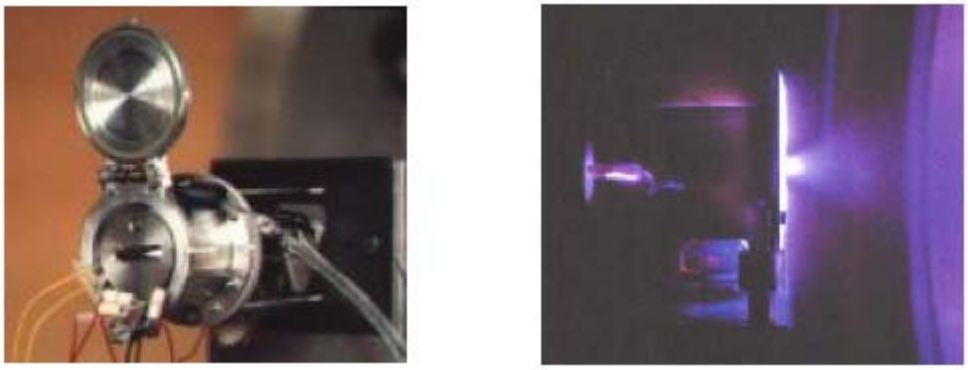

Figure 2.4.1-4: Caesium FEEP developed by Centrospazio/Alta in Pisa, Italy, Ref. [17]

The current baseline FEEP system on each LISA spacecraft consists of three four-thruster clusters positioned around the spacecraft at 120º intervals (Figure 2.4.1-5 left side). The thrusters in each cluster are mounted at 90º separation from each other (Figure 2.4.1-5 right side) and angled such that they do not act within the same plane and also to ensure that the thrust plumes do not impinge on the sunshield or cross the telescope FOVs. Additionally, a full second set of FEEP clusters is included in order to provide full redundancy. This FEEP configuration provides the required full 6 DOF control authority to the spacecraft.

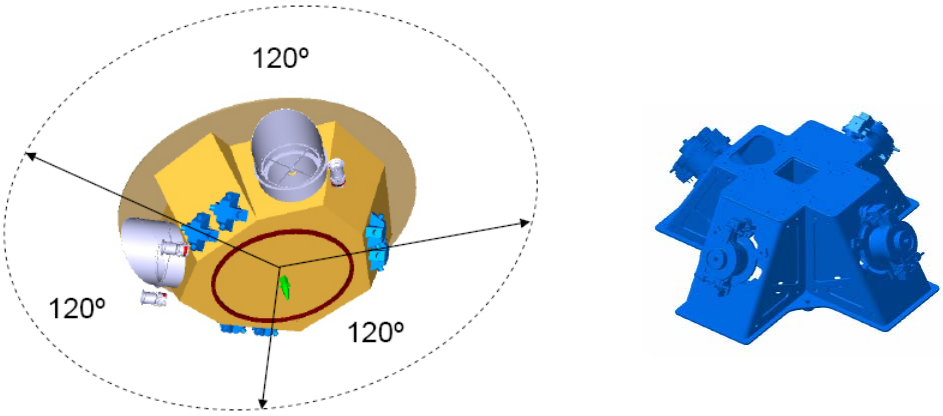

Figure 2.4.1-5: FEEP geometrical layout on the spacecraft (left) and FEEP cluster module geometry (right), Ref. [11]

2.4.2 Electrostatic Suspension System

The electrostatic suspension system must provide force and torque actuation capability of all 6 degree of freedom (3 linear and 3 angular coordinates) of the test mass.

The electrode configuration of the electrode housing assembly providing electrostatic actuation and read-out is presented in Figure 2.4.2-1. The yellow electrodes are the actuation electrodes in the sensitive axis. The red electrodes are the actuation electrodes in the non-sensitive axes and the green electrodes are the injection electrodes. The injection electrodes in the z-axis are split into two smaller sets due to the large hole for the plungers of the caging mechanism.

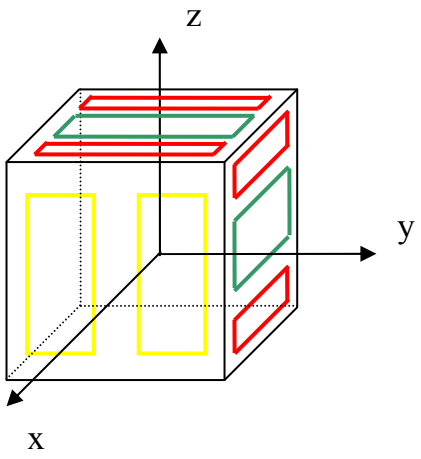

Figure 2.4.2-1: LISA electrode configuration

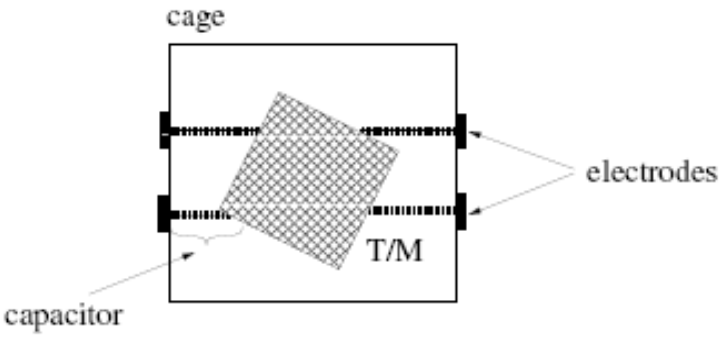

Figure 2.4.2-2: Electrostatic actuation and measurement principle, Ref. [21]

Figure 2.4.2-1 depicts the one-dimensional electrostatic actuation principle. The test mass, a cube made of gold-platinum, is nothing more than a solid, homogeneous piece

of metal. Each side of the cubic test mass can be regarded as one capacitor plate. These plates and the electrodes included in the housing cage result in several capacitors, thus the forces and torques acting on the test mass are the effect of interelectrode capacitance.

The noise shape filter for the force and the torque disturbance noise introduced by the electrostatic suspension system is shown in Figure 2.4.2-3. Note that force noise is a factor 15 worse on the y axis and z axis compared to the x axis, while the torque noise, which is computed as the corresponding force noise multiplied for the edge length of the T/M, is a factor of 100 better than the y-z axis force noise. The noise increase at lower frequencies is designed such that the acceleration noise requirement for the *science mode* is met.

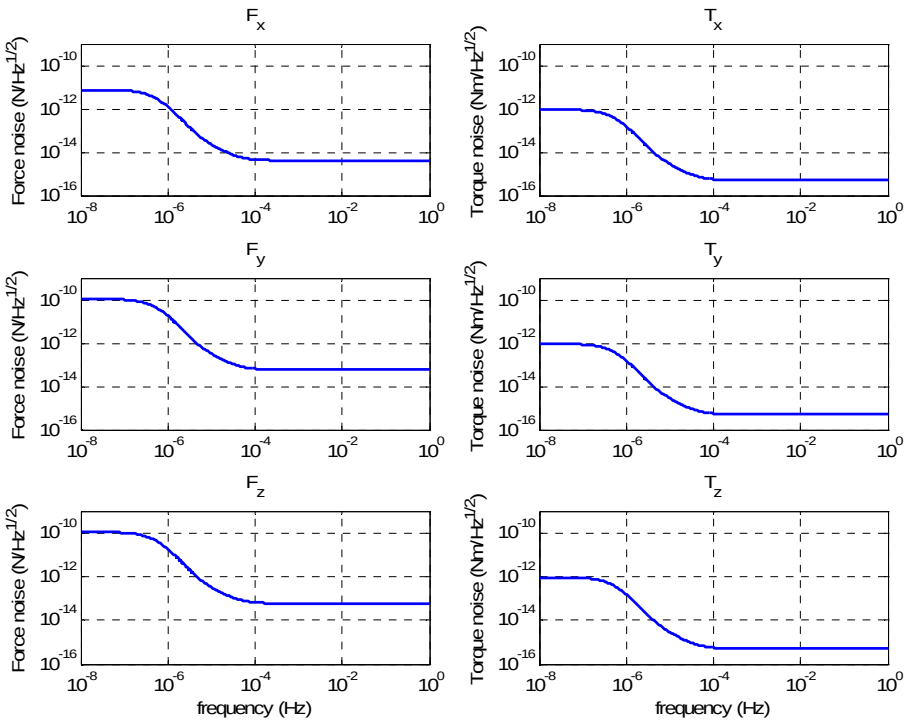

Figure 2.4.2-3: Electrostatic actuation system noise shape filter (bilogarithmic scale)

2.4.3 Telescope Pointing Actuator System

The telescope pointing actuator system is a single-axis mechanism that must provide the force to rotate around the z axis of Figure 2.4.3-1 the movable optical assembly (MOA), consisting of the telescope, the optical bench and the gravity reference sensor

containing the test mass. In this way, a change of the telescope line-of-sight is possible. For the baseline concept it's assumed that the centre of rotation is near the test mass body frame to minimize the self gravity variations.

This mechanism is addressed as the optical assembly tracking mechanism (OATM). For redundancy reason, each of the two MOA on each LISA spacecraft is equipped with an OATM, although just the in-plane angle of one telescope on each LISA spacecraft needs to be actuated. The overall operational telescope tracking range will be of ± 1.5° (TBC) around the mean position. This requirement comes from the *science mode* rather than the acquisition phase. In fact the angle between the two lines-of sight of the two telescope of one spacecraft, which is nominally 60°, is subject to seasonal variation of ±1° due to orbital mechanics.

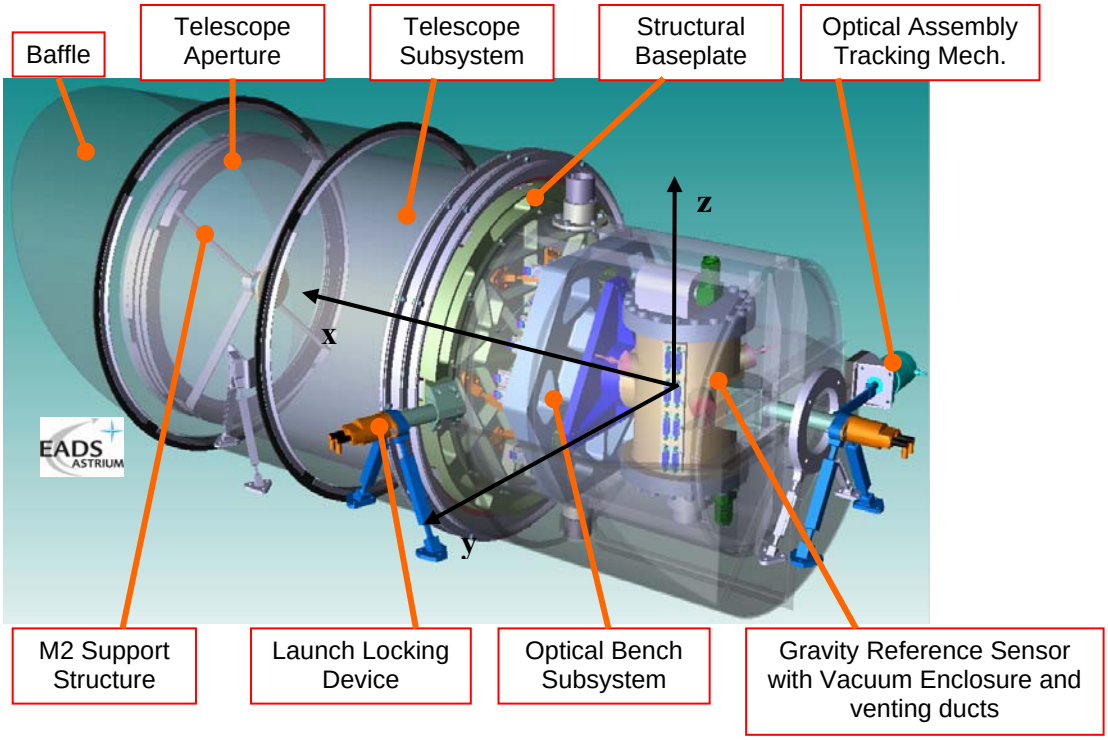

Figure 2.4.3-1: LISA movable optical assembly configuration, Ref. [11]

The actuation disturbance noise introduced by the OATM can be represented as white noise with a constant power spectral density equal to 60 nN/√Hz.

2.5 Sensors for Acquisition Control

The sensor systems used for acquisition control are:

- star trackers
- electrostatic read-out system
- telescope pointing position sensor

The sampling rates at which sensor data are considered available are limited to ~ 10 Hz for the same reasons explained in section 2.4.

2.5.1 Star Trackers

The inertial attitude angles (Θ_B, H_B, Φ_B) of the spacecraft are determined by using one autonomous star tracker (AST), even if two of them are provided for redundancy.

The principle of this measurement system is to compare the star field seen by the star tracker with a known star map. Based on this comparison, it is possible to determine the attitude angles of the spacecraft with respect to the inertial frame.

The STRs are approximately aligned with the x axis of the body fixed satellite frame (Figure 2.5.1-1) that is towards the constellation centre-point along the symmetry axis between the two LISA arms in their nominal 60 deg position.

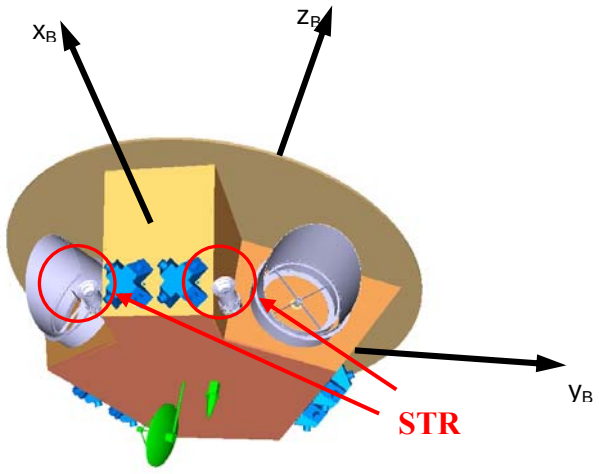

Figure 2.5.1-1: LISA star trackers location, Ref. [11]

Since Θ_B represents the roll angle of the spacecraft exactly around the x axis of the body fixed satellite frame, the read-out noise on this angle has to be considered 10 times worst than the other two angles read-out noise.

The commercial star tracker used on TerraSAR-X is assumed as a baseline and its properties are summarized in Table 2.5.1-1.

Quantity	**Requirement**
Field-of-View	17.5° x 13.5°
CCD size	1360 x 1024 pixel
Magnitude Sensitivity	+ 6.5
Overall Accuracy: - Pitch/Yaw (RMS 3σ) - Roll (RMS 3σ)	 29 μrad (6 arcsec) 290 μrad (60 arcsec)

Table 2.5.1-1: Preliminary performance requirements for the STR (TBC)

2.5.2 Electrostatic Read-Out System

The electrostatic read-out system must provide all 6 position and angular coordinate measurements of a test mass with respect to the housing cage.

The electrostatic measurement is based on the same effect (interelectrode capacitance) as the electrostatic actuation. The electrode configuration of the electrode housing assembly providing electrostatic actuation and read-out was presented in Figure 2.4.2-1. The principle for providing an electrostatic read-out is that a high-frequency signal is injected by the green injection electrodes. The other electrodes are used for electrostatic actuation and sensing.

The noise shape filter for the read-out noise introduced by the electrostatic read-out system is shown in Figure 2.5.2-1. Note that the noise on the position measurements is a factor 1.3 worse on the y axis and 4.2 worse on the z axis compared to the x axis, while the noise on the angular displacement measurements is equal on all axis.

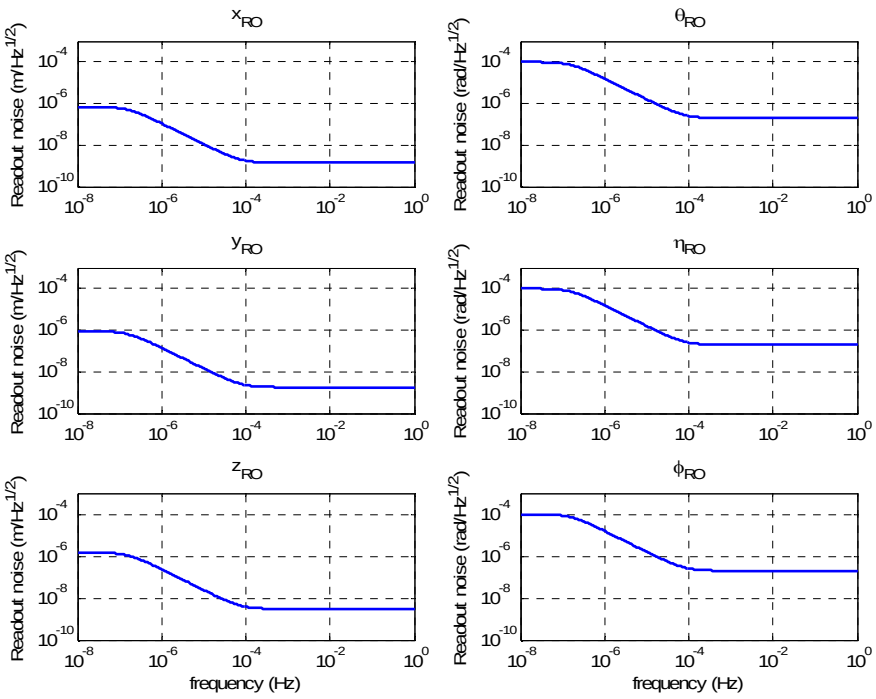

Figure 2.5.2-1: Electrostatic read-out system noise shape filter (bilogarithmic scale)

Several options are possible for providing an additional optical read-out of the test mass using laser interferometry. The major benefit of an optical read-out is a reduction in the noise level of the sensor signal. However, the optical measurement system is not available during acquisition.

2.5.3 Telescope Pointing Position Sensor

The optical assembly tracking mechanism introduced in section 2.4.3 is provided by a sensor device which measures α, the rotation angle around the z axis (in the telescope frame of Figure 2.4.3-1) of the actuated telescope with respect to its nominal position.

The read-out noise introduced by the OATM sensor can be represented as white noise with a constant power spectral density equal to 10 nrad/√Hz.

2.6 LISA Acquisition Phase Control Principle: the Gyro Mode

The process for the single-link acquisition involves two telescopes, each of which belongs to one of the two spacecraft aligned along a constellation arm.

The objective of the control system during the acquisition phase is to provide that the telescopes lines-of-sight attitude is able to follow the guidance law required to perform the acquisition sequence described in section 2.2, complying with the requirements on the allowable errors stated in section 2.3.3.

For the geometry of the constellation, one of the telescopes involved is rigidly attached to its spacecraft and the other can be rotated in the constellation plane using the OATM. Taking for example in consideration the scanning spacecraft, any of its two arms could be used to perform the acquisition. If the arm involved is the one provided with the actuated telescope, the tracking of this telescope will be realised by combining the single-axis pointing mechanism, controlling the angle between the two telescopes of the SC, and the FEEP thrusters, controlling the attitude of the entire spacecraft. The proposed telescope pointing architecture consists in using the attitude control to realise the pointing of the off-plane angle of the involved telescope and in using the pointing mechanism to control the in-plane angle of the telescope. If instead the arm involved is the one with the fixed telescope, the proposed telescope pointing architecture is to use just the attitude control to realise a complete pointing of the telescope. Exactly the same could be repeated for the receiving spacecraft. In any case (actuated or fixed telescope, scanning or receiving spacecraft), the spacecraft attitude guidance law and control are coupled with the telescope pointing guidance law and control. Moreover, the spacecraft attitude guidance law is also determined by the orbital mechanics constraints.

As already said, all this control architecture has to be realised ensuring the fulfillment of the requirements defined in section 2.3.3. Since the inertial wavefront sensor is not yet available during acquisition, the STR has to be used as a spacecraft attitude sensor and the OATM sensor has to be used as a telescope pointing sensor. Both are much more noisy than the IWS. For this reason, the control strategy adopted during the *science mode* is not sufficient by itself to allow the fulfilment of the requirements.

The strategy proposed in this thesis is to adopt a Kalman Filter which uses attitude measurements from the star tracker and pointing measurements from the OATM sensor as well as gyro-like measurements from the two IS units in order to provide an enhanced estimation of the spacecraft attitude and of the telescope in-plane pointing angle. Then the estimations will be fed in closed loop to the controller in place of the

sensors measurement signals. In this way the read-out noise introduced by the STR (which affects all the states since it is fed back in the controller) can be suppressed in the high frequency range allowing the fulfilment of the requirements. This is the so called *gyro mode*. The spacecraft attitude and the telescope pointing control are performed by the *gyro mode* for both spacecraft.

The controller design and the Kalman filter design are, therefore, considered in this work as two independent parts of the whole acquisition control architecture (Figure 1.4-1); hence, they will be presented separately. First the controller design is described demonstrating the necessity of the use of a Kalman filter during the acquisition in order to achieve the requirements, then the Kalman filter design is performed over the existing control system. In the following, *drag-free acquisition mode* addresses the control mode that does not include the Kalman Filter and *gyro mode* indicates the control mode based on the use of the Kalman filter.

Since the *gyro mode* is based on a continuous blend of sensors data (STR, OATM, IS), the gyro-like outputs of the IS must be available. Consequently, the test mass uncaging and the *drag-free mode* must be realised before the acquisition phase can commence.

2.6.1 LISA Drag-Free and Attitude Control System

The classical Drag-Free Satellite can be seen as two satellites in one. A smaller inner, the test mass, is located in a housing inside of a larger normal satellite. The housing contains sensors, which measure the position of the test mass with respect to the outer satellite. The main satellite has small thrusters which are fired such that the satellite chases the test mass which then always remains centered in the housing (Figure 2.6.1-1).

Since the test mass is shielded by the outer satellite from external disturbances (i.e. solar radiation pressure), it follows a trajectory which is determined only by gravity and by the very small internal disturbing forces from the main satellite. Hence the name Drag-Free Satellite since there is no “drag” on the inner test mass and the drag on the main satellite is exactly compensated by the thrusters.

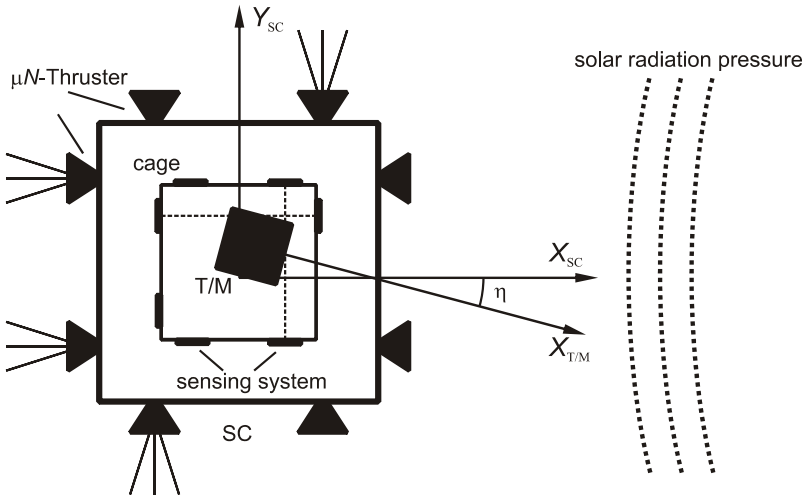

Figure 2.6.1-1: General principle of a drag-free satellite

Drag-Free Satellites offer an environment with the lowest disturbing forces in nature. A properly designed Drag-Free Satellite test mass is decoupled from the rest of the Universe to a remarkable degree. The only disturbances on the test mass arise from the satellite itself (self gravity, electrostatic forces, magnetic forces, brownian motion due to residual gas in the housing etc.) and can be reduced to tolerable values by a careful design and appropriate selection of materials. The satellite is thus forced to chase the test mass, actively shielding it from the non-gravitational forces. The largest of the external non-gravitational forces in case of LISA is the solar radiation pressure.

A more detailed description about Drag-Free Satellites in general is given in [14].

The Drag-Free Satellite LISA is equipped with a disturbance compensation system, the so-called Drag-Free and Attitude Control System (DFACS). Its task is to control the attitude of the spacecraft (Θ_B, H_B, Φ_B), the in-plane pointing angle of telescope 1 (α) and the position and attitude of the two test masses (x_i, y_i, z_i, θ_i, η_i, φ_i; i =1,2). Thus, a total of 16 coordinates have to be controlled. While the spacecraft attitude has to be controlled in the inertial frame, the telescope articulation is controlled with respect to the spacecraft and the test masses are controlled relatively to their housing frames. All coordinates are independently controlled by SISO controllers. For the control of the test mass coordinates, two different control principles are available, either drag-free or suspension control.

2.6.2 Drag-Free Control Principle

As already mentioned above, in order to have pure free-fall conditions, the test masses must be shielded from any external influence (drag-free). This is accomplished by placing each test mass in a housing in the spacecraft and forcing the satellite to follow the test masses very fast. In other words, the displacement of the test mass in the housing frame is continuously sensed by using the electrostatic read-out of the IS and the measured deviation from the nominal position is used as an input to the propulsion system, that cleans out all the gravitational disturbance forces.

Obviously, since there are two test masses inside each spacecraft, it cannot chase both of them at the same time. In fact the propulsion system can provide 6 force and torque actuation signals, thus a maximum of 6 linear independent test mass coordinates can be drag-free controlled. The main science requirement asks for a complete drag-free control along the sensitive axis (x axis) of the two test masses. Including also the displacement along the z direction of the first test mass in order to compensate the solar dynamic pressure, a set of three drag-free coordinates (x_1, z_1, x_2) results and, therefore, only the translational command (forces) capability of the micro-propulsion system is required.

The concept is illustrated by Figure 2.6.2-1.

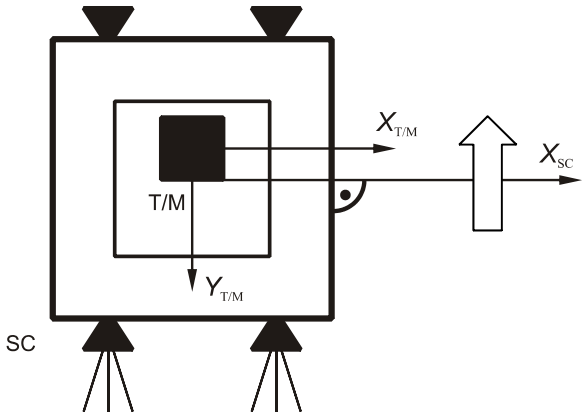

Figure 2.6.2-1: Principle of drag-free controller

2.6.3 Suspension Control Principle

The 9 test mass coordinates that do not have drag-free requirements have to be kept at their nominal position with respect to the housing cages by using the electrostatic

suspension actuation system of the IS. In other words, the suspension system has to make the suspension coordinates following the spacecraft. This is especially necessary due to the inherent negative stiffness of the test masses dynamics which would otherwise yield an unstable system.

The principle of the electrostatic suspension system is shown in Figure 2.6.3-1.

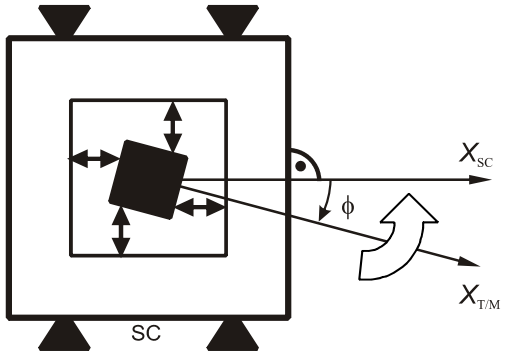

Figure 2.6.3-1: Principle of suspension controller

The suspension control loop operates at frequencies below the science measurement bandwidth. In other words, the suspension coordinates can only be moved very "soft" and slow, otherwise the science measurement is influenced.

2.6.4 Spacecraft Attitude Control Principle

During the *drag-free acquisition mode*, the inertial spacecraft attitude control is performed by feeding back the attitude measurements from the star tracker to the micro-propulsion system. Torque command capability of the FEEP can be entirely used for this purpose since, as already stated, only the force capability is required for the drag-free control.

2.6.5 Telescopes Pointing Control Principle

Telescope tracking control is a process in which the telescope is moved continuously over its working range at extremely low velocity and at extremely high accuracy. It is mandatory to control this process in closed loop by feeding back the sensing signal provided by the OATM sensor to the telescope pointing mechanism.

Remark

The acquisition controller requirements consist of spacecraft attitude and telescope in-plane pointing angle requirements as they are presented in section 2.3.3, while there is no need to fulfil the science requirements in term of acceleration noise or jitter on the test masses during acquisition even if the acquisition controller must be design such that the required suspension actuation forces and torques could be reasonably provided by the IS.

All the performance requirements, the sensors and actuators constraints introduced in this chapter have to be considered as a baseline for the controller design process. Within the purpose of this thesis is to verify the fulfilment of the performance requirements under the baseline constraints and, moreover, to derive different requirements (stricter or more relaxed) for the sensor system and for the acquisition controller when it is proved to be necessary or convenient.

Chapter 3

Mathematical Modelling of a Drag-Free Satellite

In order to perform a control engineering design, it is mandatory to have a mathematical model of the plant to be controlled. In this chapter, the equations of motion (EoM) of a drag-free satellite are illustrated. Their analytical derivation can be found in [5].
In general, a drag-free controlled satellite consists of the following rigid bodies:

- the rigid satellite body (6 DOF)
- one or more rigid test masses (6 DOF each)
- fixed or moving rigid test mass cages (6 DOF each if moving)

Each LISA satellite is a particular case of a drag-free satellite: it features a satellite (6 DOF) with two test masses (12 DOF), one of the test masses is floated inside a one-axis movable cage (1 DOF), the other is moving freely inside a fixed cage (0 DOF). This leads a rather complex 19 DOF system.

3.1 Nomenclature, Definitions and Reference Frames

For the derivation of the equations of motion, all necessary vector definitions are depicted in Figure 3.1-1.

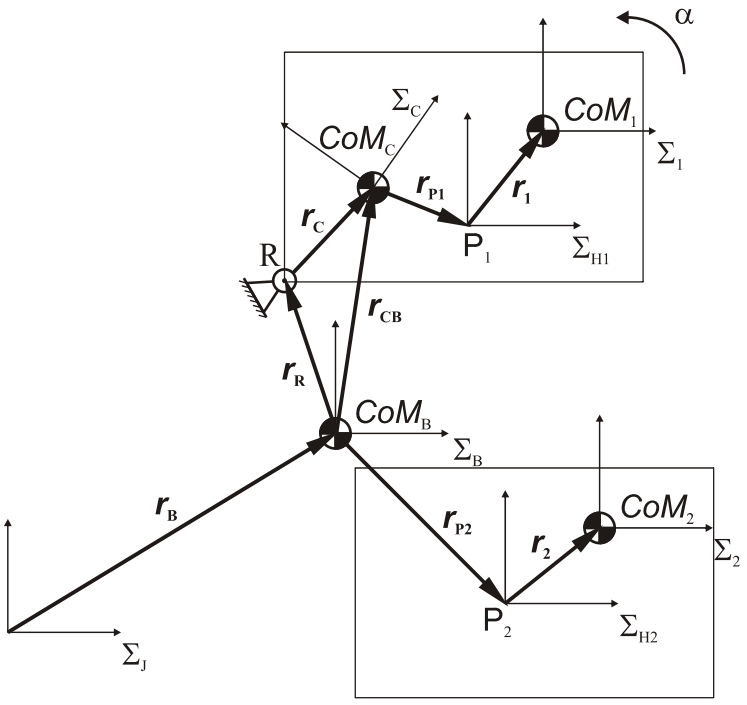

Figure 3.1-1: Definition of vectors and reference frames

3.1.1 Reference Frames

The reference frames used are hereby listed:

- Σ_J is the inertial reference frame;
- Σ_B is the spacecraft (body fixed) reference frame; it is attached to the CoM of the SC with the x-axis pointing along the symmetry axis between the two LISA arms in their nominal 60° position, the z-axis pointing toward the solar panel and the y-axis augments the system to a right-handed coordinate frame (Figure 3.1.1-1);
- Σ_C is the reference frame of the moving cage (telescope, cage and telescope/cage have to be considered synonyms); its x-axis is parallel to the sensitive axis pointing from the inner to the outer of the SC, the z-axis pointing toward the solar panel and the y-axis augments the system to a right-handed coordinate frame. The moving cage, indicated as cage 1 and containing the test mass 1 (T/M1), is located in the SC body frame on the positive y_B axis side (Figure 3.1.1-1), while the fixed cage, indicated as cage 2 and containing the test mass 2 (T/M2), is located in the SC body frame on the negative y_B axis side;

- Σ_{Hi} is the IS housing reference frame; it is used for the T/M position and attitude measurements;
- Σ_i is T/Mi (body fixed) reference frame; it is attached to the CoM of the test mass with its x-axis parallel to the sensitive axis, the z-axis pointing toward the solar panel and the y-axis augments the system to a right-handed coordinate frame.

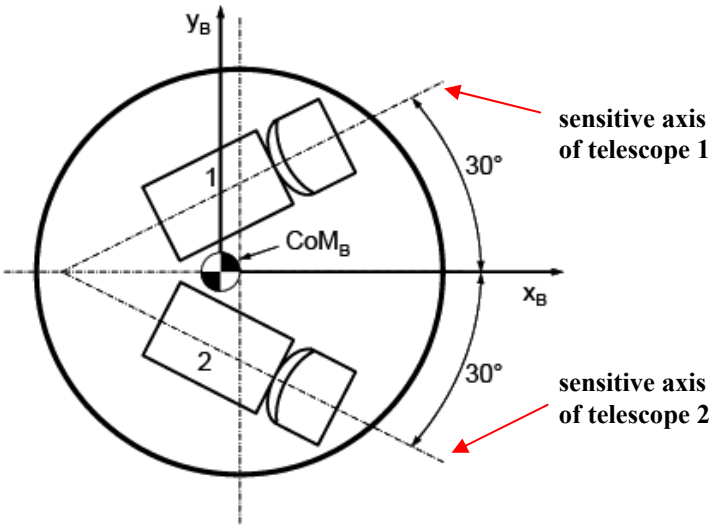

Figure 3.1.1-1: Definition of the spacecraft body frame, Ref. [10]

Scalars are presented as small, normal letters. Vectors are presented as small, bold letters. Matrices are presented as capital, bold letters.

The vector notation adopted is defined by the following rules: a vector named $\mathbf{r_X}$ is the vector for the body X given in its local frame (i.e. the origin vector), as defined in Figure 3.1-1; a vector named $\mathbf{r_{XY}}$ gives the vector position of the body X w.r.t the body Y in the local frame of the latter.

Furthermore, in order to clarify the meaning of the angular velocities, the following definitions are given:

- $\boldsymbol{\omega}_\mathbf{B} = [\dot{\Theta}_B \;\; \dot{H}_B \;\; \dot{\Phi}_B]^T$: angular velocity of the spacecraft in Σ_B w.r.t. Σ_J;
- $\dot{\alpha}$: angular velocity of the moving cage in Σ_C w.r.t. Σ_B;
- $\boldsymbol{\omega}_\mathbf{i} = [\dot{\theta}_i \;\; \dot{\eta}_i \;\; \dot{\phi}_i]^T$: angular velocity of the T/Mi in Σ_i w.r.t. Σ_{Hi}.

As custom, given a generic vector $\mathbf{v}$, then the definition

$$\tilde{v} = \begin{pmatrix} 0 & -v_z & v_y \\ v_z & 0 & -v_x \\ -v_y & v_x & 0 \end{pmatrix}$$

follows and, thus, it can be written $\mathbf{v} \times \mathbf{r} = \tilde{\mathbf{v}}\,\mathbf{r}$ and $\tilde{\mathbf{v}}\,\tilde{\mathbf{v}} = \tilde{\mathbf{v}}^2$.

The symbols **l** and **f** are applied torques and forces. All torques are given in the associated body frame, while all forces are given in the inertial coordinate frame. Further symbols are given in Tables 3.1.1-1 and 3.1.1-2.

Symbol	Description
B or SC	Spacecraft Body
C	Telescope/Cage
H	Test Mass Housing
1	Test mass 1
2	Test mass 2
P	Reference Point for Test Mass Measurement
R	Telescope Rotation Point
A	Telescope Actuator Mounting Point

Table 3.1.1-1: List of indices

Symbol	Description
$\mathbf{q}$	Generalized coordinates vector
$\mathbf{E}_{i\times i}$	Unit diagonal matrix of size *i*
$\mathbf{0}_{X\times Y}$	Matrix of zeros
m_X	Mass of body X
$\mathbf{I}_X$	Matrix of inertia around the CoM for body X
$\mathbf{T}_{XY}$	Transformation matrix from body X frame to body Y frame
$\mathbf{j}_R$	Orientation vector of the cage rotational axis given in the cage frame
$\mathbf{i}_A$	Orientation vector of the cage actuation force given in the cage frame

Table 3.1.1-2: Symbols and definitions

3.2 Equations of Motion

In order to derive the EoM of the satellite, the test masses and the cage bodies, as well as for the overall system differential equations, d'Alembert's Principle is used. Combined with the Newton-Euler equations of rigid body dynamics, the derivation process for the equations of motion is done in a very formal approach and it is reported in reference [5].

The linearization, which is described in [8], is done assuming a unity matrix for the reference attitudes and reference positions at the equilibrium point.

Finally, the linear second-order differential equations of motion of each LISA satellite are

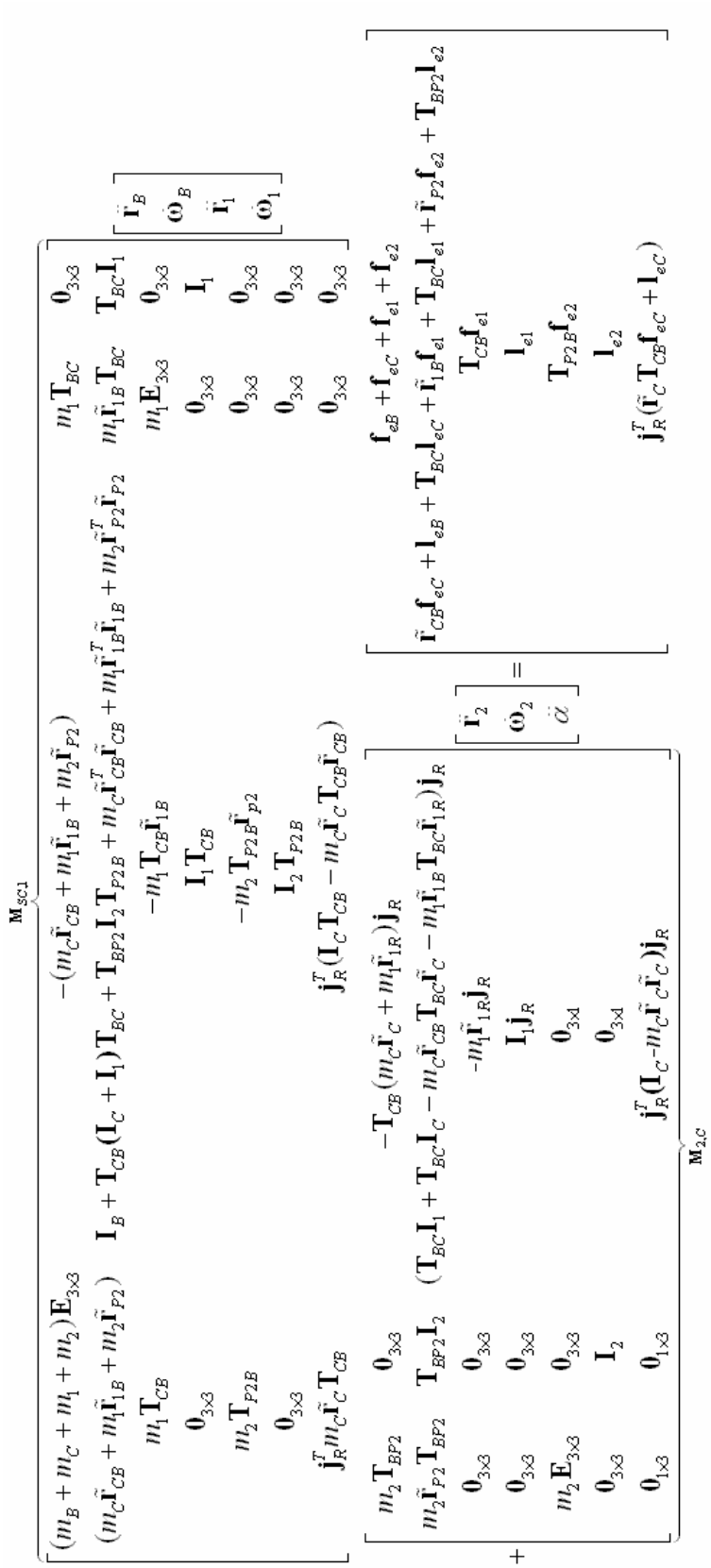

$$\mathbf{M}_{SC1}\begin{bmatrix} \ddot{\mathbf{r}}_B \\ \dot{\boldsymbol{\omega}}_B \\ \ddot{\mathbf{r}}_1 \\ \dot{\boldsymbol{\omega}}_1 \end{bmatrix} + \mathbf{M}_{2C}\begin{bmatrix} \ddot{\mathbf{r}}_2 \\ \dot{\boldsymbol{\omega}}_2 \\ \ddot{\alpha} \end{bmatrix} = \begin{bmatrix} \mathbf{f}_{eB}+\mathbf{f}_{eC}+\mathbf{f}_{e1}+\mathbf{f}_{e2} \\ \tilde{\mathbf{r}}_{CB}\mathbf{f}_{eC}+\mathbf{l}_{eB}+\mathbf{T}_{BC}\mathbf{l}_{eC}+\tilde{\mathbf{r}}_{1B}\mathbf{f}_{e1}+\mathbf{T}_{BC}\mathbf{l}_{e1}+\tilde{\mathbf{r}}_{P2}\mathbf{f}_{e2}+\mathbf{T}_{BP2}\mathbf{l}_{e2} \\ \mathbf{T}_{CB}\mathbf{f}_{e1} \\ \mathbf{l}_{e1} \\ \mathbf{T}_{P2B}\mathbf{f}_{e2} \\ \mathbf{l}_{e2} \\ \mathbf{j}_R^T(\tilde{\mathbf{r}}_C\mathbf{T}_{CB}\mathbf{f}_{eC}+\mathbf{l}_{eC}) \end{bmatrix} \tag{3.1}$$

$$\mathbf{M}_{SC1} = \begin{bmatrix} (m_B+m_C+m_1+m_2)\mathbf{E}_{3\times3} & -(m_C\tilde{\mathbf{r}}_{CB}+m_1\tilde{\mathbf{r}}_{1B}+m_2\tilde{\mathbf{r}}_{P2}) & m_1\mathbf{T}_{BC} & \mathbf{0}_{3\times3} \\ (m_C\tilde{\mathbf{r}}_{CB}+m_1\tilde{\mathbf{r}}_{1B}+m_2\tilde{\mathbf{r}}_{P2}) & \mathbf{I}_B+\mathbf{T}_{CB}(\mathbf{I}_C+\mathbf{I}_1)\mathbf{T}_{BC}+\mathbf{T}_{BP2}\mathbf{I}_2\mathbf{T}_{P2B}+m_C\tilde{\mathbf{r}}_{CB}^T\tilde{\mathbf{r}}_{CB}+m_1\tilde{\mathbf{r}}_{1B}^T\tilde{\mathbf{r}}_{1B}+m_2\tilde{\mathbf{r}}_{P2}^T\tilde{\mathbf{r}}_{P2} & m_1\tilde{\mathbf{r}}_{1B}\mathbf{T}_{BC} & \mathbf{T}_{BC}\mathbf{I}_1 \\ m_1\mathbf{T}_{CB} & -m_1\mathbf{T}_{CB}\tilde{\mathbf{r}}_{1B} & m_1\mathbf{E}_{3\times3} & \mathbf{0}_{3\times3} \\ \mathbf{0}_{3\times3} & \mathbf{I}_1\mathbf{T}_{CB} & \mathbf{0}_{3\times3} & \mathbf{I}_1 \\ m_2\mathbf{T}_{P2B} & -m_2\mathbf{T}_{P2B}\tilde{\mathbf{r}}_{P2} & \mathbf{0}_{3\times3} & \mathbf{0}_{3\times3} \\ \mathbf{0}_{3\times3} & \mathbf{I}_2\mathbf{T}_{P2B} & \mathbf{0}_{3\times3} & \mathbf{0}_{3\times3} \\ \mathbf{j}_R^Tm_C\tilde{\mathbf{r}}_C\mathbf{T}_{CB} & \mathbf{j}_R^T(\mathbf{I}_C\mathbf{T}_{CB}-m_C\tilde{\mathbf{r}}_C\mathbf{T}_{CB}\tilde{\mathbf{r}}_{CB}) & \mathbf{0}_{3\times3} & \mathbf{0}_{3\times3} \end{bmatrix}$$

$$\mathbf{M}_{2C} = \begin{bmatrix} m_2\mathbf{T}_{BP2} & \mathbf{0}_{3\times3} & -\mathbf{T}_{CB}(m_C\tilde{\mathbf{r}}_C+m_1\tilde{\mathbf{r}}_{1R})\mathbf{j}_R \\ m_2\tilde{\mathbf{r}}_{P2}\mathbf{T}_{BP2} & \mathbf{T}_{BP2}\mathbf{I}_2 & (\mathbf{T}_{BC}\mathbf{I}_1+\mathbf{T}_{BC}\mathbf{I}_C-m_C\tilde{\mathbf{r}}_{CB}\mathbf{T}_{BC}\tilde{\mathbf{r}}_C-m_1\tilde{\mathbf{r}}_{1B}\mathbf{T}_{BC}\tilde{\mathbf{r}}_{1R})\mathbf{j}_R \\ \mathbf{0}_{3\times3} & \mathbf{0}_{3\times3} & -m_1\tilde{\mathbf{r}}_{1R}\mathbf{j}_R \\ \mathbf{0}_{3\times3} & \mathbf{0}_{3\times3} & \mathbf{I}_1\mathbf{j}_R \\ m_2\mathbf{E}_{3\times3} & \mathbf{0}_{3\times3} & \mathbf{0}_{3\times1} \\ \mathbf{0}_{3\times3} & \mathbf{I}_2 & \mathbf{0}_{3\times1} \\ \mathbf{0}_{1\times3} & \mathbf{0}_{1\times3} & \mathbf{j}_R^T(\mathbf{I}_C-m_C\tilde{\mathbf{r}}_C\tilde{\mathbf{r}}_C)\mathbf{j}_R \end{bmatrix}$$

The whole system of forces and torques (right hand side of Eq. (3.1)) acting on the satellite, the two test masses and on the telescope/cage are described, broken down and partially neglected according to what is reported in [13] and in [8]. The following outline resembles the actual way forces and torques are schematized in the simulator for the controller design process.

Actions on the spacecraft are:

- control forces and torques inputs (FEEP actuations);
- disturbance forces and torques divided in:
  - FEEP actuation noises
  - solar pressure forces and torques noises
  - DC solar forces and torques
- counter-forces and counter-torques due to T/M2 (electrostatic suspension actuations);
- counter-forces due to telescope/cage (telescope pointing actuation and telescope bearing reactions).

Controls and disturbances constitute the external forces and torques which are illustrated in Figure 3.2-1 together with all the other mentioned actions. The solar radiation force shape filter is shown in Figure 3.2-2.

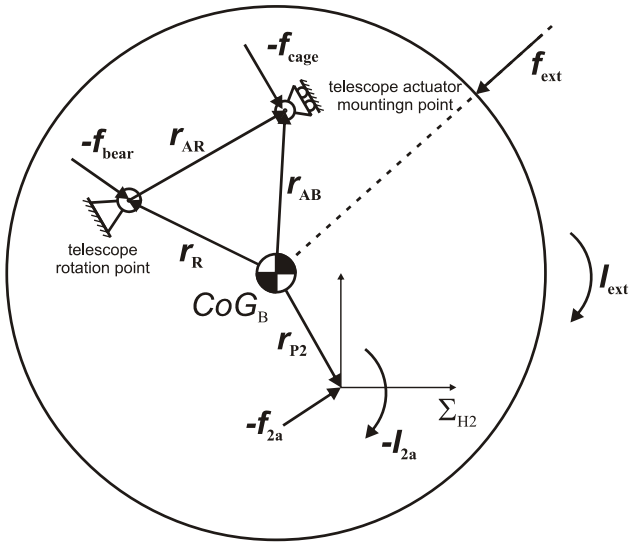

Figure 3.2-1: Forces and torques acting on the spacecraft, Ref. [8]

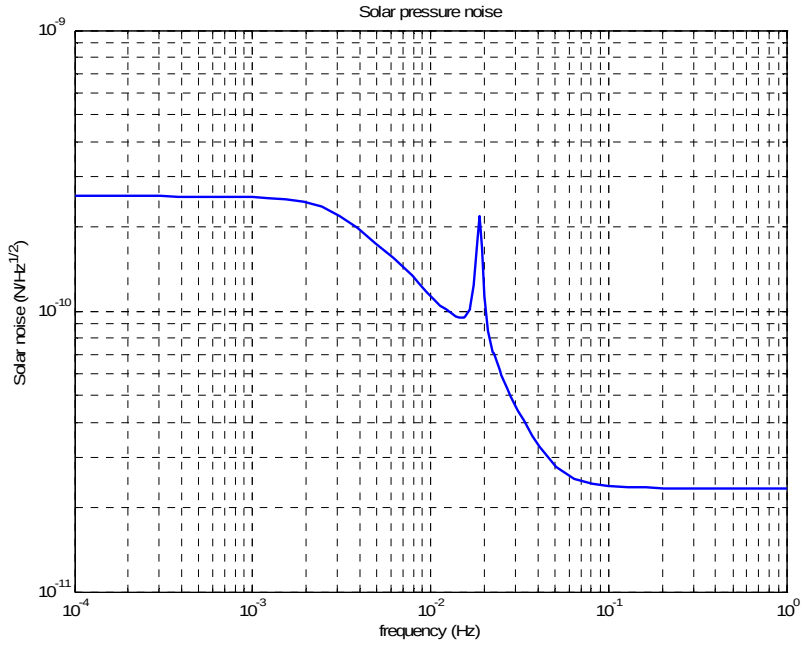

Figure 3.2-2: Solar pressure noise shape filter

Actions on the telescope/cage are (Figure 3.2-3):

- control force (telescope pointing actuation);
- disturbance force (telescope pointing actuation noise);
- counter-forces and counter-torques due to T/M1 (electrostatic suspension actuations);
- bearing force.

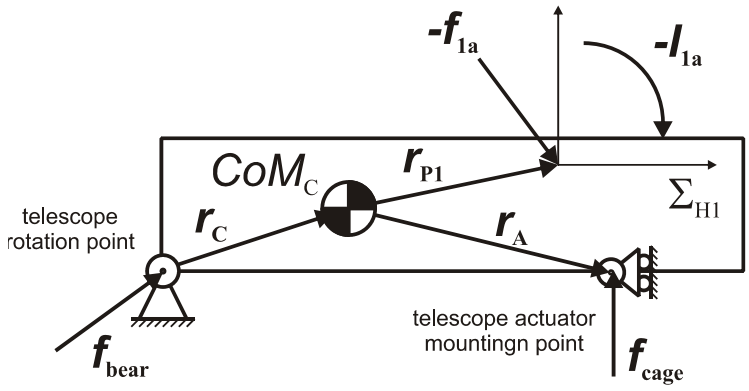

Figure 3.2-3: Forces and torques acting on the telescope cage, Ref. [8]

Actions on the test masses are:

- control forces and torques inputs (electrostatic suspension actuations);
- disturbance forces and torques (electrostatic suspension actuation noises);
- forces and torques due to satellite and test mass coupling (i.e. stiffness); their origin can be:
  - gravitational
  - electrostatic
  - magnetic
- DC parasitic forces and torques coming from the following physical phenomena:
  - electric fields
  - magnetic fields
  - thermal gradients via radiation pressure, radiometer effect or out-gassing
  - laser radiation pressure (if the optical read-out is used)
  - gravity field

Introducing the above stated forces and torques in the right hand side of Eq. (3.1) and operating the simplifications described in [8], the mentioned right hand side becomes

$$\mathbf{M}\overbrace{\begin{bmatrix}\mathbf{0}_{6\times6} & \mathbf{0}_{6\times6} & \mathbf{0}_{6\times6} & \mathbf{0}_{6\times1}\\ \mathbf{0}_{6\times6} & \boldsymbol{\Omega}_1 & \mathbf{0}_{6\times6} & \mathbf{0}_{6\times1}\\ \mathbf{0}_{6\times6} & \mathbf{0}_{6\times6} & \boldsymbol{\Omega}_2 & \mathbf{0}_{6\times1}\\ \mathbf{0}_{1\times6} & \mathbf{0}_{1\times6} & \mathbf{0}_{1\times6} & \mathbf{0}_{1\times1}\end{bmatrix}}^{\boldsymbol{\Omega}_{19\times19}}\begin{bmatrix}\mathbf{r}_B\\ \boldsymbol{\alpha}_B\\ \mathbf{r}_1\\ \boldsymbol{\alpha}_1\\ \mathbf{r}_2\\ \boldsymbol{\alpha}_2\\ \alpha\end{bmatrix}+\overbrace{\begin{bmatrix}\mathbf{E}_{3\times3} & \mathbf{0}_{3\times3}\\ \mathbf{0}_{3\times3} & \mathbf{E}_{3\times3}\\ \mathbf{0}_{13\times3} & \mathbf{0}_{13\times3}\end{bmatrix}}^{\hat{\mathbf{B}}_{sc}}\begin{bmatrix}\mathbf{f}_{FEEP}\\ \mathbf{l}_{FEEP}\end{bmatrix}+\overbrace{\begin{bmatrix}\mathbf{0}_{3\times3} & \mathbf{0}_{3\times3} & \mathbf{0}_{3\times3} & \mathbf{0}_{3\times3} & \mathbf{0}_{3\times1}\\ \mathbf{0}_{3\times3} & \mathbf{0}_{3\times3} & \mathbf{0}_{3\times3} & \mathbf{0}_{3\times3} & \mathbf{0}_{3\times1}\\ & & \mathbf{h}_{IS} & & \mathbf{0}_{3\times1}\\ & & & & \mathbf{0}_{3\times1}\\ & & & & \mathbf{0}_{3\times1}\\ & & & & \mathbf{0}_{3\times1}\\ -\mathbf{j}_R^T\tilde{\mathbf{r}}_{1R} & -\mathbf{j}_R^T & \mathbf{0}_{1\times3} & \mathbf{0}_{1\times3} & \mathbf{j}_R^T(\tilde{\mathbf{r}}_C+\tilde{\mathbf{r}}_A)\end{bmatrix}}^{\hat{\mathbf{B}}_{12,C}}\begin{bmatrix}\mathbf{f}_{1a}^{(C)}\\ \mathbf{l}_{1a}\\ \mathbf{f}_{2a}^{(2)}\\ \mathbf{l}_{2a}\\ \mathbf{i}_A^{(C)}f_{cage}\end{bmatrix}+$$

$$+\underbrace{\begin{bmatrix}\mathbf{E}_{3\times3} & \mathbf{0}_{3\times3} & \mathbf{E}_{3\times3} & \mathbf{0}_{3\times3}\\ \mathbf{0}_{3\times3} & \mathbf{E}_{3\times3} & \mathbf{0}_{3\times3} & \mathbf{E}_{3\times3}\\ \mathbf{0}_{13\times3} & \mathbf{0}_{13\times3} & \mathbf{0}_{13\times3} & \mathbf{0}_{13\times3}\end{bmatrix}}_{\hat{\mathbf{F}}_{sc}}\begin{bmatrix}\mathbf{f}_{sol,d}\\ \mathbf{l}_{sol,d}\\ \mathbf{f}_{FEEP,d}\\ \mathbf{l}_{FEEP,d}\end{bmatrix}+\underbrace{\begin{bmatrix}\mathbf{T}_{BC} & \mathbf{0}_{3\times3} & \mathbf{T}_{BP2} & \mathbf{0}_{3\times3} & \mathbf{0}_{3\times1}\\ \tilde{\mathbf{r}}_{1B}\mathbf{T}_{BC} & \mathbf{T}_{BC} & \tilde{\mathbf{r}}_{2B}\mathbf{T}_{BP2} & \mathbf{T}_{BP2} & \mathbf{0}_{3\times1}\\ \mathbf{E}_{3\times3} & \mathbf{0}_{3\times3} & \mathbf{0}_{3\times3} & \mathbf{0}_{3\times3} & \mathbf{0}_{3\times1}\\ \mathbf{0}_{3\times3} & \mathbf{E}_{3\times3} & \mathbf{0}_{3\times3} & \mathbf{0}_{3\times3} & \mathbf{0}_{3\times1}\\ \mathbf{0}_{3\times3} & \mathbf{0}_{3\times3} & \mathbf{E}_{3\times3} & \mathbf{0}_{3\times3} & \mathbf{0}_{3\times1}\\ \mathbf{0}_{3\times3} & \mathbf{0}_{3\times3} & \mathbf{0}_{3\times3} & \mathbf{E}_{3\times3} & \mathbf{0}_{3\times1}\\ \mathbf{0}_{1\times3} & \mathbf{0}_{1\times3} & \mathbf{0}_{1\times3} & \mathbf{0}_{1\times3} & \mathbf{j}_R^T(\tilde{\mathbf{r}}_C+\tilde{\mathbf{r}}_A)\end{bmatrix}}_{\hat{\mathbf{F}}_{12,C}}\begin{bmatrix}\mathbf{f}_{1d}^{(C)}\\ \mathbf{l}_{1d}\\ \mathbf{f}_{2d}^{(2)}\\ \mathbf{l}_{2d}\\ \mathbf{i}_A^{(C)}f_{cage,d}\end{bmatrix} \tag{3.2}$$

where:

$\mathbf{f}_{FEEP}, \mathbf{l}_{FEEP}$	FEEP actuations
$\mathbf{f}_{FEEP,d}, \mathbf{l}_{FEEP,d}$	FEEP actuations noise
$\mathbf{f}_{sol,d}, \mathbf{l}_{sol,d}$	Solar disturbances
$\mathbf{f}_{1a}, \mathbf{l}_{1a}$	Electrostatic suspension actuations on T/M1
$\mathbf{f}_{1d}, \mathbf{l}_{1d}$	Disturbances on T/M1
$\mathbf{f}_{2a}, \mathbf{l}_{2a}$	Electrostatic suspension actuations on T/M2
$\mathbf{f}_{2d}, \mathbf{l}_{2d}$	Disturbances on T/M2
f_{cage}	Telescope pointing actuation
$f_{cage,d}$	Telescope pointing actuation noise

$\mathbf{h}_{IS} \in \mathbb{R}^{12x12}$ is a matrix that accounts for the cross-talk effect between different degrees freedom of the electrostatic actuation of the inertial sensors, **M** is the *mass matrix*

$$\mathrm{M} = [\mathrm{M}_{SC,1} \quad \mathrm{M}_{2,C}] \tag{3.3}$$

and $\mathbf{\Omega}_{19\times19}$ is the *stiffness matrix* which provides a coupling between the acceleration and the position coordinates of each test mass while it does not involve the spacecraft and the telescope degrees of freedom.

Using the definitions

$$\hat{\mathbf{B}} = [\hat{\mathbf{B}}_{SC} \quad \hat{\mathbf{B}}_{12,C}] \qquad \hat{\mathbf{F}} = [\hat{\mathbf{F}}_{SC} \quad \hat{\mathbf{F}}_{12,C}]$$

$$\hat{\mathbf{x}} = [\mathbf{r}_B \quad \boldsymbol{\alpha}_B \quad \mathbf{r}_1 \quad \boldsymbol{\alpha}_1 \quad \mathbf{r}_2 \quad \boldsymbol{\alpha}_2 \quad \alpha]^T$$

and introducing the *control input vector* $\mathbf{u} \in \mathbb{R}^{19x1}$ and the *disturbance input vector* $\mathbf{d} \in \mathbb{R}^{25x1}$

$$\mathbf{u} = \begin{bmatrix} \mathbf{f}_{FEEP} \\ \mathbf{l}_{FEEP} \\ \mathbf{f}_{1a}^{(C)} \\ \mathbf{l}_{1a} \\ \mathbf{f}_{2a}^{(2)} \\ \mathbf{l}_{2a} \\ \mathbf{i}_A^{(C)} f_{cage} \end{bmatrix} \qquad \mathbf{d} = \begin{bmatrix} \mathbf{f}_{sol,d} \\ \mathbf{l}_{sol,d} \\ \mathbf{f}_{FEEP,d} \\ \mathbf{l}_{FEEP,d} \\ \mathbf{f}_{1d}^{(C)} \\ \mathbf{l}_{1d} \\ \mathbf{f}_{2d}^{(2)} \\ \mathbf{l}_{2d} \\ \mathbf{i}_A^{(C)} f_{cage,d} \end{bmatrix} \tag{3.4}$$

the complete set of linearized equations of motion can be rewritten as

$$\mathbf{M}\ddot{\hat{\mathbf{x}}} = \mathbf{M}\boldsymbol{\Omega}_{19\times19}\hat{\mathbf{x}} + \hat{\mathbf{B}}\mathbf{u} + \hat{\mathbf{F}}\mathbf{d} \tag{3.5}$$

The dynamics equations (3.5) is exploited for performing the controller design in chapter 4; however, it is convenient to transform Eq. (3.5) into a system of first-order differential linear equations that, together with the measurement equations introduced in section 3.3, constitutes the state space realization of the LISA open-loop dynamics used for the digital implementation in the Matlab/Simulink® environment.

Introducing the *state vector* $\mathbf{x} \in \mathbb{R}^{38x1}$

$$\mathbf{x} = [\dot{\mathbf{r}}_B \;\; \boldsymbol{\omega}_B \;\; \dot{\mathbf{r}}_1 \;\; \boldsymbol{\omega}_1 \;\; \dot{\mathbf{r}}_2 \;\; \boldsymbol{\omega}_2 \;\; \dot{\alpha} \;\; \mathbf{r}_B \;\; \boldsymbol{\alpha}_B \;\; \mathbf{r}_1 \;\; \boldsymbol{\alpha}_1 \;\; \mathbf{r}_2 \;\; \boldsymbol{\alpha}_2 \;\; \alpha]^T \tag{3.6}$$

Eq. (3.5) can be rewritten as

$$\dot{\mathbf{x}} = \underbrace{\begin{bmatrix} \mathbf{0}_{19\times19} & \boldsymbol{\Omega}_{19\times19} \\ \mathbf{E}_{19\times19} & \mathbf{0}_{19\times19} \end{bmatrix}}_{\mathbf{A}}\mathbf{x} + \underbrace{\begin{bmatrix} \mathbf{M}^{-1}\hat{\mathbf{B}} \\ \mathbf{0}_{19\times19} \end{bmatrix}}_{\mathbf{B}}\mathbf{u} + \underbrace{\begin{bmatrix} \mathbf{M}^{-1}\hat{\mathbf{F}} \\ \mathbf{0}_{19\times25} \end{bmatrix}}_{\mathbf{F}}\mathbf{d} \tag{3.7}$$

where:

- **A**: *dynamic matrix*
- **B**: *control input coupling matrix*
- **F**: *disturbance input coupling matrix*

3.3 Measurement Equations

In order to complete the state space system, a set of measurement equations must be introduced

$$\mathbf{y} = \mathbf{H}\mathbf{x} + \mathbf{D}_\mathbf{u}\mathbf{u} + \mathbf{D}_\mathbf{d}\mathbf{d} + \boldsymbol{\nu} \tag{3.8}$$

where **x**, **u**, **d** are defined in section 3.2; instead, $\mathbf{y} \in \mathbb{R}^{16x1}$ is the *measurement vector* representing the measurable states of Eq. (3.7) and it is provided by the sensors system (Eq. 3.9). Note that $\mathbf{q}_{STR_m}$ are the spacecraft inertial attitude angles expressed as rotation around the Σ_B axis and measured by the STR, $\mathbf{q}_{IS_m}$ are the T/M1 and T/M2 coordinates measured by the suspension system in Σ_i w.r.t Σ_{Hi} and $q_{Telescope1_m}$ is the telescope 1 in-plane pointing angle measured by the OATM sensor in Σ_C w.r.t Σ_B:

$$\mathbf{y} = \begin{bmatrix} \boldsymbol{\alpha}_{B_m} \\ \mathbf{r}_{1_m} \\ \boldsymbol{\alpha}_{1_m} \\ \mathbf{r}_{2_m} \\ \boldsymbol{\alpha}_{2_m} \\ \alpha_m \end{bmatrix} = \begin{bmatrix} \mathbf{q}_{STR_m} \\ \mathbf{q}_{IS_m} \\ q_{Telescope1_m} \end{bmatrix} \tag{3.9}$$

H is the *measurement matrix* representing the relationship between measurements and states. Noteworthy is that this relationship is fully linear. The term $\mathbf{g}_{IS} \in \mathbb{R}^{12x12}$ is a cross-talk matrix describing the cross-talk between different degrees of freedom of the electrostatic read-out of the inertial sensors:

$$\mathbf{H} = \begin{bmatrix} \mathbf{0}_{3\times3} & \mathbf{0}_{3\times3} & \mathbf{0}_{3\times12} & \mathbf{0}_{3\times1} & \mathbf{0}_{3\times3} & \mathbf{E}_{3\times3} & \mathbf{0}_{3\times12} & \mathbf{0}_{3\times1} \\ \mathbf{0}_{12\times3} & \mathbf{0}_{12\times3} & \mathbf{0}_{12\times12} & \mathbf{0}_{12\times1} & \mathbf{0}_{12\times3} & \mathbf{0}_{12\times3} & \mathbf{g}_{IS} & \mathbf{0}_{12\times1} \\ \mathbf{0}_{1\times3} & \mathbf{0}_{1\times3} & \mathbf{0}_{1\times12} & \mathbf{0}_{1\times1} & \mathbf{0}_{1\times3} & \mathbf{0}_{1\times3} & \mathbf{0}_{1\times12} & \mathbf{E}_{1\times3} \end{bmatrix} \tag{3.10}$$

D is the *input/output coupling matrix*; since there is no direct relationship between the measurement vector and the control-disturbance inputs, this matrix is empty and will be omitted in the following:

$$\mathbf{D} = [\mathbf{D}_\mathbf{u} \quad \mathbf{D}_\mathbf{d}] = \mathbf{0}_{16\times44} \tag{3.11}$$

Finally, $\mathbf{v} \in \mathbb{R}^{16x1}$ is the *read-out noise vector*:

$$\mathbf{v} = \begin{bmatrix} \mathbf{STR}_{ROnoise} \\ \mathbf{IS}_{ROnoise} \\ \mathbf{CAGE}_{ROnoise} \end{bmatrix} \tag{3.12}$$

where:

- $\mathbf{STR}_{ROnoise} \in \mathbb{R}^{3x1}$ is the read-out noise introduced by the STR
- $\mathbf{IS}_{ROnoise} \in \mathbb{R}^{12x1}$ is the read-out noise introduced by the electrostatic read-out system (Inertial System, IS)
- $\mathbf{CAGE}_{ROnoise} \in \mathbb{R}^{1x1}$ is the read-out noise introduced by the OATM sensor

The state equation (3.7) and the measurement equation (3.8) together form the state space dynamics equations, summarized in Figure 3.3-1. It constitutes the linear, time-invariant model representing the LISA open-loop plant.

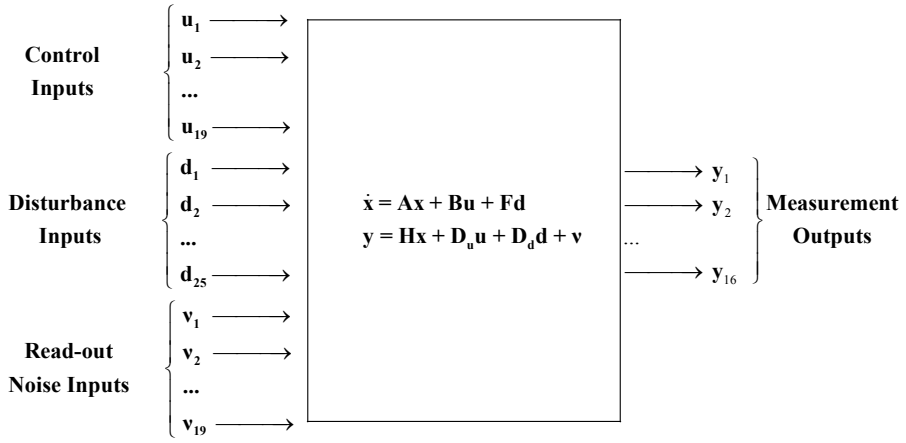

Figure 3.3-1: Block diagram of the open-loop system

Chapter 4

Controller Design

In this chapter, the fundamental points of the controller design strategy are introduced. A more detailed description can be found in [8].

The basic idea for the control system design is to reduce the original MIMO problem into a set of SISO designs by applying a control input decoupling that only relies on mass and geometric properties and, therefore, is completely general. Each SISO design is then performed individually in order to achieve the closed-loop requirements in the measurement bandwidth of the *science mode* and also in order to provide adequate gains and phase margins over a proper range of variations of the SISO plant parameters.

4.1 Decoupling

The starting point for the decoupling strategy is the linearized equations of motion derived in chapter 3 (Eq. (3.5)):

$$\mathbf{M}\ddot{\hat{\mathbf{x}}} = \mathbf{M}\boldsymbol{\Omega}_{19\times19}\hat{\mathbf{x}} + \hat{\mathbf{B}}\mathbf{u} + \hat{\mathbf{F}}\mathbf{d} \tag{3.5}$$

Dividing both sides of Eq. (3.5) for the *mass matrix* **M**, yields

$$\ddot{\hat{\mathbf{x}}} = \boldsymbol{\Omega}_{19\times19}\hat{\mathbf{x}} + \mathbf{M}^{-1}\hat{\mathbf{B}}\mathbf{u} + \mathbf{M}^{-1}\hat{\mathbf{F}}\mathbf{d}$$

As far as the stiffness matrix is concerned, since it is in the form

$$\mathbf{\Omega}_{19\times19} = \begin{bmatrix} \mathbf{0}_{6\times6} & \mathbf{0}_{6\times6} & \mathbf{0}_{6\times6} & \mathbf{0}_{6\times1} \\ \mathbf{0}_{6\times6} & \mathbf{\Omega}_1 & \mathbf{0}_{6\times6} & \mathbf{0}_{6\times1} \\ \mathbf{0}_{6\times6} & \mathbf{0}_{6\times6} & \mathbf{\Omega}_2 & \mathbf{0}_{6\times1} \\ \mathbf{0}_{1\times6} & \mathbf{0}_{1\times6} & \mathbf{0}_{1\times6} & \mathbf{0}_{1\times1} \end{bmatrix}$$

it provides a coupling between the acceleration and the position coordinates of each test mass, while it does not involve the spacecraft and the telescope degrees of freedom.

Having broken down the inputs into controls and disturbances, the disturbance input term $\mathbf{M}^{-1}\hat{\mathbf{F}}$ can obviously be cancelled out from the controller equations, while the control input term $\mathbf{M}^{-1}\hat{\mathbf{B}}$, indicated as $\mathbf{B}^*$ for shortness, has the following structure:

	Col#	1-3	4-6	7-9	10-12	13-15	16-18	19
Row#		$\mathbf{f}_{FEEP}$	$\mathbf{l}_{FEEP}$	$\mathbf{f}_{1a}$	$\mathbf{l}_{1a}$	$\mathbf{f}_{2a}$	$\mathbf{l}_{2a}$	f_{cage}
1-3	$\dot{\mathbf{V}}_{SC}$	…	…	…	…	…	…	…
4-6	$\dot{\boldsymbol{\omega}}_{SC}$	$\mathbf{B}^*_{46,13}$	$\mathbf{B}^*_{46,46}$	…	…	…	…	$\mathbf{B}^*_{46,1919}$
7-18	$\ddot{\mathbf{q}}$	$\mathbf{B}^*_{718,13}$	$\mathbf{B}^*_{718,46}$	$\mathbf{B}^*_{718,79}$	$\mathbf{B}^*_{718,1012}$	$\mathbf{B}^*_{718,1315}$	$\mathbf{B}^*_{718,1618}$	$\mathbf{B}^*_{718,1919}$
19	$\ddot{\alpha}$	$\mathbf{B}^*_{1919,13}$	$\mathbf{B}^*_{1919,46}$	…	…	…	…	$\mathbf{B}^*_{1919,1919}$

$$\mathbf{M}^{-1}\hat{\mathbf{B}} = \mathbf{B}^*$$

Since the feedback from the suspension actuators to the telescope degree of freedom and to the spacecraft degrees of freedom is negligible for the control design (as indicated by the dots), the following definitions can be used

$$\mathbf{B}_{DF} = \begin{bmatrix} \mathbf{B}^*_{718,13} & \mathbf{B}^*_{718,1919} \\ \mathbf{B}^*_{1919,13} & \mathbf{B}^*_{1919,1919} \end{bmatrix}$$

$$\mathbf{B}_{att} = \mathbf{B}^*_{46,46}$$

$$\mathbf{B}_{sus} = \begin{bmatrix} \mathbf{B}^*_{718,79} & \mathbf{B}^*_{718,1012} & \mathbf{B}^*_{718,1315} & \mathbf{B}^*_{718,1618} \end{bmatrix}$$

where:

- $\mathbf{B}_{DF}$: drag-free control matrix
- $\mathbf{B}_{att}$: spacecraft attitude control matrix
- $\mathbf{B}_{sus}$: suspension control matrix

The previous matrices have been determined on the basis of the control principles described in chapter 2:

- The three drag-free coordinates (x_1, z_1, x_2) control is obtained by using only the translational command (forces) capability of the micro-propulsion system;
- The telescope 1 in-plane pointing angle (α) is controlled by using the force provided by the telescope pointing mechanism, which has been included in the drag-free control matrix just for convenience;
- The spacecraft inertial attitude (Θ_B, H_B, Φ_B) control is performed by using the torque commanding capability of the micro-propulsion system;
- The nine remaining non-drag-free coordinates of the test masses (y_1, θ_1, η_1, φ_1, y_2, z_2, θ_2, η_2, φ_2) are controlled by using the electrostatic suspension system provided by the IS;
- The spacecraft position and velocity are not controlled in closed loop and the corresponding terms can be neglected (as indicated by the dots).

Since all the test mass coordinates are measured by the same electrostatic read-out system of the IS, two selection matrices must be defined in order to separate the drag-free coordinates (including the telescope 1 in-plane pointing angle) from the non-drag-free coordinates:

$$\mathbf{S}_{DF} = \begin{bmatrix} \overbrace{1\ 0\ 0\ 0\ 0\ 0}^{TM\,1} & \overbrace{0\ 0\ 0\ 0\ 0\ 0}^{TM\,2} & \overbrace{0}^{Cage} \\ 0\ 0\ 1\ 0\ 0\ 0 & 0\ 0\ 0\ 0\ 0\ 0 & 0 \\ 0\ 0\ 0\ 0\ 0\ 0 & 1\ 0\ 0\ 0\ 0\ 0 & 0 \\ 0\ 0\ 0\ 0\ 0\ 0 & 0\ 0\ 0\ 0\ 0\ 0 & 1 \end{bmatrix}$$

$$\mathbf{S}_{sus} = \begin{bmatrix} \overbrace{0 & 1 & 0 & 0 & 0 & 0}^{TM1} & \overbrace{0 & 0 & 0 & 0 & 0 & 0}^{TM2} \\ 0 & 0 & 0 & 1 & 0 & 0 & 0 & 0 & 0 & 0 & 0 & 0 \\ 0 & 0 & 0 & 0 & 1 & 0 & 0 & 0 & 0 & 0 & 0 & 0 \\ 0 & 0 & 0 & 0 & 0 & 1 & 0 & 0 & 0 & 0 & 0 & 0 \\ 0 & 0 & 0 & 0 & 0 & 0 & 0 & 1 & 0 & 0 & 0 & 0 \\ 0 & 0 & 0 & 0 & 0 & 0 & 0 & 0 & 1 & 0 & 0 & 0 \\ 0 & 0 & 0 & 0 & 0 & 0 & 0 & 0 & 0 & 1 & 0 & 0 \\ 0 & 0 & 0 & 0 & 0 & 0 & 0 & 0 & 0 & 0 & 1 & 0 \\ 0 & 0 & 0 & 0 & 0 & 0 & 0 & 0 & 0 & 0 & 0 & 1 \end{bmatrix}$$

4.1.1 Decoupling Matrix for Drag-Free and Telescope Pointing Control Loop

As a consequence of the assumptions described in section 4.1, the equations of motion of the drag-free coordinates (including the telescope coordinate) become

$$\ddot{\mathbf{p}}_{DF} - \Omega_{DF}\mathbf{p}_{DF} = \mathbf{S}_{DF}\mathbf{B}_{DF}\mathbf{u}_{DF} \tag{4.1}$$

where $\mathbf{p}_{DF} = [x_1\ z_1\ x_2\ \alpha]^T$ is the vector of the drag-free coordinates, $\mathbf{u}_{DF} = [\mathbf{f}_{FEEP}, \mathbf{f}_{cage}]^T$ is the vector of the control inputs of the drag-free control loop and $\mathbf{\Omega}_{DF}$ is the stiffness matrix associated with the drag-free coordinates.

In order to perform a decoupling, a virtual control signal $\boldsymbol{\eta}_{DF}$ must be introduced

$$\mathbf{u}_{DF} = (\mathbf{S}_{DF}\mathbf{B}_{DF})^{-1}\boldsymbol{\eta}_{DF} \tag{4.2}$$

and substituting Eq. (4.2) in Eq. (4.3), the decoupling results completed

$$\ddot{\mathbf{p}}_{DF} - \Omega_{DF}\mathbf{p}_{DF} = (\mathbf{S}_{DF}\mathbf{B}_{DF})(\mathbf{S}_{DF}\mathbf{B}_{DF})^{-1}\boldsymbol{\eta}_{DF} = \boldsymbol{\eta}_{DF} \tag{4.3}$$

In fact, applying the Laplace transform to Eq. (4.3), the design plant for each drag-free control loop becomes

$$G_{DF} = \frac{1}{s^2 - \omega_p^2} \tag{4.4}$$

where ω_p^2 is the main-diagonal stiffness of the corresponding control loop and it is obviously absent for the cage coordinate.

Therefore, the task of designing the drag-free controllers and the telescope/cage controller reduces to design four independent SISO controllers for each plant, $\boldsymbol{\eta}_{DF}$ being a vector of four virtual signals, each of which controls one of the four SISO plants and

$$\mathbf{P}_{DF} = (\mathbf{S}_{DF}\mathbf{B}_{DF})^{-1}$$

being the required decoupling matrix for the drag-free control loop, which returns the real coupled control signals $\mathbf{u}_{DF}$ given the virtual signal $\boldsymbol{\eta}_{DF}$. Figure 4.1.1-1 shows the drag-free and telescope pointing control loop structure. Note that $\mathbf{K}_{DF}$ is a diagonal matrix and its four main diagonal elements represent the SISO controllers for each of the four SISO plants of the drag-free control loop.

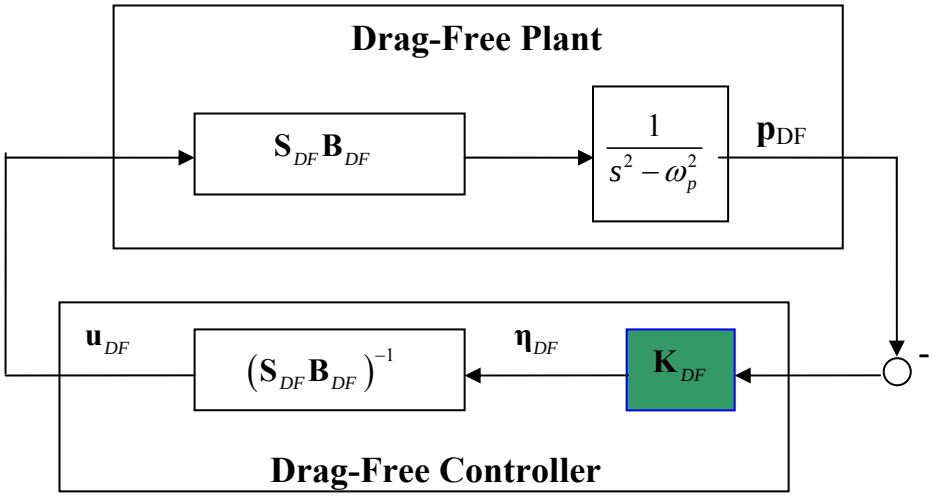

Figure 4.1.1-1: Drag-free and telescope pointing control loop structure

4.1.2 Decoupling Matrix for Spacecraft Attitude Control Loop

Proceeding in the decoupling exactly as in the previous section, the equations of motion of the spacecraft inertial attitude become

$$\ddot{\mathbf{p}}_{att} = \mathbf{B}_{att}\mathbf{u}_{att}$$

where $\mathbf{p}_{att} = [\Theta_B\ H_B\ \Phi_B]^T$ is the vector of the SC attitude coordinates, $\mathbf{u}_{att} = \mathbf{l}_{FEEP}$ is the vector of the control inputs of the spacecraft attitude control loop. Noteworthy is that the stiffness matrix is not present anymore.

Introducing a virtual control signal $\boldsymbol{\eta}_{att}$

$$\mathbf{u}_{att} = \mathbf{B}_{att}^{-1}\boldsymbol{\eta}_{att}$$

the decoupling results in

$$\ddot{\mathbf{p}}_{att} = \mathbf{B}_{att}(\mathbf{B}_{att}^{-1}\boldsymbol{\eta}_{att}) = \boldsymbol{\eta}_{att} \tag{4.5}$$

Applying the Laplace transform to Eq. (4.5), the design plant for each SC attitude control loop results in a simple double integrator plant

$$G_{att} = \frac{1}{s^2}$$

Therefore, the task of designing the spacecraft attitude controller reduces to design three independent SISO controllers for each plant, $\boldsymbol{\eta}_{att}$ being a vector of three virtual signals, each of which controls one of the three SISO plants and

$$\mathbf{P}_{att} = \mathbf{B}_{att}^{-1}$$

being the corresponding decoupling matrix. Since $\mathbf{B}_{att}$ is approximately coincident with the spacecraft inertia tensor, its inversion can easily be performed. Figure 4.1.2-1 shows the spacecraft attitude control loop structure. Note that $\mathbf{K}_{att}$ is a diagonal matrix and its three main diagonal elements represent the SISO controllers for each of the three SISO plants of the spacecraft attitude control loop.

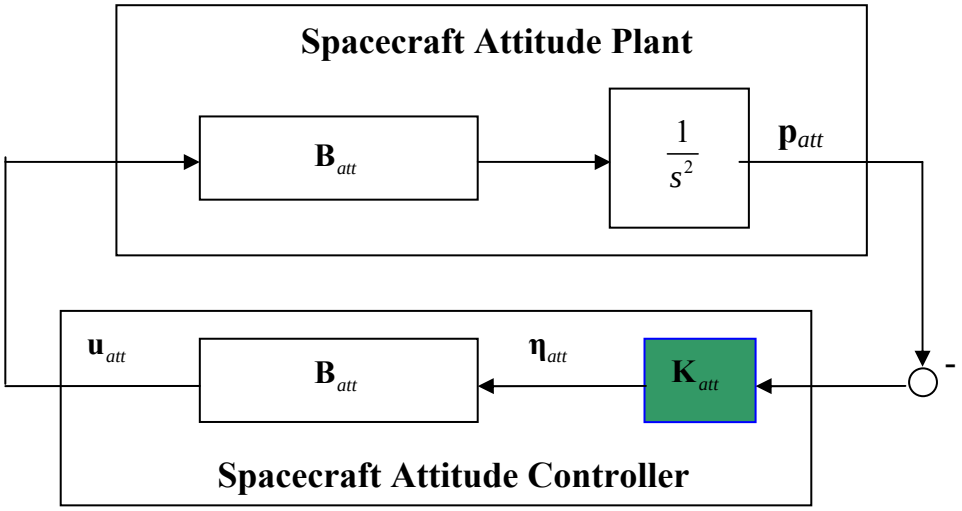

Figure 4.1.2-1: Spacecraft attitude control loop structure

4.1.3 Decoupling Matrix for Suspension Control Loop

The decoupling procedure for the remaining non-drag-free coordinates of the test masses is identical to that performed for the drag-free coordinates. The EoMs for these coordinates are

$$\ddot{\mathbf{p}}_{sus} - \Omega_{sus}\mathbf{p}_{sus} = \mathbf{S}_{sus}\mathbf{B}_{sus}\mathbf{u}_{sus}$$

where $\mathbf{p}_{sus}$ is the vector of the non-drag-free coordinates, $\mathbf{u}_{sus}$ is the vector of the electrostatic suspension actuation and $\mathbf{\Omega}_{sus}$ is the stiffness matrix associated with the non-drag-free coordinates.

Therefore, the design plant for each suspension control loop results in:

$$G_{sus} = \frac{1}{s^2 - \omega_p^2}$$

where ω_p^2 is the main-diagonal stiffness of the corresponding control loop and the corresponding decoupling matrix for the suspension control loop is:

$$\mathbf{P}_{sus} = (\mathbf{S}_{sus}\mathbf{B}_{sus})^{-1}$$

Since $\mathbf{B}_{sus}$ is a diagonal matrix (when the T/M inertia tensor is assumed to be a diagonal matrix and the cross-talk effect between different degrees freedom of the

electrostatic actuation of the inertial sensors $\mathbf{h}_{IS}$ is neglected) its inversion can easily be performed. Figure 4.1.3-1 shows the suspension control loop structure. Again note that $\mathbf{K}_{sus}$ is a diagonal matrix and its nine main diagonal elements represent the SISO controllers for each of the nine SISO plants of the suspension control loop.

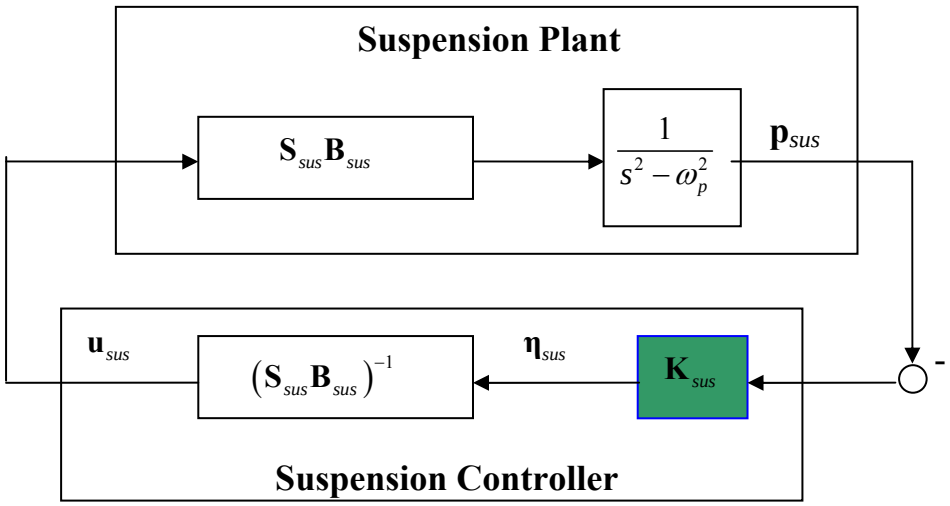

Figure 4.1.3-1: Suspension control loop structure

4.2 Controller Structure

The whole controller design for LISA has been reduced to design 16 independent SISO controllers for the same number of SISO systems. Each SISO controller is designed in order to satisfy the closed-loop requirements in the measurement bandwidth of the *science mode* and also in order to provide adequate gains and phase margins over a proper range of variations of the SISO plant parameters (i.e. gains and stiffness). The purpose of the next section is to summarize the main drivers for the design of each control loop.

4.2.1 Drag-Free and Telescope Pointing Control Loop

Since the required bandwidth of the drag-free controllers is significantly larger than the expected stiffness in the controlled degrees of freedom (x_1 z_1 x_2), the stiffness ω_p^2 can be neglected in the design and Eq. (4.4) reduces to a double integrator plant. This

happens because the SC has to follow the T/M very fast in order to achieve the science requirements.

The main drivers for the drag-free and telescope pointing controller are:

- Reduction of external disturbances (i.e. micro-propulsion actuation noise, solar pressure)
- Available sampling rate (10 Hz)
- Control loop time delay due to:
  - Latency of the micro-propulsion system until physical trust is realized
  - Computational delay
  - Delay in the sensor read-out
  - Communication delay between systems
- Achievement of gain and phase margin for variations in the plant gain and poles

4.2.2 Spacecraft Attitude Control Loop

The main drivers for the spacecraft attitude controller are:

- Achievement of the shielding of the test masses against external disturbances (i.e. micro-propulsion actuation noise, solar pressure)
- Reduction of the spacecraft attitude jitter through measurement noise suppression and actuation noise due to read-out noise limitation
- Control loop time delay due to:
  - Latency of the micro-propulsion system until physical trust is realized
  - Computational delay
  - Delay in the sensor read-out
  - Communication delay between systems
- Achievement of gain and phase margin for variations in the plant gain

4.2.3 Suspension Control Loop

Since the required bandwidth of the suspension control loop is below the science measurement bandwidth (the suspension coordinates can only be moved very slow, otherwise the science measurement is influenced), the diagonal terms of the stiffness matrix $\mathbf{\Omega}_{sus}$ are very close to the minimum possible bandwidth of the suspension controller and cannot be neglected in the controller design process.

Consequently, the suspension control design is the most demanding and its main drivers are:

- Stabilization of the non-drag free coordinates of the test masses due to the inherent negative stiffness
- Reduction of the T/M jitter through measurement noise suppression and actuation noise due to read-out noise limitation
- Control loop time delay due to:
  - Computational delay
  - Delay in sensor read-out
  - Communication delay between systems
- Achievement of gain and phase margin for variations in the plant gain (T/M mass) and poles (T/M stiffness)

4.3 Conclusions

The whole DFACS control structure results in 16 SISO controllers which are provided by EADS/Astrium. The *science mode*, the *drag-free acquisition mode* and the *gyro mode* are all based on the controller structure presented in this chapter.

Chapter 5

Overall Model Architecture

In this chapter, a linear performance analysis of the controller designs described in chapter 4 is presented over the operative conditions of the acquisition phase. To this end, an overall model, based on the linearized dynamics system given in chapter 3, the control system shown in chapter 4 and the noise system that is introduced in this chapter, is set in both Matlab® and Simulink® environments.
The objectives of this chapter are:

- To prove that the performances that are achievable in the *drag-free acquisition mode* (*science mode* controller + operative conditions of the acquisition on CCD phase) do not fulfil the desired requirements defined in section 2.3.3.
- To build a Matlab® model[1] and a Simulink® model for a LISA satellite, usable as design tools for the acquisition controller and for performance evaluations. The Matlab® model provides a tool for a fast linear transfer-function analysis allowing a rapid insight in the partitioning between different noise sources. However, the development of a Simulink® model is necessary since:
  - the verification of the fulfilment of the acquisition requirements (Table 2.3.3-3) asks for a time-domain performance analysis
  - the acquisition controller has to be included in the integrated E2E LISA simulator

[1] The Matlab® model presented in this work follows the Matlab® model developed by EADS/Astrium for the performance analysis of the *science mode*

- the dicrete-time Kalman filter implementation requires a recursive solution of the Riccati Equations that can be more easily managed by using a simulator.

5.1 Matlab® Model

The Matlab® model is obtained using the following procedure:

- The continuous-time state space model given by Eq. (3.7 - 3.8) is implemented as first. It constitutes the linear, time-invariant system representing the LISA satellite open-loop plant (G) (Figure 5.1-1).

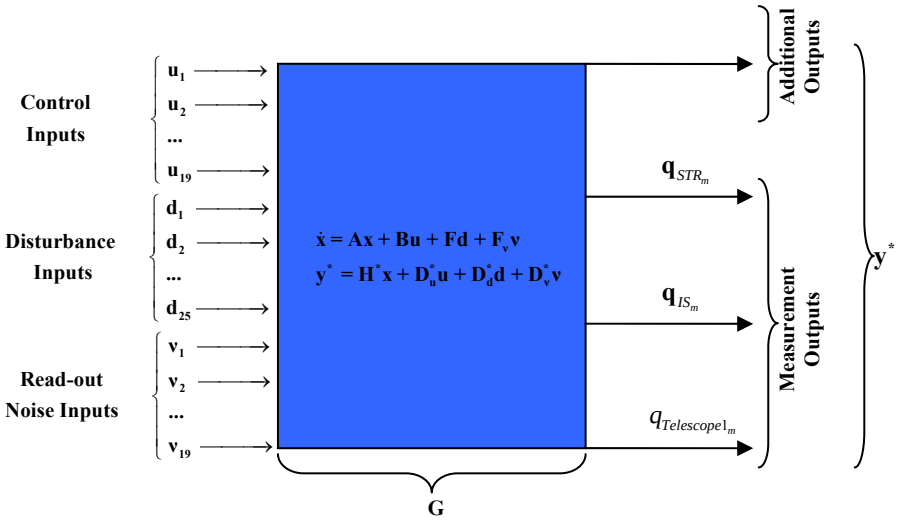

Figure 5.1-1: Open-loop system architecture

Note that the state equation (Eq. (3.7)) has been modified including the *read-out noise vector* $\mathbf{v}$ between the inputs in order to implement the whole system as a Matlab® state-space model

$$\dot{\mathbf{x}} = \mathbf{Ax} + \mathbf{Bu} + \mathbf{Fd} + \mathbf{F}_v\mathbf{v} \tag{3.7*}$$

where $\mathbf{F}_v \in \mathbb{R}^{38x16}$ is an empty matrix. Moreover note that, although the measurement vector represents the only information that is physically achievable from the plant, several additional outputs can be obtained, for performance

analysis purpose, just manipulating the measurement equation (3.8), which can be rewritten as a more general output equation

$$\mathbf{y}^* = \mathbf{H}^*\mathbf{x} + \mathbf{D}_u^*\mathbf{u} + \mathbf{D}_d^*\mathbf{d} + \mathbf{D}_v^*\mathbf{v} \qquad (3.8^*)$$

where the asterisk indicates the modified elements.

- The close-loop LTI system is realised attaching sequentially, in feedback, the drag-free controller, the suspension controller and the spacecraft attitude controller to the plant (Figure 5.1-2). Each of them is represented by a LTI continuous-time system consisting of a selection matrix, a system of SISO controllers and a decoupling matrix, as illustrated in chapter 4.

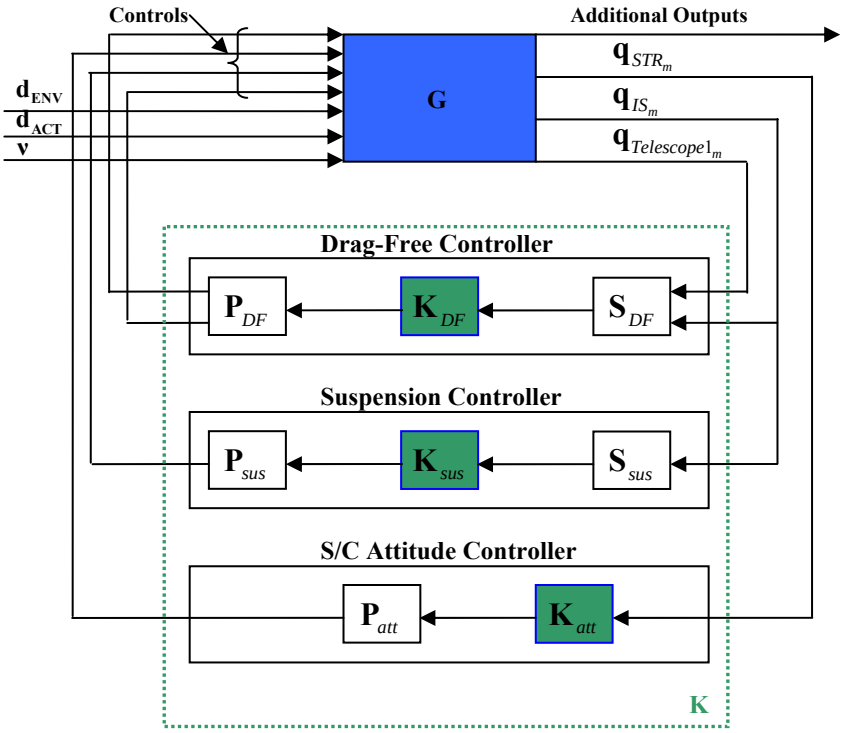

Figure 5.1-2: Closed-loop system architecture

- Finally, the Matlab® model is completed appending in series the noise system to the close-loop system (Figure 5.1-3). The noise system is a LTI continuous-time MIMO system consisting of the noise shape filters used to generate the several types of disturbances that affect the open-loop. These input disturbances are divided in three categories:

- Environment noises

  They are represented by the solar radiation pressure and their influence over the plant is modelled by the first 6 elements of the *disturbance input vector*

$$\mathbf{d}_{\mathbf{ENV}} = \begin{bmatrix} \mathbf{f}_{sol,d} \\ \mathbf{l}_{sol,d} \end{bmatrix}$$

- Actuation noises

  They are represented by the FEEP actuation noises, the electrostatic suspension actuation noises and the telescope pointing actuation noise. Their influence over the plant is modelled by the remaining 19 elements of the *disturbance input vector*

$$\mathbf{d}_{\mathbf{ACT}} = \begin{bmatrix} \mathbf{f}_{FEEP,d} \\ \mathbf{l}_{FEEP,d} \\ \mathbf{f}_{1d}^{(C)} \\ \mathbf{l}_{1d} \\ \mathbf{f}_{2d}^{(2)} \\ \mathbf{l}_{2d} \\ \mathbf{i}_{A}^{(C)} f_{cage,d} \end{bmatrix}$$

- Read-out noises

  They are represented by the STR read-out noises, the electrostatic system read-out noises and the OATM sensor read-out noise. They are modelled by the *read-out noise vector*:

$$\mathbf{v} = \begin{bmatrix} \mathbf{STR}_{ROnoise} \\ \mathbf{IS}_{ROnoise} \\ \mathbf{CAGE}_{ROnoise} \end{bmatrix} \tag{3.12}$$

Each noise of each category is generated by using a noise shape filter. A noise shape filter is a SISO or MIMO LTI system that, fed by one or more white noises, gives as output one or more coloured noises. The noise shape filters has

been provided by EADS/Astrium and their Bode diagrams are shown in Chapter 2 and Chapter 3. A more detailed explanation can be found in Appendix B.

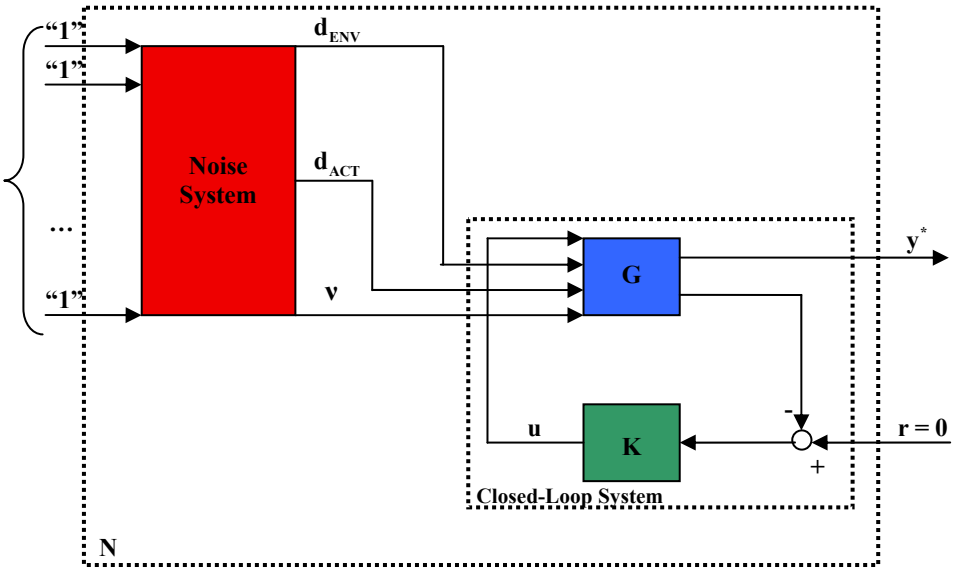

Figure 5.1-3: Overall Matlab® model architecture

The whole Matlab® code that performs this procedure is reported in [CD-ROM]. The model achieved (Figure 5.1-3) is a LTI continuous-time system whose inputs are white noises of unitary power (the reference signal **r** for the controlled states is assumed to be a zero vector**)**. Since the overall model is a linear model, the principle of superimposition of the effects can be applied and it is possible to visualize the effect of each source of noise over each output.

Simulink® Model

The Simulink® model has the same structure of the Matlab® model (Figure 5.1-3). The main structure of the simulator is depicted in Figure 5.2-1. In the following sections, a description of the simulator subsystems is provided. All the simulator systems are considered continuous as if the sensor data and the actuation commands were provided continuously in time.

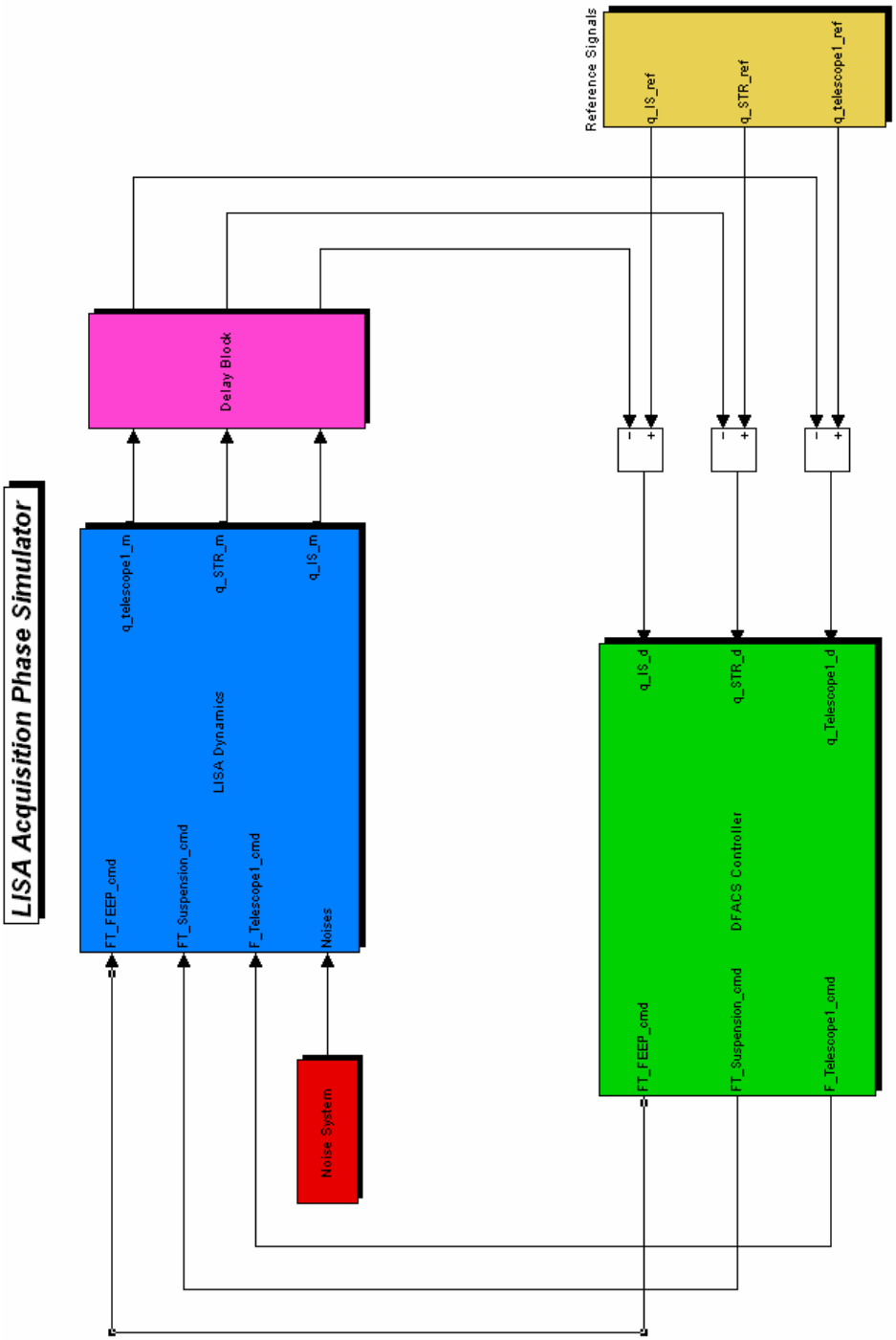

Figure 0-1: Main structure of the LISA acquisition phase simulator

5.1.1 LISA Dynamics

The *LISA Dynamics* subsystem implements the continuous-time state space LTI model (SC_LTP_dist_sys) given by Eq. (3.7* - 3.8*), which represents the LISA

satellite open-loop plant. In other words, it simulates the dynamics of the LISA spacecraft including the test masses and the movable cage (telescope1). Since the number of differential equations to solve is very high (the state vector x of Eq. (3.6) has 38 elements), the LTI system block, provided by the *Control System Toolbox,* is used in order to make the Simulink® model more readable.

Figure 5.2.1-1 represents the *LISA Dynamics* block which receives as inputs the control signals provided by the controller (section 5.2.4) and the noise signals provided by the noise system (section 5.2.5). Within the outputs of the LISA open-loop plant, the measurements are selected to be sent in feedback to the controller.

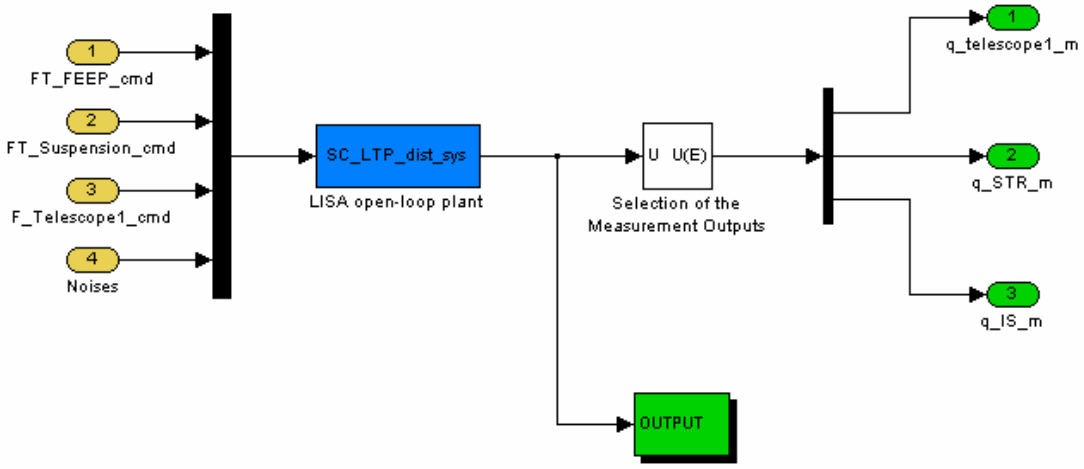

Figure 5.1.1-1: LISA dynamics block

Noteworthy is the *OUTPUT* block. In fact, it selects the signals that are sent to the workspace for the performance analysis and computes the attitude of each telescope line-of-sight in its own telescope frame w.r.t. the inertial frame for the statistic analysis (Figure 5.2.1-2). Since the telescope 2 is fixed to the SC, its line-of-sight attitude coincides with the SC attitude computed in the telescope 2 body-fixed frame. It is calculated transforming the SC angular velocity from the SC reference frame to the telescope 2 frame

$$\boldsymbol{\omega}_B^{(T2)} = \mathbf{T}_{P2B}\boldsymbol{\omega}_B^{(B)}$$

The transformation matrix between the spacecraft frame and the telescope 2 frame is represented by a constant elementary rotation matrix of -30° around the common z-axis

$$T_{P2B} = \begin{pmatrix} \frac{\sqrt{3}}{2} & -\frac{1}{2} & 0 \\ \frac{1}{2} & \frac{\sqrt{3}}{2} & 0 \\ 0 & 0 & 1 \end{pmatrix}$$

The rotated SC angular velocity ($\boldsymbol{\omega}_B^{(T2)}$) is integrated and the result represents the SC attitude in the telescope 2 frame (SC_attx_T2, SC_atty_T2, SC_attz_T2) and, consequently, the desired telescope 2 line-of-sight inertial attitude.

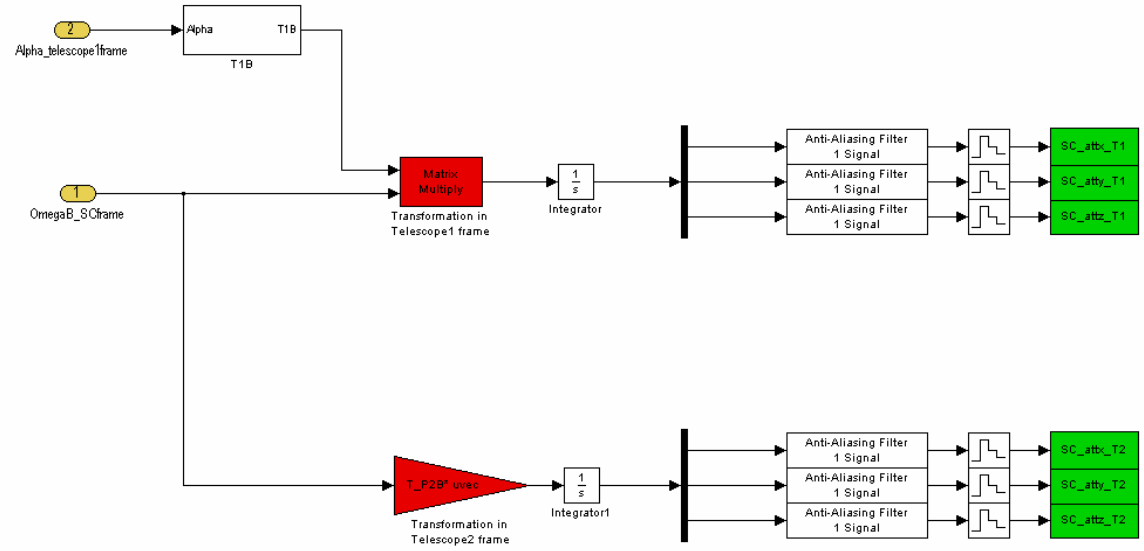

Figure 5.1.1-2: Coordinates transformation block

On the contrary, since the telescope 1 can rotate around the z-axis, its line-of-sight attitude is given by

$$\begin{bmatrix} \text{SC\_attx\_T1} \\ \text{SC\_atty\_T1} \\ \text{SC\_attz\_T1} \end{bmatrix} + \begin{bmatrix} 0 \\ 0 \\ \alpha \end{bmatrix}$$

where $[\text{SC\_attx\_T1}\ \ \text{SC\_atty\_T1}\ \ \text{SC\_attz\_T1}]^T$ is the SC attitude computed in the telescope 1 body-fixed frame. In the *Coordinate Transformation* block, just the SC attitude in the telescope 1 frame is calculated, while the telescope 1 line-of-sight attitude

is computed in the analysis files. Proceeding as for telescope 2, the SC angular velocity is transformed from the SC reference frame to the telescope 1 body-fixed frame

$$\boldsymbol{\omega}_B^{(T1)} = \mathbf{T}_{1B}\boldsymbol{\omega}_B^{(B)}$$

The transformation matrix is represented by an elementary rotation matrix of $(30°+\alpha)$ around the common z-axis

$$\mathrm{T}_{1B} = \begin{pmatrix} cos(30+\alpha) & sin(30+\alpha) & 0 \\ -sin(30+\alpha) & cos(30+\alpha) & 0 \\ 0 & 0 & 1 \end{pmatrix}$$

Since α is small, the transformation matrix can be linearized

$$\mathrm{T}_{1B} \approx \begin{pmatrix} cos(30)-\alpha\cdot sin(30) & sin(30)+\alpha\cdot cos(30) & 0 \\ -(sin(30)+\alpha\cdot cos(30)) & cos(30)-\alpha\cdot sin(30) & 0 \\ 0 & 0 & 1 \end{pmatrix}$$

Being α a time-varying signal, T_{1B} is also time dependent and must be updated at each time-step.

The rotated SC angular velocity is integrated and the results represent the SC attitude in the telescope 1 frame w.r.t. the inertial frame (SC_attx_T1, SC_atty_T1, SC_attz_T1).

5.1.2 Delay Block

The *Delay Block* introduces the control loop time delay (300 ms TBC) over the measurement vector components. An explanation of the control loop time delay can be found in section 4.2.

5.1.3 Reference Signals Block

The *Reference Signals* block introduces the guidance laws that the SC inertial attitude, the T/M position and attitude and the telescope 1 in-plane pointing angle are

driven to follow by the controller. Regarding the test masses, they are always forced to remain in their zero reference position as in the *science mode*.

5.1.4 DFACS Controller

The *DFACS Controller* subsystem implements the LISA controller described in chapter 4 (Figure 5.2.4-1).

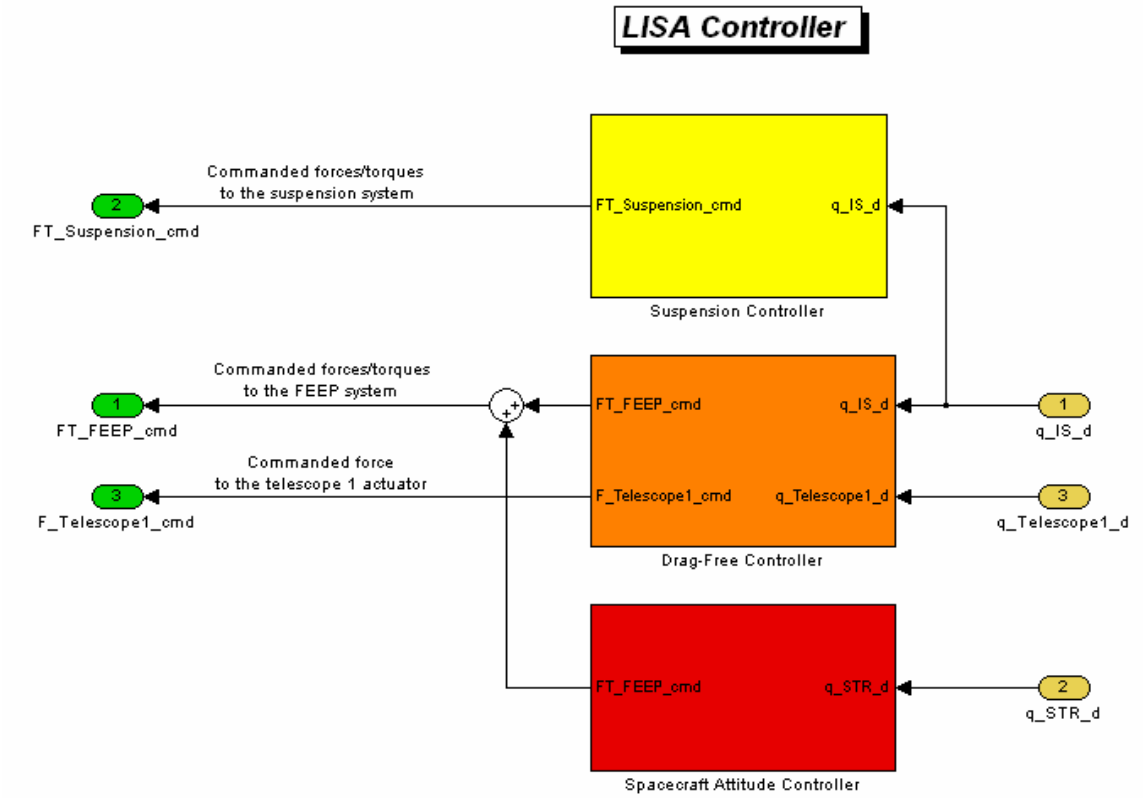

Figure 5.1.4-1: DFACS controller block

The drag-free controller (Figure 5.2.4-2) receives as inputs the deviations of the test masses translational and rotational coordinates from the reference values

$$\mathbf{q}_{IS_d} = \mathbf{q}_{IS_{ref}} - \mathbf{q}_{IS_m}$$

and the telescope 1 in-plane pointing angle deviation from the nominal (reference) telescope pointing expressed as an angle around the telescope joint

$$q_{Telescope1_d} = q_{Telescope1_{ref}} - q_{Telescope1_m}$$

The T/M drag-free coordinates are selected using the selection matrix $\mathbf{S}_{DF}$ and the control of each coordinate is performed individually by using SISO controllers. The achieved control signals are converted by the decoupling matrix $\mathbf{P}_{DF}$ in force commands for the FEEP system and in force command for the OATM mechanism.

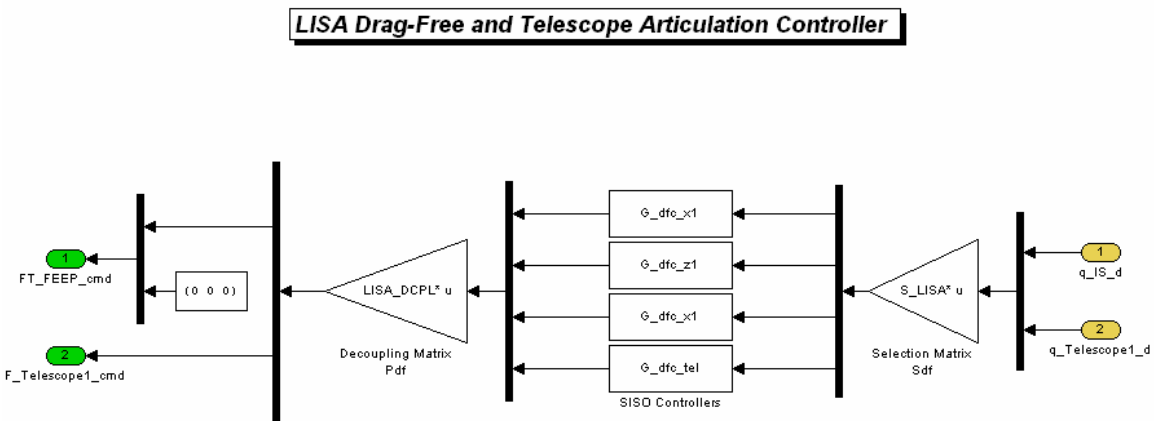

Figure 5.1.4-2: Drag-free controller block

The suspension controller and the spacecraft attitude controller are implemented likewise the drag-free controller. In particular, the suspension controller (Figure 5.2.4-3) receives as inputs $\mathbf{q}_{IS_d}$ and provides as outputs the commanded forces and torques for the electrostatic suspension system.

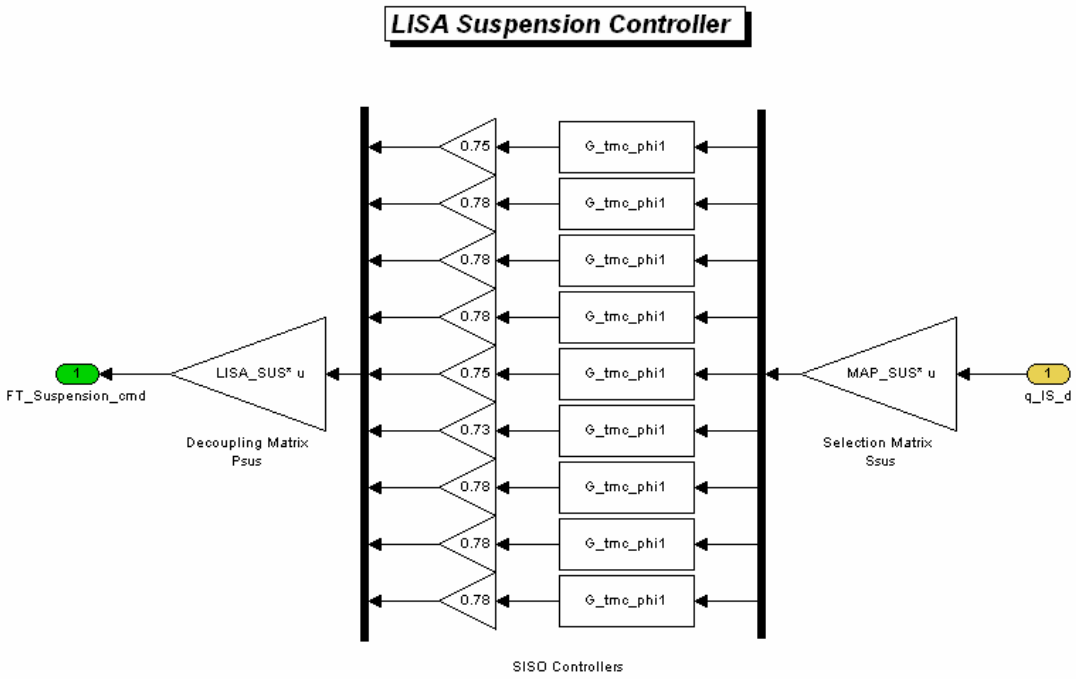

Figure 5.1.4-3: Suspension controller block

The spacecraft attitude controller (Figure 5.2.4-4) receives as inputs the spacecraft attitude deviation from the nominal attitude expressed as angles (three rotations around the Σ_B axis)

$$\mathbf{q}_{STR_d} = \mathbf{q}_{STR_{ref}} - \mathbf{q}_{STR_m}$$

and gives as outputs the commanded torques for the FEEP system.

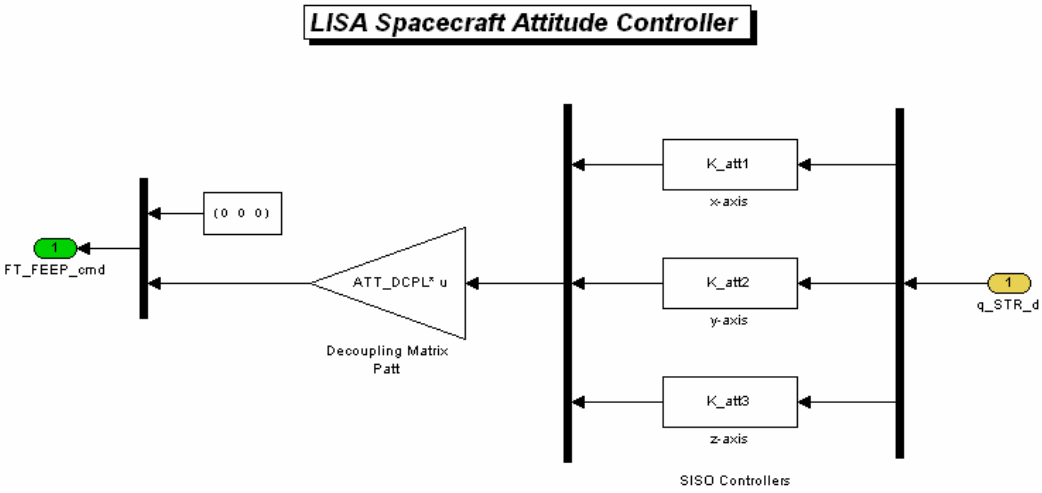

Figure 5.1.4-4: Spacecraft attitude controller block

5.1.5 Noise System

The *Noise System* block (Figure 5.2.5-1) generates the noise inputs for the *LISA Dynamics* block. The noise sources are divided in three categories as stated in section 5.1 and are implemented in the simulator accordingly. Figure 5.2.5-1 shows the structure of the noise system model.

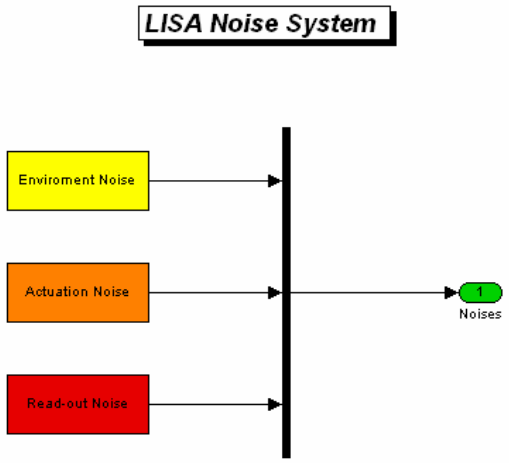

Figure 5.1.5-1: Noise system block

The generation of the signals that resemble these various types of noises is performed according to [6]. As an example, Figure 5.2.5-2 depicts the way the FEEP actuation noise is simulated. A MIMO LTI shape filter (thr_noise) is used.

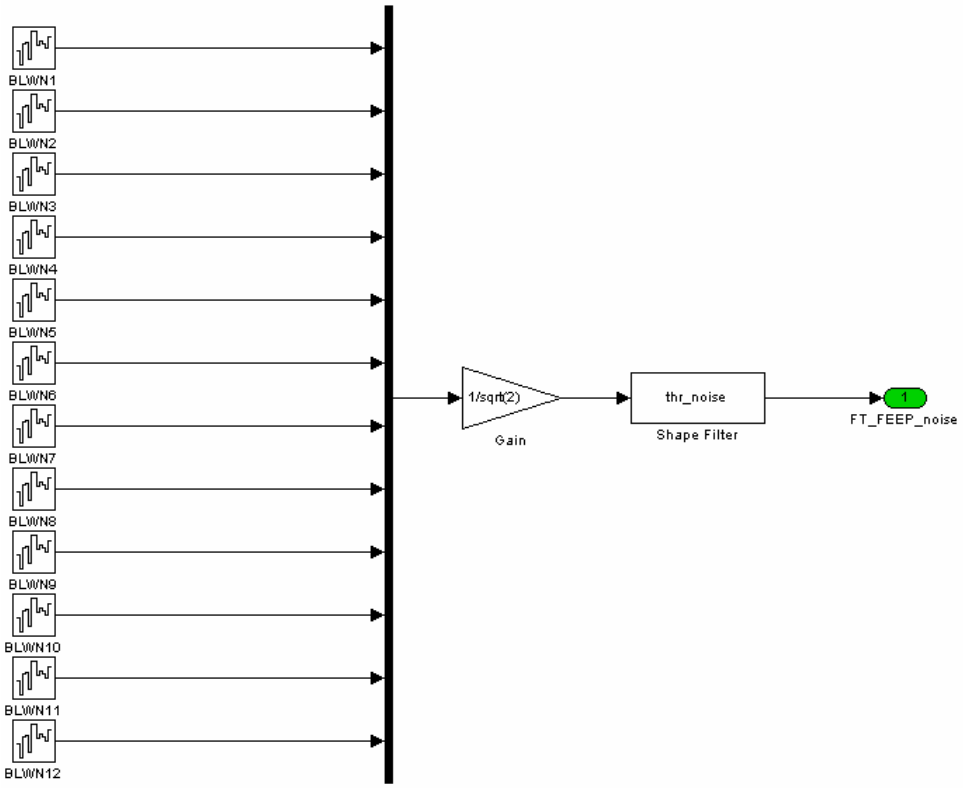

Figure 5.1.5-2: FEEP actuation noise block

5.1.6 Simulation Parameters

The simulation parameters are the ensemble of data that are needed to initialize the Simulink® model described above. The mentioned initial simulation parameters are loaded in the Matlab® workspace by running the initialization file which is reported in [CD-ROM]. Whereupon it is possible to start the simulation[1].

The following simulation parameters deserve to be discussed

$$t_{sim} = 30000 \text{ s}$$
$$\text{stepsize} = 0.1 \text{ s}$$
$$dt_{output} = 0.1 \text{ s}$$

[1] This procedure has to be repeated before launching each simulation.

The simulation time and the stepsize are solver configuration parameters (Figure 5.2.6-1 represents the solver pane of the configuration parameters dialog box of the simulator).

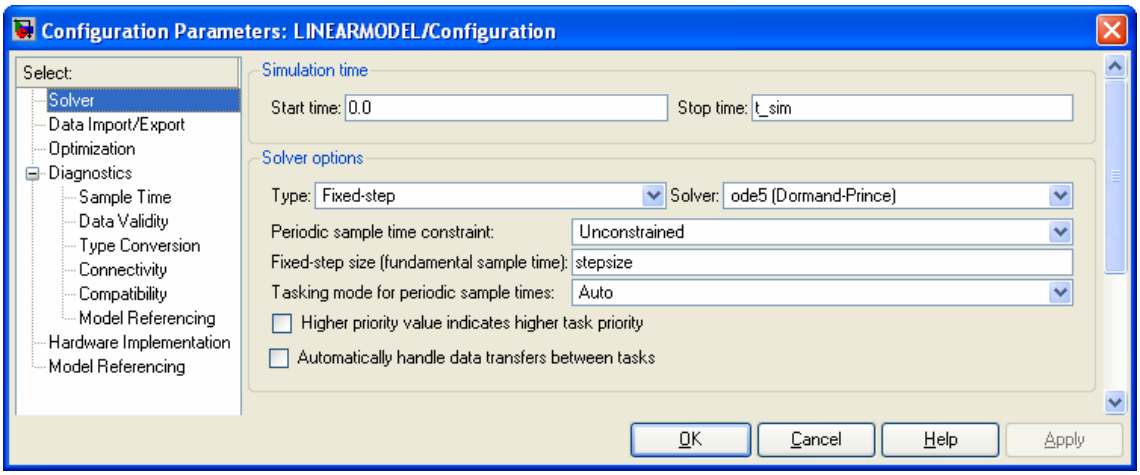

Figure 5.1.6-1: Solver pane

The simulation time is chosen sufficiently high in order to reach sufficiently low frequencies. In this way it is possible to generate more accurate PSD plots to compare with the Matlab® model results and it is possible to highlight the effect of the coloured noises that affect the system. (In fact, LISA coloured noises behave as white noises at high frequency and show a significant dependency from the frequency only under specific frequencies (see noise shape filters)). Moreover, since the duration of the acquisition phase has to be determined, a longer simulation time is desiderable in order to perform the statistic analysis described in section 2.3.3. The stepsize is chosen in order to have sampling rates of 10 Hz as required in section 2.4 - 2.5.

The last parameter represents the sample time at which the output signals are collected. It coincides with the stepsize (i.e. 0.1 s) in order to avoid the use of anti-aliasing filters for the downsampling. In fact, the use of anti-aliasing filters, cutting the high frequencies of the signals, would fake the output time-series for the time-domain analysis.

Remark

The DC solar forces and torques acting on the spacecraft and the DC parasitic forces and torques acting on the test masses are not included in the noise systems of both Matlab® and Simulink® models; this topic is treated in Chapter 9.

5.2 Performance Analysis

The congruence of the Matlab® model and the Simulink® model has to be verified. To this end, Figure 5.3-1 compares the spacecraft inertial attitude error curves obtained by means of two proposed models.

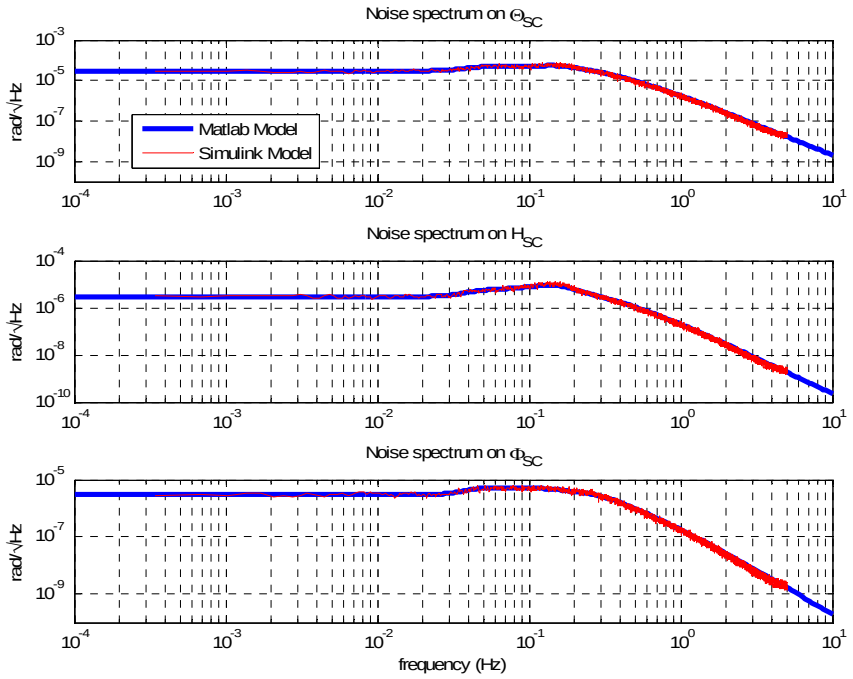

Figure 5.2-1: Spacecraft inertial attitude error

It can clearly be seen that the square root of the power spectral density plot generated from the Simulink® time-series coincides with the correspondent plot achieved from the Matlab® model. The noise spectrum of other state errors can be found in Appendix A.

Note that the spacecraft inertial attitude error is given by

$$\mathbf{q}_{STR_{err}} = \mathbf{q}_{STR_{ref}} - \mathbf{q}_{STR}$$

and represents the deviation of the real SC attitude from the reference attitude (to be not confused with $\mathbf{q}_{STR_d}$). Therefore, in the following, the term *error* addresses

Error = Reference Signal – Real Plant State

if not explicitly mentioned otherwise.

Figures 5.3-2, 5.3-3, 5.3-4 and 5.3-5 show the time-series respectively of the test masses coordinates errors, the spacecraft inertial attitude error and the telescope 1 in-plane pointing error achieved by means of the Simulink® model.

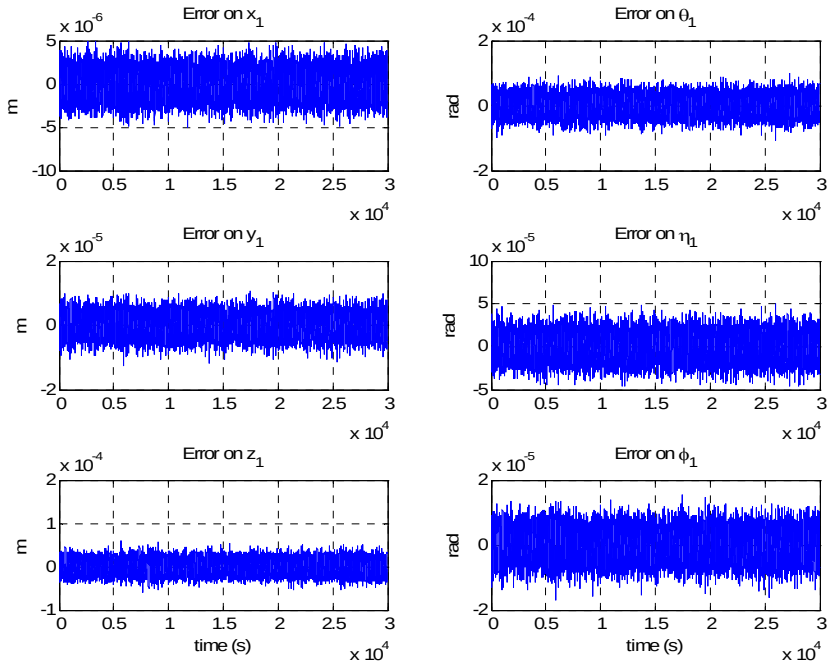

Figure 5.2-2: T/M 1 position and attitude error

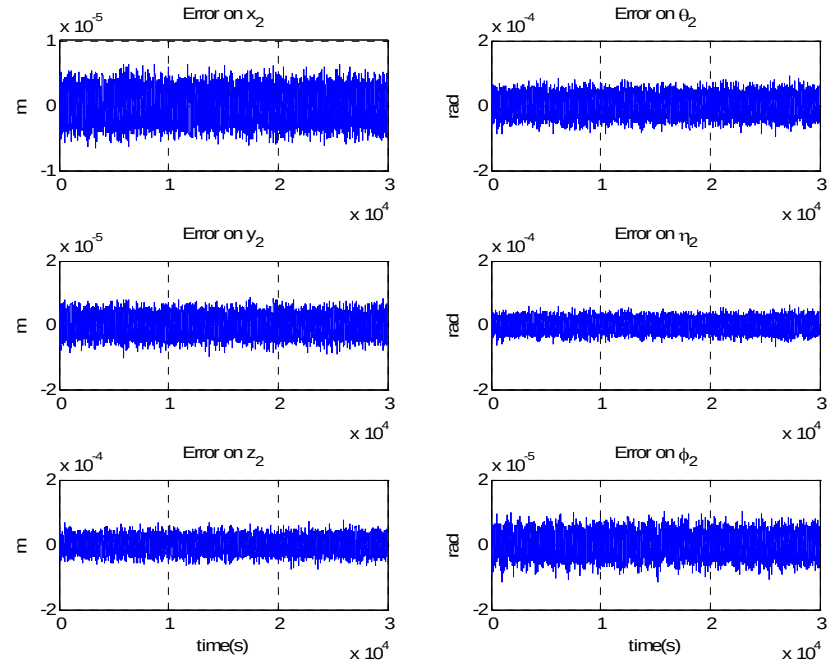

Figure 5.2-3: T/M 2 position and attitude error

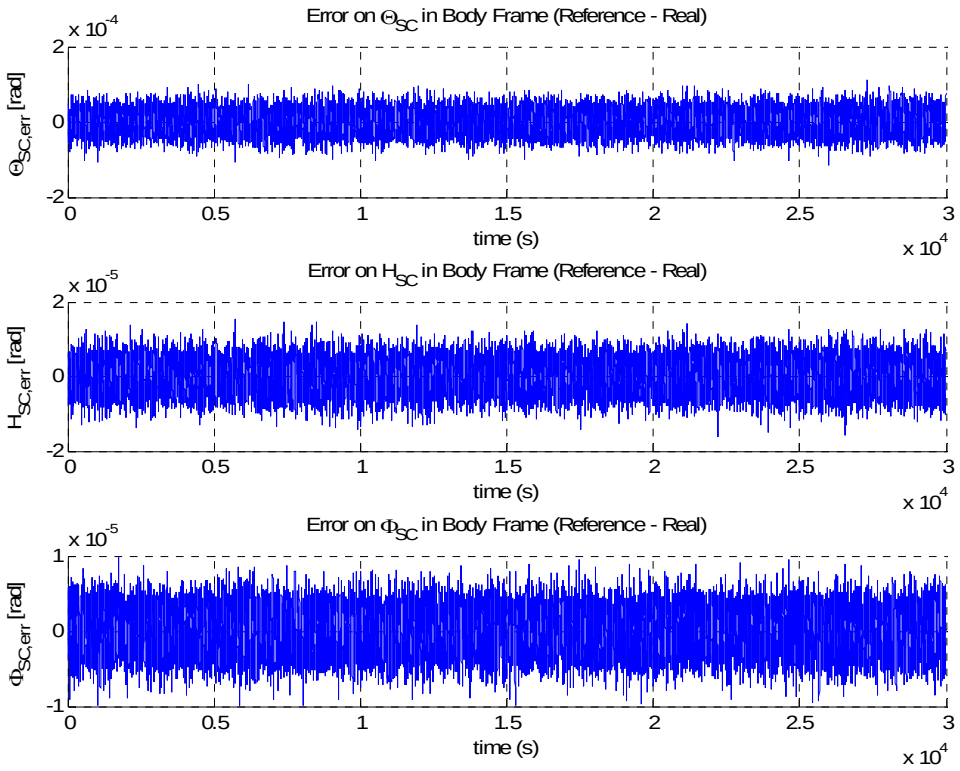

Figure 5.2-4: Spacecraft inertial attitude error

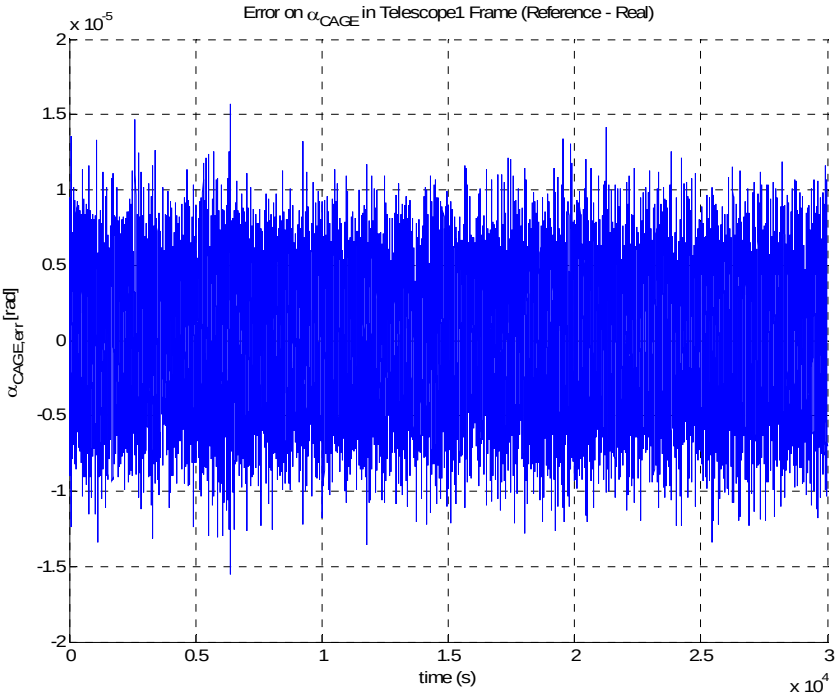

Figure 5.2-5: Telescope 1 in-plane pointing error

All the state errors behave as unbiased noisy signals with large jitters and negligible drifts. As consequence, the requirements on the short-term jitters are largely unsatisfied as it is shown in Table 5.3-1 and 5.3-2. In particular, note (Figure 5.3-4) that the spacecraft inertial roll angle error is an order of magnitude noisier than the others SC attitude angle errors because of the larger STR read-out noise on this axis. This influences both the inertial roll and the pitch angles errors of telescope 1 line-of-sight (Table 5.3-1) and telescope 2 line-of-sight (Table 5.3-2).

Error (reference - real)	**Requirements (μrad)**	**Drag-free acquisition mode (μrad)**
$\Theta_{1,err}$	-	25.73
$H_{1,err}$	0.1	13.17
$\Phi_{1,err}$	$\sqrt{0.1^2+0.05^2} \approx 0.118$	4.30
$\alpha_{CAGE,err}$	0.05	3.90

Table 5.2-1: Comparison between the short-term jitter requirements and the short-term jitter performances in drag-free acquisition mode (maximum RMS 1σ over a time window of 1000 s) for the telescope 1 LOS attitude error ($\Theta_{1,err}$, $H_{1,err}$, $\Phi_{1,err}$) and for the telescope 1 in-plane pointing angle error ($\alpha_{CAGE,err}$)

Error (reference - real)	**Requirements (μrad)**	**Drag-free acquisition mode (μrad)**
$\Theta_{2,err}$	-	23.95
$H_{2,err}$	0.1	16.22
$\Phi_{2,err}$	0.1	2.73

Table 5.2-2: Comparison between the short-term jitter requirements and the short-term jitter performances in drag-free acquisition mode (maximum RMS 1σ over a time window of 1000 s) for the telescope 2 LOS attitude error ($\Theta_{2,err}$, $H_{2,err}$, $\Phi_{2,err}$)

On the contrary, the requirements on the long-term drift are largely fulfilled by all degrees of freedom (Table 5.3-3 and 5.3-4). Note that the absence of significant drifts would be observed also in presence of DC force and torque disturbances (Chapter 9) since the controller provides a perfect DC forces and torques compensation.

Error (reference - real)	Requirements (μrad)	Drag-free acquisition mode (μrad)
$\Theta_{1,err}$	-	5.57
$H_{1,err}$	5	3.12
$\Phi_{1,err}$	$\sqrt{5^2+1^2} \approx 5.099$	0.78
$\alpha_{CAGE,err}$	1	0.09

Table 5.2-3: Comparison between the long-term drift requirements and the long-term drift performances in drag-free acquisition mode (over a time window of 1000 s) for the telescope 1 LOS attitude error ($\Theta_{1,err}$, $H_{1,err}$, $\Phi_{1,err}$) and for the telescope 1 in-plane pointing angle error ($\alpha_{CAGE,err}$)

Error (reference - real)	Requirements (μrad)	Drag-free acquisition mode (μrad)
$\Theta_{2,err}$	-	5.33
$H_{2,err}$	5	3.42
$\Phi_{2,err}$	5	0.8

Table 5.2-4: Comparison between the long-term drift requirements and the long-term drift performances in drag-free acquisition mode (over a time window of 1000 s) for the telescope2 LOS attitude error ($\Theta_{2,err}$, $H_{2,err}$, $\Phi_{2,err}$)

Additional information can be achieved by the transfer-function analysis performed by means of the Matlab® model. Figure 5.3-6, 5.3-7, 5.3-8 and 5.3-9 show the square root of the power spectral densities respectively on the test masses coordinates errors, the spacecraft inertial attitude error and the telescope 1 in-plane pointing error.

As expected, the high noise level shown by the time-series of all the error signals and the resulting non-fulfilment of the short-term requirements are due to the level of the star-tracker read-out noise. In fact, this is the major contribution which clearly dominates the other noise sources over all the states (since it is fed back in the spacecraft attitude controller, then in the torque commands for the FEEP system and from there, given the dynamic coupling, it is spread over all the states). Only at low frequencies the IS read-out noise drives the T/M coordinates and the OATM read-out noise drives the telescope 1 pointing angle.

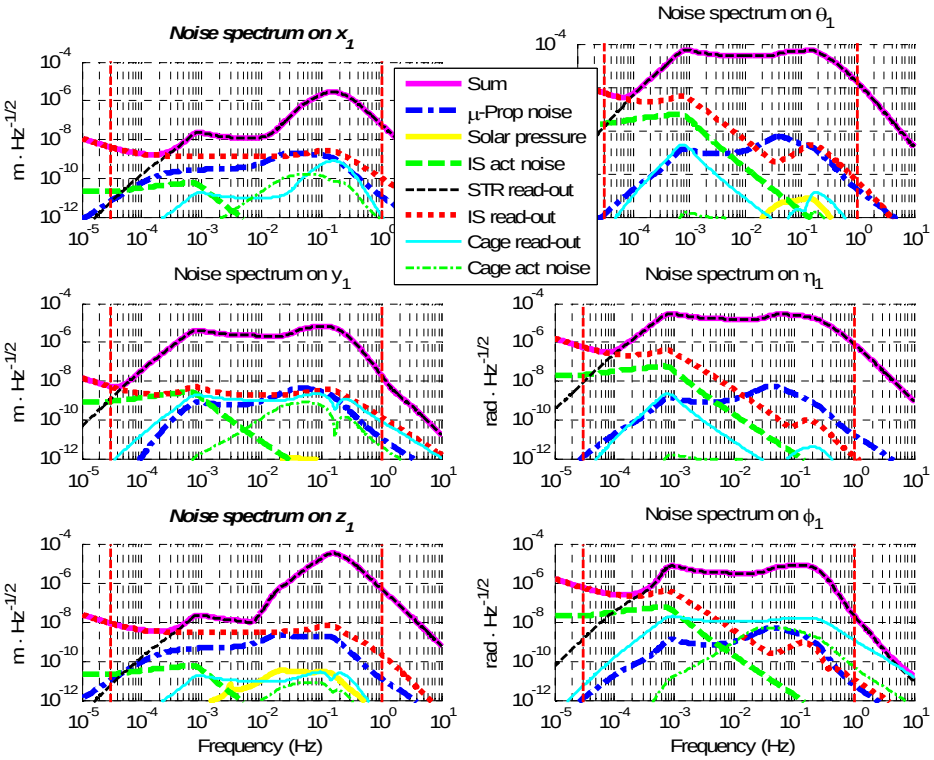

Figure 5.2-6: T/M 1 position and attitude error

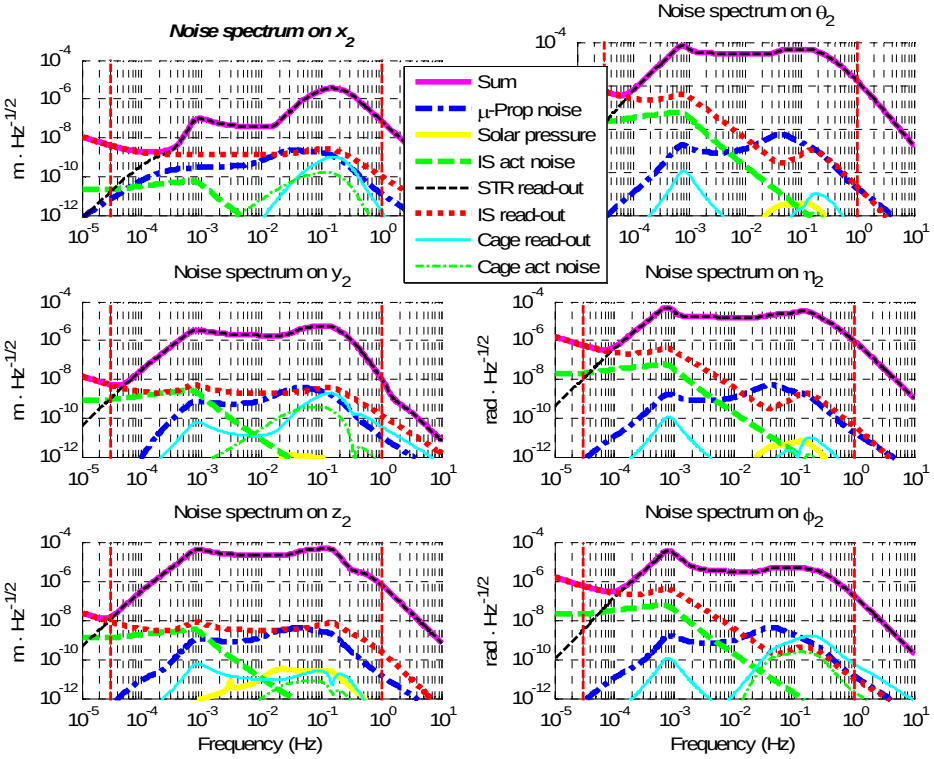

Figure 5.2-7: T/M 2 position and attitude error

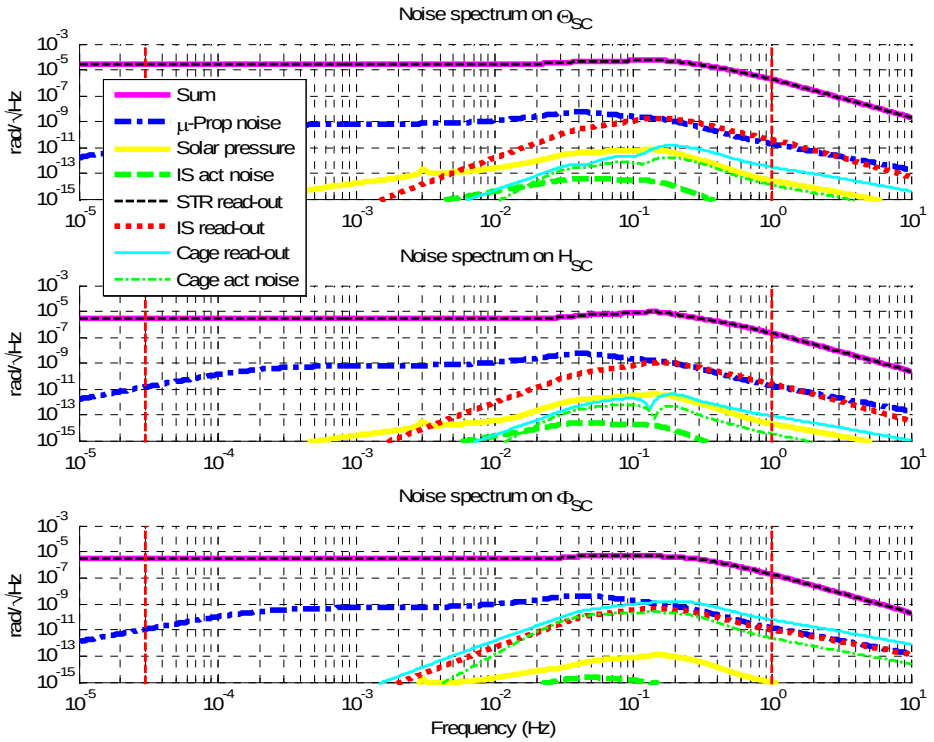

Figure 5.2-8: Spacecraft inertial attitude error

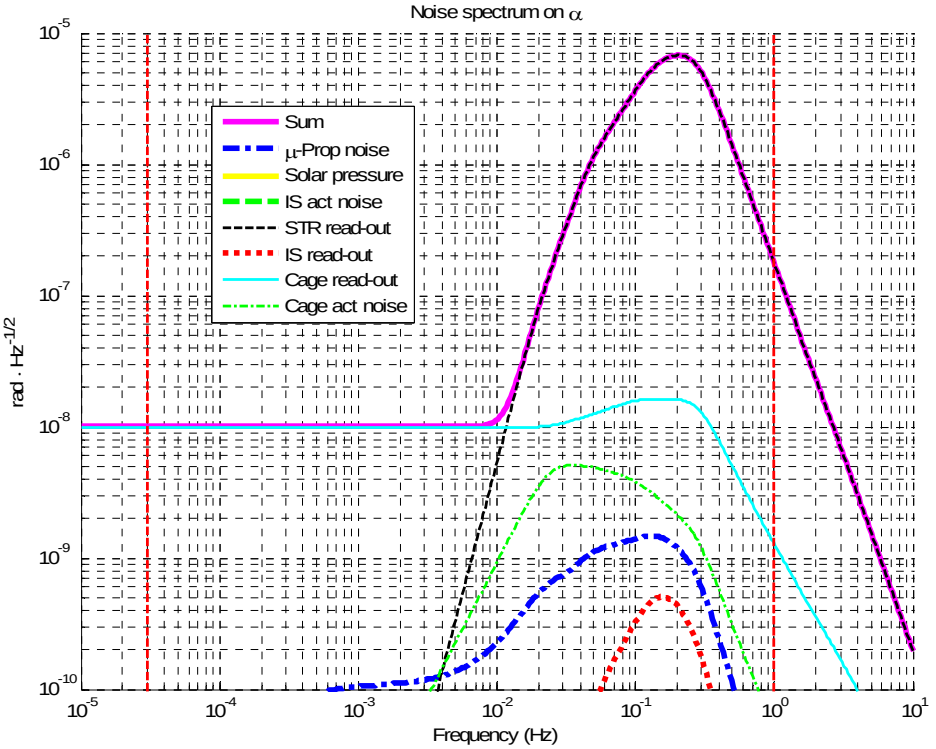

Figure 5.2-9: Telescope 1 in-plane pointing angle error

5.3 Remarks

The results achieved in this chapter prove that the *drag-free acquisition mode*, based on the controller developed for the *science mode*, is not able to fulfil the requirements for the acquisition on CCD phase because of the STR read-out noise that, at least in the high frequency range, drives all the degrees of freedom. This happens because the STR read-out noise is continuously sent in feedback to the plant through the measurements, which are directly (i.e. spacecraft attitude) or indirectly (i.e. test masses coordinates and telescope 1 pointing angle, through dynamic coupling) affected by the STR read-out noise. It stands to reason that a possible solution is to send in feedback improved estimations of the real system states in place of their noisy measurements. Therefore, the strategy proposed is to use a Kalman filter, in order to pre-process the measurement data and to provide the desired enhanced signals to the controller, which mantains the very same control structure used in the *drag-free acquisition mode*.

Part II

Kalman Filter Design

Chapter 6

Kalman Filter Theory

The purpose of this chapter is to provide a basic knowledge of the Kalman filter main concepts, introducing the assumptions, the implementation equations and the main issues that are necessary to be aware of in order to perform the design of the Kalman filter for the LISA control system during the acquisition phase. More details about the Kalman filter design theory can be found in [26] and [27].

6.1 Introduction

The Kalman filter is a recursive algorithm based on the least-squares method and developed by the Hungarian mathematician R.E. Kalman in 1960. Figure 6.1-1 represents the application context in which the Kalman filter is typically used.

Figure 6.1-1 shows a physical system, e.g. the LISA satellite, which is driven by a composition of external inputs and controls and whose outputs are evaluated by measuring devices or sensors. Thus, the knowledge of the system's behaviour is solely given by the inputs and the observed outputs. Note that the observations convey the measurement noise (i.e. sensor read-out noise) and the process noise (i.e. actuation noise, environment noise, uncertainties in the used models, etc.).

The task of the Kalman filter is to obtain an optimised estimate of the system states using the available information consisting of control inputs and measurements, which can be provided by different sensor devices.

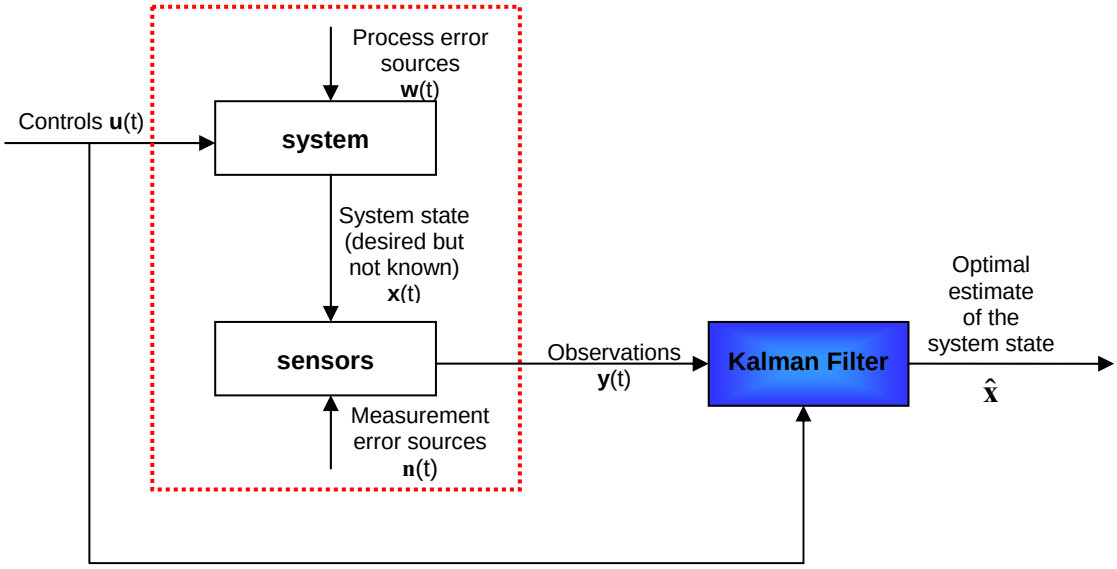

Figure 6.1-1: Typical application of the Kalman Filter

The elements that the Kalman filter needs to achieve the desired estimations are:

- a mathematical model of the physical process under examination, constituted of a set of state equations to model the system state dynamics and a set of measurements equations to model the sensor devices dynamics;
- a statistical description of the measurements noises, the process noises and the uncertainties in the dynamics models;
- any available information about the initial conditions of the system states of interest.

6.2 Mathematical Formulation

6.2.1 The Discrete-Time Kalman Filter

The discrete-time Kalman filter represents the original version of the Kalman filter presented in 1960 [30]. It can be applied to both discrete-time or continuous-time linear system models. In fact, if the physical system is modelled by a linear (time-variant) continuous-time set of stochastic equations

$$\begin{cases} \dot{\mathbf{x}}(t) = \mathbf{A}(t)\mathbf{x}(t) + \mathbf{B}(t)\mathbf{u}(t) + \mathbf{G}(t)\mathbf{w}(t) & (6.1a) \\ \mathbf{y}(t) = \mathbf{H}(t)\mathbf{x}(t) + \mathbf{n}(t) & (6.1b) \end{cases}$$

where:

- $\mathbf{x}(t)$ is the *system state vector* that has to be estimated $\in \mathbb{R}^{n\times 1}$
- $\mathbf{y}(t)$ is the *measurement vector* $\in \mathbb{R}^{m\times 1}$
- $\mathbf{u}(t)$ is the *control input vector* $\in \mathbb{R}^{r\times 1}$
- $\mathbf{w}(t)$ is the *process noise vector* $\in \mathbb{R}^{s\times 1}$
- $\mathbf{n}(t)$ is the *measurement (read-out) noise vector* $\in \mathbb{R}^{m\times 1}$
- $\mathbf{A}(t)$ is the *dynamic matrix* $\in \mathbb{R}^{n\times n}$
- $\mathbf{B}(t)$ is the *control input coupling matrix* $\in \mathbb{R}^{n\times r}$
- $\mathbf{G}(t)$ is the *process noise input coupling matrix* $\in \mathbb{R}^{n\times s}$
- $\mathbf{H}(t)$ is the *measurement matrix* $\in \mathbb{R}^{m\times n}$

it is possible to pass to the discrete form

$$\begin{cases} \mathbf{x}_k = \mathbf{\Phi}_{k-1}\mathbf{x}_{k-1} + \mathbf{\Lambda}_{k-1}\mathbf{u}_{k-1} + \mathbf{\Gamma}_{k-1}\mathbf{w}_{k-1} & (6.2a) \\ \mathbf{y}_k = \mathbf{H}_k\mathbf{x}_k + \mathbf{n}_k & (6.2b) \end{cases}$$

where:

- $\mathbf{x}_k$ is the *system state vector* $\in \mathbb{R}^{n\times 1}$ computed at the time step t_k, i.e. $\mathbf{x}_k = \mathbf{x}(t_k)$ [1]
- $\mathbf{w}_{k-1}$ is the *discrete process noise vector* $\in \mathbb{R}^{s\times 1}$ at the time step t_{k-1}
- $\mathbf{n}_{k-1}$ is the *discrete measurement (read-out) noise vector* $\in \mathbb{R}^{m\times 1}$ at the time step t_{k-1}
- $\mathbf{\Phi}_{k-1}$ is the *state transition matrix* $\in \mathbb{R}^{n\times n}$ which relates the state at the time step t_{k-1} to the state at the time step t_k in the absence of either a driving function or process noise

by computing the following expressions

$$\mathbf{\Phi}_{k-1} = \mathbf{\Phi}(t_k, t_{k-1}) \xrightarrow{\text{if } \mathbf{A} \text{ is time invariant}} \mathbf{\Phi}_{k-1} = e^{\mathbf{A}(t_k - t_{k-1})} = \sum_{i=0}^{\infty} \frac{(t_k - t_{k-1})^i}{i!}\mathbf{A}^i \qquad (6.3)$$

[1] The same can be repeated for $\mathbf{y}_k$, $\mathbf{H}_k$

$$\boldsymbol{\Gamma}_{k-1}\mathbf{w}_{k-1} = \int_{t_{k-1}}^{t_k} \boldsymbol{\Phi}(t_k,\tau)\mathbf{G}(\tau)\mathbf{w}(\tau)\mathrm{d}\tau \tag{6.4}$$

$$\boldsymbol{\Lambda}_{k-1}\mathbf{u}_{k-1} = \int_{t_{k-1}}^{t_k} \boldsymbol{\Phi}(t_k,\tau)\mathbf{B}(\tau)\mathbf{u}(\tau)\mathrm{d}\tau \xrightarrow[\text{over } [t_{k-1},t_k]]{\text{Assuming } \mathbf{u} \text{ constant}} \boldsymbol{\Lambda}_{k-1}\mathbf{u}_{k-1} = \mathbf{u}(t_{k-1})\int_{t_{k-1}}^{t_k} \boldsymbol{\Phi}(t_k,\tau)\mathbf{B}(\tau)\mathrm{d}\tau \tag{6.5}$$

Note that, the models are both constituted of a linear set of state (differential in the continuous case, difference in the discrete case) equations (Eq. (6.1a - 6.2a)) and a linear set of measurement equations (Eq. (6.1b - 6.2b)).

Therefore, the discrete-time Kalman filter addresses the problem of estimating, in an optimal way, the states of the linear, time-varying, discrete-time stochastic system

$$\begin{cases} \mathbf{x}_k = \boldsymbol{\Phi}_{k\text{-}1}\mathbf{x}_{k\text{-}1} + \boldsymbol{\Lambda}_{k\text{-}1}\mathbf{u}_{k\text{-}1} + \boldsymbol{\Gamma}_{k\text{-}1}\mathbf{w}_{k\text{-}1} & k \geq 0 \quad (6.2a) \\ \mathbf{y}_k = \mathbf{H}_k\mathbf{x}_k + \mathbf{n}_k & (6.2b) \end{cases}$$

independently from how the discrete dynamic model of the process (Eq. (6.2)) is obtained.

The basic assumptions that must be satisfied to solve the estimation problem in an optimal way are the linearity of the system (state and measurement) dynamics and the following conditions concerning the random vector involved:

- the process ($\mathbf{w}_k$) and the measurement ($\mathbf{n}_k$) noise have to be uncorrelated (e.g. white), Gaussian process, independent of each other, with zero mean and given covariance matrices ($\mathbf{Q}_k^d$ is the *discrete process noise covariance matrix* and $\mathbf{R}_k^d$ is the *discrete measurement noise covariance matrix* at time step t_k)[1]

$$p(\mathbf{w}_k) = N(\mathbf{0}, \mathbf{Q}_k^d) \longrightarrow \mathrm{E}\left[\mathbf{w}_k\mathbf{w}_j^T\right] = \mathbf{Q}_k^d \cdot \Delta(k - j) \tag{6.6}$$

$$p(\mathbf{n}_k) = N(\mathbf{0}, \mathbf{R}_k^d) \longrightarrow \mathrm{E}\left[\mathbf{n}_k\mathbf{n}_j^T\right] = \mathbf{R}_k^d \cdot \Delta(k - j) \tag{6.7}$$

$$\mathrm{E}\left[\mathbf{w}_k\mathbf{n}_j^T\right] = \mathbf{0} \ \forall\ k, j \tag{6.8}$$

[1] $N(\bar{\mathbf{x}}, \mathbf{P})$ indicates a n-dimensional Gaussian distribution with mean vector $\bar{\mathbf{x}}$ and covariance matrix $\mathbf{P}$; $\Delta(k - j)$ stands for the *Kronecker delta function*.

- the initial *system state vector* $\mathbf{x}_0$ has to be a Gaussian random vector with

$$p(\mathbf{x}_0) = N(\bar{\mathbf{x}}_0, \boldsymbol{\Sigma}_0) \tag{6.9}$$

Defining $\hat{\mathbf{x}}_k^- \in \mathbb{R}^{n\times 1}$ as the *a priori state estimate* (which represents the estimate of the state $\mathbf{x}_k$ at the time step t_k before the acquisition of the measurement $\mathbf{y}_k$ at the time step t_k) and $\hat{\mathbf{x}}_k \in \mathbb{R}^{n\times 1}$ as the *a posteriori state estimate* (which represents the estimate of the state $\mathbf{x}_k$ at the time step t_k after the acquisition of the measurement $\mathbf{y}_k$ at the time step t_k), associating to these estimates the *a priori estimate error* $\mathbf{e}_k^-$ and the *a posteriori estimate error* $\mathbf{e}_k$

$$\mathbf{e}_k^- = \mathbf{x}_k - \hat{\mathbf{x}}_k^- \tag{6.10}$$

$$\mathbf{e}_k = \mathbf{x}_k - \hat{\mathbf{x}}_k \tag{6.11}$$

defining the *a priori error covariance matrix* $\mathbf{P}_k^-$ and the *a posteriori error covariance matrix* $\mathbf{P}_k$, which represent the mean square errors of the correspondent estimate errors, as

$$\mathbf{P}_k^- = \mathrm{E}\left[\mathbf{e}_k^-\mathbf{e}_k^{-\mathrm{T}}\right] = \mathrm{E}\left[\left(\mathbf{x}_k - \hat{\mathbf{x}}_k^-\right)\left(\mathbf{x}_k - \hat{\mathbf{x}}_k^-\right)^{\mathrm{T}}\right] \tag{6.12}$$

$$\mathbf{P}_k = \mathrm{E}\left[\mathbf{e}_k\mathbf{e}_k^{\mathrm{T}}\right] = \mathrm{E}\left[\left(\mathbf{x}_k - \hat{\mathbf{x}}_k\right)\left(\mathbf{x}_k - \hat{\mathbf{x}}_k\right)^{\mathrm{T}}\right] \tag{6.13}$$

the discrete-time Kalman filter is an observer in the form

$$\hat{\mathbf{x}}_k = \hat{\mathbf{x}}_k^- + \mathbf{K}_k(\mathbf{y}_k - \mathbf{H}_k\hat{\mathbf{x}}_k^-) \tag{6.14}$$

where the *Kalman gain matrix* $\mathbf{K}_k$ is chosen such that Eq. (6.14) evaluates the *a posteriori state estimate* $\hat{\mathbf{x}}_k$ that minimizes the mean square error between the state and the a posteriori state estimate given by Eq. (6.13). The extensive derivation of the Kalman filter algorithm can be found in [27] and can be summarized in this way:

- Eq. (6.14) and Eq. (6.2a) are substituted in Eq. (6.11);

- the result of the previous point is substituted in Eq. (6.13) and the expression of $\mathbf{P}_k$ is obtained;
- the derivative of the trace of $\mathbf{P}_k$ with respect to $\mathbf{K}_k$ is taken and the result is set equal to zero;
- the obtained equation is solved for $\mathbf{K}_k$.

Therefore, if all the listed assumptions are satisfied, the resulting Kalman Filter is a linear, discrete-time, finite dimensional, time-varying system, whose inputs are the control inputs and the measurements and which:

- evaluates the *state estimate* $\hat{\mathbf{x}}_k$ that minimizes the mean square error between the state and the state estimate $\mathbf{P}_k$
- maintains and propagates the first two moments of the state distribution:

$$\hat{\mathbf{x}}_k = \mathrm{E}\left[\mathbf{x}_k\right] \tag{6.15}$$

$$\mathrm{E}\left[\left(\mathbf{x}_k - \hat{\mathbf{x}}_k\right)\left(\mathbf{x}_k - \hat{\mathbf{x}}_k\right)^{\mathrm{T}}\right] = \mathrm{E}\left[\left(\mathbf{x}_k - \mathrm{E}\left[\mathbf{x}_k\right]\right)\left(\mathbf{x}_k - \mathrm{E}\left[\mathbf{x}_k\right]\right)^{\mathrm{T}}\right] \tag{6.16}$$

The Kalman filter alghoritm is depicted in Figure 6.2.1-1.

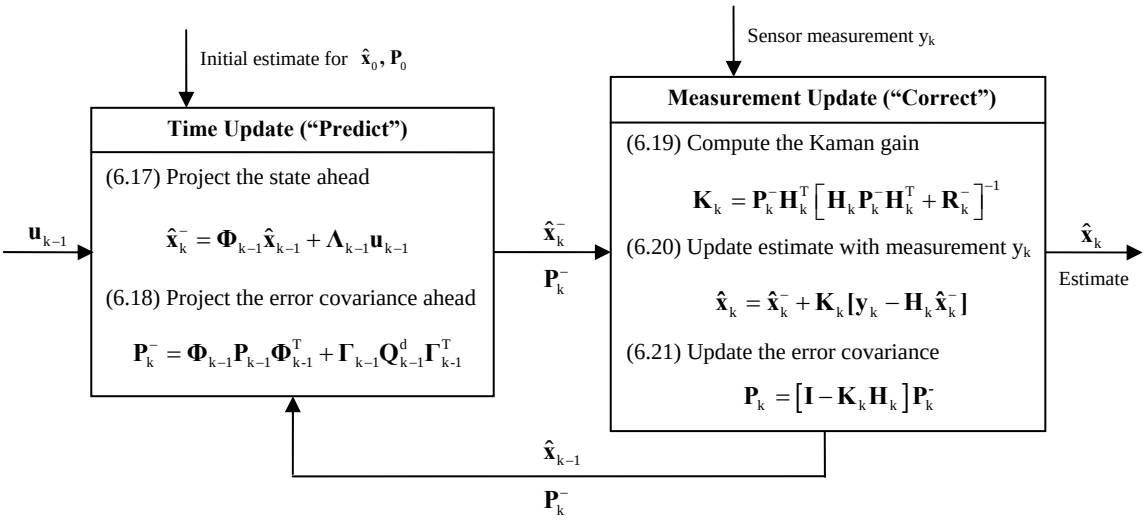

Figure 6.2.1-1: Discrete-time Kalman filter algorithm

As can be noted, the Kalman filter has to be initialized by the initial conditions $\hat{\mathbf{x}}_0 = \overline{\mathbf{x}}_0$ and $\mathbf{P}_0 = \boldsymbol{\Sigma}_0$, then the estimation process is a form of feedback control. In fact the Kalman filter equation can be divided into two groups: the *time update equations*, that are responsible for projecting forward in time the current state (by using only the deterministic part of the state dynamic model, Eq. (6.17)) and the error covariance matrix (Eq. (6.18)) in order to obtain the *a priori* estimates for the next step, and the *measurement update equations* (Eq. (6.19-6.20-6.21)) that are responsible for the feedback, in other words they correct the *a priori* estimates incorporating a new measurement in order to obtain improved *a posteriori* estimates. After each time and measurement update pair, the process is repeated with the previous *a posteriori* estimates used to predict the new *a prio*ri estimates. This recursive nature is one of the main advantage of the Kalman filter: it needs to store only the last state estimate and the correspondent last error covariance matrix in order to compute the new ones,thus saving memory, increasing the computational velocity and making it particularly suitable for real-time applications.

As can be seen from Eq. (6.20), the Kalman gain matrix weights the *innovation*, which is the difference between the measurements and the measurement predictions

$$\mathbf{i}_k = (\mathbf{y}_k - \mathbf{H}_k \hat{\mathbf{x}}_k^-) \tag{6.22}$$

Eq. (6.19) shows that the innovation and, in particular, the measurements are weighted in function of their reliability, in other words the Kalman gains are in inverse relation to the measurement noise level. Moreover note that the Kalman gain matrix is proportional to the *a priori error covariance matrix*.

Again note that the discrete Riccati equations (6.18-6.19-6.21), which provided the error covariance matrices and the Kalman gain matrix, could be computed off-line, before the filter is actually run, since they are independent from the measurements, the controls and the states. This is not true anymore in the adaptive filtering approach where $\mathbf{Q}_k^d$ and/or $\mathbf{R}_k^d$ depend on the innovation sequence. This adaptive technique is adopted when the properties of the process and the measurement noise are not known with sufficient accuracy and there is the necessity to adapt their amplitude during the process.

6.2.2 The Discrete-Time Steady-State Kalman Filter

If the linear system (6.2) is time-invariant (i.e. all the model matrices are constant)

$$\begin{cases} \mathbf{x}_k = \mathbf{\Phi}\ \mathbf{x}_{k-1} + \mathbf{\Lambda}\ \mathbf{u}_{k-1} + \mathbf{\Gamma}\ \mathbf{w}_{k-1} \\ \mathbf{y}_k = \mathbf{H}\ \mathbf{x}_k + \mathbf{n}_k \end{cases}$$

with $\mathbf{w}_{k-1}$ and $\mathbf{n}_k$ mutually independent sequences of zero mean, uncorrelated, Gaussian noise with time-invariant discrete covariance matrices $\mathbf{Q}^d$ and $\mathbf{R}^d$, and if

- $\mathbf{\Gamma Q}^d\mathbf{\Gamma}^T = \left(\mathbf{\Gamma Q}^d\mathbf{\Gamma}^T\right)^T > \mathbf{0}$, i.e. is a positive-definite matrix
- $\mathbf{R}^d = \left(\mathbf{R}^d\right)^T > \mathbf{0}$, i.e. is a positive-definite matrix
- the pair $\mathbf{(\Phi, \Gamma Q}^d\mathbf{\Gamma}^T\mathbf{)}$ is controllable, i.e.

$$\text{rank}\left[\mathbf{\Gamma Q}^d\mathbf{\Gamma}^T \mid \mathbf{\Phi\Gamma Q}^d\mathbf{\Gamma}^T \mid \mathbf{\Phi}^2\mathbf{\Gamma Q}^d\mathbf{\Gamma}^T \mid \ldots \mid \mathbf{\Phi}^{n-1}\mathbf{\Gamma Q}^d\mathbf{\Gamma}^T\right] = n$$

- the pair $\mathbf{(\Phi, H)}$ is observable, i.e.

$$\text{rank}\left[\mathbf{H}^T \mid \mathbf{\Phi}^T\mathbf{H}^T \mid \left(\mathbf{\Phi}^T\right)^2\mathbf{H}^T \mid \ldots \mid \left(\mathbf{\Phi}^T\right)^{n-1}\mathbf{H}^T\right] = n$$

then

- the *a priori error covariance matrix* $\mathbf{P}_k^-$ converges to a constant symmetric positive-definite matrix

$$\lim_{k\to\infty}\mathbf{P}_k^- = \mathbf{P}_\infty^-$$

that represents the unique solution of the discrete algebraic Riccati equation

$$\mathbf{P}_\infty^- = \mathbf{\Phi P}_\infty^-\mathbf{\Phi}^T - \mathbf{\Phi P}_\infty^-\mathbf{H}^T\left[\mathbf{HP}_\infty^-\mathbf{H}^T + \mathbf{R}^d\right]^{-1}\mathbf{HP}_\infty^-\mathbf{\Phi}^T + \mathbf{\Gamma}_k\mathbf{Q}^d\mathbf{\Gamma}_k^T$$

Since it is unique, it is independent of the initial condition $\mathbf{P}_0$

- as a consequence, the *Kalman gain matrix* converges to

$$\mathbf{K}_\infty = \lim_{k\to\infty}\mathbf{K}_k = \mathbf{P}_\infty\mathbf{H}^T\left[\mathbf{HP}_\infty\mathbf{H}^T + \mathbf{R}^d\right]^{-1}$$

The corresponding filter

$$\hat{\mathbf{x}}_k^- = \mathbf{\Phi}\ \hat{\mathbf{x}}_{k-1} + \mathbf{\Lambda}\ \mathbf{u}_{k-1} \tag{6.1a}$$

$$\hat{\mathbf{x}}_k = \hat{\mathbf{x}}_k^- + \mathbf{K}_\infty(\mathbf{y}_k - \mathbf{H}\ \hat{\mathbf{x}}_k^-) \tag{6.1b}$$

is known as the steady-state discrete-time Kalman filter and its dynamics is time-invariant.

6.2.3 The Continuous-Time Kalman Filter

In analogy to the discrete-time case, the continuous-time Kalman filter (Kalman-Bucy filter [31]) addresses the problem of estimating, in an optimal way, the states of the linear, time-varying, continuous-time stochastic system

$$\begin{cases} \dot{\mathbf{x}}(t) = \mathbf{A}(t)\mathbf{x}(t) + \mathbf{B}(t)\mathbf{u}(t) + \mathbf{G}(t)\mathbf{w}(t) \\ \mathbf{y}(t) = \mathbf{H}(t)\mathbf{x}(t) + \mathbf{n}(t) \end{cases}$$

If the process ($\mathbf{w}(t)$) and the measurement ($\mathbf{n}(t)$) noise vectors are uncorrelated (e.g. white), Gaussian process, independent of each other, with zero mean and given covariance matrices ($\mathbf{Q}(t)$ is the *process noise covariance matrix* and $\mathbf{R}(t)$ is the *measurement noise covariance matrix*)

$$p(\mathbf{w}(t)) = N(\mathbf{0}, \mathbf{Q}(t)) \quad \longrightarrow \quad E\left[\mathbf{w}(t)\mathbf{w}^T(\tau)\right] = \mathbf{Q}(t)\cdot\delta(t-\tau)$$

$$p(\mathbf{n}(t)) = N(\mathbf{0}, \mathbf{R}(t)) \quad \longrightarrow \quad E\left[\mathbf{n}(t)\mathbf{n}^T(\tau)\right] = \mathbf{R}(t)\cdot\delta(t-\tau)$$

$$E\left[\mathbf{w}(t)\mathbf{n}^T(\tau)\right] = \mathbf{0} \ \ \forall\ t, \tau$$

where $\delta(t-\tau)$ is the *Dirac delta function*, and if the initial *system state vector* $\mathbf{x}_0$ is a Gaussian random vector with

$$p(\mathbf{x}_0) = N(\bar{\mathbf{x}}_0, \mathbf{\Sigma}_0)$$

it can be shown [27] that the discrete-time Kalman filter equations can be manipulated in order to obtain a continuous-time Kalman estimator in the form

$$\begin{cases} \dot{\hat{\mathbf{x}}}(t) = \mathbf{A}(t)\hat{\mathbf{x}}(t) + \mathbf{B}(t)\mathbf{u}(t) + \mathbf{K}(t)[\mathbf{y}(t) - \mathbf{H}(t)\hat{\mathbf{x}}(t)] \\ \hat{\mathbf{x}}(0) = E[\mathbf{x}(0)] = E[\mathbf{x}_0] = \bar{\mathbf{x}}_0 \end{cases}$$

where the *Kalman gain matrix*

$$\mathbf{K}(t) = \mathbf{P}(t)\mathbf{H}^{T}(t)\mathbf{R}^{-1}(t)$$

can be computed solving previously the continuous-time Riccati equation

$$\begin{cases} \dot{\mathbf{P}}(t) = \mathbf{A}(t)\mathbf{P}(t) + \mathbf{P}(t)\mathbf{A}^{T}(t) + \mathbf{G}(t)\mathbf{Q}(t)\mathbf{G}^{T}(t) - \mathbf{P}(t)\mathbf{H}^{T}(t)\mathbf{R}^{-1}(t)\mathbf{H}(t)\mathbf{P}(t) \\ \mathbf{P}(0) = \mathbf{P}_0 = \mathrm{E}\left[\left(\mathbf{x}_0 - \overline{\mathbf{x}}_0 \right) \left(\mathbf{x}_0 - \overline{\mathbf{x}}_0 \right)^{T} \right] \end{cases}$$

In the previous expressions

- $\hat{\mathbf{x}}(t)$ is the *system state estimate* $\in \mathbb{R}^{n\times 1}$ that minimizes the mean square error between the state and the state estimate
- $\mathbf{e}(t) = \mathbf{x}(t) - \hat{\mathbf{x}}(t)$ is the *estimate error*
- $\mathbf{P}(t) = \mathrm{E}\left[\mathbf{e}(t)\mathbf{e}^{T}(t) \right] = \mathrm{E}\left[\left(\mathbf{x}(t) - \hat{\mathbf{x}}(t) \right) \left(\mathbf{x}(t) - \hat{\mathbf{x}}(t) \right)^{T} \right]$ is the *error covariance matrix*

6.2.4 The Continuous-Time Steady-State Kalman Filter

If the linear system (6.1) is time-invariant

$$\begin{cases} \dot{\mathbf{x}}(t) = \mathbf{A}\mathbf{x}(t) + \mathbf{B}\mathbf{u}(t) + \mathbf{G}\mathbf{w}(t) \\ \mathbf{y}(t) = \mathbf{H}\mathbf{x}(t) + \mathbf{n}(t) \end{cases}$$

with $\mathbf{w}(t)$ and $\mathbf{n}(t)$ mutually independent sequences of zero mean, uncorrelated, Gaussian noise with time-invariant covariance matrices $\mathbf{Q}$ and $\mathbf{R}$, and if

- $\mathbf{GQG}^{T} = (\mathbf{GQG}^{T})^{T} > \mathbf{0}$, i.e. is a positive-definite matrix
- $\mathbf{R} = \mathbf{R}^{T} > \mathbf{0}$, i.e. is a positive-definite matrix
- the pair $\mathbf{(A, GQG}^{T}\mathbf{)}$ is controllable
- the pair $\mathbf{(A, H)}$ is observable

then

- the *error covariance matrix* $\mathbf{P}(t)$ converges to a constant symmetric positive-definite matrix

$$\lim_{t\to\infty}\mathbf{P}(t)=\mathbf{P}_{\infty}$$

which represents the unique solution of the algebraic Riccati equation

$$\mathbf{0}=\mathbf{A}\mathbf{P}_{\infty}+\mathbf{P}_{\infty}\mathbf{A}^{T}+\mathbf{G}\mathbf{Q}\mathbf{G}^{T}-\mathbf{P}_{\infty}\mathbf{H}^{T}\mathbf{R}^{-1}\mathbf{H}\mathbf{P}_{\infty}^{T} \tag{6.23}$$

-

Since it is unique, it is independent of the initial condition $\mathbf{P}_0$

- as a consequence, the *Kalman gain matrix* converges to

$$\mathbf{K}_{\infty}=\lim_{t\to\infty}\mathbf{K}(t)=\mathbf{P}_{\infty}\mathbf{H}^{T}\mathbf{R}^{-1}$$

The corresponding filter

$$\begin{cases}\dot{\hat{\mathbf{x}}}(t)=\mathbf{A}\hat{\mathbf{x}}(t)+\mathbf{B}\mathbf{u}(t)+\mathbf{K}_{\infty}[\mathbf{y}(t)-\mathbf{H}\hat{\mathbf{x}}(t)]\\ \hat{\mathbf{x}}(0)=\mathrm{E}[\mathbf{x}(0)]=\mathrm{E}[\mathbf{x}_0]=\overline{\mathbf{x}}_0\end{cases}$$

is known as the steady-state continuous-time Kalman filter (or the steady-state continuous-time Kalman-Bucy filter); its dynamics is time-invariant and it is identical to the Wiener filter.

Remark

Note that the process and measurement noise covariance matrices $(\mathbf{Q}(t),\mathbf{R}(t))$ appearing in the continuous Riccati equations have the same role than the discrete process and measurement noise covariance matrices $(\mathbf{Q}_k^d,\mathbf{R}_k^d)$ appearing in the discrete Riccati equations, but they have different physical units and different numerical values. The relationship between $\mathbf{Q}_k^d$ and $\mathbf{Q}(t)$ is given by

$$\mathbf{\Gamma}_k\mathbf{Q}_k^d\mathbf{\Gamma}_k^T=\int_{t_k}^{t_{k+1}}\mathbf{\Phi}(t_{k+1},\tau)\mathbf{G}(\tau)\mathbf{Q}(\tau)\mathbf{G}^T(\tau)\mathbf{\Phi}^T(t_{k+1},\tau)\mathrm{d}\tau \tag{6.24}$$

while the relationship between $\mathbf{R}_k^d$ and $\mathbf{R}(t)$ depends upon the way the discrete-time sensors process the noise. If they are integrating sensors, then

$$\mathbf{R}_k^d = \frac{1}{t_k - t_{k-1}} \int_{t_{k-1}}^{t_k} \mathbf{R}(\tau) d\tau$$

6.3 Modelling Problems

The purpose of section 6.3 - 6.4 is to explain the practical problems encountered in this work for the Kalman filter design process and implementation and to describe the adopted solutions.

6.3.1 State Augmentation

For many physical systems (e.g. the LISA satellite), the process and the measurement noise cannot be modelled by uncorrelated (e.g. white) Gaussian noise processes. Even if unbiased, correlated noises violate the signal conditions for the optimality of the Kalman filter. The solution to this problem is provided by the *state augmentation technique*, which consists in including the noise dynamics in the system dynamics using shaping filters. In fact, a correlated (e.g. coloured) Gaussian noise can be modelled by a linear system (i.e. a shaping filter) driven by noise with flat spectrum (white), which the filter "shapes" to represent the spectrum of the actual coloured noise. Thus, the state vector can be "augmented" by appending to it the state vector components of the shaping filter, with the resulting model having the form of a linear dynamic system driven by white noise. In this way the signal conditions are satisfied and the Kalman filter algorithm applied to the state augmented system provides an optimal estimate of the system states.

The mathematical procedure for the state augmentation in presence of correlated process noise is described hereby. If the system model is

$$\begin{cases} \dot{\mathbf{x}}(t) = \mathbf{A}(t)\mathbf{x}(t) + \mathbf{B}(t)\mathbf{u}(t) + \mathbf{F}(t)\mathbf{d}(t) \\ \mathbf{y}(t) = \mathbf{H}(t)\mathbf{x}(t) + \mathbf{n}(t) \end{cases} \tag{6.25}$$

where $\mathbf{d}(t)$ is non-white correlated Gaussian noise and can be modelled by a linear shaping filter

$$\begin{cases} \dot{\mathbf{x}}_{SF}(t) = \mathbf{A}_{SF}(t)\mathbf{x}_{SF}(t) + \mathbf{B}_{SF}(t)\mathbf{w}(t) \\ \mathbf{d}(t) = \mathbf{C}_{SF}(t)\mathbf{x}_{SF}(t) + \mathbf{D}_{SF}(t)\mathbf{w}(t) \end{cases} \tag{6.26}$$

where $\mathbf{w}(t)$ is a white Gaussian noise, it is possible to define a new *augmented state vector*

$$\mathbf{x}_A(t) = \left[\mathbf{x}(t)\ \mathbf{x}_{SF}(t)\right]^T$$

and to combine Eq. (6.24) and Eq. (6.25) into the matrix form

$$\begin{cases} \overbrace{\begin{bmatrix} \dot{\mathbf{x}}(t) \\ \dot{\mathbf{x}}_{SF}(t) \end{bmatrix}}^{\dot{\mathbf{x}}_A(t)} = \overbrace{\begin{bmatrix} \mathbf{A}(t) & \mathbf{F}(t)\mathbf{C}_{SF}(t) \\ \mathbf{0} & \mathbf{A}_{SF}(t) \end{bmatrix}}^{\mathbf{A}_A(t)} \overbrace{\begin{bmatrix} \mathbf{x}(t) \\ \mathbf{x}_{SF}(t) \end{bmatrix}}^{\mathbf{x}_A(t)} + \overbrace{\begin{bmatrix} \mathbf{B}(t) \\ \mathbf{0} \end{bmatrix}}^{\mathbf{B}_A(t)} \mathbf{u}(t) + \overbrace{\begin{bmatrix} \mathbf{F}(t)\mathbf{D}_{SF}(t) \\ \mathbf{B}_{SF}(t) \end{bmatrix}}^{\mathbf{G}_A(t)} \mathbf{w}(t) \\ \mathbf{y}(t) = \underbrace{[\mathbf{H}(t)\ \mathbf{0}]}_{\mathbf{H}_A(t)} \begin{bmatrix} \mathbf{x}(t) \\ \mathbf{x}_{SF}(t) \end{bmatrix} + \mathbf{n}(t) \end{cases} \tag{6.27}$$

The state augmented system Eq. (6.27) is a linear time-varying, stochastic system driven by white Gaussian noise as the Kalman filter basic assumptions require. Note that the size of the original dynamic system is increased by the size of the shaping filter.

A similar development is feasible also for the case of time-correlated measurement noise and the detailed procedure can be found in [27]. Then it is possible to combine both, process and measurement noise state augmentation.

Note that only zero-mean (white or coloured) noises satisfy the Kalman Filter assumptions. However several techniques exist to estimate and remove disturbance biases. (Chapter 9)

The main advantage of the state augmentation technique is that, since the state augmented system (6.27) fulfils the Kalman filter signal conditions, it provides the ground for an optimal filter design. However, the disadvantages of a fully optimal filter are that it could impose an unacceptable computer burden (since the size of the problem can be considerably enlarged), it could be too sensitive to uncertainties in the dynamics model parameters and it could be unstable (due to a possible un-osservability and un-controllability of the augmented system) producing divergence. In these cases, it is

necessary to implement suboptimal or reduced order filters by sacrificing some optimality.

6.3.2 Suboptimal and Reduced Order Filter

In this thesis, the design of suboptimal Kalman filters is based on two methods:

a) *State reduction*: choice of simplified system models obtained by deleting process and/or measurement noise states. This means that the state augmentation is not performed at all or it is just partially performed (for the process noise or for the measurement noise). This technique consists in designing the noise covariance matrices $(\mathbf{Q}(t), \mathbf{R}(t))$ as if the system was driven by "fictitious" white Gaussian noises which have the same overall effects of the "real" correlated noises. In other words, the variances of the coloured noises are computed or approximated in the high frequency range as it is described in Appendix B. Then, they are used to build the noise covariance matrices for the Riccati equations. In this way the filter "believes" that the process and the measurement noises are white noises with variances that are equal to the real variances of the coloured noises or to theirs values in the high frequency range. This is a good suboptimal filtering method if the correlated noises "behaves" as white noise at least in the frequency bandwidth of interest (i.e. if the shape filters are flat at high frequencies).

b) *Steady-state filtering*: choice of simplified system gains approximating the optimal time-varying gains with the correspondent steady-state gains. This is a good suboptimal filtering method if the steady-state conditions (sections 6.2.2–6.2.4) are satisfied and if the error covariance matrices and the Kalman gains stabilize quickly.

The previous methods can also be combined.

6.3.3 Filter Parameters and Tuning

The Kalman filter design process is actually something more complex than the application of scholastic theoretical methods. In fact, it requires a fine tuning of the

filter parameters (that in large dimension systems, as a LISA satellite is, are really a lot!) which is largely heuristic.
In fact, the performances of a the designed (suboptimal) Kalman filter can be degraded (sometimes till to divergence) when:

- the designed Kalman filter does not model with sufficient accuracy the real system dynamics;
- the designed Kalman filter is too sensitive towards uncertainties in the dynamics model parameters.

In order to improve the performances of the Kalman filter, several tuning strategies can be applied:

1. add fictitious process noise **w,** thus increasing one or more elements of the process noise covariance matrix **Q**
2. introduce a lower bound for one or more elements of the (*a posteriori*, in the discrete-time filter) error covariance matrix

$$\mathbf{P} = \max(\mathbf{P}, \mathbf{P}_{\max})$$

3. use an adaptive filter

The techniques 1 and 2 produce the same effects: they increase one or more elements of the error covariance matrix **P** and, consequently, the correspondent Kalman gains (Eq. (6.19)). The Kalman filter has a low-pass behaviour since it weights the measurements in function of their noise level. Therefore,to increase the Kalman gains implies to enhance the filter bandwidth: the measurements are passed more and, with them, the noise they convey. The filter is more able to track the real states, but the estimates result more noisy. This procedure is particularly useful when the filter has to operate for long time or converge quickly to low steady Kalman gains. When the Kalman gains are too low, the estimates are less noisy since new measurements are very poorly weighted, but the filter is slow and saturate (it could also diverge). This bears the risk that sudden changes in the reference signals (maneuvers) may not be detected immediately, but only with a significant delay. The choice of the appropriate level of the elements of **Q** and **P** is largely heuristic and depends to a great extent upon what is known about the physical system, the unmodeled states, etc. The main difference

between the two techniques is that the second one is not applicable to the steady-state filters, while the first is always usable.

The adaptive filtering technique is based on the equations reported in [34]. This method was studied and applied during the orientation phase of this thesis, but is not used in the LISA framework since it consists in a complex sensitive algorithm, with a poor physical meaning and with an high risk of instability.

6.4 Numerical Specialties

Truncation and roundoff errors, due to the inherently finite nature of the computer, can seriously degrade the performances of the Kalman filter. Hence, it is necessary to use implementation methods and numerical tricks which are robust against roundoff errors, but have an acceptable computational cost.

The main numerical specialities that are used in this work are presented in the following points:

a) Particular attention is posed into the discretization which involves the numerical computation of Eq. (6.3 - 6.4 - 6.5 - 6.24). In particular Eq. (6.24) is computed using the matrix exponential formulas that can be found in [26].

b) The covariance matrices are symmetrical by definition, but this condition might be violated by rounding errors of the update process. The symmetry of the a posteriori error covariance matrix is ensured by the use of the Joseph's formula

$$\mathbf{P}_k = (\mathbf{I} - \mathbf{K}_k\mathbf{H}_k)\mathbf{P}_k^-(\mathbf{I} - \mathbf{K}_k\mathbf{H}_k)^T + \mathbf{K}_k\mathbf{R}_k^d\mathbf{K}_k^T$$

in place of Eq. (6.21). The symmetry of $\mathbf{P}_k^-$, $\mathbf{R}_k^d$, $\mathbf{\Gamma}_k\mathbf{Q}_k^d\mathbf{\Gamma}_k^T$ and of the correspondent continuous-time matrices is ensured by posing

$$\mathbf{S} = \frac{\mathbf{S} + \mathbf{S}^T}{2}$$

at each time step.

c) In the discrete Kalman filter, the inversion of the following matrix has to be performed

$$\mathbf{H}_k\mathbf{P}_k^-\mathbf{H}_k^T + \mathbf{R}_k^d \tag{6.28}$$

If the measurement noise covariance matrix $\mathbf{R}_k^d$ is a diagonal matrix, meaning that the individual components of $\mathbf{n}_k$ are uncorrelated, the components of the measuring vector can be considered as independent scalar measurements rather than as a vector measurement. In this way, the inversion of Eq. (6.28) can be avoided (since it becomes a scalar) improving numerical accuracy. This procedure is called *decorrelation of the measurement matrix* and a detailed description of its mathematical implementation can be found in [27].

d) Minimize the number of calculations (e.g. by reusing partial results in the discrete-time implementation)

e) The initial conditions indicated for the optimality are

$$\hat{\mathbf{x}}_0 = \overline{\mathbf{x}}_0$$

$$\mathbf{P}_0 = \mathbf{\Sigma}_0$$

hoever the values of $\overline{\mathbf{x}}_0$ and $\mathbf{\Sigma}_0$ are not a priori known. If the system is stable and quickly convergent to the steady-state, the choice of the initial conditions influences only the initial transient of the filter. However, some shrewdness is recommended. The initial error covariance matrix $\mathbf{P}_0$ tells the filter how much it can trust the initial estimate $\hat{\mathbf{x}}_0$. Therefore it must be ensured that

$$\left|\hat{\mathbf{x}}_0 - \mathbf{x}_0\right|^2 << \text{trace}(\mathbf{P}_0)$$

On the other side, the misscaling between the initial state estimation uncertainty and the measurement uncertainty could case an ill-conditioning in the computation of

$$\mathbf{K}_0 = \mathbf{P}_0^- \mathbf{H}_0^T (\mathbf{H}_0 \mathbf{P}_0^- \mathbf{H}_0^T + \mathbf{R}_0^d)^{-1}$$

where, if

$$\mathbf{P}_0^- >> \mathbf{R}_0^d$$

because of the roundoff errors, the consequence is that

$$\mathbf{H}_0 \mathbf{P}_0^- \mathbf{H}_0^T + \mathbf{R}_0^d \cong \mathbf{H}_0 \mathbf{P}_0^- \mathbf{H}_0^T$$

And, from Eq.(6.21) follows

$$\mathbf{P}_1 = \mathbf{0}$$

Chapter 7

Kalman Filter Design for the LISA Constellation Acquisition Control

7.1 Kalman Filter Design Principle: the Gyro Mode

The objective of the Kalman filter (KF) is to process the measurements data coming from all the available sensors (star-tracker, OATM sensor and IS unit) providing enhanced estimates of the SC attitude, the telescope 1 in-plane pointing angle and the test masses coordinates, such that the SC and the telescope, and consequently the laser beams, are able to follow the acquisition guidance laws with an error[1] that fulfils the requirements established for the acceptable jitter and drift of the telescopes line-of sight attitude during the acquisition on CCD phase Table(2.3.3-3).

This control mode is addressed as the *gyro mode* since it is based on the same principle, which is often used for spacecraft attitude determination in high accuracy pointing applications and which relies on the hybridisation of STR and gyroscope measurement data. In analogy to the STR and gyros data fusion approach, the IS measurements are used as gyro-like measurements to filter, smoothen and propagate the STR data, supporting in this way the attitude control system over short-time periods. This can happen because the two signals have complementary error characteristics: the STR has a very good long-term stability but suffers from short and medium-term noise, on the contrary the IS ("gyro") has a very good short-term stability but suffers from

[1] In the sense introduced in section 5.3: Error = Reference Signal – Real Plant State

medium and long-term drifts[1]. Therefore, the goal of the Kalman filter is to obtain a reduction of the STR noise effect in the high frequency range of the states signals, while it is expected that the signals behave at low frequencies as if the filter is not applied. This should allow the satisfaction of the requirements in the time-domain.

Considering the state and measurements equations of the LISA satellite Eq. (3.7-3.8), it can be noted that the coupling between the SC and the telescope states with the T/M states comes from the control matrix **B** (i.e. there is no direct coupling between the states or the measurements). Therefore, the physical principle of the estimation process can be qualitatively explained in this way: an improved estimate of the T/M coordinates, which means a reduction of the STR effects over them, produces more accurate suspension control signals. This improves the estimate of the SC attitude through the dynamic coupling (since the non-drag-free T/M coordinates are obliged to follow the SC via the suspension controller). In other words, a better estimate and control of the T/M coordinates imply a better estimation and control of the SC attitude and the telescope in-plane pointing angle. The STR is used only in the medium and long-term period in order to correct the long term drift.

In the following sections, the design of the Kalman filter is performed. Three suitable Kalman filters are identified: the advantages/disadvantages of each type are pointed out and their performances are analysed and compared. An indication for the final choice is provided in chapter 10 and it is also based on the results of the sensitivity analysis towards uncertainties in the dynamics models (chapter 8) and on the DC effects and compensation analysis (chapter 9).

7.2 Kalman Filter Parameters (Process Models)

A mathematical model of the states dynamics and of the sensor devices dynamics, together with a statistical description of the measurement noises and of the process noises of the LISA satellite, are required. The ensemble of this information constitutes the ***Kalman filter process model*** of the LISA satellite. The starting point for its derivation is constituted by the state equation (3.7) and the measurement equation (3.8)

[1] This happens in particularly when the DC (constant) parasitic forces and torques acting on the T/M are taken in consideration. If the test masses move or rotate because of the DC actions, the spacecraft, which is forced to follow the T/M, also moves and rotates. Therefore a long-term drift on the satellite attitude is expected.

which represent the ***real model*** of the LISA satellite (i.e. used to simulate the real behaviour of the satellite).

7.2.1 System State Cancellation

The state vector has to be reduced since the position and the velocity of the spacecraft are not observable. The *system state cancellation* procedure consists in eliminating the equations of motion involving the SC position. Introducing the reduced *state vector* $\mathbf{x} \in \mathbb{R}^{32x1}$

$$\mathbf{x} = [\boldsymbol{\omega}_B \;\; \dot{\mathbf{r}}_1 \;\; \boldsymbol{\omega}_1 \;\; \dot{\mathbf{r}}_2 \;\; \boldsymbol{\omega}_2 \;\; \dot{\alpha} \;\; \boldsymbol{\alpha}_B \;\; \mathbf{r}_1 \;\; \boldsymbol{\alpha}_1 \;\; \mathbf{r}_2 \;\; \boldsymbol{\alpha}_2 \;\; \alpha]^T$$

and setting

- $\boldsymbol{\Omega}_{16\times16} = \begin{bmatrix} \mathbf{0}_{3\times3} & \mathbf{0}_{3\times6} & \mathbf{0}_{3\times6} & \mathbf{0}_{3\times1} \\ \mathbf{0}_{6\times3} & \boldsymbol{\Omega}_1 & \mathbf{0}_{6\times6} & \mathbf{0}_{6\times1} \\ \mathbf{0}_{6\times3} & \mathbf{0}_{6\times6} & \boldsymbol{\Omega}_2 & \mathbf{0}_{6\times1} \\ \mathbf{0}_{1\times3} & \mathbf{0}_{1\times6} & \mathbf{0}_{1\times6} & \mathbf{0}_{1\times1} \end{bmatrix}$
- $\mathbf{M}^{-1}\hat{\mathbf{B}}_{419,119}$ is $\mathbf{M}^{-1}\hat{\mathbf{B}}$ without the first three rows
- $\mathbf{M}^{-1}\hat{\mathbf{F}}_{419,119}$ is $\mathbf{M}^{-1}\hat{\mathbf{F}}$ without the first three rows

the state equation (3.7) can be rewritten as

$$\dot{\mathbf{x}}(t) = \underbrace{\begin{bmatrix} \mathbf{0}_{16\times16} & \boldsymbol{\Omega}_{16\times16} \\ \mathbf{E}_{16\times16} & \mathbf{0}_{16\times16} \end{bmatrix}}_{\mathbf{A}} \mathbf{x}(t) + \underbrace{\begin{bmatrix} \mathbf{M}^{-1}\hat{\mathbf{B}}_{419,119} \\ \mathbf{0}_{16\times19} \end{bmatrix}}_{\mathbf{B}} \mathbf{u}(t) + \underbrace{\begin{bmatrix} \mathbf{M}^{-1}\hat{\mathbf{F}}_{419,125} \\ \mathbf{0}_{16\times25} \end{bmatrix}}_{\mathbf{G}} \mathbf{d}(t) \qquad (7.1)$$

where $\mathbf{u}(t)$ and $\mathbf{d}(t)$ are the same of section 3.2, while the measurement equation (3.8) can be rewritten as

$$\mathbf{y}(t) = \underbrace{\begin{bmatrix} \mathbf{0}_{3\times3} & \mathbf{0}_{3\times12} & \mathbf{0}_{3\times1} & \mathbf{E}_{3\times3} & \mathbf{0}_{3\times12} & \mathbf{0}_{3\times1} \\ \mathbf{0}_{12\times3} & \mathbf{0}_{12\times12} & \mathbf{0}_{12\times1} & \mathbf{0}_{12\times3} & \mathbf{g}_{IS} & \mathbf{0}_{12\times1} \\ \mathbf{0}_{1\times3} & \mathbf{0}_{1\times12} & \mathbf{0}_{1\times1} & \mathbf{0}_{1\times3} & \mathbf{0}_{1\times12} & \mathbf{E}_{1\times3} \end{bmatrix}}_{\mathbf{H}} \mathbf{x}(t) + \mathbf{v}(t) \qquad (7.2)$$

where $\mathbf{y}(t)$ and $\mathbf{v}(t)$ are the same of section 3.3.

Eq.(7.1) and Eq. (7.2) constitute a linear, time-invariant, continuous-time stochastic system driven by the read-out noise vector $\mathbf{v}(t)$ and the disturbance input vector $\mathbf{d}(t)$. This model is linear, but it does not satisfied the Kalman filter signal conditions since the elements of the measurement vector and the disturbance input vector are not all white Gaussian process. In order to solve this problem, the state augmentation (section 6.3.1) or the state reduction (section 6.3.2 **a)**) modelling strategies are adopted.

7.2.2 Preliminary Remarks

The LISA satellite real model is continuous-time. Therefore, the Kalman filter process models are continuous-time.

The LISA satellite real model is time-invariant. Therefore, the Kalman filter process models are time-invariant. All the matrices are time-invariant and their time dependence is omitted in the following.

All the measurement and process noise components are assumed to be uncorrelated between them. Therefore, the measurement noise covariance matrix **R** and the process noise covariance matrix **Q** are diagonal

$$\mathrm{E}\left[\mathbf{w}(t)\mathbf{n}^{T}(\tau)\right]=\mathbf{0}\ \ \forall\ t,\tau$$

$$\mathbf{R}=\begin{pmatrix}\sigma_{n_1}^2 & & 0\\ & \ddots & \\ 0 & & \sigma_{n_m}^2\end{pmatrix}$$

$$\mathbf{Q}=\begin{pmatrix}\sigma_{w_1}^2 & & 0\\ & \ddots & \\ 0 & & \sigma_{w_m}^2\end{pmatrix}$$

where $\sigma_{n_i}^2$ is the variance of the i-th component of the measurement noise vector and $\sigma_{w_i}^2$ is the variance of the i-th component of the process noise vector.

The Kalman filter parameters that are necessary to define a Kalman filter process model are summarised in Table (7.2.2-1).

KF parameters	Task
x(t)	system state vector
y(t)	measurement vector
u(t)	control input vector
A	dynamic matrix
B	control input coupling matrix
G	process noise input coupling matrix
H	measurement matrix
Q	process noise covariance matrix
R	measurement noise covariance matrix

Table 7.2.2-1: Continuous-time Kalman filter parameters

The vectors **y**(t), **u**(t) for the Kalman filter process models are the same of Eq.(7.1) and Eq. (7.2) for all the proposed models.

7.2.3 Model 1: State Reduction

The matrices **A**, **B**, **G**, **H** and the system state vector **x**(t) for the KF process model are the same of Eq.(7.1) and Eq. (7.2)

The state reduction (section 6.3.2 **a)**) modelling strategy is adopted in order to define the noise covariance matrices **Q** and **R**. The process noise **w**(t) and the measurement noise **n**(t) of the KF process model are assumed to be coincident with the disturbance input vector **d**(t) and the read-out noise vector **v**(t) of Eq.(7.1) and Eq. (7.2) (even if they are not all white noises) respectively and their variances are computed according to what is reported in Appendix B.

The achieved KF process model has to estimate 32 states since $\mathbf{x}(t) \in \mathbb{R}^{32\times 1}$.

7.2.4 Model 2: State Augmentation for the Process Noise

The state augmentation (section 6.3.1) modelling strategy is applied for the process noise. The shaping filters that are used to model the disturbance input vector of Eq.(7.1) are added to the system dynamics according to the procedure described in (section 6.3.1). The KF process model results in

$$\begin{cases} \overbrace{\begin{bmatrix} \dot{\mathbf{x}}(t) \\ \dot{\mathbf{x}}_{SF}(t) \end{bmatrix}}^{\dot{\mathbf{x}}_A(t)} = \overbrace{\begin{bmatrix} \mathbf{A} & \mathbf{F}\mathbf{C}_{SF} \\ \mathbf{0} & \mathbf{A}_{SF} \end{bmatrix}}^{\mathbf{A}_A} \overbrace{\begin{bmatrix} \mathbf{x}(t) \\ \mathbf{x}_{SF}(t) \end{bmatrix}}^{\mathbf{x}_A(t)} + \overbrace{\begin{bmatrix} \mathbf{B} \\ \mathbf{0} \end{bmatrix}}^{\mathbf{B}_A} \mathbf{u}(t) + \overbrace{\begin{bmatrix} \mathbf{F}\mathbf{D}_{SF} \\ \mathbf{B}_{SF} \end{bmatrix}}^{\mathbf{G}_A} \mathbf{w}(t) \\ \mathbf{y}(t) = \underbrace{[\mathbf{H} \quad \mathbf{0}]}_{\mathbf{H}_A} \begin{bmatrix} \mathbf{x}(t) \\ \mathbf{x}_{SF}(t) \end{bmatrix} + \mathbf{v}(t) \end{cases} \tag{7.3}$$

where $\mathbf{w}(t) \in \mathbb{R}^{25\times 1}$ is a vector of unitary power, white, Gaussian noise.

The matrices **A**, **B**, **G**, **H** and the system state vector **x**(t) for the KF process model are those indicated with the subindex "A" in Eq. (7.3); **R** is computed as in Model 1; **Q** is a diagonal matrix whose elements are the variances of the components of $\mathbf{w}(t)$.

The achieved KF process model has to estimate 100 states since $\mathbf{x}_A(t) \in \mathbb{R}^{100\times 1}$, but only the first 32 are of interest.

7.2.5 Model 3: State Augmentation for the Measurement Noise

The state augmentation (section 6.3.1) modelling strategy is applied for the measurement noise. The procedure to obtain the KF process model is basically the same as for Model 2. The achieved KF process model has to estimate 44 states, but the performances of the filters implemented with this model are of the same order than those achievable with Model 1. In fact, the read-out noise vector of Eq. (7.2) is

$$\mathbf{v} = \begin{bmatrix} \mathbf{STR}_{ROnoise} \\ \mathbf{IS}_{ROnoise} \\ \mathbf{CAGE}_{ROnoise} \end{bmatrix} \tag{3.12}$$

where only the IS read-out noises are correlated. Moreover, their shaping filters (Figure 2.5.2-1) show a flat spectrum down to 10^{-4} Hz. Thus, a white noise approximation is suitable for the considered simulation times.

7.2.6 Model 4: State Augmentation for Process and Measurement Noise

The state augmentation (section 6.3.1) modelling strategy is applied for both, process and measurement noise. The procedure to obtain the KF process model is basically the same as for Model 2. The achieved KF process model has to estimate 112 states, but the performances of the filters implemented with this model are of the same order than those achievable with Model 2 for the same reasons explained in the previous section.

Remark

Model 3 and Model 4 produce an increase of computational cost (due to an increase of the size of the KF process model) without providing better performances. Their use is avoidable and, in this work, only the results achieved with Model 1 and Model 2 are presented.

7.3 Kalman Filter Algorithm

7.3.1 Algorithm 1: Time-Varying Discrete-Time Kalman Filter

The time-varying discrete-time Kalman filter algorithm (Figure 6.2.1-1) represents the usual approach for Kalman filtering.

Discretization

As it is known from chapter 6, in order to apply the discrete-time Kalman filter algorithm to the continuous-time models of the LISA satellite derived in the previous sections, they have to be discretized. The discretization of the models is performed as indicated in section 6.2.1 and uses the numerical specialties mentioned in section 6.4-**a)**.

Implementation

The time-varying discrete-time Kalman filter algorithm implementation is performed in the Simulink® environment. The main structure of the simulator for the LISA acquisition phase is depicted in Figure 7.3.1-1.

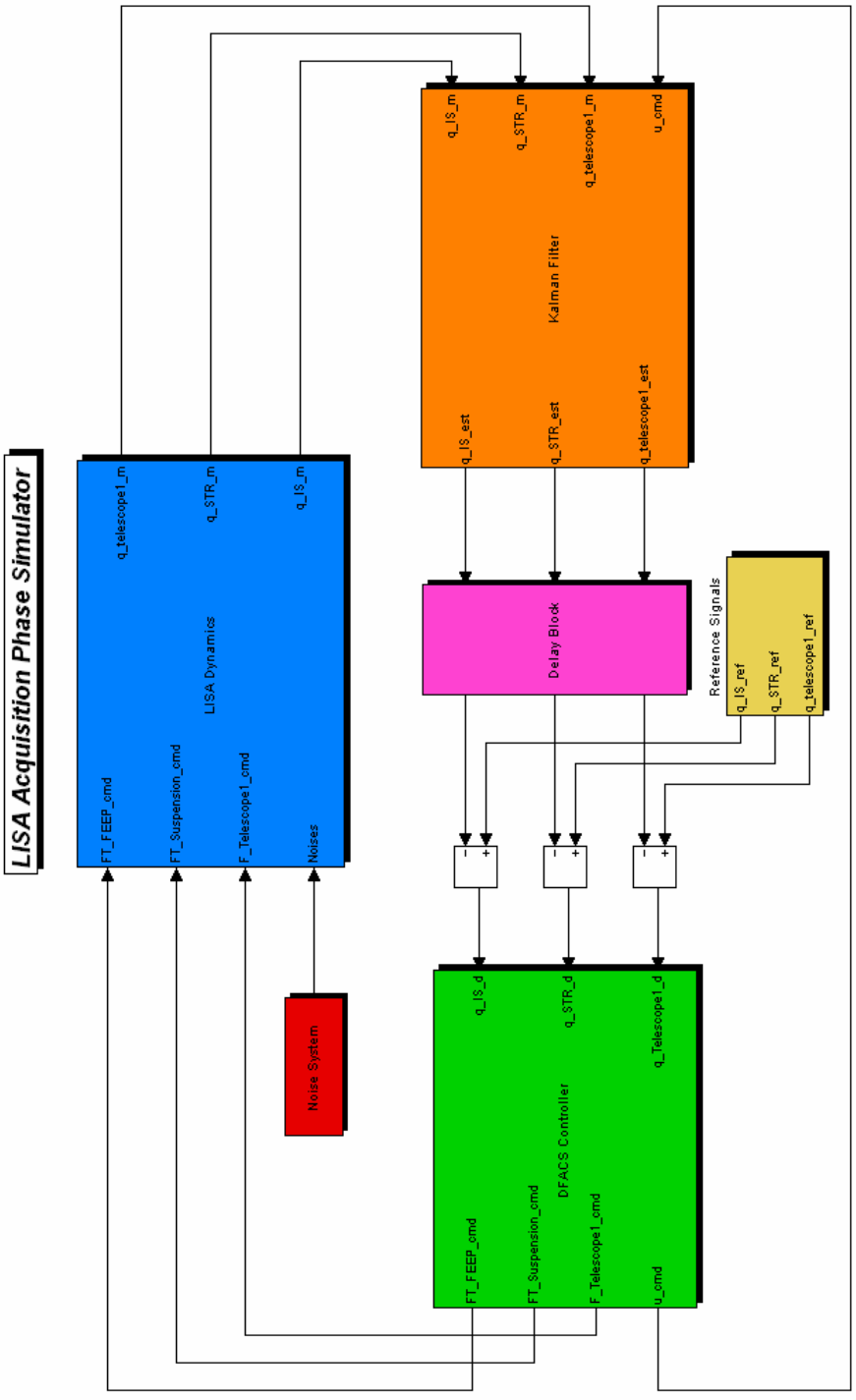

Figure 7.3.1-1: Main structure of the LISA acquisition phase simulator

Note that it is identical to the one presented in chapter 5, except for the addition of the *Kalman Filter* block, which is illustrated in Figure 7.3.1-2.

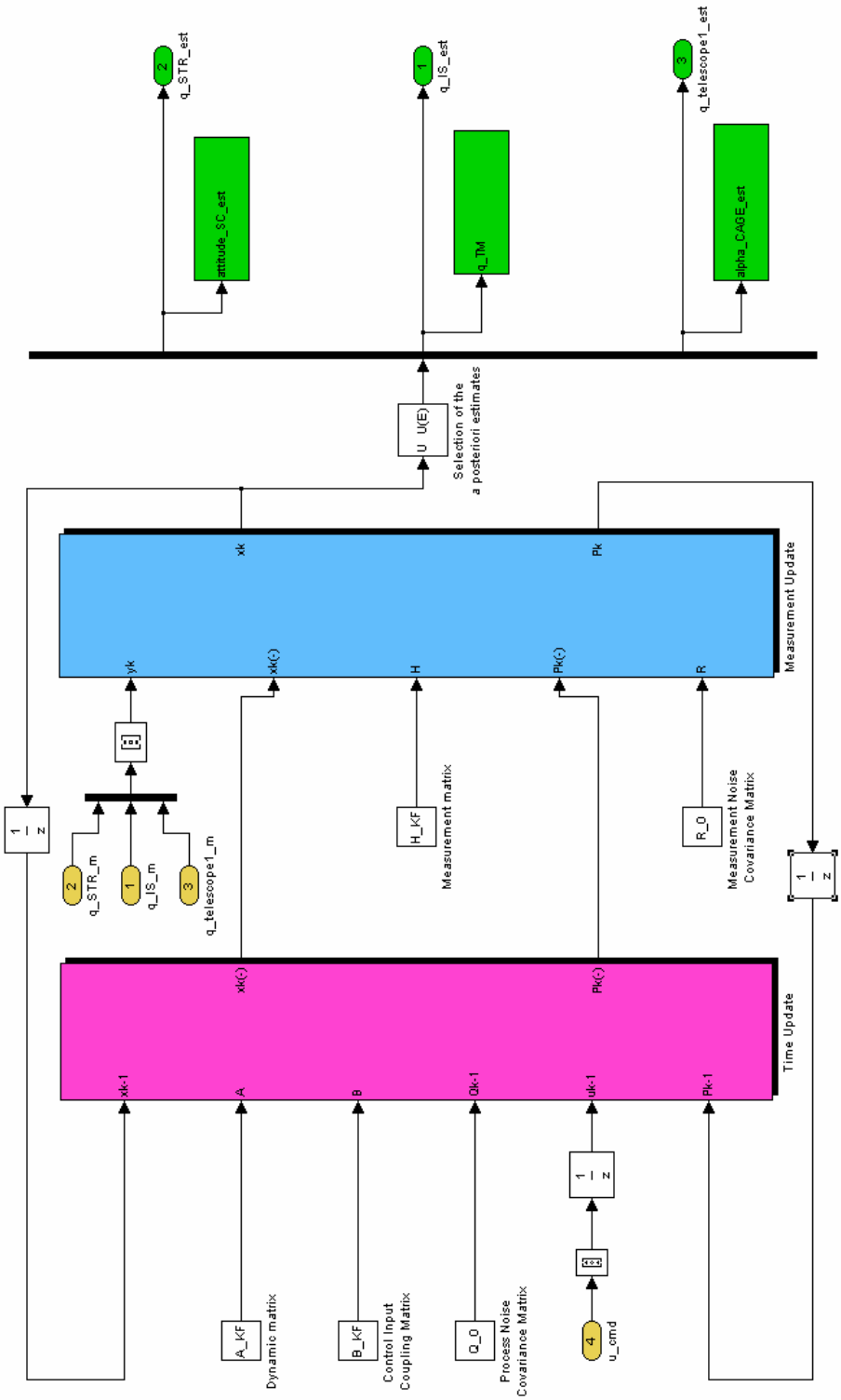

Figure 7.3.1-2: Kalman filter block

The KF subsystem inputs are the measurement data, coming from the STR, the OATM sensor and the IS unit, as well as the control commands, provided by the

controller before they are sent to the FEEP system, the OATM actuator and the IS actuator. The KF output ports are the estimates of the SC attitude, of the telescope in-plane pointing angle and of the T/M coordinates, which are selected between the components of the *a posteriori* state estimate vector $\hat{\mathbf{x}}_k$ (whose composition depends on which model is implemented). The estimated states are sent to the controller in place of the measurements.

The KF block implements the discrete-time Kalman filter algorithm. The *Time Update* subsystem implements the time update equations, which project forward in time the current state $\hat{\mathbf{x}}_k^-$ and the error covariance matrix $\mathbf{P}_k^-$

$$\hat{\mathbf{x}}_k^- = \mathbf{\Phi}_{k-1}\hat{\mathbf{x}}_{k-1} + \mathbf{\Lambda}_{k-1}\mathbf{u}_{k-1}$$

$$\mathbf{P}_k^- = \mathbf{\Phi}_{k-1}\mathbf{P}_{k-1}\mathbf{\Phi}_{k-1}^{\mathrm{T}} + \mathbf{\Gamma}_{k-1}\mathbf{P}_{k-1}\mathbf{\Gamma}_{k-1}^{\mathrm{T}}$$

and the *Measurement Update* subsystem (Figure 7.3.1-3) implements the measurement update equations, which accomplish a weighted correction of the prediction $\hat{\mathbf{x}}_k$ and the error covariance matrix $\mathbf{P}_k$ by means of the respective sensor measurements $\mathbf{y}_k$.

$$\mathbf{K}_k = \mathbf{P}_k^-\mathbf{H}_k^{\mathrm{T}}\left[\mathbf{H}_k\mathbf{P}_k^-\mathbf{H}_k^{\mathrm{T}} + \mathbf{R}_k^-\right]^{-1}$$

$$\hat{\mathbf{x}}_k = \hat{\mathbf{x}}_k^- + \mathbf{K}_k[\mathbf{y}_k - \mathbf{H}_k\hat{\mathbf{x}}_k^-]$$

$$\mathbf{P}_k = \left[\mathbf{I} - \mathbf{K}_k\mathbf{H}_k\right]\mathbf{P}_k^-$$

The time update block requires as inputs the control command vector **u**(t), provided by the controller, the state transition matrix (in Figure 7.3.1-2, $\mathbf{\Phi} = \mathbf{A}_{KF}$), the discrete control input matrix and the discrete process noise covariance matrix. These matrices, coming from the discretization of a time-invariant system, are time-invariant and are loaded by running the initialization file. The measurement update block requires as inputs the measurement vector **y**(t), provided by the sensors, the measurement matrix and the discrete measurement noise covariance matrix. These matrices are also time-invariant.

Note that the KF block is a completely general tool for the implementation of the discrete-time Kalman filter algorithm. Therefore, it could be used to estimate the states

of any system, also time-varying, just by changing the model matrices (and the size of some selector).

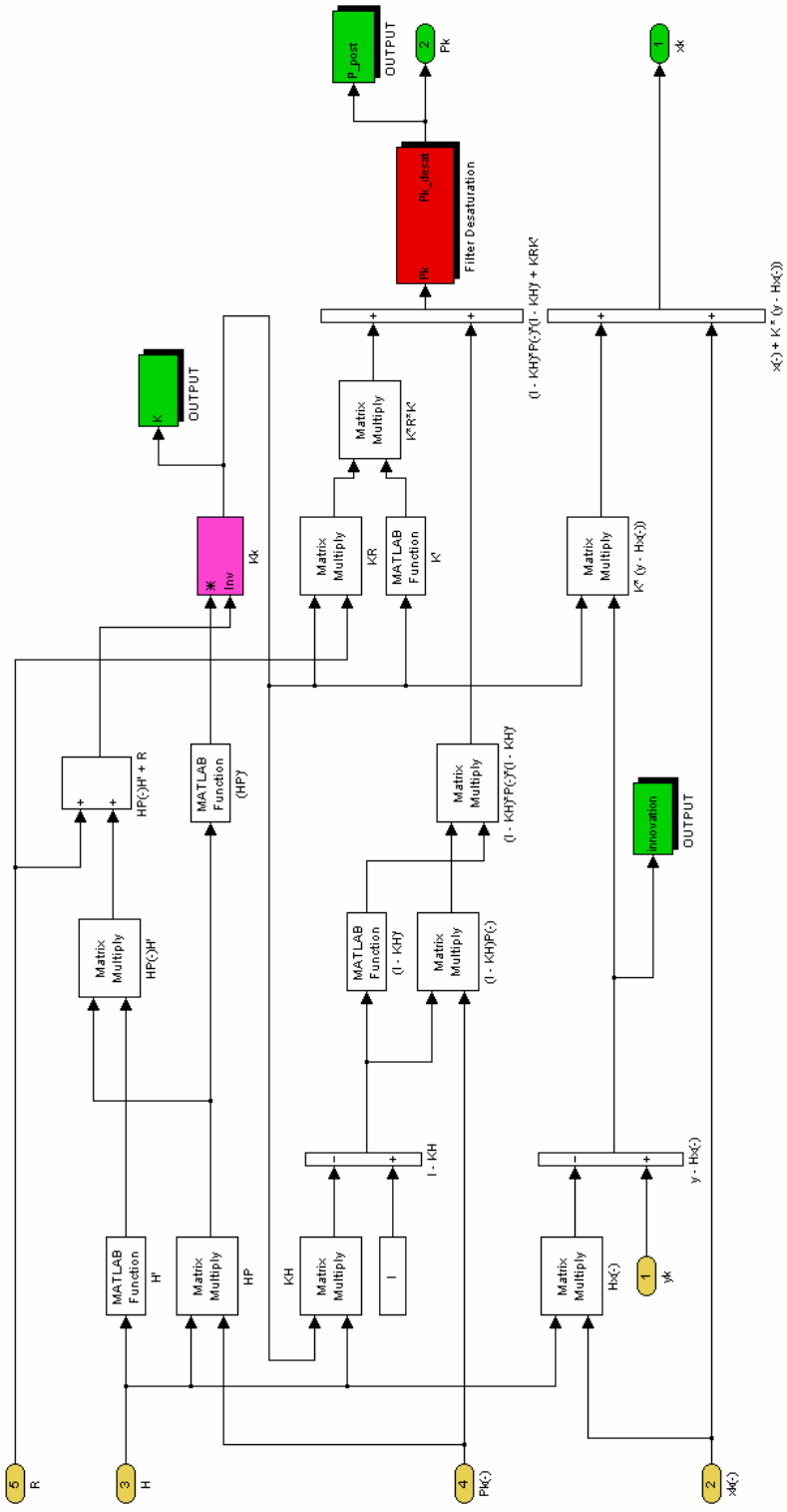

Figure 7.3.1-3: Measurement update subsystem

Additional logic

The KF algorithm is implemented using the numerical specialities described in section 6.4-**b)** and **d).**

The *decorrelation of the measurement matrix* technique (section 6.4-**c))** has been also tested. The violet block of Figure 7.3.1-3 has to be replaced by the algorithm that performs the mentioned decorrelation. The performances achieved are of the same order than the actual implementation's, while the computational time is considerably increased.

The *Filter Desaturation* block in Figure 7.3.1-3 allows the use of the tuning technique described in section 6.3.3-2 and consists in the introduction of an upper bound for the elements of $\mathbf{P}_k$. In order to activate the desaturation block, it is sufficient to click on the manual switch and select the components of $\mathbf{P}_k$ on which apply the desaturation. The logic of this block could be improved in a later stage.

Initialization

A study of the filter sensitivity towards the initial conditions ($\hat{\mathbf{x}}_0, \mathbf{P}_0$) has been performed. Since the process models satisfy the conditions for the existence of the steady-state solution of the Riccati equations, the initial conditions influence only the transient period after which $\mathbf{P}_k$ and $\mathbf{K}_k$ reach the same steady values.

Therefore, different choices of $\mathbf{P}_0$ influence only the duration of the transient. For example, choosing $\mathbf{P}_0 = \mathbf{0}_{n\times n}$ the transient is very fast, while choosing any different value for $\mathbf{P}_0$ implies a much longer transient especially for the spacecraft attitude dynamics, which is much slower than the T/M or the telescope pointing angle dynamics.

Physically, to choice $\mathbf{P}_0 = \mathbf{0}_{n\times n}$ means that the initial guess for the estimate $\hat{\mathbf{x}}_0$ is correct because the error covariance is zero and this is obviously false. It can be shown that, if the last measurement is taken as initial estimate, to choose $\mathbf{P}_0 = \mathbf{0}_{n\times n}$ produces a stable, convergent result.

However, in literature [40], it is found that it is always preferable to choose a $\mathbf{P}_0$ different from zero (also because, otherwise, the desaturation procedure is not

applicable). Therefore, remembering the discussion of section 6.4-**e)**, it is suitable to choose

$$\hat{\mathbf{x}}_0 = \mathbf{0}_{n\times n}$$

$$\mathbf{0}_{n\times n} < \mathbf{P}_0 < 10^{-1}\cdot \mathbf{E}_{n\times n}$$

The choice and the loading of the other simulation parameters proceed as described in section 5.2.6

7.3.2 Algorithm 2: Steady-State Continuous-Time Kalman Filter

The continuous-time KF process models of the LISA satellite satisfy the conditions of existence of a steady-state solution of the Riccati equations. The Matlab® command of the *Control System Toolbox*

$$[P_\infty, L, K_\infty^T, report] = care(A^T, H^T, GQG^T, R, 0_{n\times n}, E_{n\times n})$$

is used to solve the continuous-time algebraic Riccati equation (6.23) and the Matlab® command

$$[Kalmf, K_\infty, P_\infty] = kalman(KF\_sys\_mod,\ Q,\ R)$$

where `KF_sys_mod` is the state-space representation of the Kalman filter process model, returns the steady-state Kalman gain matrix K_∞, the steady-state error covariance P_∞ and an LTI state-space representation of the continuous-time Kalman estimator (`Kalmf`)

$$\begin{cases} \dot{\hat{\mathbf{x}}}(t) = (\mathbf{A} - \mathbf{KH})\hat{\mathbf{x}}(t) + \begin{bmatrix}\mathbf{B} & \mathbf{K}\end{bmatrix}\begin{bmatrix}\mathbf{u}(t)\\ \mathbf{y}(t)\end{bmatrix} \\ \begin{bmatrix}\hat{\mathbf{y}}(t)\\ \hat{\mathbf{x}}(t)\end{bmatrix} = \begin{bmatrix}\mathbf{H}\\ \mathbf{E}_{n\times n}\end{bmatrix}\hat{\mathbf{x}}(t) + \begin{bmatrix}\mathbf{0}_{m\times r} & \mathbf{0}_{m\times m}\\ \mathbf{0}_{n\times r} & \mathbf{0}_{n\times m}\end{bmatrix}\begin{bmatrix}\mathbf{u}(t)\\ \mathbf{y}(t)\end{bmatrix} \end{cases}$$

which can be implemented in both Matlab® and Simulink® environments. Note that the `Kalmf` outputs are the state estimates $\hat{\mathbf{x}}(t)$ and the measurement estimates $\hat{\mathbf{y}}(t)$. Since

H is almost the identity matrix, to propagate $\hat{\mathbf{x}}(t)$ instead of $\hat{\mathbf{y}}(t)$ does not produce considerable changes in the performances, but reduces the algorithm sensitivity to the uncertainties on the cross-talk coefficients of the electrostatic read-out system and therefore, it is preferable.

Matlab® Implementation

The procedure used to obtain a Matlab® model that simulates the behaviour of the whole closed-loop including the Kalman filter is basically the same described in chapter 5. The only difference is that the measurement data, obtained by the LISA open-loop plant, are not sent directly in feedback to the controller by they have to be pre-processed by the Kalman filter system (`Kalmf`). Figure 7.3.2-1 illustrates the overall Matlab® model architecture including the Kalman filter.

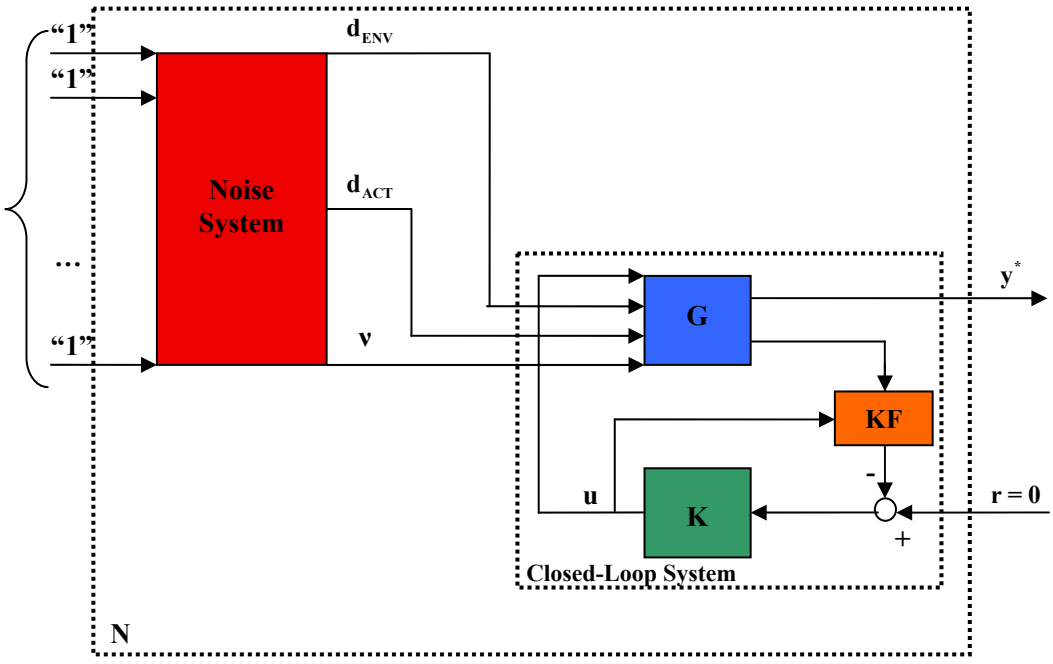

Figure 7.3.2-1: Overall Matlab® model architecture including the Kalman filter

Therefore, after having implemented the LISA open-loop equations, the Kalman filter LTI system is attached in parallel to the LISA plant (Figure 7.3.2-2)

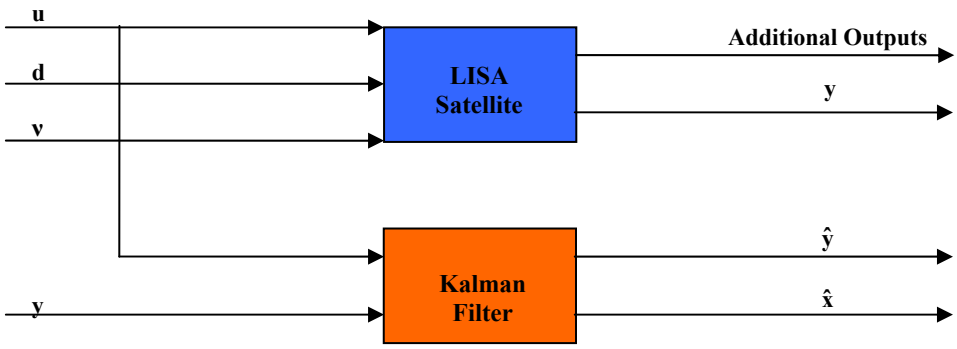

Figure 7.3.2-2: Step 1 for the introduction of the Kalman Filter in the Matlab® model

and the measurement outputs of the plant are connected to the filter inputs with positive feedback (Figure 7.3.2-2).

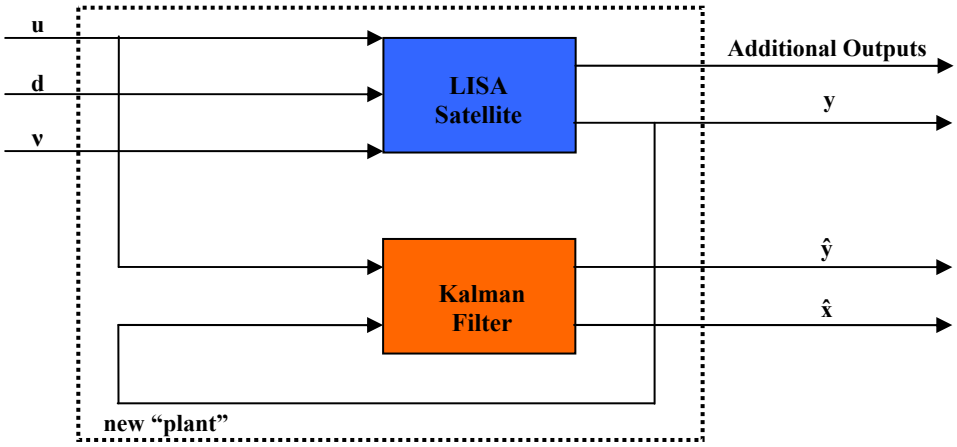

Figure 7.3.2-3: Step 2 for the introduction of the Kalman Filter in the Matlab® model

In this way, it is achieved a new "plant" that receives as inputs the same inputs of the LISA plant and which produces as outputs the same outputs of the LISA plants plus the outputs of the Kalman filter system (state and measurement estimates).

The state estimates of interest are sent in feedback to the controller and the noise system is added in the same way described in chapter 5.

Simulink® Implementation

The main structure of the simulator is the same of Figure 7.3.1-1, where the *Kalman Filter* block (Figure 7.3.2-4) contains the Kalman filter estimator which is implemented

by means of an LTI system block.

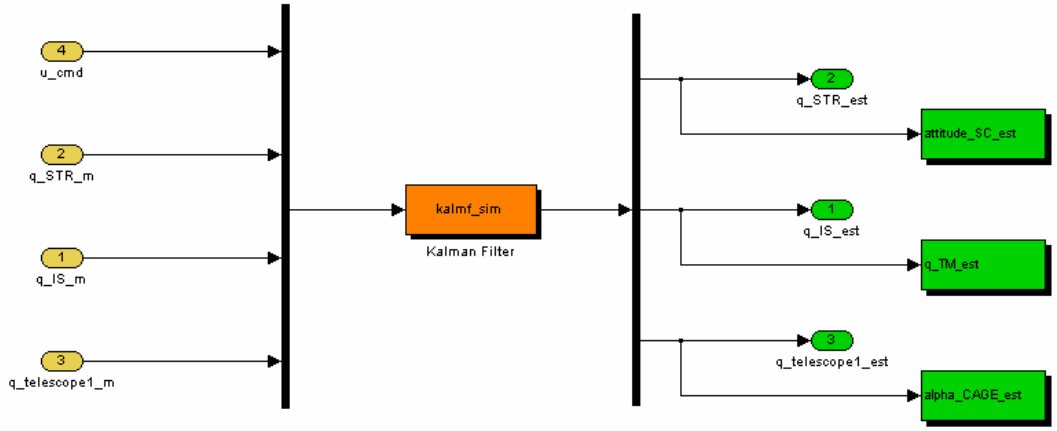

Figure 7.3.2-4: Kalman filter block

Remarks

- Comparison between the algorithms implemented:
  - Time-varying discrete-time KF algorithm
    - Advantages: optimal filter (if the signal conditions are fulfilled, but, in any case, it is the best filtering approach for linear system); all the tuning strategies (section 6.3.3) are applicable.
    - Disadvantages: complex algorithm, time-consuming simulations required (state augmented models realistically not implementable), additional logic necessary for tuning strategies, problem of the initial conditions choice, round-off errors introduced by the discretization, high number of parameters to tune.
  - Steady-state continuous-time KF algorithm
    - Advantages: linear transfer-function analysis possible thanks to the Matlab® model, reduced complexity, shorter-time simulations (state-augmented model implementation possible), no additional logic required, no dependence from the initial conditions, no discretization required, reduced number of parameters to tune

- Disadvantages: suboptimal filter, steady-state existence conditions must be verified in order to solve the Riccati equation, only the tuning of the process noise covariance matrix is possible (no desaturation, no adaptive filtering strategies applicable)

Since the time required for the simulation is considerably reduced in the steady-state filter case, it provides a tool for a fast analysis of the role of the tuning parameters.

- In the Simulink® implementation of both algorithms, the "run out of memory" problem was encountered since the use of anti-aliasing filters has to be avoided in order to not lose the high-frequency information. Therefore, an effort in saving memory is mandatory.
- A steady-state discrete-time KF was also designed and implemented in order to have a complete scenario. This algorithm has the same advantages and disadvantages of the continuous-time type, but the models are continuous-time (they have to be discretized introducing roundoff errors) and the tuning is more complex in the discrete case (the discrete process noise covariance matrix is full, while the continuous one is diagonal). Therefore, the performances of this filter are lower than the continuous ones.

7.4 Kalman Filter Design

The Kalman filter process models derived in section 7.2 are combined with the Kalman filter algorithms, whose implementation is described in section 7.3, producing four different Kalman filters:

1) Model 1 + Algorithm 1: time-varying discrete-time Kalman filter without state augmentation

2) Model 2 + Algorithm 1: time-varying discrete-time Kalman filter with state augmentation for the process noise

3) Model 1 + Algorithm 2: steady-state continuous-time Kalman filter without state augmentation

4) Model 2 + Algorithm 2: steady-state continuous-time Kalman filter with state augmentation for the process noise

The Kalman filters without state augmentation (filters **1)** and **3**) require additional tuning because the error between the real states and their estimate is too large. In particular, the SC inertial roll and pitch angles (Θ_B, H_B) result as the states worst estimated together with the T/M roll and pitch angles ($\theta_1, \eta_1, \theta_2, \eta_2$). This is not surprising since, from a dynamic point of view, Θ_B and H_B are related to the correspondent T/M attitude coordinates ($\theta_1, \eta_1, \theta_2, \eta_2$) and to z_2. In fact, if a test mass rotates around the x or y axis of Σ_C, the suspension controller produces a torque around that axis in order to bring the test mass back in its reference position. The corresponding counter torque generated on the SC influences the SC attitude in the constellation plane (i.e. Θ_B and H_B). In analogy, if T/M 2 moves in the z direction of Σ_C, the suspension controller produces a force along that direction that causes a torque around the x and y axis of Σ_C. For the same reason, the SC inertial yaw angle Φ_B is influenced especially by ϕ_1 and ϕ_2, while the telescope in-plane pointing angle α is influenced by all the states that can induce a rotation around the z axis of Σ_C. Therefore, a better estimate of the T/M coordinates implies a better estimation and control of the SC attitude and the telescope in-plane pointing angle.

From a theoretical point of view, the explanation for this non-optimal behaviour of the filter is that the error covariance matrix elements **P** and the Kalman gains **K** converge to values that are too small and, thus, all the new measurements are very poorly weighted and not only the STR ones as it is desired. Therefore, the objective of the tuning is to increase the 'right' Kalman gains in order to produce a better estimation of the T/M coordinates (and consequently of all the states), but being careful in not reintroducing the STR read-out noise in the estimates.

In the model without state augmentation, the measurement and the process noise states are not modelled. Neglecting the measurement noise states is not a problem (section 7.2.5-7.2.6). Considering the process noise covariance matrix **Q**, its diagonal elements, computed according to Appendix B are

$$\begin{aligned}\mathrm{diag}(\mathbf{Q}) = [&5.58e-021 \;\; 2.24e-019 \;\; 1.37e-016 \;\; 2.56e-020 \;\; 6.33e-022 \;\; 5.24e-024\\ &3.75e-013 \;\; 3.75e-013 \;\; 4.50e-013 \;\; 1.62e-013 \;\; 1.62e-013 \;\; 3.25e-013\\ &1.87e-028 \;\; 3.83e-026 \;\; 3.83e-026 \;\; 2.82e-030 \;\; 2.82e-030 \;\; 2.82e-030\\ &1.87e-028 \;\; 3.83e-026 \;\; 3.83e-026 \;\; 2.82e-030 \;\; 2.82e-030 \;\; 2.82e-030\\ &3.60e-014]\end{aligned}$$

The dominant noise sources are the FEEP actuator (blue) and the OATM system (green). Their variances are several order of magnitude larger than the variances of the solar noise and of the IS actuation noise. The telescope pointing actuation noise is white and satisfies the Kalman filter assumptions. On the contrary, the shape filter for the FEEP actuation noise is a MIMO LTI system with 24 states which are completely neglected. Moreover, its noise spectrum (Figure 2.4.1-1) rises up already at 10^{-1} Hz. Concluding, the FEEP actuation noise is badly modelled in the filters without state augmentation and this produces the observed degradation in the filter performances.

The adopted solution consists in adding fictitious process noise on the FEEP actuation noise components: taking variances of the same order as the FEEP shaping filter gains (i.e. 10^{-8}, this means to increase the corresponding process noise covariance matrix elements with a factor of 10^{5}), all the error estimates of all the states (especially $\theta_1, \eta_1, \theta_2, \eta_2$ and consequently Θ_B, H_B) decrease considerably. Moreover, considering the Kalman gain matrix, its elements are increased, but not proportionally: the gains that weight the STR measurements are almost unmodified, while the IS gains are considerably increased. The actual tuning choice derives from a long optimization process and provides the best performances.

Note that the same results could be obtained with the desaturation technique or introducing an adaptive filter for the process noise. However, since the physical reason of the problem is found in the unmodelled states of the FEEP actuation noise, this is the most physical way to proceed.

The continuous-time KF with state augmentation (filters **4)**) provides the desired results already without tuning (in fact, the process noise is modelled correctly). However, it is possible to choose

$$\frac{\mathbf{Q}}{c} \qquad \text{with} \qquad 1 \le c \le 5$$

in order to reduce the Kalman gains and, consequently, the noise that the measurements convey over the estimates.

The discrete case (filters 2)) is numerically ill-conditioned, since its convergence depends on the choice of the initial conditions. It was decided not to spend too much time in the investigation of this problem since the implementation time of this filter is unacceptable, even when it converges, and also because the other filters achieve already suitable results.

7.5 Performances Analysis

In the previous section, three Kalman filters are selected as the most qualified for the *gyro mode*. Their main features are summarized in Table 7.5-1; an identification number is associated to each filter (1, 2, 3) and it is often used in the following in place of the complete filter descriptive name.

Kalman Filter		**Initial Conditions**		**Tuning**		**State Augmentation**
		$\hat{\mathbf{x}}_0$	$\mathbf{P}_0$	**Q**	**R**	
1	**Time-varying discrete-time**	$\mathbf{0}_{32\times32}$	$10^{-10}\cdot\mathbf{E}_{32\times32}$	$\sigma^2_{\text{FEEP}}\cdot10^5$	$\mathbf{R}^{\text{d}}=\mathbf{R}$	NO
2	**Steady-state continuous-time**	-	-	$\sigma^2_{\text{FEEP}}\cdot10^5$	-	NO
3	**Steady-state continuous-time**	-	-	$\frac{\mathbf{Q}}{\text{c}}$ $\text{c}=5$	-	Process Noise

Table 7.5-1: Designed Kalman filter characterization

Note that in the time-varying discrete-time Kalman filter (KF 1) the sensor data are considered as if they were provided continuously in time and, as consequence, the corresponding measurement noise covariance matrix is not discretized.

Since the correct guidance laws are TBD, the filter performances are tested over several reference signals. The following ones are taken as exemplification

State	**Reference Law**
Spacecraft Inertial Attitude	$r = 10^{-6}\sin(10^{-2}\cdot t)$
Test Masses Coordinates	$r = 0$
Telescope 1 in-plane pointing angle	$r = 0$

Table 7.5-2: Reference laws used for the simulation

Figure 7.5.1 depicts the time-series of the SC inertial pitch angle achieved in the *drag-free acquisition mode* conditions (i.e. without the use of a Kalman filter), compared with its reference signal, which represents the ideal performance. The signal of the SC pitch angle is completely submerged by the noise and the sinusoidal trend is not even recognizable.

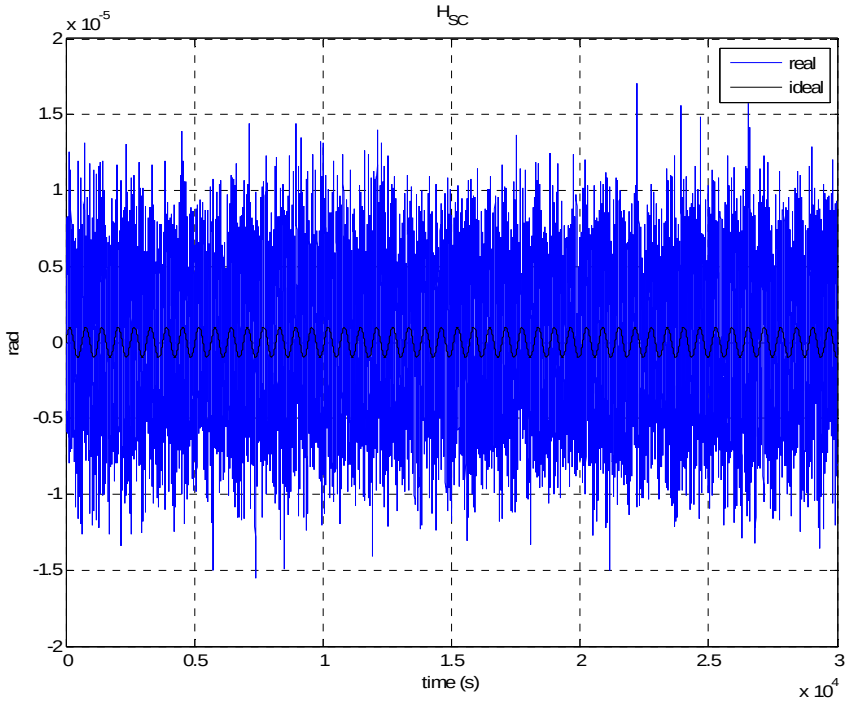

Figure 7.5-1: Spacecraft inertial pitch angle without Kalman filter

Figures 7.5-2, 7.5-4 and 7.5-6 show the time-series of the SC inertial pitch angle[1] achieved respectively with the use of the Kalman filter 1, 2 and 3. The reference and the estimated signals are also represented. Figures 7.5-3, 7.5-5 and 7.5-7 provide a zoom and Figures 7.5-8, 7.5-9 and 7.5-10 represent the SC pitch angle error in following its guidance law for the same filters. The noise on the real signal of H_{SC} is sensitively reduced such that the signal is able to follow its reference.

The error signals show that the residual long-term drifts are very small once DC forces and torques are compensated and the fulfilment of the long-term drift requirements is not a matter in these circumstances (refer to Appendix A for the statistical analysis involving the long term-drifts). Therefore, in the following of the current chapter, only the short-term jitters are analyzed.

Comparing the plots of the error for the three different Kalman filters, it can be said that the KF 3 produces the best performances.

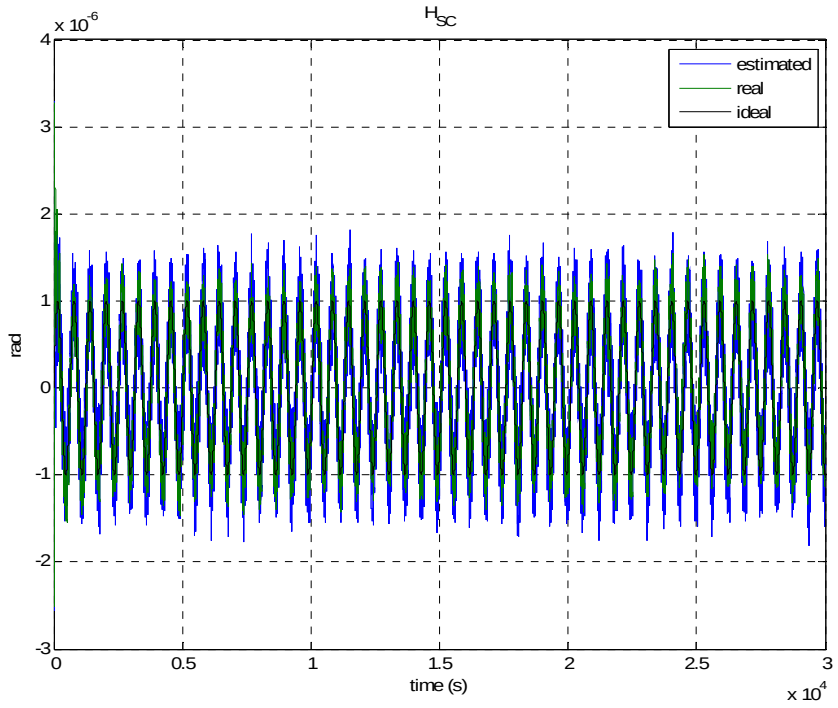

Figure 7.5-2: Spacecraft inertial pitch angle with Kalman filter 1

[1] Analogous plots for the other SC inertial attitude angles can be found in Appendix A

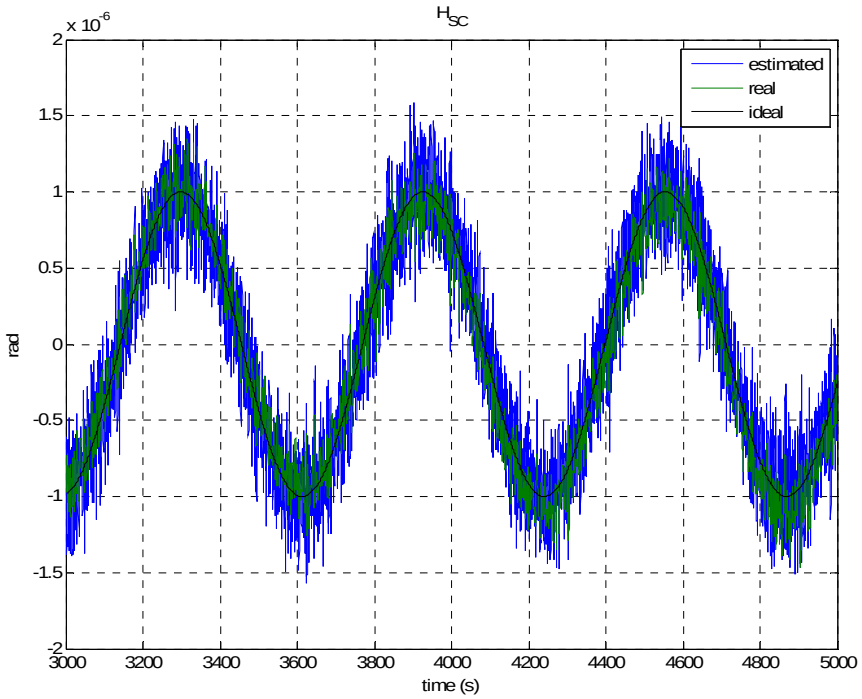

Figure 7.5-3: Zoom of the spacecraft inertial pitch angle with Kalman filter 1

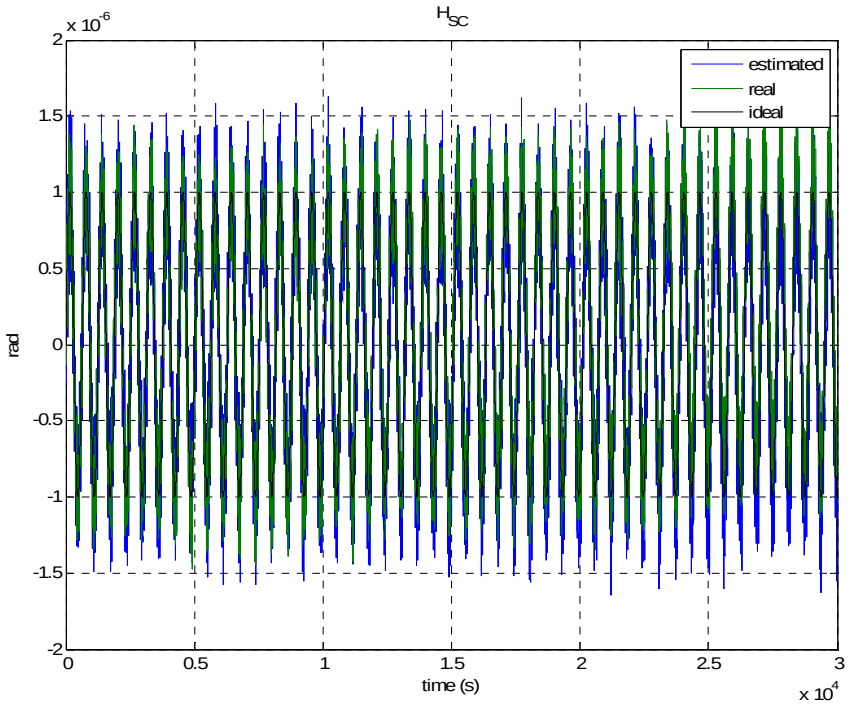

Figure 7.5-4: Spacecraft inertial pitch angle with Kalman filter 2

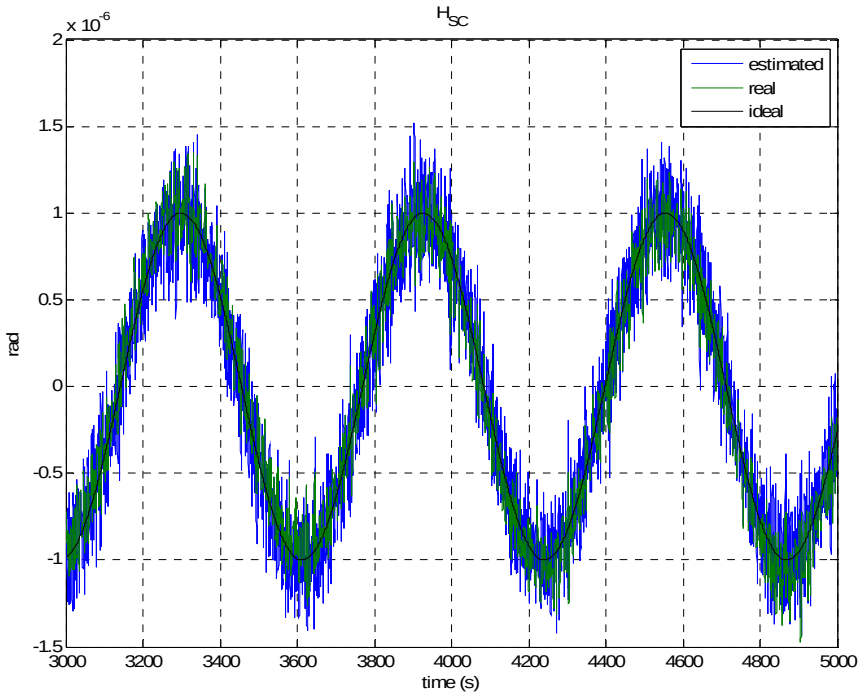

Figure 7.5-5: Zoom of the spacecraft inertial pitch angle with Kalman filter 2

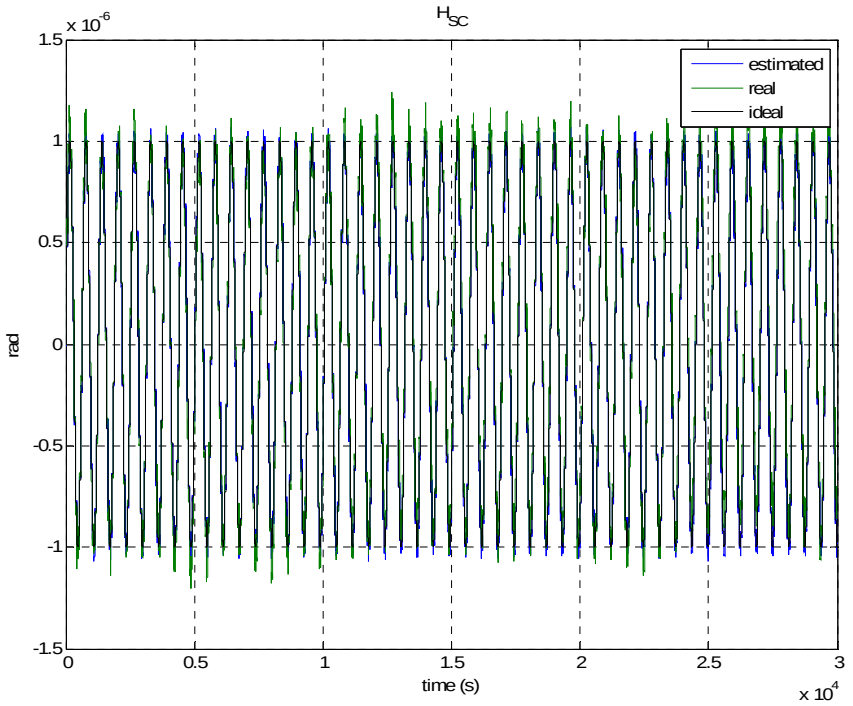

Figure 7.5-6: Spacecraft inertial pitch angle with Kalman filter 3

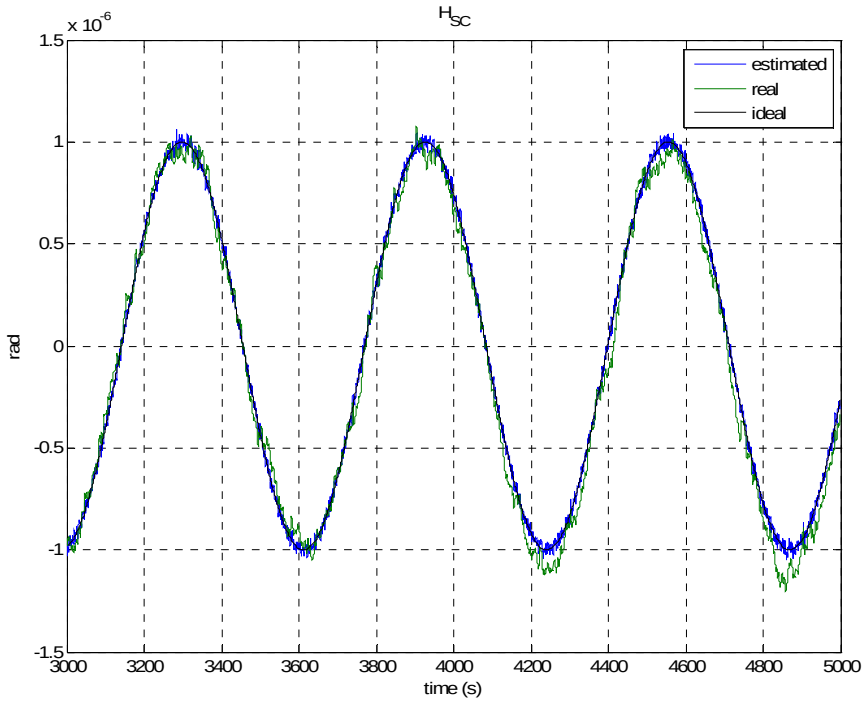

Figure 7.5-7: Zoom of the spacecraft inertial pitch angle with Kalman filter 3

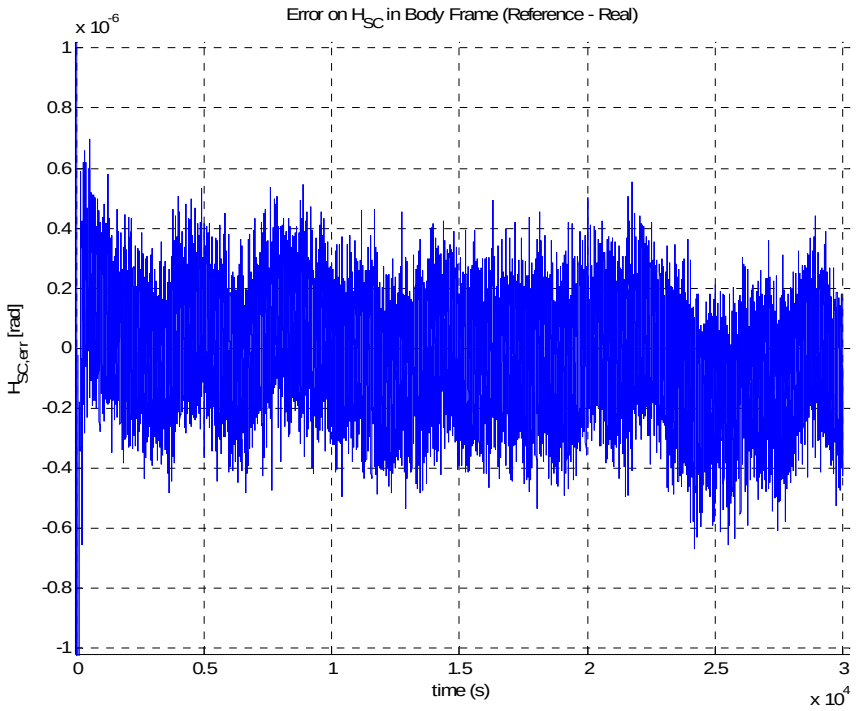

Figure 7.5-8: Spacecraft inertial pitch angle error with Kalman filter 1

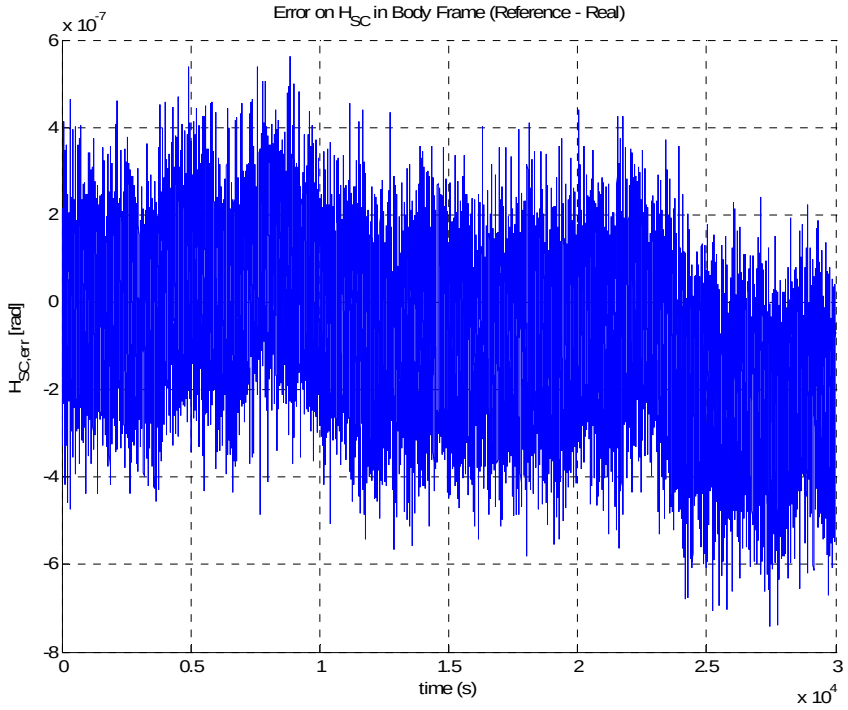

Figure 7.5-9: Spacecraft inertial pitch angle error with Kalman filter 2

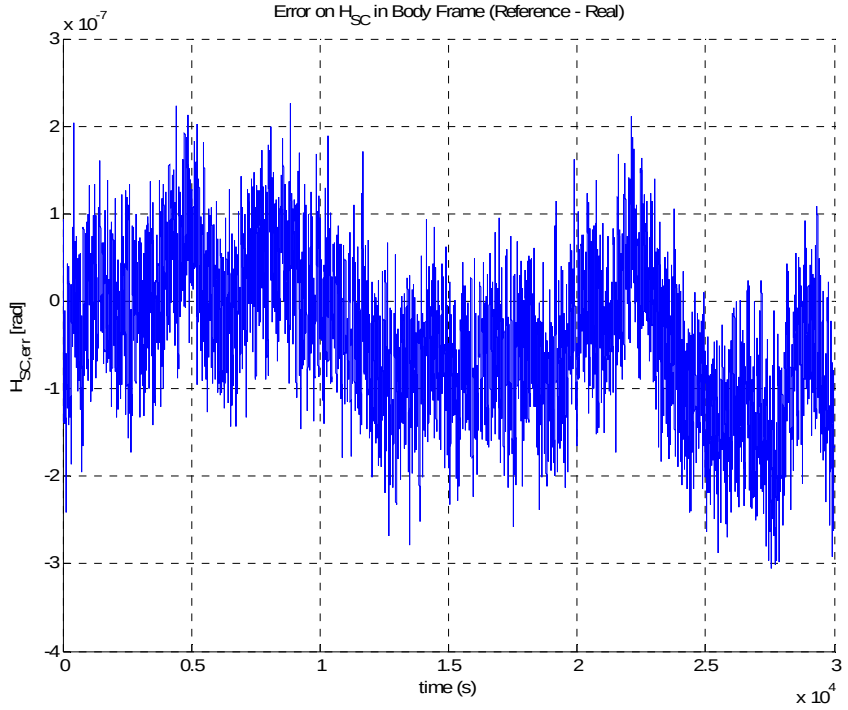

Figure 7.5-10: Spacecraft inertial pitch angle error with Kalman filter 3

		Short-term jitter: maximum RMS 1σ in μrad over a time window of 1000 s of the signal error (reference - real)						
		$\Theta_{1,err}$	$H_{1,err}$	$\Phi_{1,err}$	$\Theta_{2,err}$	$H_{2,err}$	$\Phi_{2,err}$	$\alpha_{CAGE,err}$
Requirements		**-**	**0.1**	**≈ 0.118**	**-**	**0.1**	**0.1**	**0.05**
Drag-free acquis. mode		**25.73**	**13.17**	**4.30**	**23.95**	**16.22**	**2.73**	**3.90**
Gyro mode	**Kalman Filter 1**	0.1958	0.1404	0.0269	0.1599	0.1730	0.0254	0.0107
	Kalman Filter 2	0.1045	0.1154	0.0134	0.5990	0.1452	0.0097	0.0104
	Kalman Filter 3	0.0778	0.0709	0.0176	0.0730	0.0764	0.0154	0.0087

Table 7.5-3: Comparison between the short-term jitter requirements, the short-term jitter performances in the *drag-free acquisition mode* and the short-term jitter performances in the *gyro mode*

The statistical analysis, whose results are reported in Table 7.5-3, is in perfect agreement with the conclusions derived from the time series: the Kalman filter 3 has the better performances and this depends on the fact that the state augmentation provides to the filter a better model of the 'real' satellite dynamics. The performances of filter 1 are degraded with respect to the performance of the filter 2. This depends on the fact that, even if the first 4000 s of simulation are not considered for the computation of the time-varying filter statistics, the transient effects have a longer permanency especially on Θ_{SC}, Φ_{SC}, and consequently on the corresponding telescope line-of-sight inertial

attitude angles (Θ_1, Φ_1, Θ_2, Φ_2), since the convergence time of the corresponding error covariance elements is the longest.

However, even if the Kalman filter 3 is the only one that provides a complete fulfilment of the requirements, all the filters show a great improvement in the performances with respect to the *drag-free acquisition mode*. The physical reason stands in a better estimation of the test mass states, as it is confirmed by Figures 7.5-11 and 7.5-12 which show the test mass coordinate errors for the Kalman filter 3: the TM jitter is reduced of at least 2 orders of magnitude with respect to the corresponding Figures 5.3-2 and 5.3-3 of chapter 5. For completeness, the other SC attitude angle errors and the telescope 1 in-plane pointing angle error are shown for the Kalman filter 3 in Figures 7.5-13, 7.5-14 and 7.5-15. The error signals of the other filters are of the same kind and can be found in Appendix A.

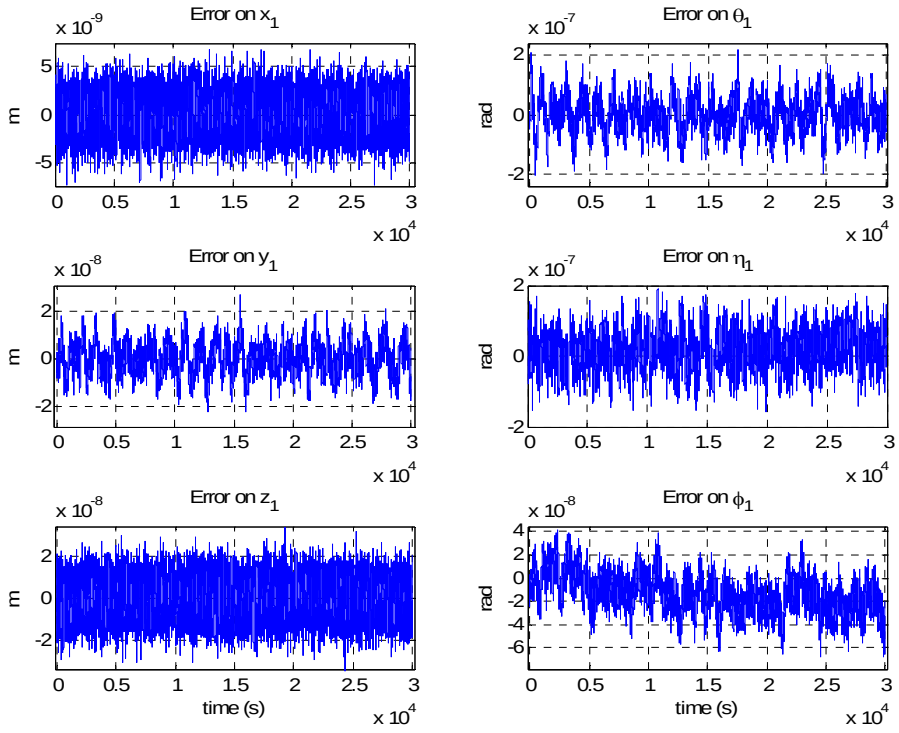

Figure 7.5-11: Test mass 1 position and attitude error with Kalman filter 3

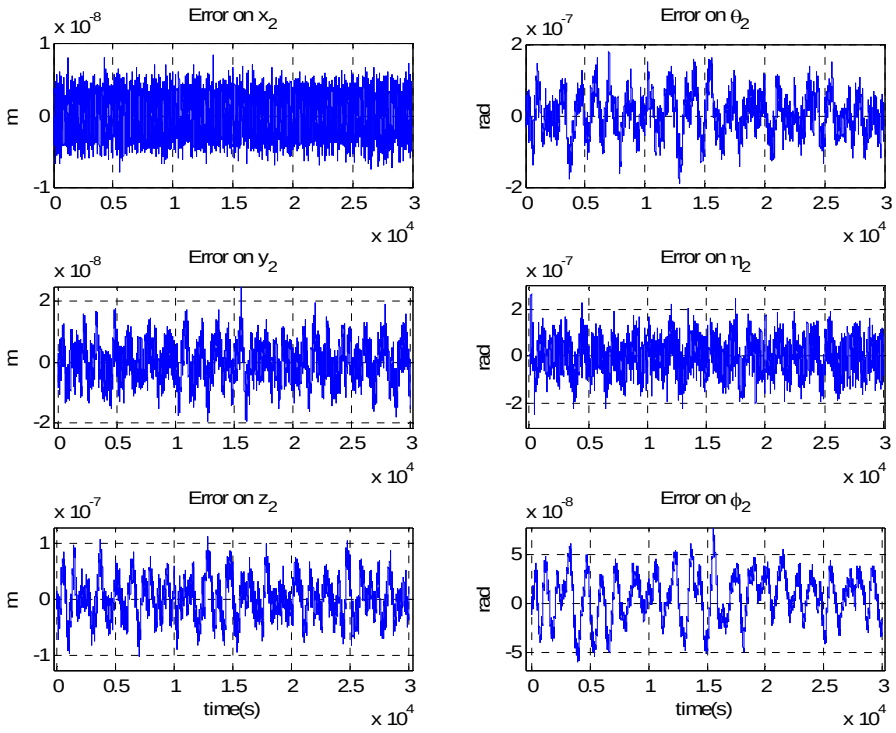

Figure 7.5-12: Test mass 2 position and attitude error with Kalman filter 3

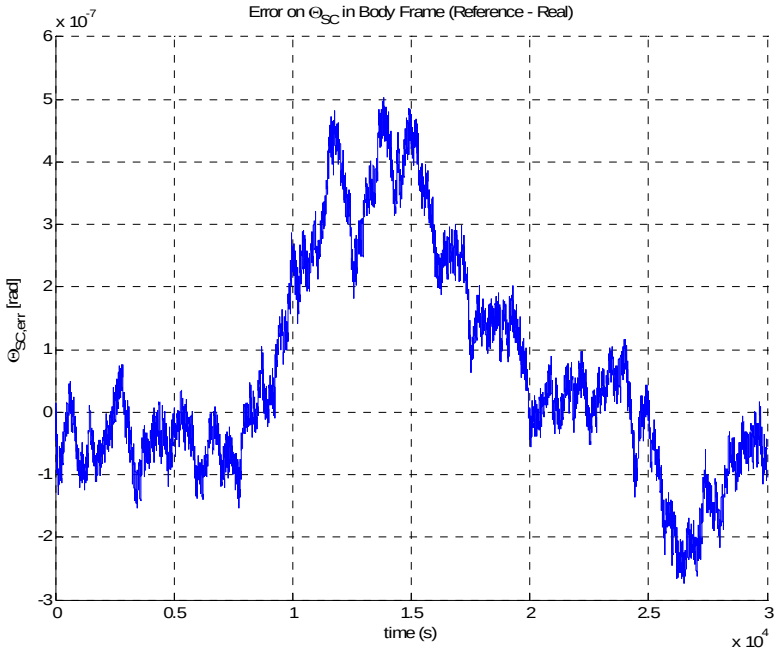

Figure 7.5-13: Spacecraft inertial roll angle error with Kalman filter 3

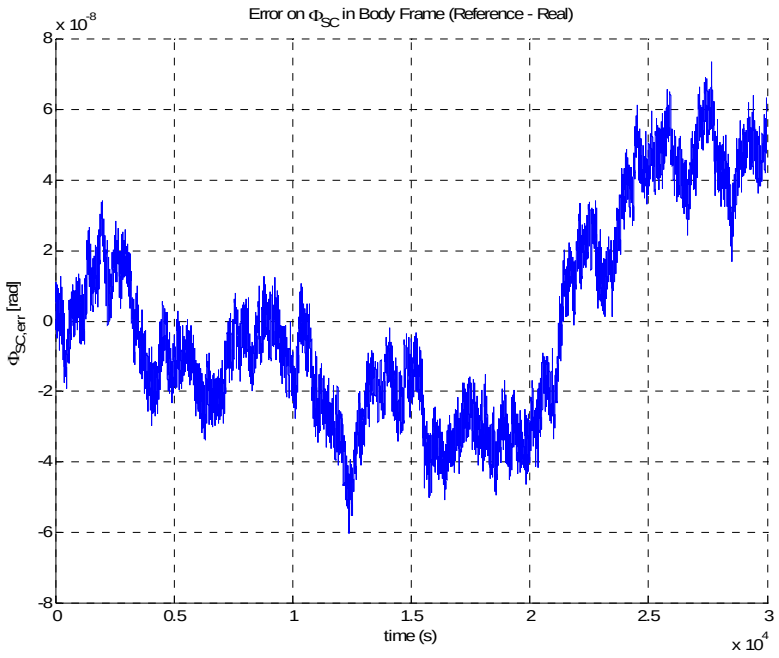

Figure 7.5-14: Spacecraft inertial yaw angle error with Kalman filter 3

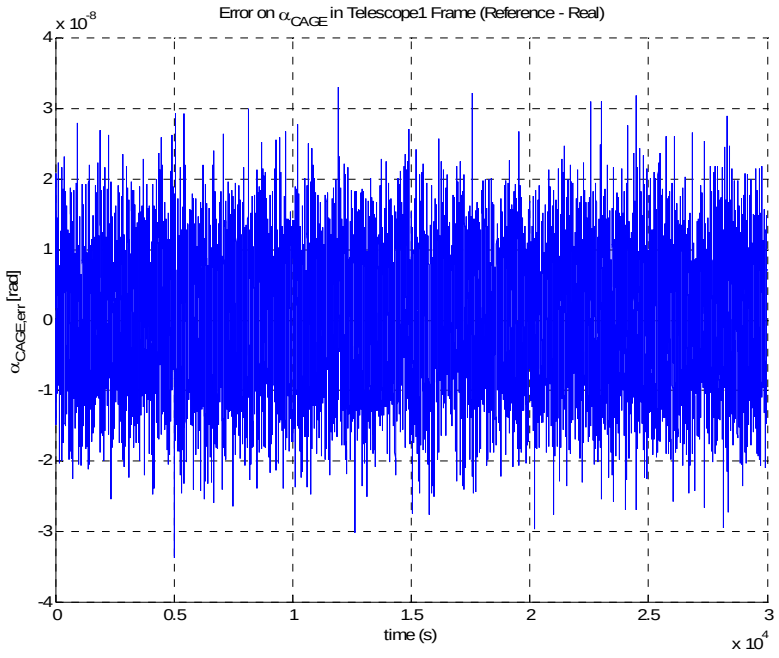

Figure 7.5-15: Telescope 1 in-plane pointing angle error with Kalman filter 3

Additional information can be achieved by a frequency domain analysis. Figures 7.5-16 and 7.5-17 show the effect of the application of the Kalman filter 3 to the drag-free acquisition controller, comparing the square root of the power spectral densities of

the SC attitude error (Figure 7.5-16) and of the telescope 1 in-plane pointing angle error (Figure 7.5-17) obtained with the application of the Kalman filter 3 (red line) and without the application of the filter (blue line). It can be noted a large noise reduction in the high frequency range, while, as expected, the curves tend nearly to coincide at low frequencies.

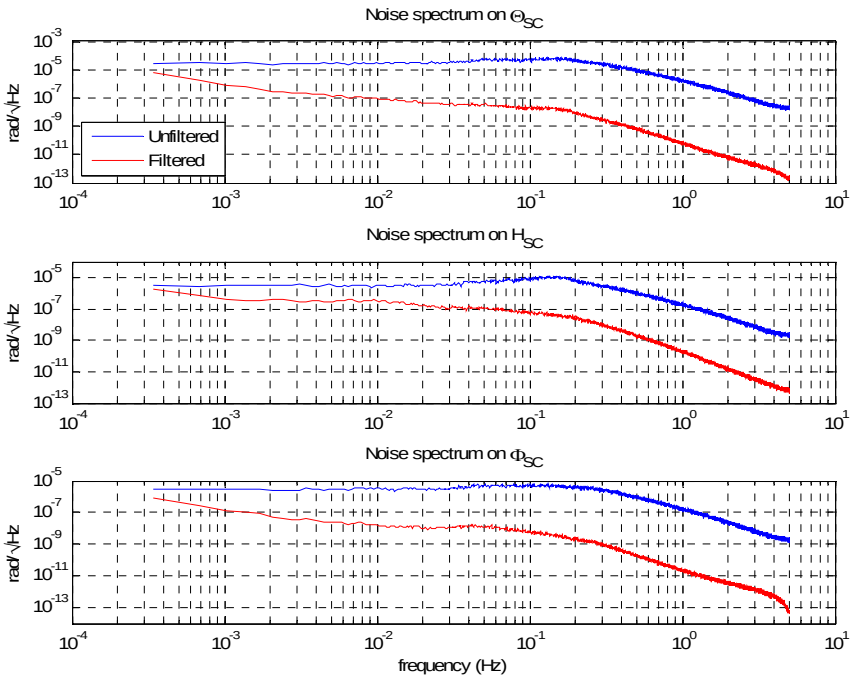

Figure 7.5-16: Spacecraft inertial attitude error with and without Kalman filter 3

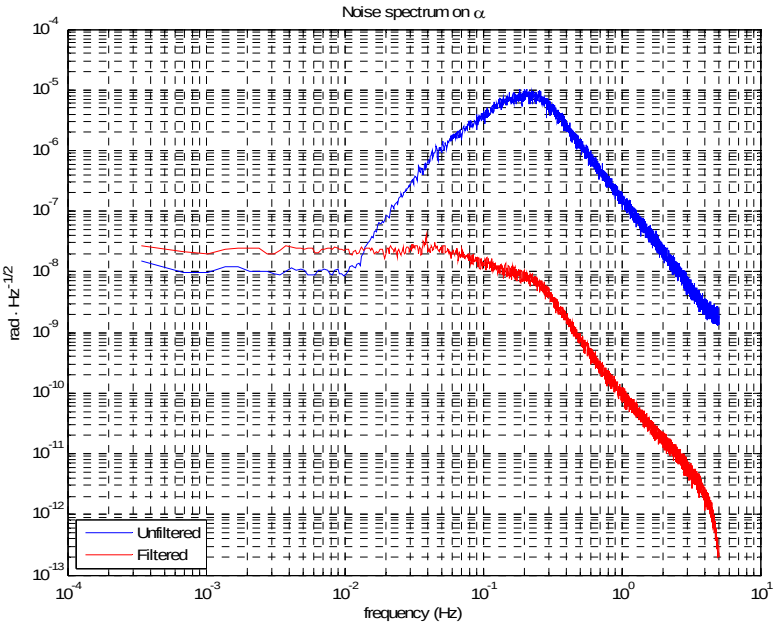

Figure 7.5-17: Telescope 1 in-plane pointing angle error with and without Kalman filter 3

In particular, note that the telescope 1 in-plane pointing angle signals differs for a factor of 2 in the low frequency range for the Kalman filter 3, while the other filters do exactly approach the unfiltered signals (ref. Appendix A).

More detailed information comes from the transfer-function analysis performed by means of the Matlab® model. Figure 7.5.18 has the scope to validate the Matlab® model by observing that the square root of the power spectral density plots generated from the Simulink® time-series coincide with the corresponding plots achieved from the Matlab® model. Then, Figures 7.5.19, 7.5.20, 7.5.21 and 7.5.22 show the results of the detailed transfer-function analysis. In the high-frequency range, the STR noise is not anymore the leading factor and this produces the noise reduction observed in Figures 7.5.16 and 7.5.17. In particular, the IS read-out noise drives the SC inertial attitude error confirming that the *gyro mode* principle is applied. The telescope 1 in-plane pointing angle error is instead mainly dominated by the OATM read-out noise indicating that, once the STR noise effect is reduced, the OATM sensor is not so bad for the control of the articulated telescope (see also Table 7.5-4). In the low frequency range, the STR noise is still the dominating noise source for the SC attitude, again confirming the expectations. Similar results for the others filters can be found in Appendix A.

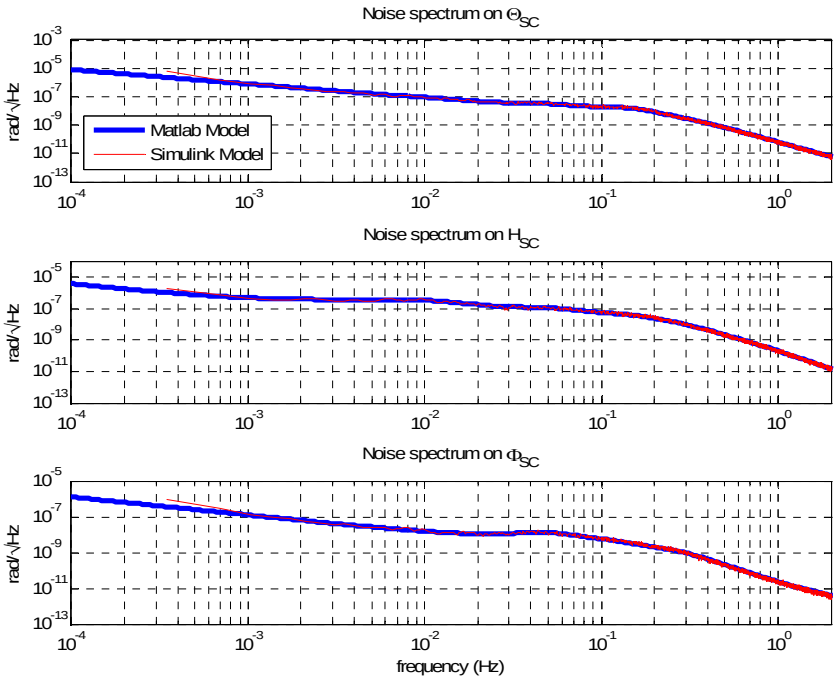

Figure 7.5-18: Spacecraft inertial attitude error obtained with the Simulink® model and with the Matlab® model of Kalman filter 3

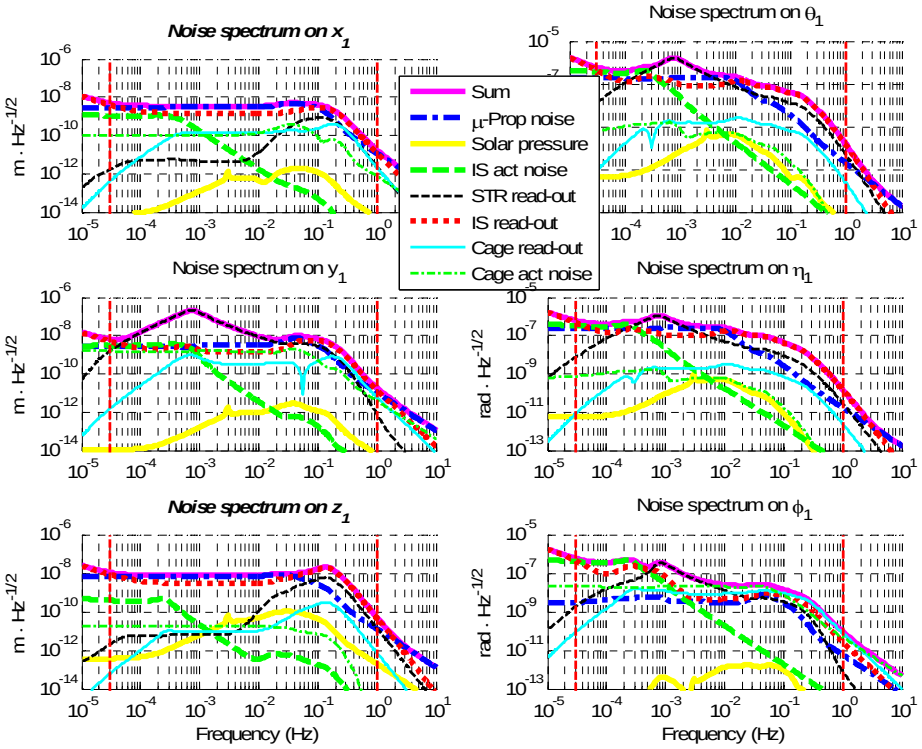

Figure 7.5-19: Test mass 1 position and attitude error with Kalman filter 3

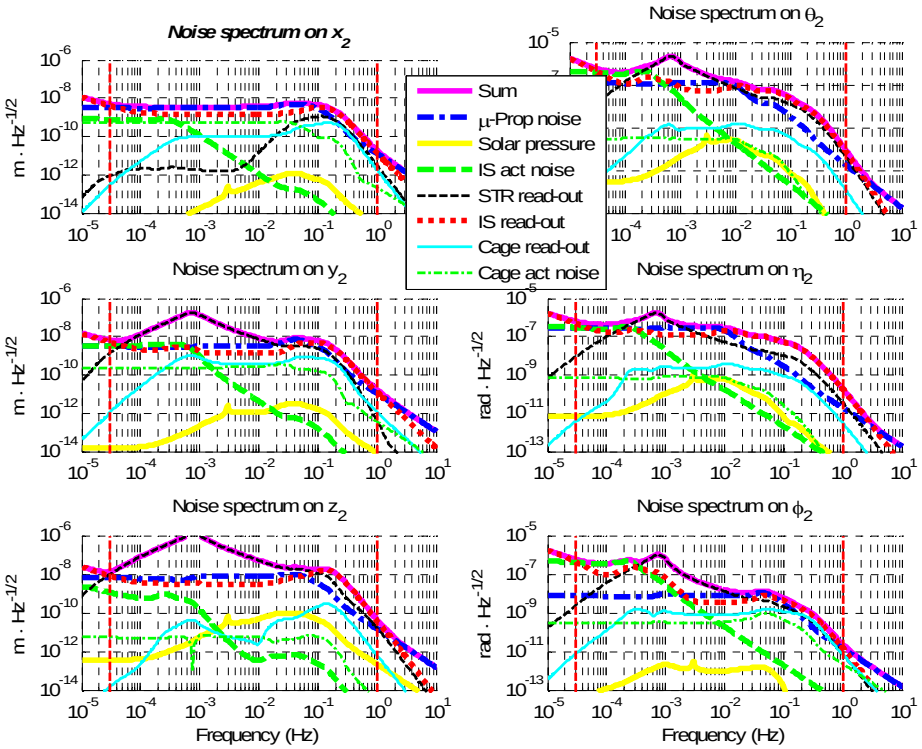

Figure 7.5-20: Test mass 2 position and attitude error with Kalman filter 3

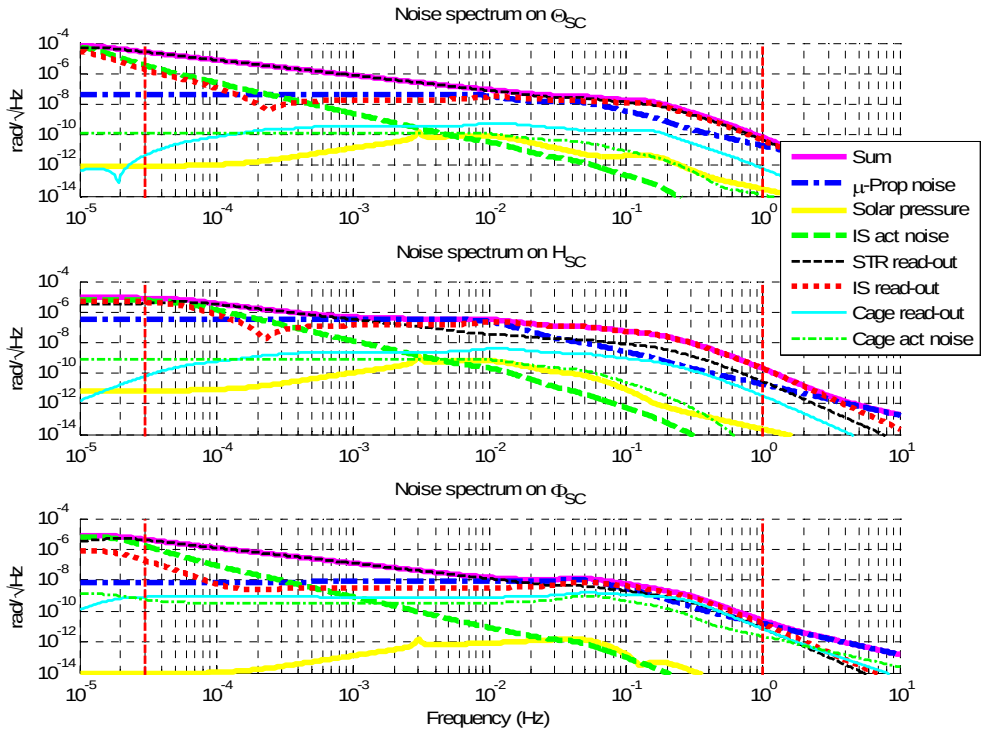

Figure 7.5-21: Spacecraft inertial attitude error with Kalman filter 3

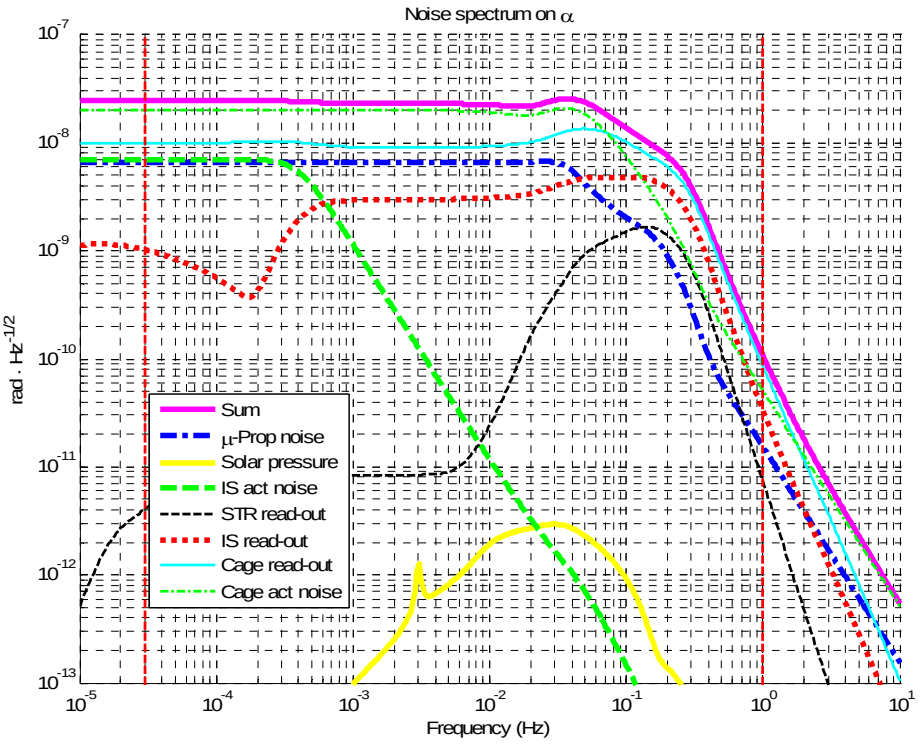

Figure 7.5-22: Telescope 1 in-plane pointing error with Kalman filter 3

Finally, a sensitivity analysis towards the noise levels of the sensors dedicated to the acquisition phase (the star tracker and the OATM sensor) and towards the acquisition phase duration is performed.

The effect of increasing the OATM sensor noise level by a factor of 100 is shown in Table 7.5-4. As it is expectable, the impact on the spacecraft attitude jitter is negligible (and consequently on the telescopes LOS attitude), since the OATM sensor noise effect on the SC attitude is absolutely secondary (Figure 7.5-21). On the contrary, the impact on the telescope 1 in-plane pointing angle and, consequently, on the telescope 1 LOS yaw angle is more consistent, but still far from approaching the requirements. Therefore, the telescope 1 in-plane pointing angle, the telescopes (1 and 2) in-plane attitude angle requirements could be more stringent and/or the OATM sensor requirements could be relaxed.

	Kalman Filter 1		**Kalman Filter 2**		**Kalman Filter 3**	
	OATM noise level $1000\frac{\text{nrad}}{\sqrt{\text{Hz}}}$	**OATM noise level** $10\frac{\text{nrad}}{\sqrt{\text{Hz}}}$	**OATM noise level** $1000\frac{\text{nrad}}{\sqrt{\text{Hz}}}$	**OATM noise level** $10\frac{\text{nrad}}{\sqrt{\text{Hz}}}$	**OATM noise level** $1000\frac{\text{nrad}}{\sqrt{\text{Hz}}}$	**OATM noise level** $10\frac{\text{nrad}}{\sqrt{\text{Hz}}}$
$\Theta_{1,err}$	0.19590	0.19580	0.10429	0.10449	0.07755	0.07762
$H_{1,err}$	0.14049	0.14041	0.11503	0.11543	0.07095	0.07092
$\Phi_{1,err}$	0.03826	0.02688	0.02786	0.01341	0.02970	0.01716
$\Theta_{2,err}$	0.15993	0.15988	0.05985	0.05990	0.07300	0.07301
$H_{2,err}$	0.17318	0.17299	0.14494	0.14518	0.07654	0.07644
$\Phi_{2,err}$	0.02543	0.02537	0.00993	0.00967	0.01540	0.01539
$\alpha_{CAGE,err}$	0.03984	0.01069	0.02871	0.01039	0.02777	0.00874

Table 7.5-4: Kalman filter short-term jitter (maximum RMS 1σ in μrad over a time window of 1000 s of the signal errors) sensitivity towards OATM sensor noise level

Figures 7.5.23, 7.5.24, 7.5.25, 7.5.26 show the sensitivity of the Kalman filter 3 towards the duration of the scanning phase (i.e time-window length) and towards the STR noise level. Star trackers with an increased quality (noise level reduced by a factor of 2.5 and 5 with respect to the baseline) are considered. The plots show a large sensitivity of

$\Theta_{2,err}$ to the star tracker noise level which increases with the scanning duration. $H_{2,err}$ and $\Phi_{2,err}$ have qualitatively the same behaviour than $\Theta_{2,err}$, but with a reduced sensitivity. $\alpha_{CAGE,err}$ is insensitive to the STR noise level, but quite sensitive to the time-window length. These results must not surprise. In fact, $\alpha_{CAGE,err}$ is independent from the STR measurements (Figure 7.5-22) and it behaves as a white noise (Figure 7.5-15) with constant variance (since the variance is defined as stated in Appendix B, the real variance of the signal appears when a sufficient number of points is considered, i.e. over 1500 s). The attitude results depend on the fact that, augmenting the time-windows length, a considerably part of the residual drift enters in the computation of the short-term jitter and, therefore, the corresponding curves arise with the time-window length. On the other hand, the STR read-out noise still dominates the low frequency range (i.e. the long-term drift). Reducing the STR noise, the residual drifts also reduce since the STR measurements are more able to correct the drifts in shorter times. Therefore, keeping constant the time-window length, the drift reduces and the short-term performances increase as the STR noise decreases. This is particularly true for $\Theta_{2,err}$ since the STR noise level is 10 times worse on this angle. In any case, the Kalman filter 3 fulfils the requirements even for longer duration of the acquisition on CCD phase.

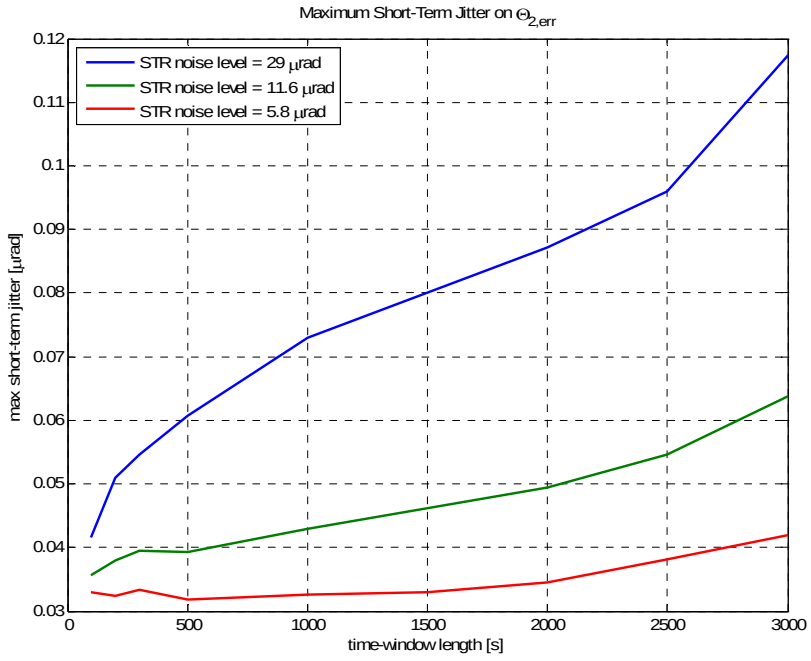

Figure 7.5-23: Telescope 2 line-of sight inertial roll angle error with Kalman filter 3

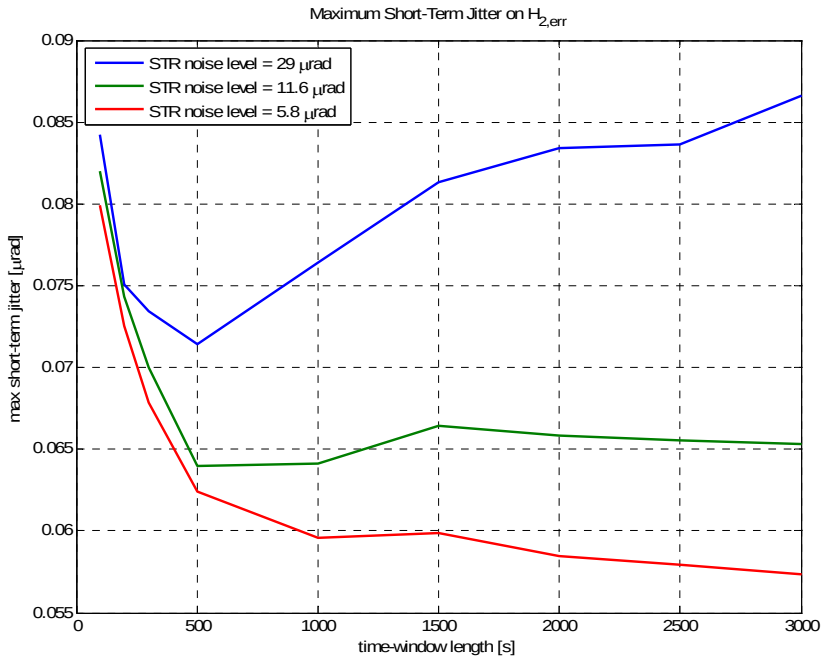

Figure 7.5-24: Telescope 2 line-of sight inertial pitch angle error with Kalman filter 3

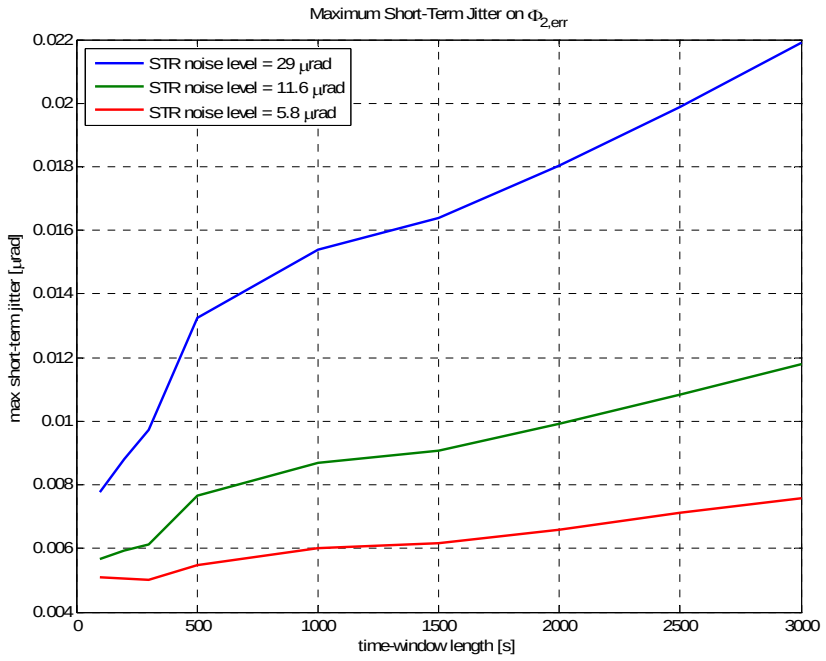

Figure 7.5-25: Telescope 2 line-of sight inertial yaw angle error with Kalman filter 3

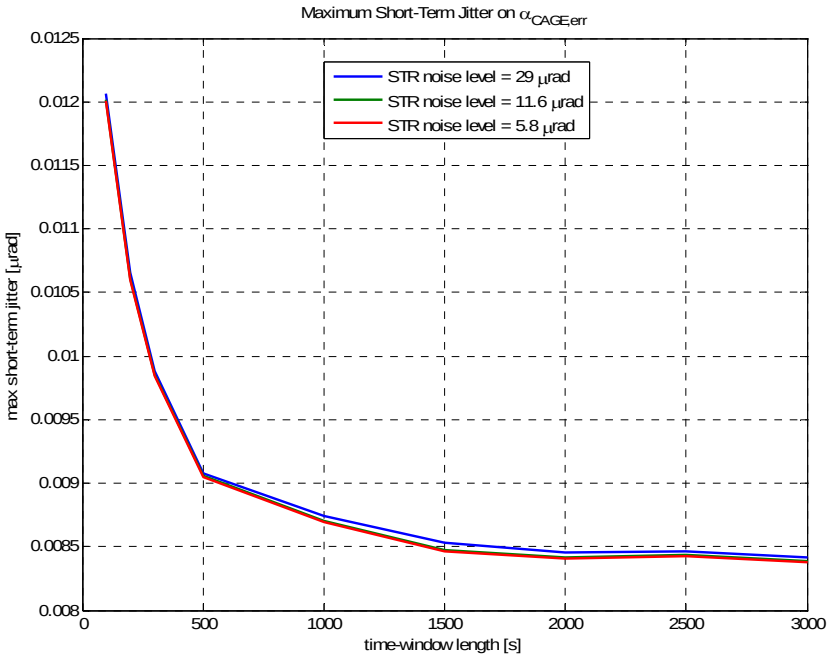

Figure 7.5-26: Telescope 1 in-plane pointing angle error with Kalman filter 3

Figure 7.3.2-27 depicts the sensitivity of the maximum short-term jitter of the telescope 2 LOS pitch angle error $H_{2,err}$ towards STR noise level and acquisition duration achieved with the Kalman filter 2. It can be noted that, even by choosing a better STR, the requirement (0.1 μrad) is not met.

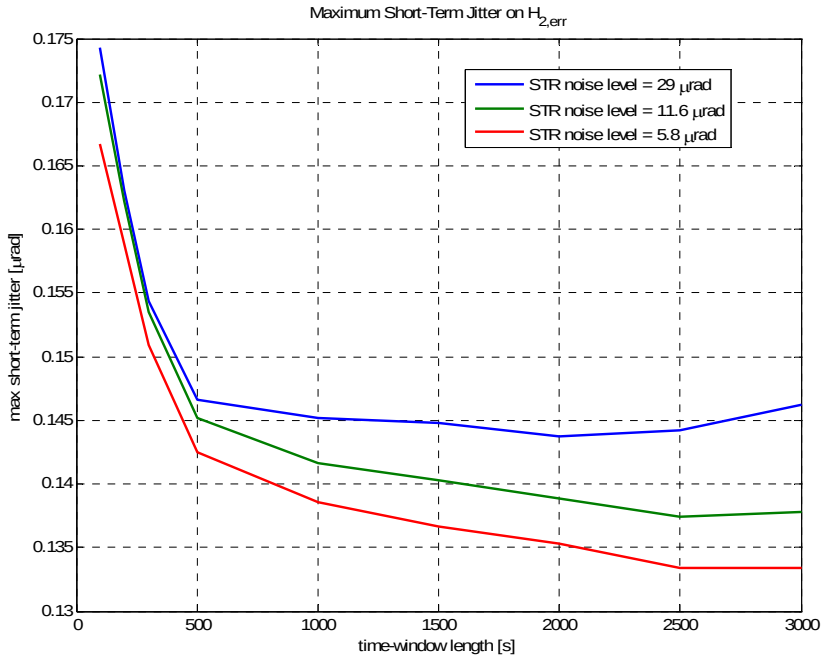

Figure 7.5-27: Telescope 2 line-of sight inertial pitch angle error with Kalman filter 2

Remark

A test of the filter performances on the correct guidance law is highly recommended when the mentioned guidance law are available. In fact, the Kalman gains are kept voluntarily low in order to increase the filter performances. This low-pass behaviour reduces the reactivity of the filter in presence of fast maneuvers and, as usual, could be cured with a different tuning by sacrificing some performances. In presence of modest and slow guidance laws, the behaviour of the filter is excellent (as shown by Figure 7.5-2, 7.5-4 and 7.5-6).

Chapter 8

Sensitivity Analysis towards Model Errors using the Monte Carlo Technique

In chapter 7, the Kalman filter process models have been derived directly from the LISA satellite dynamic model, that is also used for the simulation of the real satellite behaviour, without introducing any errors. In reality, the LISA satellite model is an approximation of the real satellite dynamics: the model parameters are affected by uncertainty (the real masses, the real geometrical constraints, etc. are known with a certain accuracy) and the non-linearity of the real system is neglected in the model.
The purpose of this chapter is to understand what happens to the filter performances when the filter itself is applied to a more realistic system, still linear, but different from the model that the filter uses. To this end, the Monte Carlo technique is used. It consists in performing a great extent of tests in order to achieve a statistical knowledge of the performance modifications.
Kalman filter 2 and Kalman filter 3 designed in chapter 7 are used for this analysis. Kalman filter 1 is not used because it has a behaviour very similar to filter 2, except for the transient.

8.1 Sensitivity Analysis Procedure

218 parameters of the LISA satellite 'real' dynamics model (Eq. 3.7-3.8) which are affected by uncertainty are selected. A model error budget is set out: it is defined an

interval in which each parameter can vary. It is further assumed that the error sources are uncorrelated Gaussian processes. Therefore, each model parameter can randomly change, independently from the others, in the interval given by its error budget (section 8.2).

The Monte-Carlo sensitivity analysis is then implemented by the Matlab-Simulink® tool provided in [CD-ROM], which performs the following procedure:

- 3000 simulations are performed. The LISA satellite open-loop plant is changed in each simulation by changing randomly the whole set of selected model parameters. All the other systems and parameters are kept constant (the filter, the controller, the noise system, the simulation parameters, etc.)
- A set of 8 performance parameters are computed for each simulation and compared with a reference performance vector (section 8.3)
- The outputs provided by the Monte Carlo sensitivity analysis tool are:
  - a matrix 3000x8 whose rows contain the performance parameters of each simulation
  - a matrix 3000x219 whose rows contain the simulation number (first element) and the model error parameters of each simulation
  - the time-series signals of the 16 simulations corresponding to the 8 worst and to the 8 best results for each performance parameter
  - the time-series signals of all the simulations where at least one of the performance parameters exceeds the correspondent element of the reference performance vector

8.2 Model Error Budget

The 218 parameters of the LISA satellite dynamics model that are affected by uncertainty are listed together with their budget error in the following sections.

8.2.1 Mass Error Budget

Symbol	Description	Nominal Value (kg)	Error
m_B	Spacecraft mass	350	± 10 %
m_1	T/M 1 mass	1.96	± 10 %
m_2	T/M 2 mass	1.96	± 10 %
m_C	Telescope 1 mass	80	± 10 %

Table 8.2.1-1: Mass error budget

The mass error budget provides 4 parameters for the sensitivity analysis.

8.2.2 Moment of Inertia (MoI) Error Budget

Symbol	Description	Nominal Value $(kg \cdot m^2)$	Error
I_B	Spacecraft MoI	$\begin{bmatrix} 158.0997 & -8.6262 & 0.8819 \\ -8.6262 & 163.0932 & 0.1913 \\ 0.8819 & 0.1913 & 297.0684 \end{bmatrix}$	± 20 %
I_1	T/M 1 MoI	$\begin{bmatrix} 6.9130e\text{-}004 & 0 & 0 \\ 0 & 6.9130e\text{-}004 & 0 \\ 0 & 0 & 6.9130e\text{-}004 \end{bmatrix}$	± 20 %
I_2	T/M 2 MoI	$\begin{bmatrix} 6.9130e\text{-}004 & 0 & 0 \\ 0 & 6.9130e\text{-}004 & 0 \\ 0 & 0 & 6.9130e\text{-}004 \end{bmatrix}$	± 20 %
I_C	Telescope 1 MoI	$\begin{bmatrix} 5 & 0 & 0 \\ 0 & 15 & 0 \\ 0 & 0 & 15 \end{bmatrix}$	± 20 %

Table 8.2.2-1: Moment of inertia error budget

Since the test masses are cubic and the telescope is modelled as a cylindrical body, it is supposed that theirs shapes are not affected by errors, therefore, the MoI tensor of each test mass can just vary proportionally (1 parameter) and the telescope MoI tensor has to remain diagonal (3 parameters). On the contrary, all the components of the spacecraft MoI can vary independently.

The moment of inertia error budget provides 11 parameters for the sensitivity analysis.

8.2.3 Position Vector Error Budget

Symbol	Description	Nominal Value (m)	Error (m)
$\mathbf{r_{P2}}$	Vector from spacecraft CoM to telescope 2 rotation point expressed in Σ_B	$\begin{bmatrix} -0.3 \\ -0.3 \\ 0 \end{bmatrix}$	$\pm \begin{bmatrix} 0.03 \\ 0.03 \\ 0.03 \end{bmatrix}$
$\mathbf{r_R}$	Vector from spacecraft CoM to telescope 1 rotation point expressed in Σ_B	$\begin{bmatrix} -0.3 \\ 0.3 \\ 0 \end{bmatrix}$	$\pm \begin{bmatrix} 0.03 \\ 0.03 \\ 0.03 \end{bmatrix}$
$\mathbf{r_C}$	Vector from telescope 1 rotation point to telescope 1 CoM expressed in Σ_C	$\begin{bmatrix} 0.1 \\ 0 \\ 0 \end{bmatrix}$	$\pm \begin{bmatrix} 0.02 \\ 0 \\ 0 \end{bmatrix}$
$\mathbf{r_{P1}}$	Vector from telescope 1 CoM to T/M 1 reference position expressed in Σ_C	$\begin{bmatrix} 0 \\ 0 \\ 0 \end{bmatrix}$	$\pm \begin{bmatrix} 0.02 \\ 0 \\ 0 \end{bmatrix}$
$\mathbf{r_{AR}}$	Vector from telescope 1 rotation point to its actuation point expressed in Σ_C	$\begin{bmatrix} 0.5 \\ 0 \\ 0 \end{bmatrix}$	$\pm \begin{bmatrix} 0.005 \\ 0 \\ 0 \end{bmatrix}$

Table 8.2.3-1: Position vector error budget

The error budgets on $\mathbf{r_{P2}}$ and $\mathbf{r_R}$ are based on the uncertainty in the spacecraft CoM position. It is assumed that the spacecraft CoM can stand in a cube with a side of 60 mm centred in its reference position.

The error budgets on $\mathbf{r_C}$ and $\mathbf{r_{P1}}$ are based on the uncertainty in the telescope 1 CoM position which can vary 20 mm from its reference position along the telescope symmetry axis.

Finally, the error budget on $\mathbf{r_{AR}}$ comes from the fact that the distance between the rotation and the actuation point of telescope 1 has 5 mm tolerance because of mounting errors.

The other position vectors are derived from these, therefore the position vector error budget provides 9 parameters for the sensitivity analysis.

8.2.4 Telescope Symmetry Axis Angular Position Error Budget

Symbol	Description	Nominal Value	Error
β_{T1}	Angle between the telescope 1 symmetry axis and the spacecraft x_B axis measured in Σ_B	30°	± 0.1°
β_{T2}	Angle between the telescope 2 symmetry axis and the spacecraft x_B axis measured in Σ_B	-30°	± 0.1°

Table 8.2.4-1: Telescope symmetry axis angular position error budget

The telescope symmetry axis angular position error budget provides 2 parameters for the sensitivity analysis.

8.2.5 Stiffness Matrix Error Budget

The stiffness matrix accounts for several parasitic effects, the most important of which is the self-gravity. It is in the form

$$\mathbf{\Omega} = \begin{bmatrix} \mathbf{\Omega_1} & \mathbf{0}_{6\times6} \\ \mathbf{0}_{6\times6} & \mathbf{\Omega_2} \end{bmatrix}$$

where $\boldsymbol{\Omega}_1$ and $\boldsymbol{\Omega}_2$ are the stiffness matrices that influence respectively the T/M 1 and T/M 2 coordinates. It would be desirable that they were zero matrix, but a plausible interval of variation for their elements is

$$\boldsymbol{\Omega}_1 = \begin{bmatrix} \pm 4.000e-7 & \pm 2.000e-8 & \pm 1.350e-8 & \pm 1.150e-9 & \pm 1.150e-9 & \pm 1.150e-9 \\ \pm 1.350e-8 & \pm 1.050e-6 & \pm 1.350e-8 & \pm 1.150e-9 & \pm 1.150e-9 & \pm 1.150e-9 \\ \pm 1.350e-8 & \pm 2.000e-8 & \pm 2.700e-6 & \pm 2.530e-9 & \pm 2.530e-9 & \pm 2.530e-9 \\ \pm 2.609e-6 & \pm 9.130e-6 & \pm 2.609e-6 & \pm 2.000e-6 & \pm 1.600e-7 & \pm 1.600e-7 \\ \pm 2.609e-6 & \pm 9.130e-6 & \pm 2.609e-6 & \pm 1.600e-7 & \pm 2.000e-6 & \pm 1.600e-7 \\ \pm 2.609e-6 & \pm 9.130e-6 & \pm 2.609e-6 & \pm 1.600e-7 & \pm 1.600e-7 & \pm 2.000e-6 \end{bmatrix}$$

$$\boldsymbol{\Omega}_2 = \begin{bmatrix} \pm 4.000e-7 & \pm 2.000e-8 & \pm 2.000e-8 & \pm 1.150e-9 & \pm 1.150e-9 & \pm 1.150e-9 \\ \pm 1.350e-8 & \pm 1.050e-6 & \pm 2.000e-8 & \pm 1.150e-9 & \pm 1.150e-9 & \pm 1.150e-9 \\ \pm 1.350e-8 & \pm 2.000e-8 & \pm 4.000e-6 & \pm 2.530e-9 & \pm 2.530e-9 & \pm 2.530e-9 \\ \pm 2.609e-6 & \pm 9.130e-6 & \pm 9.130e-6 & \pm 2.000e-6 & \pm 1.600e-7 & \pm 1.600e-7 \\ \pm 2.609e-6 & \pm 9.130e-6 & \pm 9.130e-6 & \pm 1.600e-7 & \pm 2.000e-6 & \pm 1.600e-7 \\ \pm 2.609e-6 & \pm 9.130e-6 & \pm 9.130e-6 & \pm 1.600e-7 & \pm 1.600e-7 & \pm 2.000e-6 \end{bmatrix}$$

The stiffness matrix error budget provides 72 parameters for the sensitivity analysis.

8.2.6 Cross-Talk Electrostatic Read-Out Matrix Error Budget

The cross-talk electrostatic read-out matrix accounts for the cross-talk between different degrees of freedom of the electrostatic read-out of the inertial sensors and it is in the form

$$\mathbf{g}_{\mathbf{IS}} = \begin{bmatrix} \mathbf{g}_{\mathbf{IS1}} & \mathbf{0}_{6\times 6} \\ \mathbf{0}_{6\times 6} & \mathbf{g}_{\mathbf{IS2}} \end{bmatrix}$$

where $\mathbf{g}_{\mathbf{IS1}}$ and $\mathbf{g}_{\mathbf{IS2}}$ are the cross-talk matrices that affect respectively the T/M 1 and the T/M 2 coordinate measurements. Nominally, they are identity matrices but a plausible interval of variation for their off-diagonal terms is

$$\mathbf{g}_{\mathbf{IS1}} = \begin{bmatrix} 1 & \pm 3.000e-3 & \pm 3.000e-3 & \pm 5.980e-4 & \pm 5.980e-4 & \pm 5.980e-4 \\ \pm 3.000e-3 & 1 & \pm 3.000e-3 & \pm 5.980e-4 & \pm 5.980e-4 & \pm 5.980e-4 \\ \pm 3.000e-3 & \pm 3.000e-3 & 1 & \pm 5.980e-4 & \pm 5.980e-4 & \pm 5.980e-4 \\ \pm 8.696e-2 & \pm 8.696e-2 & \pm 8.696e-2 & 1 & \pm 1.000e-3 & \pm 1.000e-3 \\ \pm 8.696e-2 & \pm 8.696e-2 & \pm 8.696e-2 & \pm 1.000e-3 & 1 & \pm 1.000e-3 \\ \pm 8.696e-2 & \pm 8.696e-2 & \pm 8.696e-2 & \pm 1.000e-3 & \pm 1.000e-3 & 1 \end{bmatrix}$$

The off-diagonal elements of $\mathbf{g}_{\mathbf{IS2}}$ can vary in the same intervals of the corresponding $\mathbf{g}_{\mathbf{IS1}}$ elements, but independently from them.

Therefore, the cross-talk electrostatic read-out matrix error budget provides 60 parameters for the sensitivity analysis.

8.2.7 Cross-Talk Electrostatic Actuation Matrix Error Budget

The cross-talk electrostatic actuation matrix describes the cross-talk between different degrees of freedom of the electrostatic actuation of the inertial sensors and it is in the form

$$\mathbf{h}_{\mathbf{IS}} = \begin{bmatrix} \mathbf{h}_{\mathbf{IS1}} & \mathbf{0}_{6\times 6} \\ \mathbf{0}_{6\times 6} & \mathbf{h}_{\mathbf{IS2}} \end{bmatrix}$$

where $\mathbf{h}_{\mathbf{IS1}}$ and $\mathbf{h}_{\mathbf{IS2}}$ are the cross-talk matrices that affect respectively the T/M 1 and the T/M 2 force and torque actuations. Nominally, they are identity matrices, but their off diagonal terms can vary between

$$\mathbf{h}_{\mathbf{IS1}} = \begin{bmatrix} 1 & \pm 5.000e-3 & \pm 5.000e-3 & \pm 2.174e-1 & \pm 2.174e-1 & \pm 2.174e-1 \\ \pm 5.000e-3 & 1 & \pm 5.000e-3 & \pm 6.522e-1 & \pm 6.522e-1 & \pm 6.522e-1 \\ \pm 5.000e-3 & \pm 5.000e-3 & 1 & \pm 6.522e-1 & \pm 6.522e-1 & \pm 6.522e-1 \\ \pm 3.680e-5 & \pm 3.680e-5 & \pm 3.680e-5 & 1 & \pm 5.000e-3 & \pm 5.000e-3 \\ \pm 3.680e-5 & \pm 3.680e-5 & \pm 3.680e-5 & \pm 5.000e-3 & 1 & \pm 5.000e-3 \\ \pm 3.680e-5 & \pm 3.680e-5 & \pm 3.680e-5 & \pm 5.000e-3 & \pm 5.000e-3 & 1 \end{bmatrix}$$

These values depend basically on the sensor configuration.

The off-diagonal elements of $\mathbf{h}_{\mathbf{IS2}}$ can vary in the same intervals of the corresponding elements $\mathbf{h}_{\mathbf{IS1}}$, but independently from them.

Therefore, the cross-talk electrostatic actuation matrix error budget provides 60 parameters for the sensitivity analysis.

8.3 Performance Parameters

The performance parameters for the sensitivity analysis are:

- the maximum RMS 1σ over a time-window of 1000 s of the telescope 2 line-of-sight attitude error ($\Theta_{2,err}$, $H_{2,err}$, $\Phi_{2,err}$) and of the telescope 1 in-plane pointing angle error ($\alpha_{CAGE,err}$) as a measure of the short-term jitter for the corresponding signals (section 2.3.3 for more details)
- the maximum slope of the interpolating line over a time-window of 1000 s of the same states as a measure of the long-term drift (section 2.3.3 for more details)

The performance parameters are compared with a reference performance vector. For the sensitivity analysis based on the Kalman filter 3, its components are the short-term jitter and the long-term drift requirements of the states

$$\begin{bmatrix} 0.1 & 0.1 & 0.1 & 0.05 & 5 & 5 & 5 & 1 \end{bmatrix}$$

Since a requirement is not defined for $\Theta_{2,err}$, it is chosen the same than $H_{2,err}$.

For the Kalman filter 2 case, the short-term requirement over $H_{2,err}$ has been relaxed, since it is not fulfilled even in the case without model errors. The corresponding reference performance vector is

$$\begin{bmatrix} 0.1 & 0.2 & 0.1 & 0.05 & 5 & 5 & 5 & 1 \end{bmatrix}$$

8.4 Performance Analysis

8.4.1 Kalman Filter 2: Steady-State Continuous-Time Kalman Filter without State Augmentation

The histograms of the short-term performance parameters of the 4 states under analysis are shown in Figure 8.4.1-1. They represent the number of simulations that have produced a certain level of short-term jitter. The mean, the standard deviation (1σ)

and the relative percentage variation of each distribution shown in Figure 8.4.1-1 are computed and reported in Table 8.4.1-1 together with the requirements and the baseline performances. The baseline represents the case in which the 'real' plant and the filter are both computed with the same, nominal values of the model parameters. In all the other simulations, the filter uses a process model based on the nominal values of the parameters and remains constant, while the 'real' plan model changes.

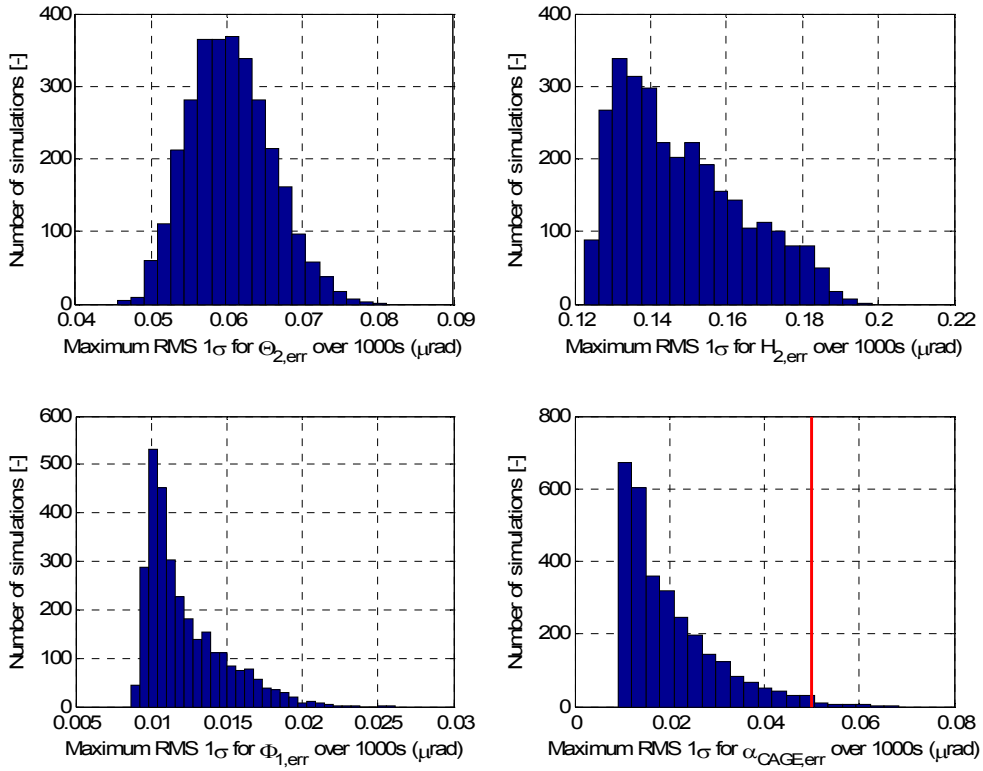

Figure 8.4.1-1: Histograms of the number of simulations vs the short-term jitter for the Kalman Filter 2

Error	Requirements (μrad)	Baseline (μrad)	Mean (μrad)	Standard Deviation (μrad)	$\frac{\text{Max-Min}}{\text{Baseline}}\times 100$
$\Theta_{2,err}$	-	0.0578	0.0605	0.0054	61.6 %
$H_{2,err}$	0.1	0.1453	0.1481	0.0163	52.2 %
$\Phi_{2,err}$	0.1	0.0099	0.0122	0.0026	176.8 %
$\alpha_{CAGE,err}$	0.05	0.0104	0.0200	0.0099	567.5 %

Table 8.4.1-1: Statistics of the sensitivity analysis for the Kalman filter 2

The vertical red line in Figure 8.4.1-1 shows that the telescope 1 in-plane pointing angle error does not satisfied the requirement in some simulations. The percentage of requirement violation is 1.3 %. The telescope 2 LOS pitch angle violate the requirement in each simulation, but this is due to the filter design (in fact, also the baseline does not fulfil the requirement on this state) more than to the sensitivity towards model errors.

In fact, the telescope 2 LOS roll and pitch angle errors are quite insensitive towards variations of the model parameters, as it is confirmed by their relative percentage variation (4th column of Table 8.4.1-1). Further investigations show that they are both sensitive to reduction of the principal moment of inertia of the spacecraft in the y_B direction (I_{By}).

On the contrary, the telescope 2 LOS yaw angle error and the telescope 1 in-plane pointing angle error are very sensitive towards model errors and, in particular, towards geometrical errors. If the z components of $\mathbf{r_{P2}}$ and of $\mathbf{r_R}$ vary in the opposite direction, or in other words if there is an arm along z_B between the test masses, the estimate of ϕ_1 and ϕ_2, and consequently the estimate of α and Φ_{SC}, get considerably worse. The telescope 1 in-plane pointing angle α is also negatively influenced by a reduction of I_{Bz} and I_{Cz}, but this effect is of the second order.

However, the system is always stable.

The long-term drifts histograms and table can be found in Appendix A. Long-term drifts are very small once DC forces and torques are estimated and subtracted (Chapter 9) and their increase due to model errors is still far from reaching the requirements.

8.4.2 Kalman Filter 3: Steady-State Continuous-Time Kalman Filter with State Augmentation on the Process Noise

The histograms of the short-term performance parameters of the 4 states under analysis are shown in Figure 8.4.2-1. The mean, the standard deviation (1σ) and the relative percentage variation of each distribution shown in Figure 8.4.2-1 are computed and reported in Table 8.4.2-1 together with the requirements and the baseline performances (plant and filter computed with the nominal value of the model parameters).

The results provided by the Kalman filter 3 are inverted with respect to the previous

case involving the Kalman filter 2. In fact, the telescope 2 LOS yaw angle error and the telescope 1 in-plane pointing angle error are quite insensitive towards model errors and satisfy the requirements. On the contrary, the telescope 2 LOS roll and pitch angle errors show a large sensitivity towards variations of the model parameters and, in particular, towards the stiffness and the cross-coupling coefficients more than towards the others geometrical parameters.

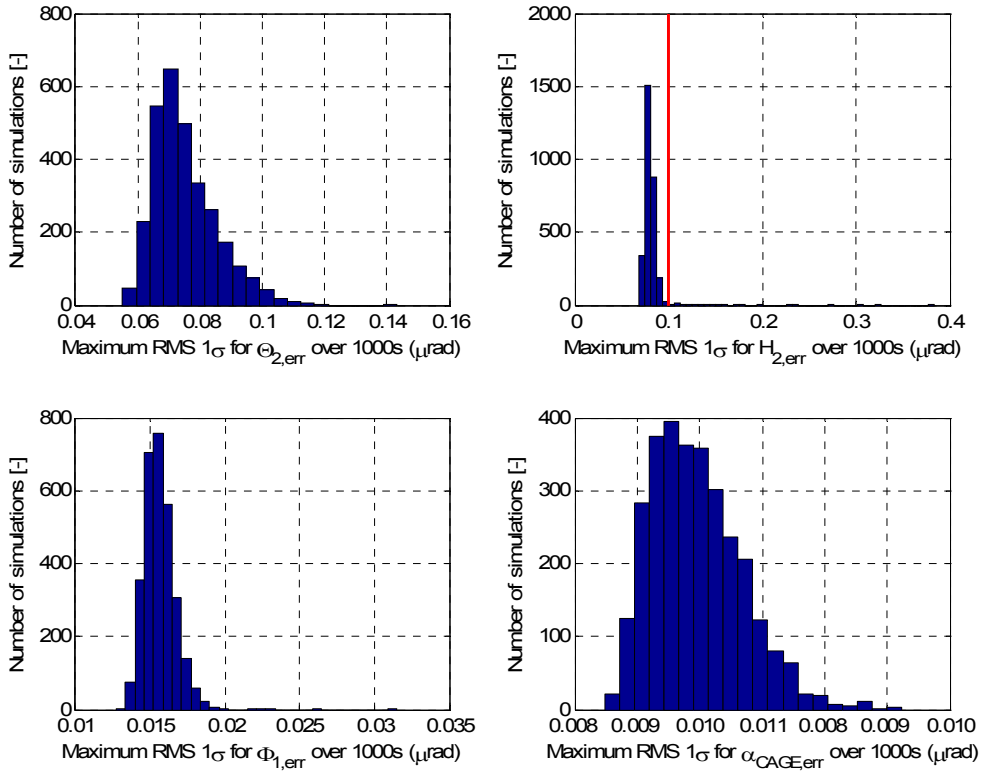

Figure 8.4.2-1: Histograms of the number of simulations vs the short-term jitter for the Kalman Filter 3

Error	Requirements (μrad)	Baseline (μrad)	Mean (μrad)	Standard Deviation (μrad)	$\frac{\text{Max-Min}}{\text{Baseline}} \times 100$
$\Theta_{2,err}$	-	0.0711	0.0751	0.0102	123.8 %
$H_{2,err}$	0.1	0.0779	0.0813	0.0127	403.8 %
$\Phi_{2,err}$	0.1	0.0154	0.0156	0.0011	122.4 %
$\alpha_{CAGE,err}$	0.05	0.0087	0.0090	0.0004	27.1 %

Table 8.4.2-1: Statistics of the sensitivity analysis for the Kalman filter 3

The percentage of requirement violation is 4.1 % and is due to the pitch angle error (vertical red line in Figure 8.4.2-1).

Moreover, in some of the un-satisfactory cases, the system becomes unstable. The instability can be recovered by changing the tuning of the filter. It has been proved that un-stable cases can be recovered by choosing $c < 5$ (c is the proportional factor that scales the $\mathbf{Q}$ matrix in the steady-state filter with state augmentation). In fact, 'model errors' mean that the plant is different from the filter process model. In order to make the filter model congruent to the reality, fictitious process noise can be added

$$\begin{array}{cc} \text{Real Plant} & \text{Kalman Filter Process Model} \\ \begin{cases} \dot{\mathbf{x}}(t) = \mathbf{A}\mathbf{x}(t) + \mathbf{B}\mathbf{u}(t) + \mathbf{G}\mathbf{w}(t) \\ \mathbf{y}(t) = \mathbf{H}\mathbf{x}(t) + \mathbf{n}(t) \end{cases} & \leftrightarrow \quad \begin{cases} \dot{\mathbf{x}}(t) = \mathbf{A}'\mathbf{x}(t) + \mathbf{B}'\mathbf{u}(t) + \mathbf{G}'\mathbf{w}(t) + \mathbf{w}'(t) \\ \mathbf{y}(t) = \mathbf{H}'\mathbf{x}(t) + \mathbf{n}(t) \end{cases} \end{array}$$

Therefore, in order to remediate the unstable cases, the usual tuning strategies can be adopted:

- Look for a better tuning of the baseline (adding process noise or desaturating the error covariance matrix) trying to maintaining the acquired performances
- Use an adaptive filter

The long-term drifts histograms and table can be found in Appendix A.

Chapter 9

Compensation of the DC Forces and Torques Effect

This chapter suggests two different methods to cancel or reduce the influence that the parasitic constant forces and torques, that are acting on the test masses, have on the performances achieved by means of the acquisition control system based on the Kalman filter designed in chapter 7. The same methods could be adopted with slight variations for the problem of the compensation of the DC solar forces and torques acting on the spacecraft.

9.1 Introduction

In the *drag-free acquisition mode*, the potential influence of the disturbance biases is suppressed by the controllers. In particular, the suspension controller requires around 7000 s to compensate completely the bias effect over the non-drag-free test mass coordinates, while the bias compensation is much faster (few seconds) over all the other controlled states (SC inertial attitude, telescope 1 in-plane pointing angle and test mass drag-free coordinates).

In the *gyro mode*, the Kalman Filter noise signal assumptions are violated (the process noises are not zero-mean processes as required) and, as a consequence, the filter is not able to estimate the controlled states properly. This happens because the Kalman filters designed for the *gyro mode* (chapter 7) use the test masses as accelerometers, i.e. they use the control commands (combined with the measurements) for the state

estimation. Nevertheless, the control commands are partly generated to compensate the disturbance biases, while the Kalman filter process models do not include the information that DC forces and torques are acting on the test masses. The Kalman filter is 'deceived' by such control commands and the result is an incorrect estimate. The methods suggested to recover the *gyro mode* performances are:

1) estimate the biases and modify the Kalman filter process model by including the estimated biases within the deterministic inputs. When the Kalman filter 'knows' the biases intensity and the way they influence the LISA satellite dynamics, it is able to perfectly subtract their effect from the control commands. In this way, the same *gyro mode* performances shown in chapter 7 are achievable. Some additional filter tuning could be required in order to compensate the uncertainties over the biases estimates;

2) compensate the biases effect by changing the tuning of the filter without modifying the Kalman filter process model. This strategy consists essentially in increasing the Kalman gains and enhancing the filter bandwidth. The filter 'relies' more on the measurements and corrects the wrong information it receives from the control commands. The main consequence is a degradation of the *gyro mode* performances shown in chapter 7.

9.2 Method 1: Biases Estimation and Correction

9.2.1 Estimation Procedure

Including the DC forces and torques in the *state vector* $\mathbf{x} \in \mathbb{R}^{44x1}$

$$\mathbf{x} = [\boldsymbol{\omega}_B \;\; \dot{\mathbf{r}}_1 \;\; \boldsymbol{\omega}_1 \;\; \dot{\mathbf{r}}_2 \;\; \boldsymbol{\omega}_2 \;\; \dot{\alpha} \;\; \boldsymbol{\alpha}_B \;\; \mathbf{r}_1 \;\; \boldsymbol{\alpha}_1 \;\; \mathbf{r}_2 \;\; \boldsymbol{\alpha}_2 \;\; \alpha \;\; \mathbf{f}_{1DC}^{(C)} \;\; \mathbf{l}_{1DC} \;\; \mathbf{f}_{2DC}^{(2)} \;\; \mathbf{l}_{2DC}]^T$$

Eq. (7.1) and Eq. (7.2) can be rewritten as

$$\dot{\mathbf{x}}(t) = \underbrace{\begin{bmatrix} \mathbf{0}_{16\times16} & \boldsymbol{\Omega}_{16\times16} & \mathbf{M}^{-1}\hat{\mathbf{F}}_{419,1324} \\ \mathbf{E}_{16\times16} & \mathbf{0}_{16\times16} & \mathbf{0}_{16\times12} \\ \mathbf{0}_{12\times16} & \mathbf{0}_{12\times16} & \mathbf{0}_{12\times12} \end{bmatrix}}_{\mathbf{A}} \mathbf{x}(t) + \underbrace{\begin{bmatrix} \mathbf{M}^{-1}\hat{\mathbf{B}}_{419,119} \\ \mathbf{0}_{16\times19} \\ \mathbf{0}_{12\times19} \end{bmatrix}}_{\mathbf{B}} \mathbf{u}(t) + \underbrace{\begin{bmatrix} \mathbf{M}^{-1}\hat{\mathbf{F}}_{419,125} \\ \mathbf{0}_{16\times25} \\ \mathbf{0}_{12\times25} \end{bmatrix}}_{\mathbf{G}} \mathbf{d}(t) \quad (9.1)$$

$$\mathbf{y}(t) = \underbrace{\begin{bmatrix} \mathbf{0}_{3\times3} & \mathbf{0}_{3\times12} & \mathbf{0}_{3\times1} & \mathbf{E}_{3\times3} & \mathbf{0}_{3\times12} & \mathbf{0}_{3\times1} & \mathbf{0}_{3\times12} \\ \mathbf{0}_{12\times3} & \mathbf{0}_{12\times12} & \mathbf{0}_{12\times1} & \mathbf{0}_{12\times3} & \mathbf{g}_{IS} & \mathbf{0}_{12\times1} & \mathbf{0}_{12\times12} \\ \mathbf{0}_{1\times3} & \mathbf{0}_{1\times12} & \mathbf{0}_{1\times1} & \mathbf{0}_{1\times3} & \mathbf{0}_{1\times12} & \mathbf{E}_{1\times3} & \mathbf{0}_{1\times12} \end{bmatrix}}_{\mathbf{H}} \mathbf{x}(t) + \mathbf{v}(t) \qquad (9.2)$$

where the symbols have the same meaning as in section 7.2.1.

Eq. (9.1) and Eq. (9.2) include the biases dynamics and are used as a Kalman filter process model for the biases estimation. The state reduction modelling strategy is adopted in order to define the noise covariance matrices **Q** and **R**.

The system (9.1) - (9.2) is observable, but not controllable in the sense expressed in section 6.2.4. This means that the biases are observable, but a unique steady solution of the Riccati equation does not exist. Therefore, the time-varying discrete-time Kalman filter algorithm has to be used.

The resulting filter requires additional tuning over the FEEP actuation noise for the same reasons explained in section 7.4.

The main filter features are summarized in Table 9.2.1-1.

Kalman Filter	**Initial Conditions**		**Tuning**		**State Augmentation**
	$\hat{\mathbf{x}}_0$	$\mathbf{P}_0$	**Q**	**R**	
Time-varying discrete-time	$\mathbf{0}_{44\times44}$	$10^{-10}\cdot\mathbf{E}_{44\times44}$	$\sigma^2_{FEEP}\cdot10^5$	$\mathbf{R}^d = \mathbf{R}$	NO

Table 9.2.1-1: Designed Kalman filter characterization

Note that the biases do not have a proper dynamics. Therefore, the corresponding elements of the initial error covariance matrix ($\mathbf{P}_0$) have to be chosen unequal to zero.

Using the designed filter, the DC torques are estimated with a high level of accuracy (Table 9.2.1-2 compares the DC torques real values and the DC torques estimated values after 3000 s. It also shows the percentage error of the estimates). The estimation principle is the same used in the *gyro mode*, i.e. the test masses are employed as

accelerometers. In fact, the attitude coordinates of the T/M are suspension controlled. This means that each DC torque is compensated directly by a corresponding constant actuation torque provided by the inertial sensor. The total actuation torque, which also includes the compensation of other disturbances acting over the same coordinate, is sent to the Kalman filter which, having a state dynamic model and a disturbances model, is able to distinguish the bias effect from that of the other disturbances and, consequently, produces a very accurate bias estimation.

DC torques		**Real (Nm)**	**Estimated (Nm)**	**error = $\frac{\text{real - estimated}}{\text{real}} \times 100$**
T/M 1	$\mathbf{l_{x1}}$	1.86651e-011	1.866425e-011	4.52495e-003 %
	$\mathbf{l_{y1}}$	1.58999e-011	1.590037e-011	2.94692e-003 %
	$\mathbf{l_{z1}}$	1.10608e-011	1.106078e-011	1.24623e-004 %
T/M 2	$\mathbf{l_{x2}}$	1.86651e-011	1.866435e-011	3.98501e-003 %
	$\mathbf{l_{y2}}$	1.58999e-011	1.589941e-011	3.10053e-003 %
	$\mathbf{l_{z2}}$	1.10608e-011	1.106081e-011	8.33945e-005 %

Table 9.2.1-2: DC torque estimation performance

The same criteria is used for the DC forces estimation, but the filter is not able to produce a reliable estimate in this case (Table 9.2.1-3). In fact, the DC forces acting on the non-drag-free coordinates (y_1, y_2, z_2) are compensated by the corresponding suspension force commands, while the DC forces acting on the drag-free coordinates (x_1, z_1, x_2) are compensated by the FEEP force commands. The main problem is that, since the SC position is not controlled, the force commands for the T/M also account for the external force disturbances acting on the satellite (i.e. FEEP noise and solar pressure). In particular, the FEEP force actuation noises are much higher than the acceleration caused by the DC forces over the test masses. Therefore, the FEEP noise, conveyed in the filter by the force commands, masks the effect of the DC forces. If, just for testing purpose, the FEEP force actuation noise is switched off, it is possible to verify that the filter is able to estimate the DC forces with the same accuracy than the DC torques.

Therefore, the suggested solution to the problem of estimate the DC forces is to define a control mode where the test mass coordinates are all suspension controlled such that the FEEP force command capability is not used at all.

DC forces		Real (Nm)	Estimated (Nm)	$\text{error} = \frac{\text{real - estimated}}{\text{real}} \times 100$
T/M 1	f_{x1}	2.548e-009	1.315e-008	616.2 %
	f_{y1}	4.312e-009	4.927e-009	14.3 %
	f_{z1}	7.252e-009	1.927e-008	165.8 %
T/M 2	f_{x2}	2.548e-009	5.835e-009	329.0 %
	f_{y2}	4.312e-009	8.978e-009	308.2 %
	f_{z2}	7.252e-009	1.928e-008	165.9 %

Table 9.2.1-3: DC force estimation performance

9.2.2 Correction Procedure

Once the DC forces and torques estimates are available, the correction procedure consists of including the bias estimates in the Kalman filter process model. To this end, Eq. (7.1) has to be modified by including the estimated biases within the deterministic inputs

$$\dot{\mathbf{x}}(t) = \underbrace{\begin{bmatrix} \mathbf{0}_{16\times16} & \mathbf{\Omega}_{16\times16} \\ \mathbf{E}_{16\times16} & \mathbf{0}_{16\times16} \end{bmatrix}}_{\mathbf{A}} \mathbf{x}(t) + \underbrace{\begin{bmatrix} \mathbf{M}^{-1}\hat{\mathbf{B}}_{419,119} & \mathbf{M}^{-1}\hat{\mathbf{F}}_{419,1324} \\ \mathbf{0}_{16\times19} & \mathbf{0}_{16\times12} \end{bmatrix}}_{\mathbf{B}} \begin{bmatrix} \mathbf{u}(t) \\ \mathbf{f}_{1DC}^{(C)} \\ \mathbf{l}_{1DC} \\ \mathbf{f}_{2DC}^{(2)} \\ \mathbf{l}_{2DC} \end{bmatrix} + \underbrace{\begin{bmatrix} \mathbf{M}^{-1}\hat{\mathbf{F}}_{419,125} \\ \mathbf{0}_{16\times25} \end{bmatrix}}_{\mathbf{G}} \mathbf{d}(t) \tag{9.3}$$

Then, the derivation of the Kalman filter process models proceeds as in chapter 7.

As already said, if the biases are estimated with the accuracy of Table 9.2.1-2, the *gyro mode* performances are maintained. If less accurate bias estimates are expected, it is convenient to modify the tuning of the filter, e.g. by adding fictitious process noise on the suspension actuation noise channels (note from Eq. (9.3) that the biases act in the same way as the suspension actuation noises act ($\mathbf{M}^{-1}\hat{\mathbf{F}}_{419,1324}$); therefore, the process noise related to the biases has to be added to the suspension process noise).

9.3 Method 2: Biases Compensation

The Kalman filter benefit is that it does not need a perfect model of the real system in order to work correctly, but just the best model that can be provided and a statistical quantification of the reliability of the model provided. Therefore, in presence of unestimated biases, it is possible to maintain the Kalman filter process models introduced in chapter 7 and to introduce a statistical information about the unmodelled biases. In other words, the process and the measurement covariance matrices have to be partially redesigned in order to keep in consideration the unmodelled states. The purpose of this retuning is to get better estimates of the T/M coordinates, since the test masses are used as accelerometers for the estimation of the other states. This can be obtained by adding process noise on the suspension actuation noise channels and by reducing the STR elements of the measurement covariance matrix **R**, forcing artificially the filter to rely more on the STR measurements. In this way, the filter is able to correct the wrong information it receives from the control commands and, consequently, it is able to produce better estimates.

		Short-term jitter: maximum RMS 1σ in μrad over a time window of 1000 s of the signal error (reference - real)						
		$\Theta_{1,err}$	$H_{1,err}$	$\Phi_{1,err}$	$\Theta_{2,err}$	$H_{2,err}$	$\Phi_{2,err}$	$\alpha_{CAGE,err}$
Requirements		**-**	**0.1**	**≈ 0.118**	**-**	**0.1**	**0.1**	**0.05**
Gyro mode	**Kalman Filter 1**	0.4406	0.3448	0.1015	0.4271	0.3383	0.1014	0.0134
	Kalman Filter 2	0.3455	0.2325	0.0573	0.2742	0.2871	0.0565	0.0113
	Kalman Filter 3	0.8069	0.4279	0.4543	0.6442	0.5983	0.4541	0.0135

Table 9.3-1: Comparison between the short-term jitter requirements and the short-term jitter performances when the bias compensation strategy is adopted

The performances achieved with the three types of Kalman filter designed in chapter 7 are shown in Tables 9.3-1, 9.3-2. The same models and the same algorithms are used with a different tuning. The main consequence of this strategy is a large degradation with respect to the *gyro mode* performances shown in chapter 7. In particular, the short-term performances are highly degraded because of the drift produced by the biases. Moreover, a long transient (15000 s or more for the SC inertial roll angle which has the slowest dynamics) is needed before the filters are able to follow the real system states. The tuning performed for each filter represents a compromise between the need to maximize the performances and the need to minimize the transient duration.

		Long-term drift in µrad over a time window of 1000 s of the signal error (reference - real)						
		$\Theta_{1,err}$	$H_{1,err}$	$\Phi_{1,err}$	$\Theta_{2,err}$	$H_{2,err}$	$\Phi_{2,err}$	$\alpha_{CAGE,err}$
Requirements		-	5	≈ 5.099	-	5	5	1
Gyro mode	**Kalman Filter 1**	1.3189	0.9021	0.3116	1.2803	0.9238	0.3140	0.0029
	Kalman Filter 2	1.0516	0.6414	0.1767	0.8003	0.7697	0.1773	0.0040
	Kalman Filter 3	2.6278	1.2347	1.5618	1.8660	1.9622	1.5619	0.0059

Table 9.3-2: Comparison between the long-term drift requirements and the long-term drift performances when the bias compensation strategy is adopted

9.4 Conclusions

The estimation and correction method over the filters designed in Chapter 7 reduces sensitively the influence of the parasitic constant forces and torques acting on the test masses and maintains the performances achieved. The use of this strategy is highly recommended even though the definition of a different control mode is required for the DC forces estimation.

Chapter 10

Summary and Prospects for Future Work

10.1 Conclusions

Three suitable Kalman filters are provided for the LISA acquisition on CCD phase:

- The steady-state continuous-time Kalman filter with state augmentation on the process noise (Kalman filter 3) satisfies the requirements with a margin larger than 23 % over the laser beam out-of-plane pointing angle and larger than 80 % over the laser beam in-plane pointing angle and the articulated telescope in-plane pointing angle w.r.t the spacecraft. Several efficient strategies to reduce the filter sensitivity or to stabilize its behaviour in presence of dynamics model errors have been identified and applied.

- The time-varying discrete-time and the steady-state continuous-time Kalman filters (Kalman filter 1 and Kalman filter 2) show a slight violation of the laser beam out-of-plane pointing angle requirements, while the desired requirements on the laser beam in-plane pointing angle and on the articulated telescope in-plane pointing angle w.r.t the spacecraft are fulfilled with a large margin. The key point for the successful design of these filters has been identified in the modelling of the FFEP actuation noise which heavily influences the achievable performances. These filters are more robust against dynamics model errors than the filter that relies on the state augmentation technique. Moreover, the

geometrical constraints that influence the filters performances have been identified providing precious information for the mechanical design and verification.

The performances achieved and the results of the sensitivity analysis towards sensor noise levels show that the requirements on the laser beam in-plane pointing angle, on the articulated telescope in-plane pointing angle and on the OATM sensor noise level could be more stringent.

The sensitivity analysis towards the sensor noise levels points out also that the use of a more accurate star-tracker could be useful to enforce the performances acquired.

The sensitivity analysis towards the acquisition phase duration shows that a longer duration does not constitute a problem.

The worth of this work stands principally in the reusability. In fact, the proposed Kalman filters can be adapted to different operative conditions, to different system and noise dynamics models since the Kalman filter design process has been divided in three mutually independent parts: a system and noise modelling phase, an algorithm implementation phase and a tuning phase. A fully compliant custom tool for the implementation and performance analysis of the Kalman filter algorithms has been developed in the Matlab/Simulink® environment. As far as the modelling and the tuning phase is concerned, the guidelines for a remodelling are provided and the physical and theoretical principles for a retuning are extensively illustrated.

10.2 Future Work

The Kalman filter performances should be accurately tested on the correct guidance law for the acquisition phase on CCD phase, since the inherent low-pass behaviour of the Kalman filter reduces its reactivity in presence of fast maneuvers. Several strategies can be adopted in case of unsatisfactory behaviour: the tuning techniques, the design of a time-varying continuous-time Kalman filter.

The Kalman filter performances need to be tested on the non-linear equations of motion of the LISA satellite in order to verify theirs insensitivity towards the unmodelled non-linearities.

A sensitivity analysis towards errors in the noise dynamics models is also recommended, especially for the steady-state continuous-time Kalman filter with state augmentation on the process noise, since its improved performances are mainly based on the better way it models the FEEP actuation noise.

The definition of a dedicated control mode for the estimation of the parasitic constant forces acting on the test masses is required. Moreover, the applicability to the DC solar forces and torques acting on the spacecraft of the estimation and correction method developed for the DC forces and torques acting on the test masses should be proved.

Once the acquisition phase on CCD is completed, the feasibility of the other single-link acquisition phases has to be verified by using the *gyro mode* strategy. However, the operative conditions of the other single link sub-phases are less demanding in terms of desired performances and available sensors.

Finally, the feasibility of the acquisition control of the whole LISA constellation must be proved by simulation. Nevertheless, after one laser-link is performed on one arm, the signal acquisition process on the second and third arm will be in principle the same, except for the fact that high-accuracy attitude knowledge is already available for one direction.

Appendixes

Appendix A

Results: Tables and Plots

Figures and Tables, which are discussed in the present thesis, are reported in this appendix for reason of space.

Figures and Tables relative to chapter 5

Verification of the congruence between the Matlab® model and the Simulink® model: noise spectrum of state errors (reference-real). Figure A-1, A-2, A-3.

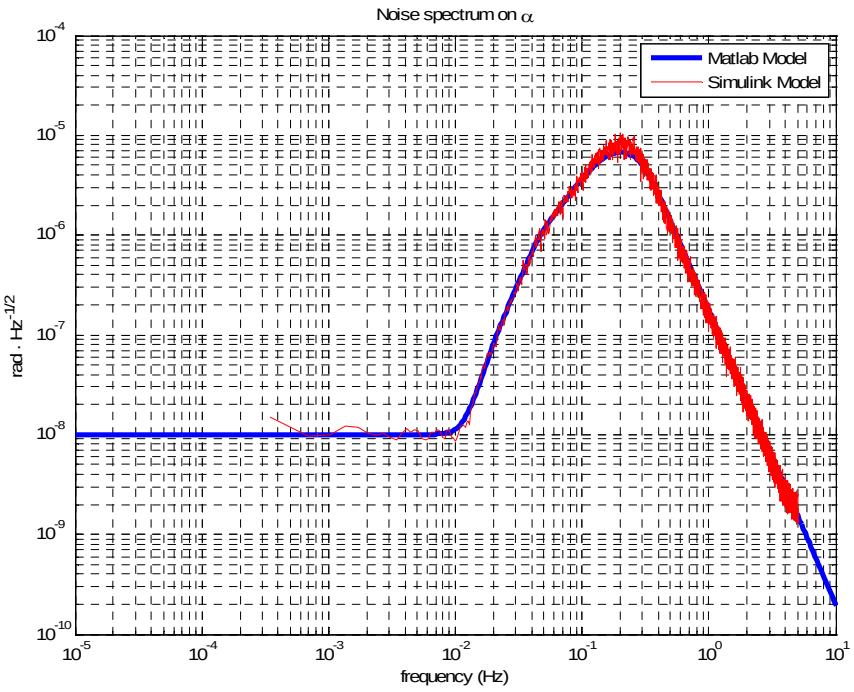

Figure A-1: Telescope 1 in-plane pointing angle error (no Kalman filter applied)

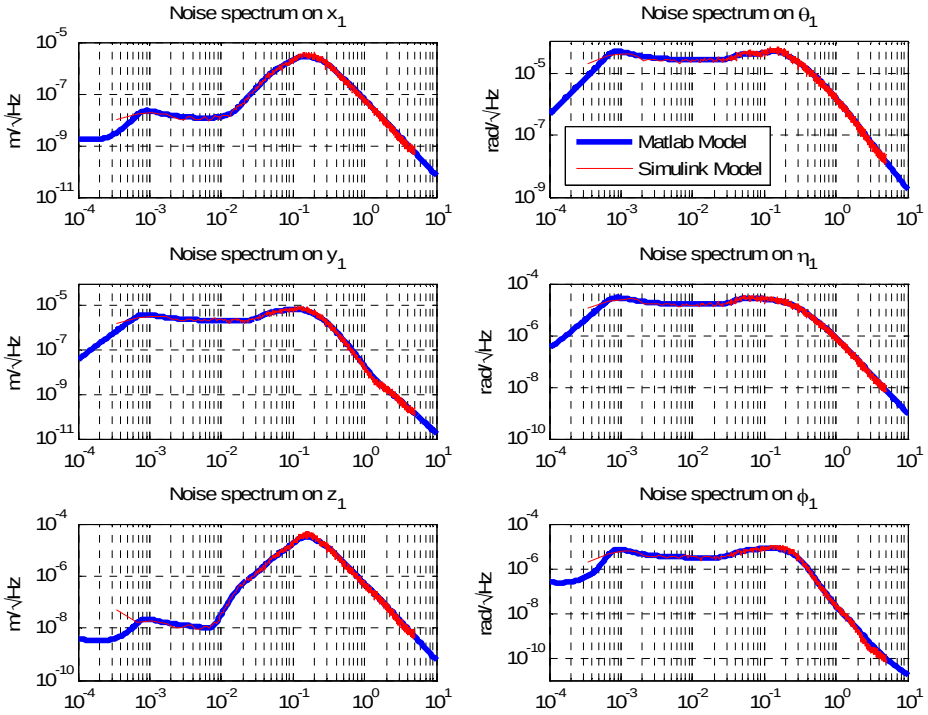

Figure A-2: T/M 1 position and attitude error (no Kalman filter applied)

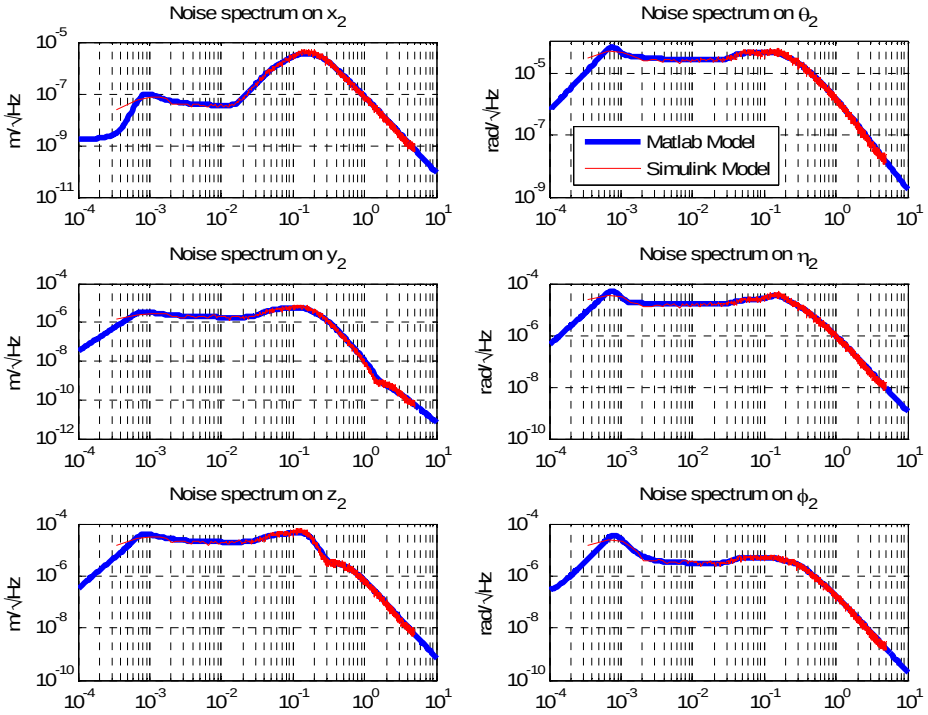

Figure A-3: T/M 2 position and attitude error (no Kalman filter applied)

Figures and Tables relative to chapter 7

Comparison between the time-series of the SC inertial attitude achieved in the *drag-free acquisition mode* conditions (i.e. without the use of a Kalman filter) and theirs reference signals which represent the ideal performances. Figure A-4.

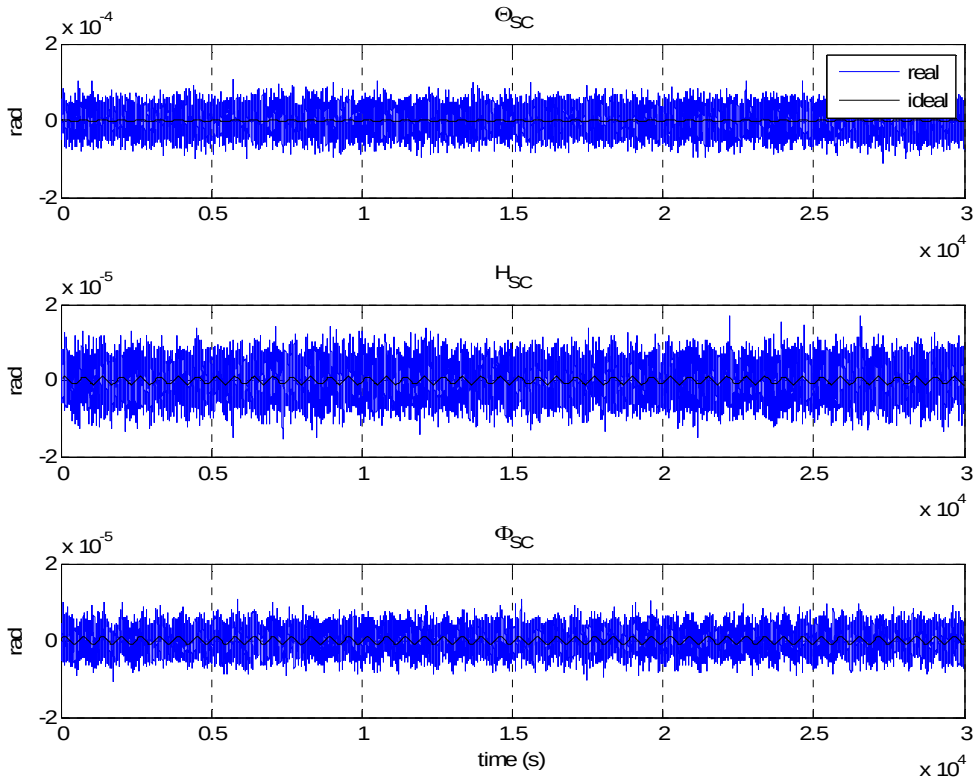

Figure A-4: Spacecraft inertial attitude without Kalman filter

Time-series of the SC inertial attitude achieved respectively with the use of the Kalman filter 1, 2 and 3. The reference and the estimated signals are also represented. Figure A-5, A-6, A-7.

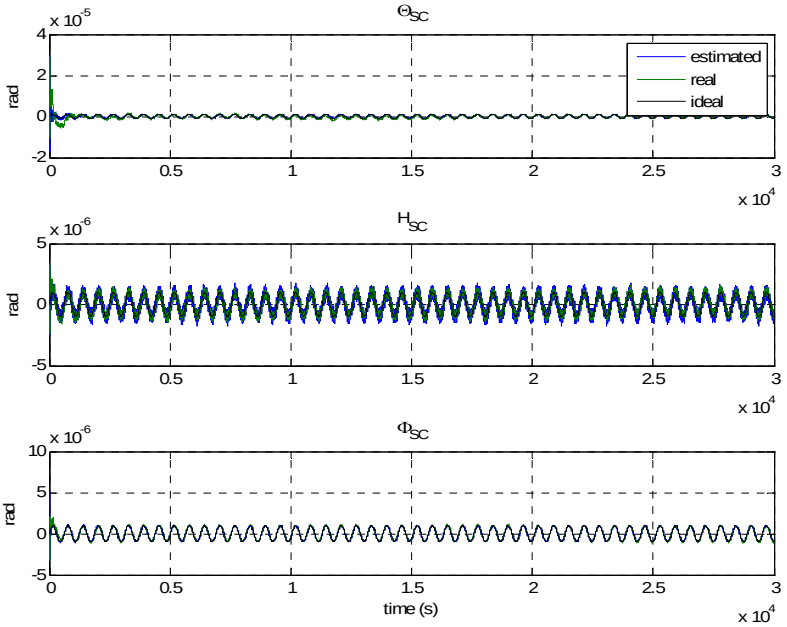

Figure A-5: Spacecraft inertial attitude with Kalman filter 1

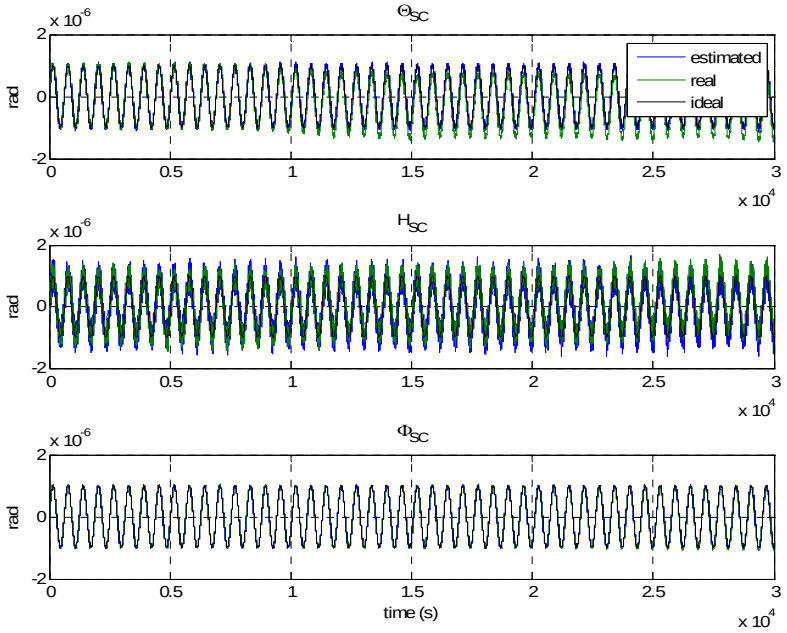

Figure A-6: Spacecraft inertial attitude with Kalman filter 2

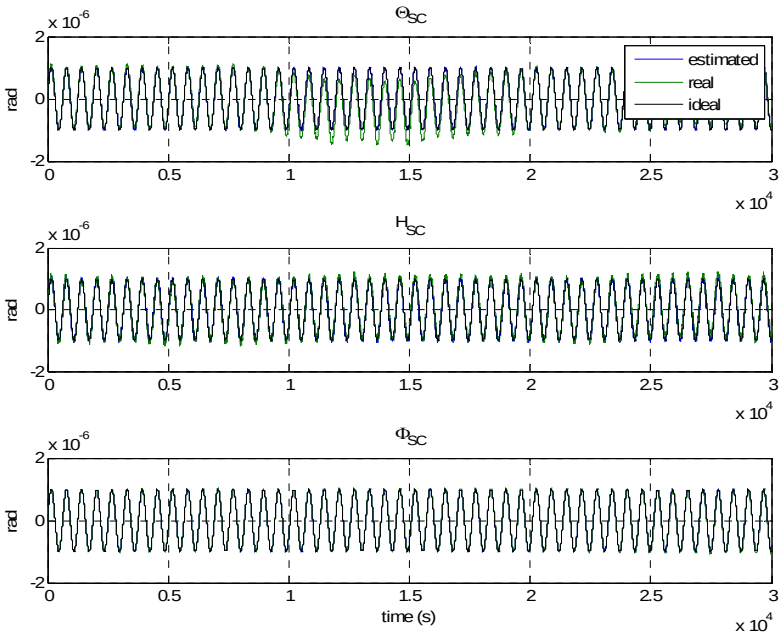

Figure A-7: Spacecraft inertial attitude with Kalman filter 3

Time-series of the test mass coordinate errors, the spacecraft inertial attitude errors and the telescope 1 in-plane pointing angle error achieved respectively with the use of the Kalman filter 1 and 2. Figure A-8, A-9, A-10, A-11, A-12, A-13, A-14, , A-15, A-16, A-17, A-18, A-19.

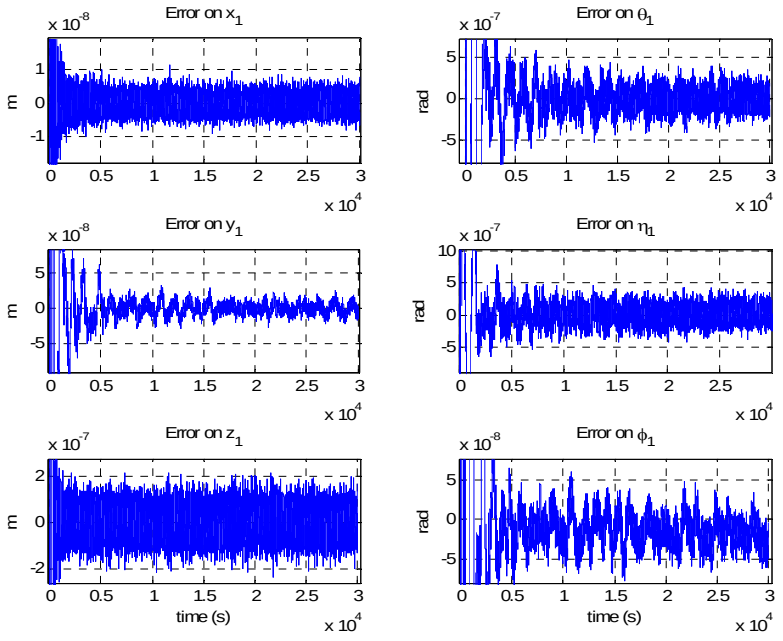

Figure A-8: Test mass 1 position and attitude error with Kalman filter 1

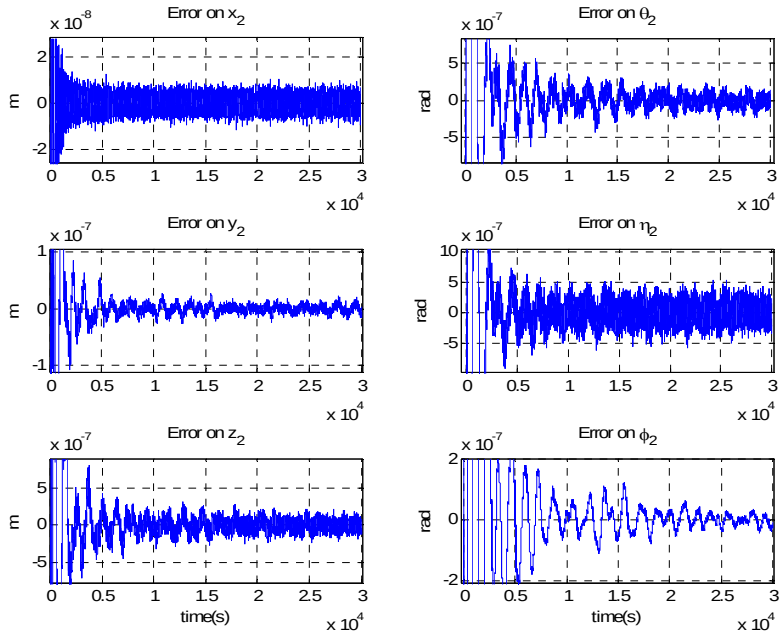

Figure A-9: Test mass 2 position and attitude error with Kalman filter 1

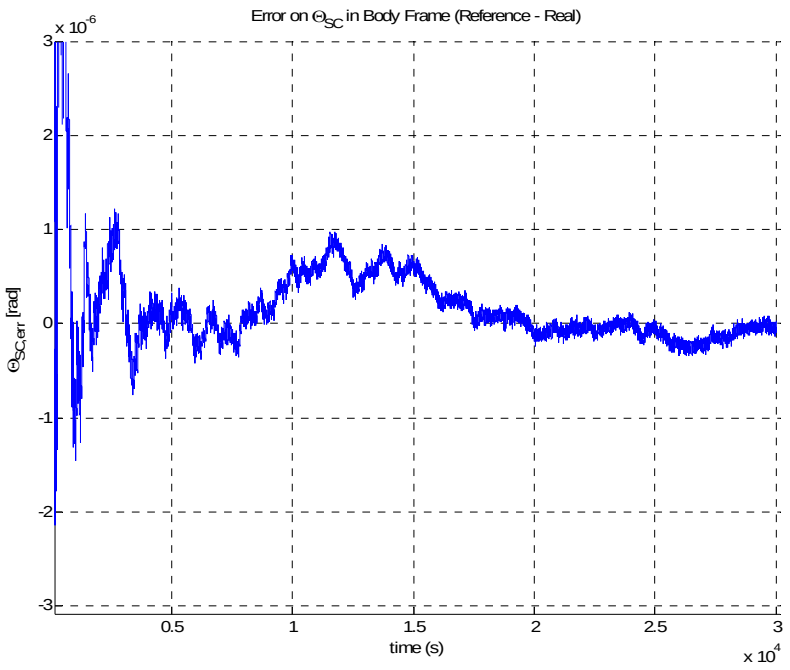

Figure A-10: Spacecraft inertial roll angle error with Kalman filter 1

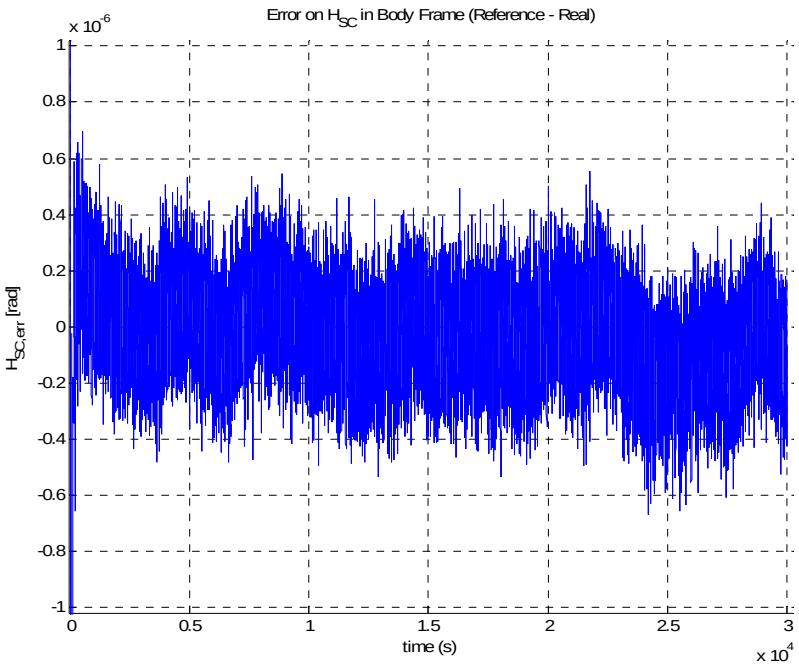

Figure A-11: Spacecraft inertial pitch angle error with Kalman filter 1

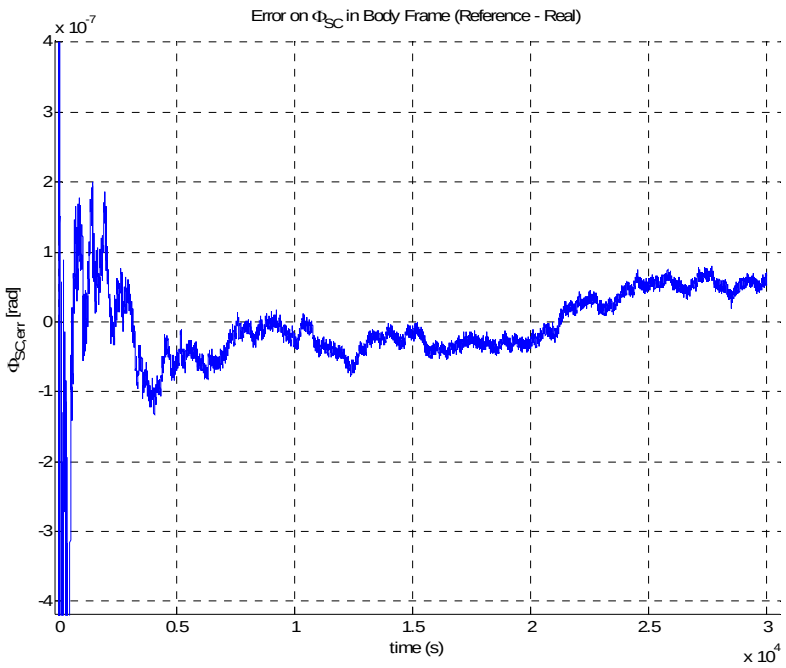

Figure A-12: Spacecraft inertial yaw angle error with Kalman filter 1

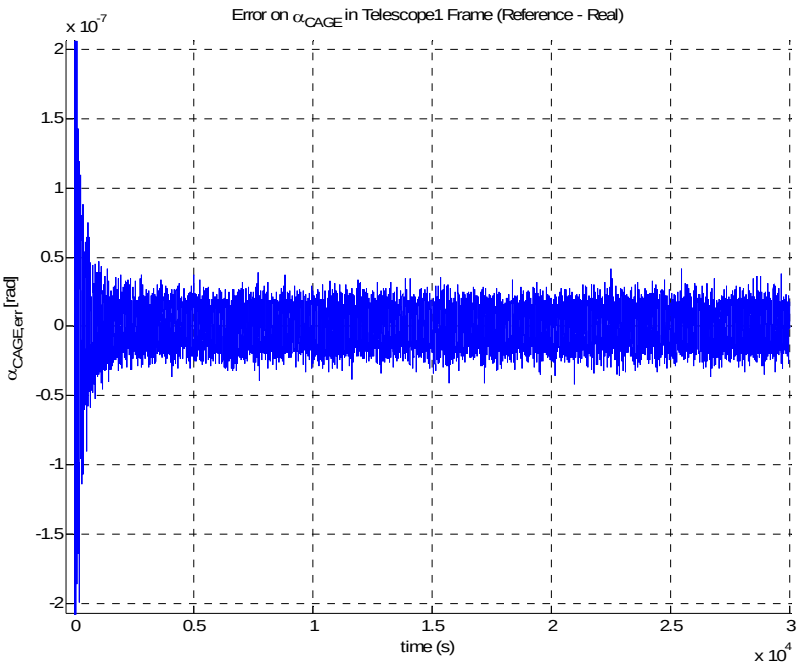

Figure A-13: Telescope 1 in-plane pointing angle error with Kalman filter 1

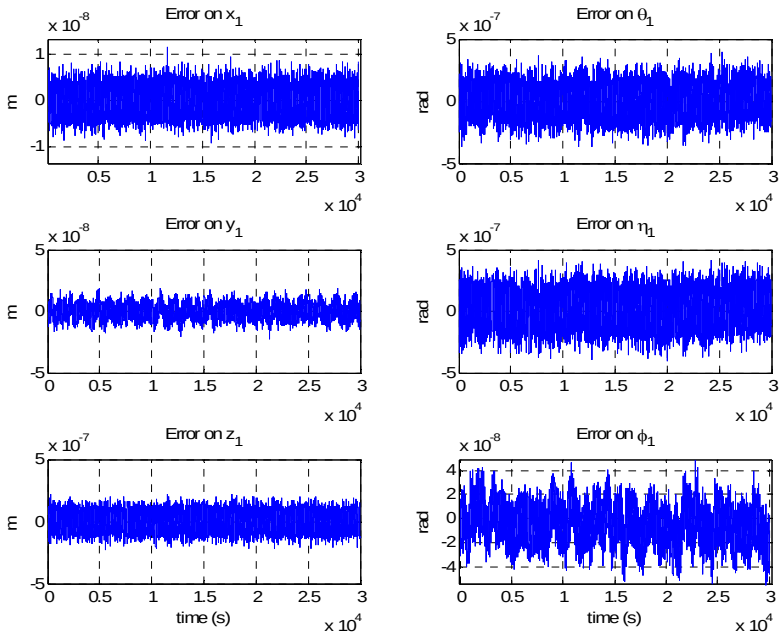

Figure A-14: Test mass 1 position and attitude error with Kalman filter 2

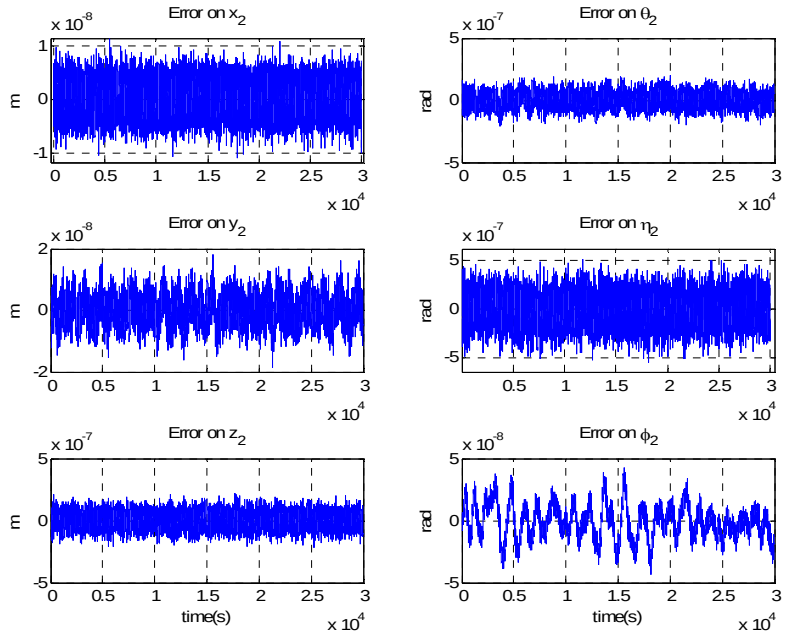

Figure A-15: Test mass 2 position and attitude error with Kalman filter 2

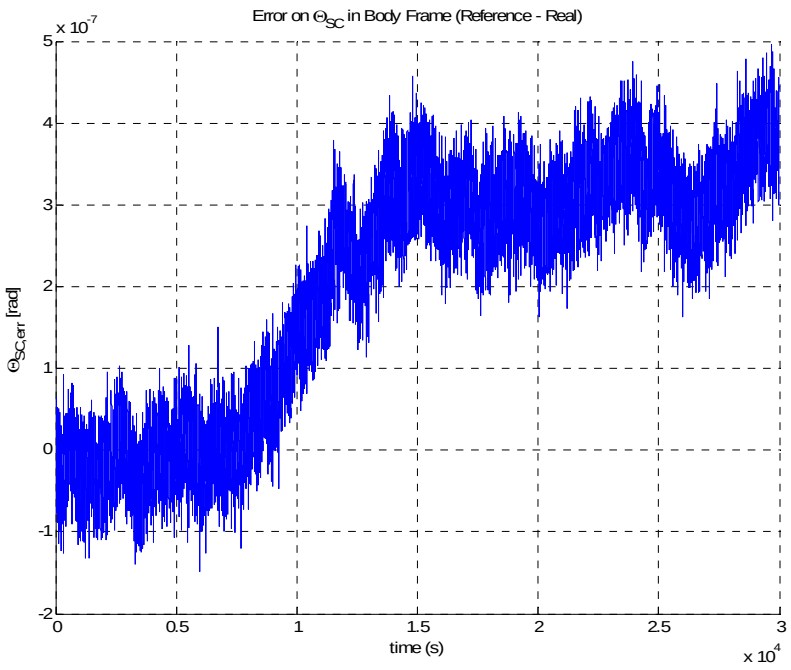

Figure A-16: Spacecraft inertial roll angle error with Kalman filter 2

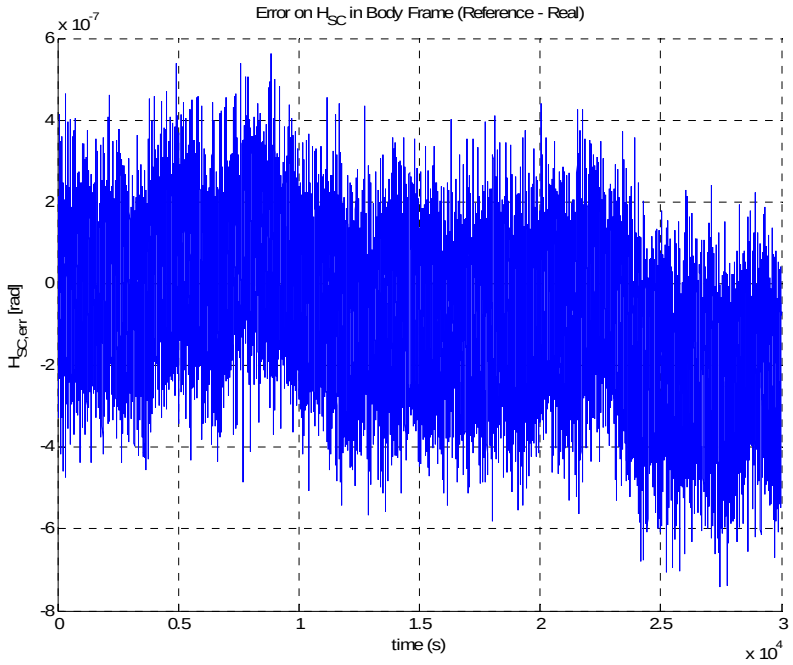

Figure A-17: Spacecraft inertial pitch angle error with Kalman filter 2

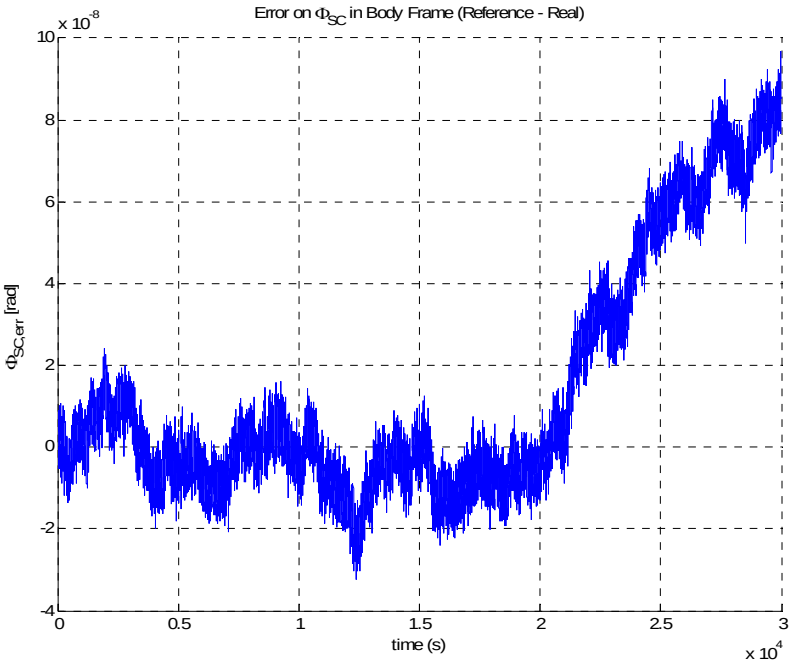

Figure A-18: Spacecraft inertial yaw angle error with Kalman filter 2

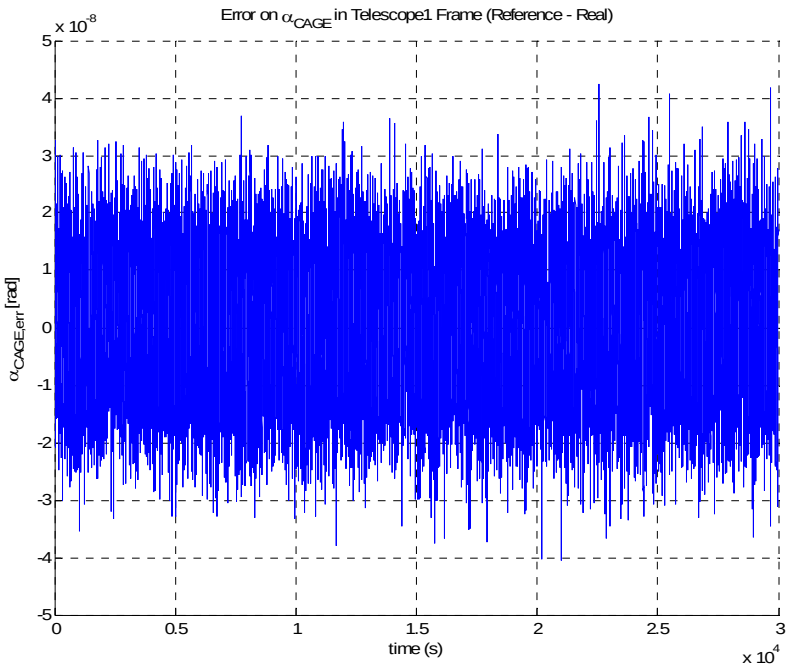

Figure A-19: Telescope 1 in-plane pointing angle error with Kalman filter 2

Statistical analysis of the Kalman filter performances over the long-term drift requirements. Table A-1.

		Long-term drift in µrad over a time window of 1000 s of the signal error (reference - real)						
		$\Theta_{1,err}$	$H_{1,err}$	$\Phi_{1,err}$	$\Theta_{2,err}$	$H_{2,err}$	$\Phi_{2,err}$	$\alpha_{CAGE,err}$
Requirements		**-**	**5**	**≈ 5.099**	**-**	**5**	**5**	**1**
Gyro mode	**Kalman Filter 1**	0.56	0.28	0.06	0.51	0.38	0.06	0.003
	Kalman Filter 2	0.12	0.13	0.03	0.13	0.14	0.03	0.004
	Kalman Filter 3	0.24	0.20	0.05	0.24	0.20	0.05	0.006

Table A-1: Comparison between the long-term drift requirements and the long-term drift performances in the *gyro mode*

Effect of the application of the Kalman filter 1 and 2 to the drag-free acquisition controller, comparing the square root of the power spectral densities of the SC attitude error and of the telescope 1 in-plane pointing angle error obtained with the application of the Kalman filters (red line) and without the application of the filters (blue line). Figure A-20, Figure A-21, Figure A-22, Figure A-23.

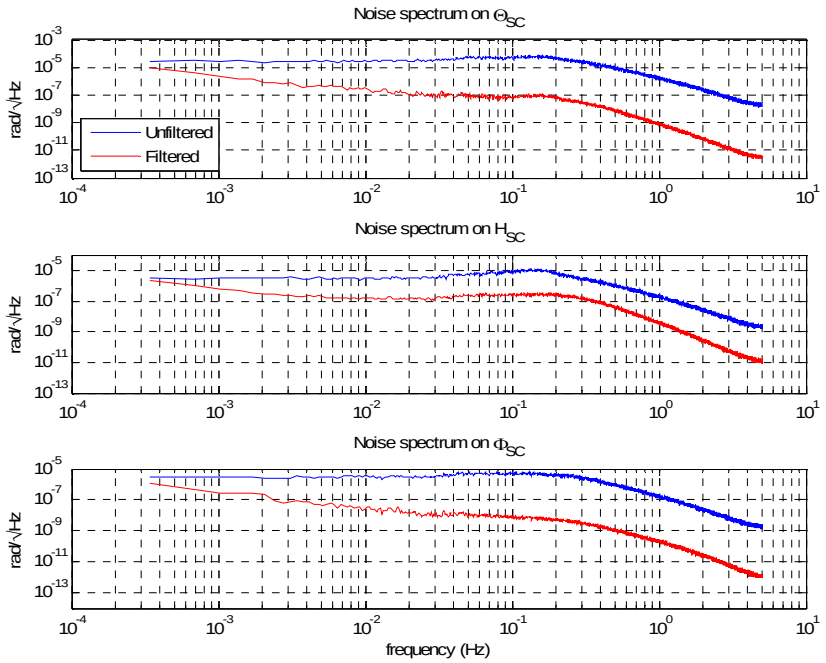

Figure A-20: Spacecraft inertial attitude error with and without Kalman filter 1

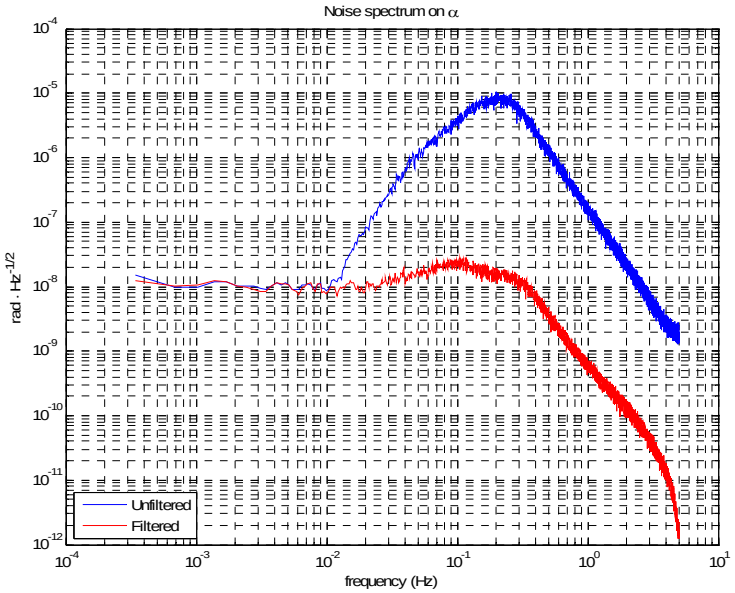

Figure A-21: Telescope in-plane pointing angle error with and without Kalman filter 1

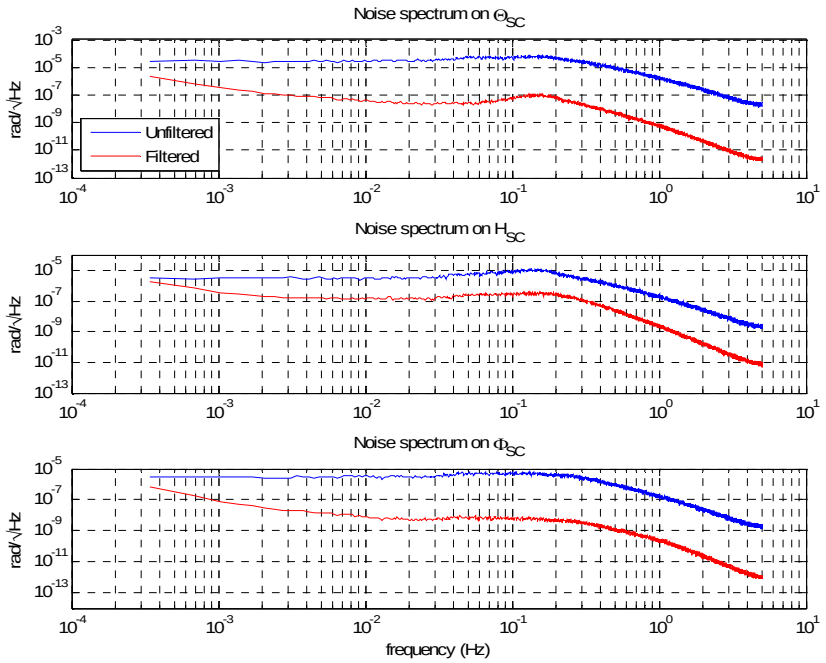

Figure A-22: Spacecraft inertial attitude error with and without Kalman filter 2

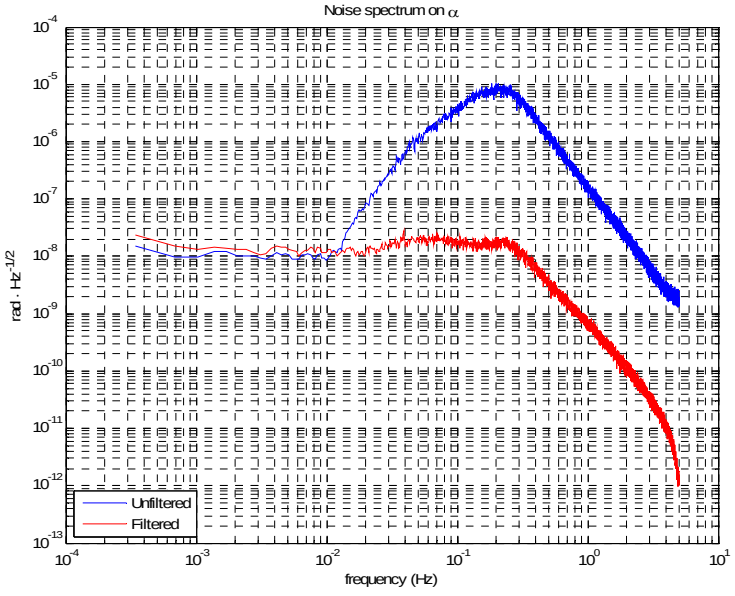

Figure A-23: Telescope in-plane pointing angle error with and without Kalman filter 2

Transfer-function analysis performed by means of the Matlab® model over the performances of the Kalman filter 2. Figure A-24, A-25, A-26, A-27.

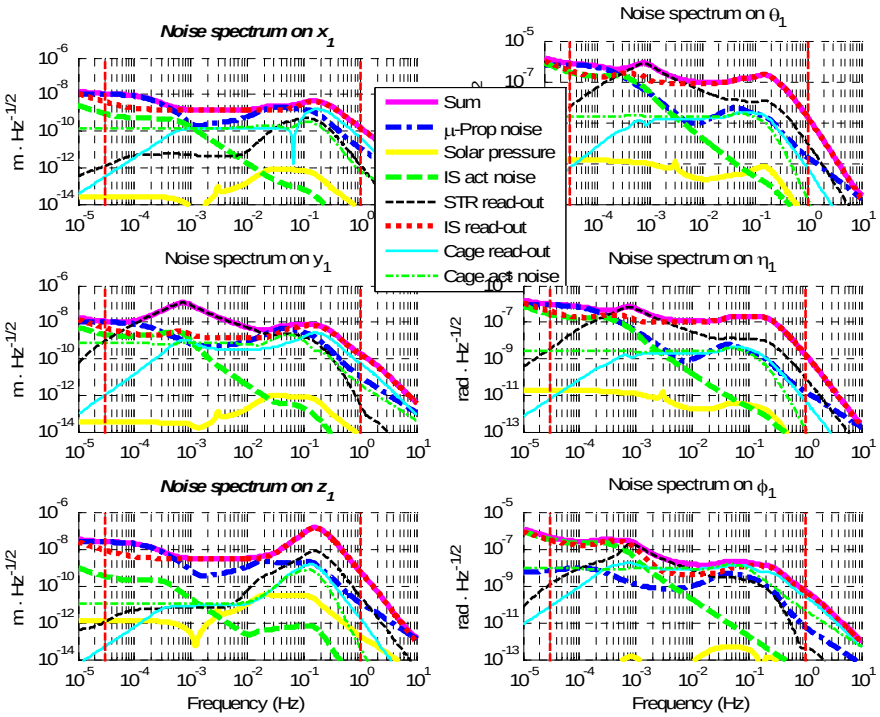

Figure A-24: Test mass 1 position and attitude error with Kalman filter 2

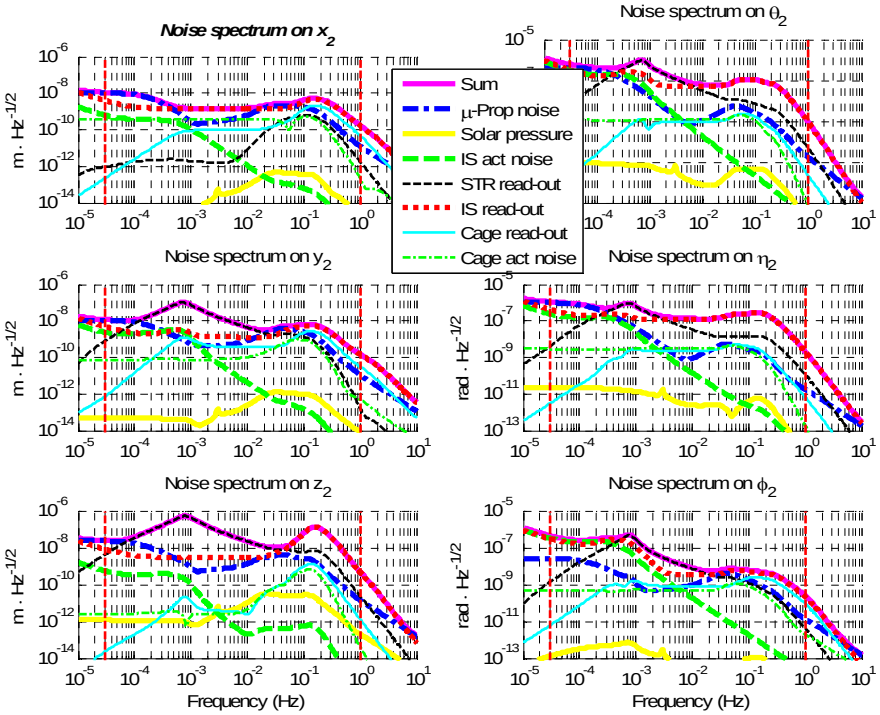

Figure A-25: Test mass 2 position and attitude error with Kalman filter 2

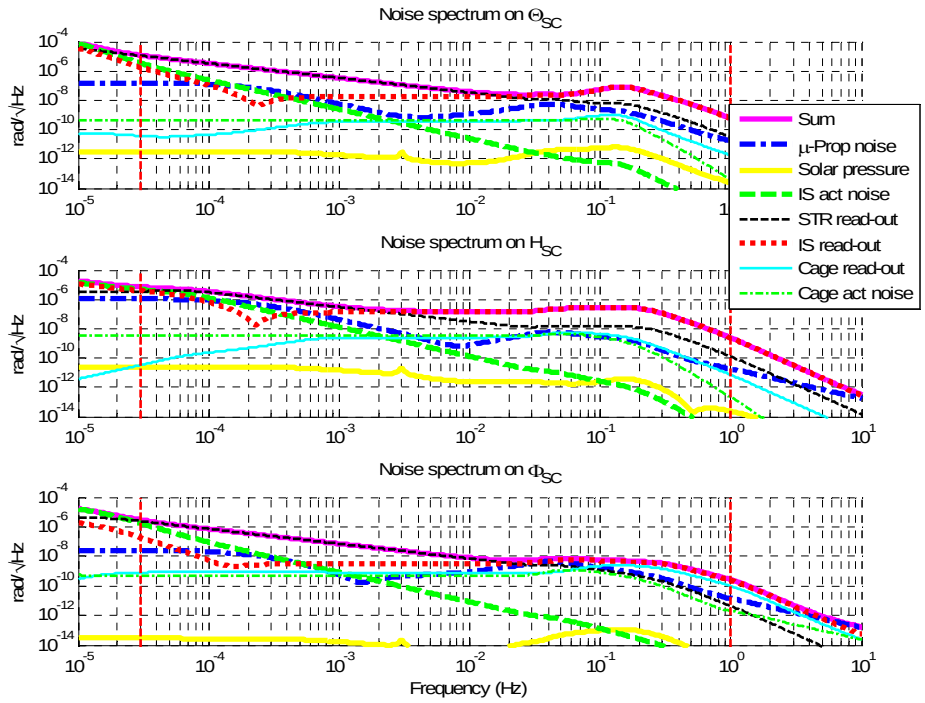

Figure A-26: Spacecraft inertial attitude error with Kalman filter 2

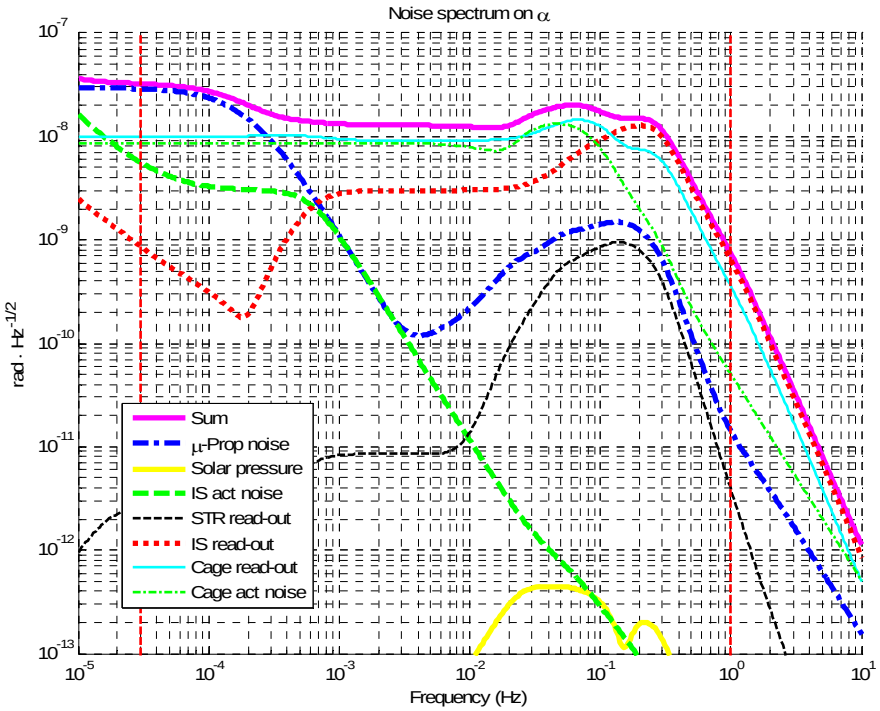

Figure A-27: Telescope 1 in-plane pointing error with Kalman filter 2

Sensitivity of the maximum long-term drift of the telescope 2 LOS inertial attitude errors and of the telescope 1 in-plane pointing angle error towards STR noise level and acquisition duration, achieved with the Kalman filter 3. Figure A-28, A-29, A-30, A-31.

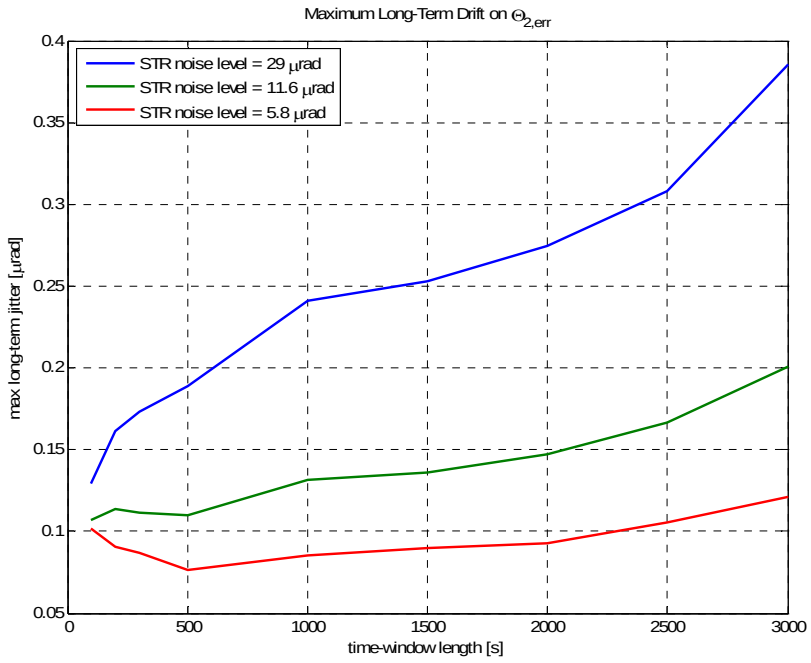

Figure A-28: Telescope 2 line-of sight inertial roll angle error with Kalman filter 3

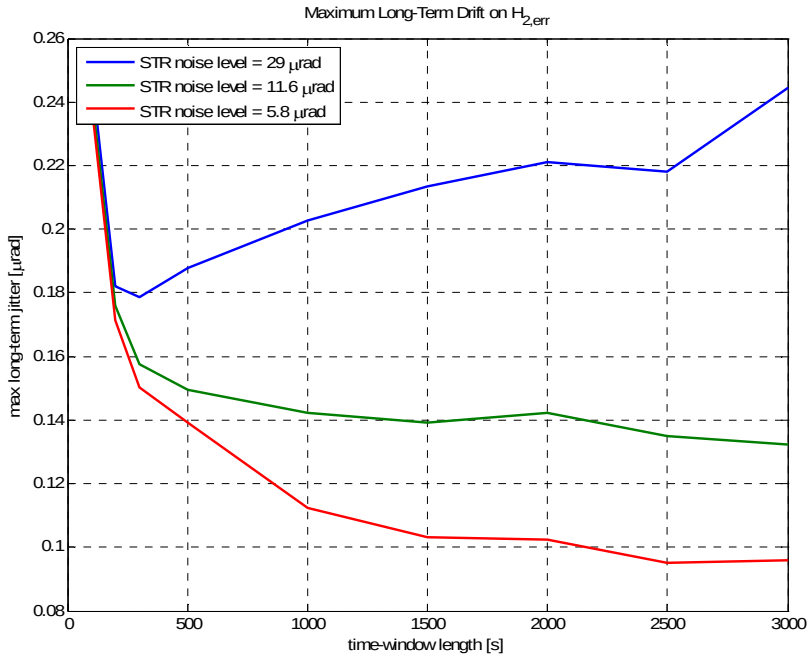

Figure A-29: Telescope 2 line-of sight inertial pitch angle error with Kalman filter 3

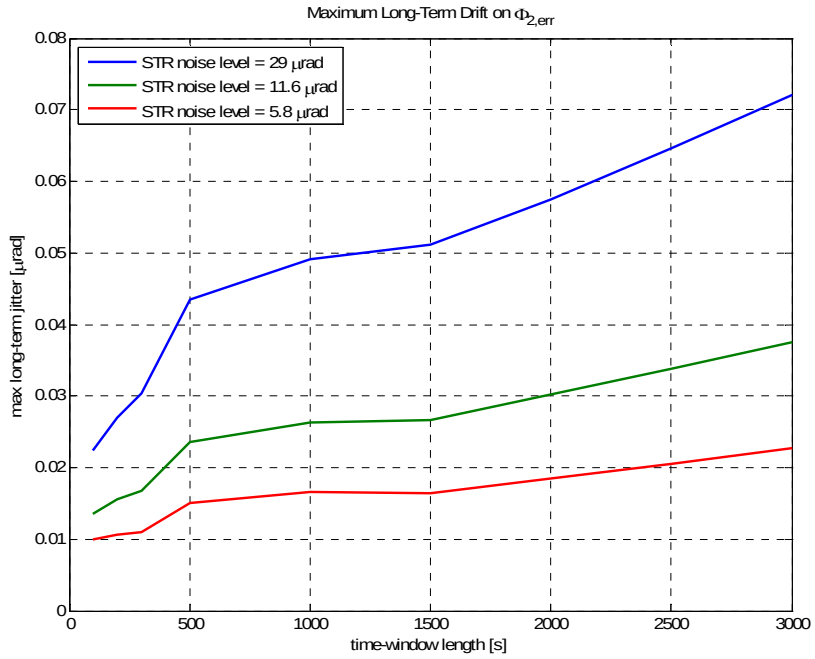

Figure A-30: Telescope 2 line-of sight inertial yaw angle error with Kalman filter 3

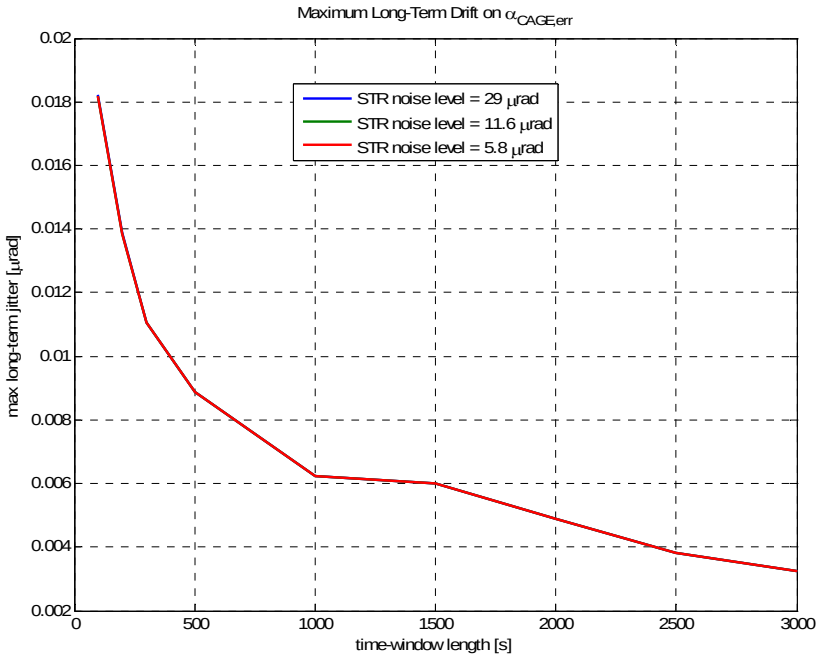

Figure A-31: Telescope 1 in-plane pointing angle error with Kalman filter 3

Sensitivity of the maximum short-term jitter and of the maximum long-term drift (of the telescope 2 LOS inertial attitude errors and of the telescope 1 in-plane pointing angle error) towards STR noise level and acquisition duration, achieved with the Kalman filter 2. Figure A-32, A-33, A-34, A-35, A-36, A-37, A-38, A-39.

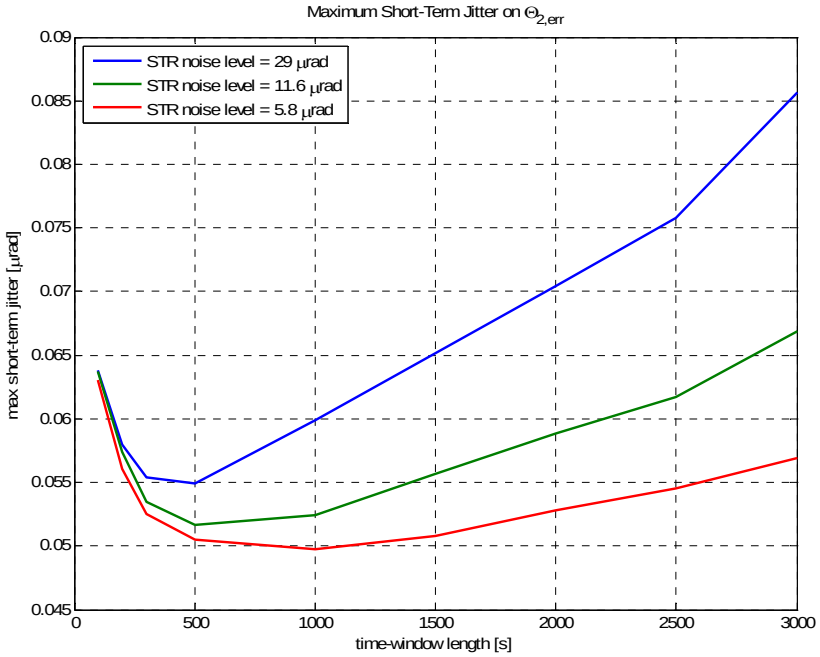

Figure A-32: Telescope 2 line-of sight inertial roll angle error with Kalman filter 2

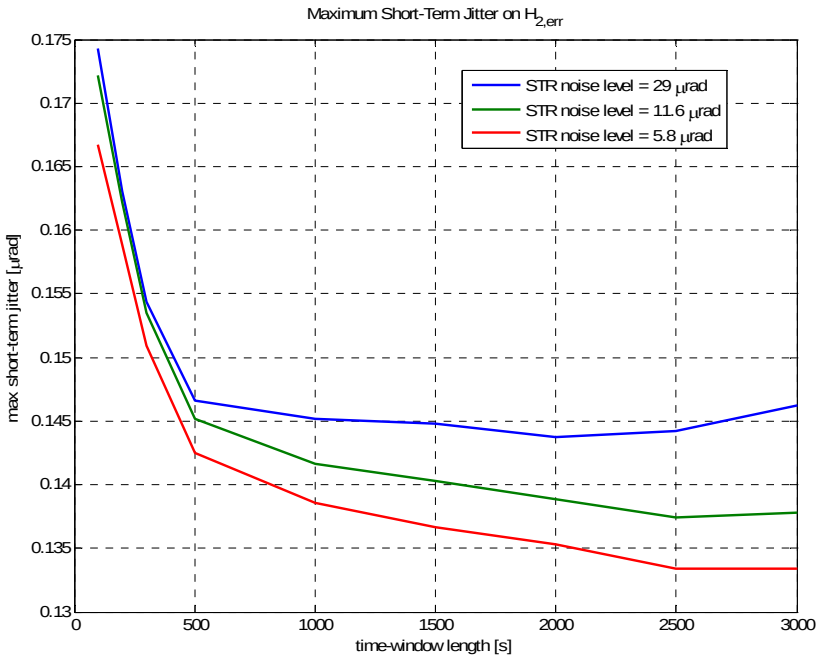

Figure A-33: Telescope 2 line-of sight inertial pitch angle error with Kalman filter 2

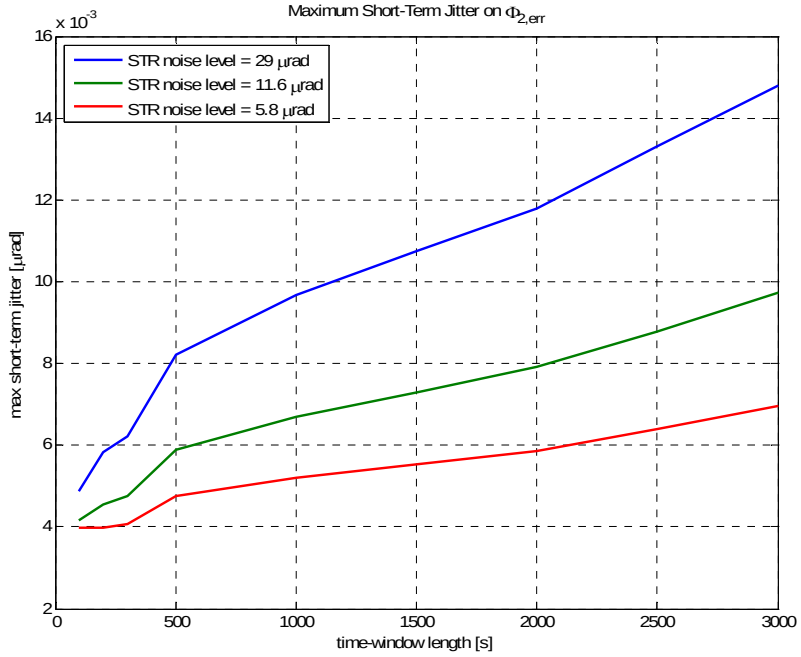

Figure A-34: Telescope 2 line-of sight inertial yaw angle error with Kalman filter 2

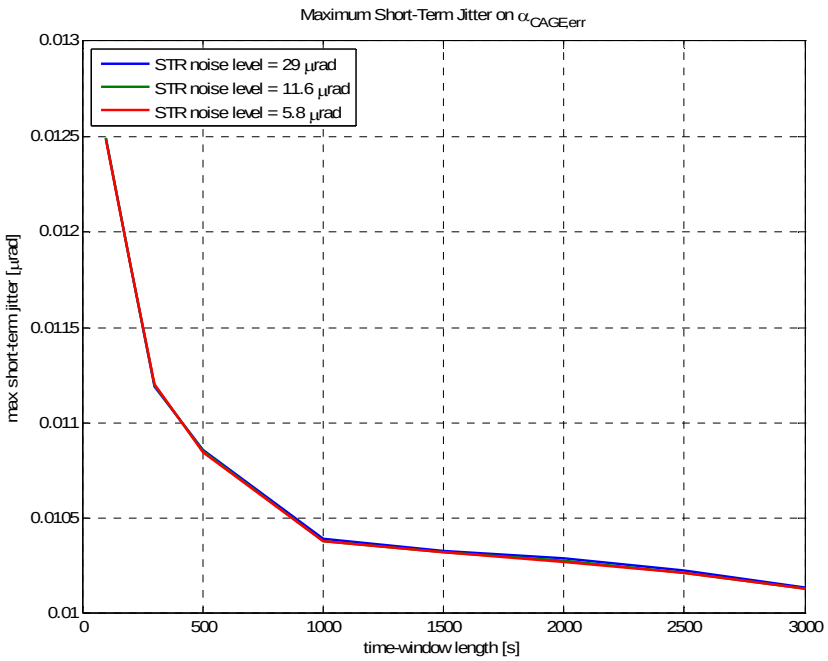

Figure A-35: Telescope 1 in-plane pointing angle error with Kalman filter 2

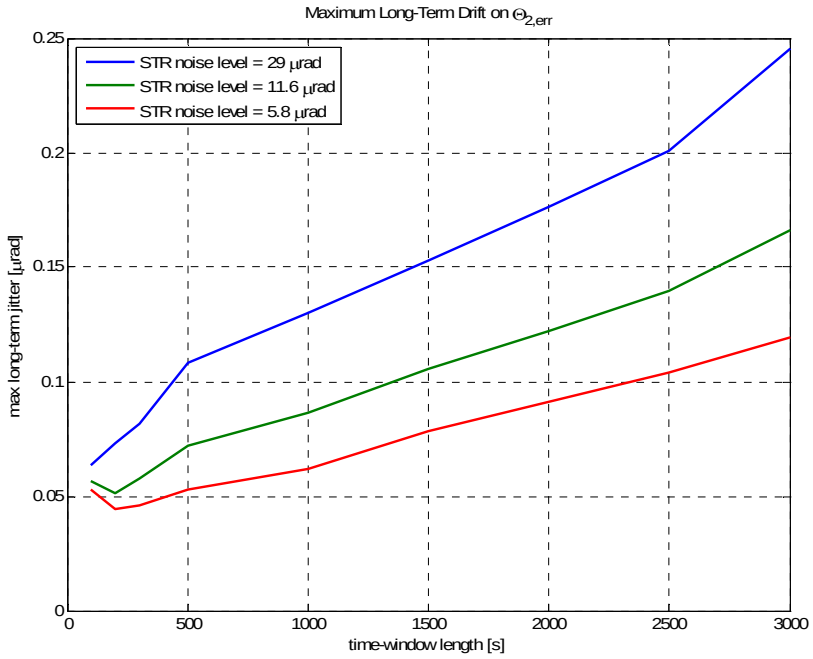

Figure A-36: Telescope 2 line-of sight inertial roll angle error with Kalman filter 2

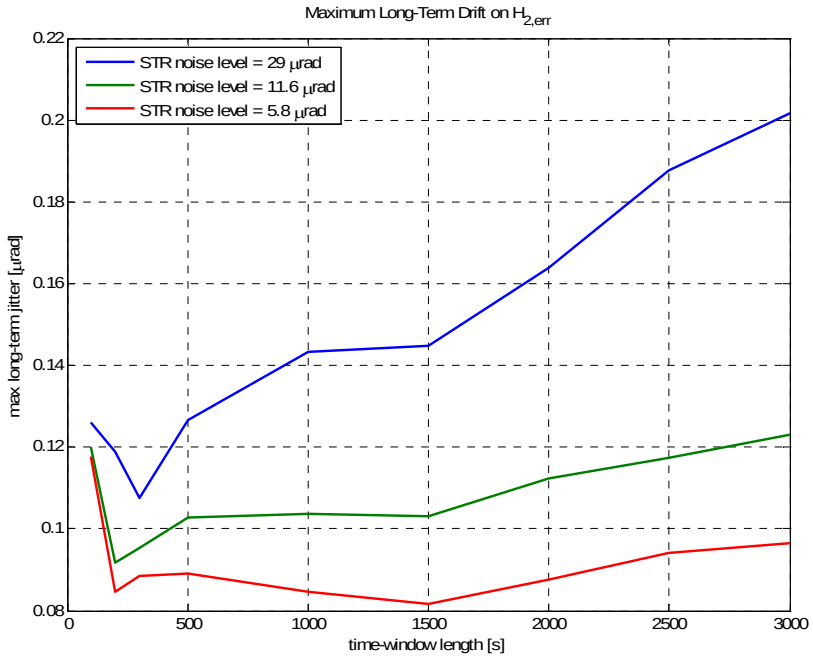

Figure A-37: Telescope 2 line-of sight inertial pitch angle error with Kalman filter 2

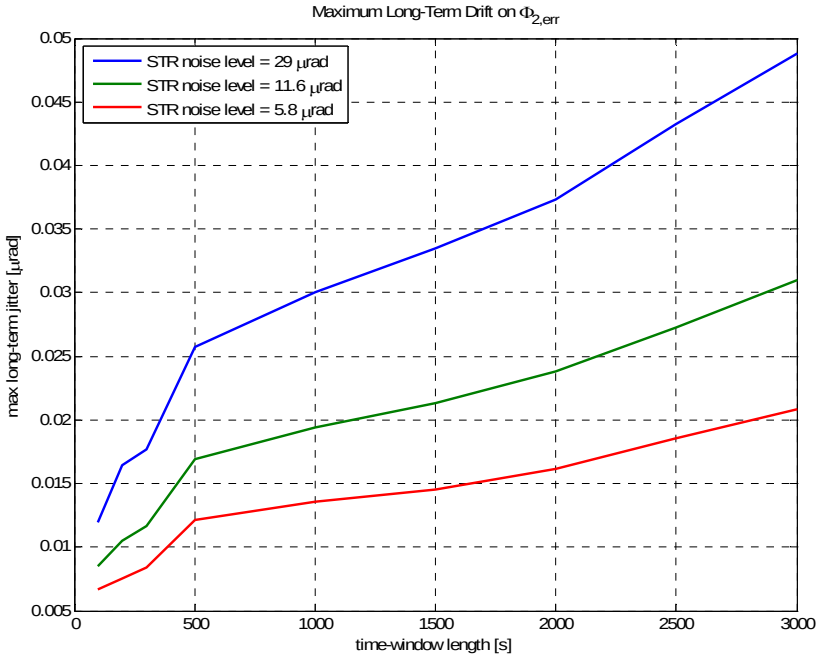

Figure A-38: Telescope 2 line-of sight inertial yaw angle error with Kalman filter 2

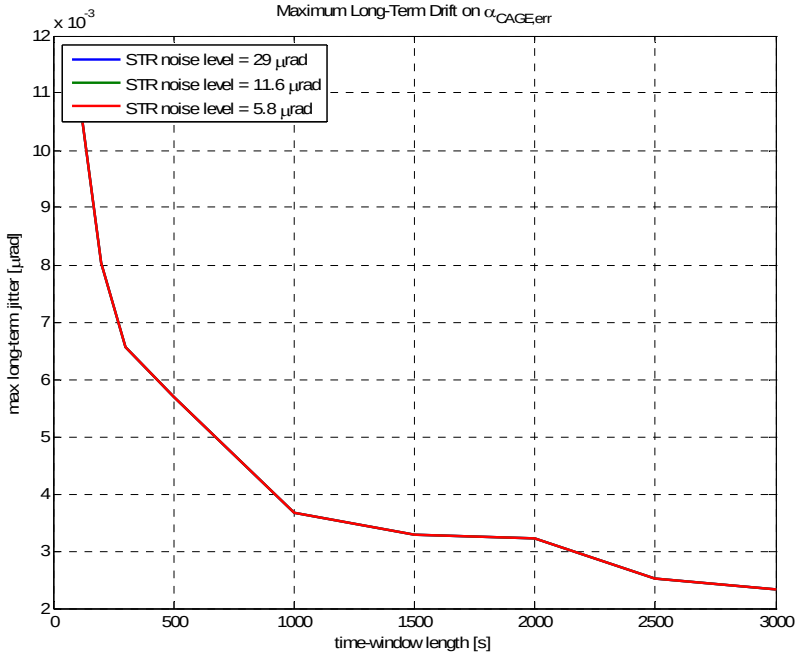

Figure A-39: Telescope 1 in-plane pointing angle error with Kalman filter 2

Figures and Tables relative to chapter 8

Long-term drifts histograms and table of the Kalman filter 2 sensitivity towards model errors. Figure A-40 and Table A-2.

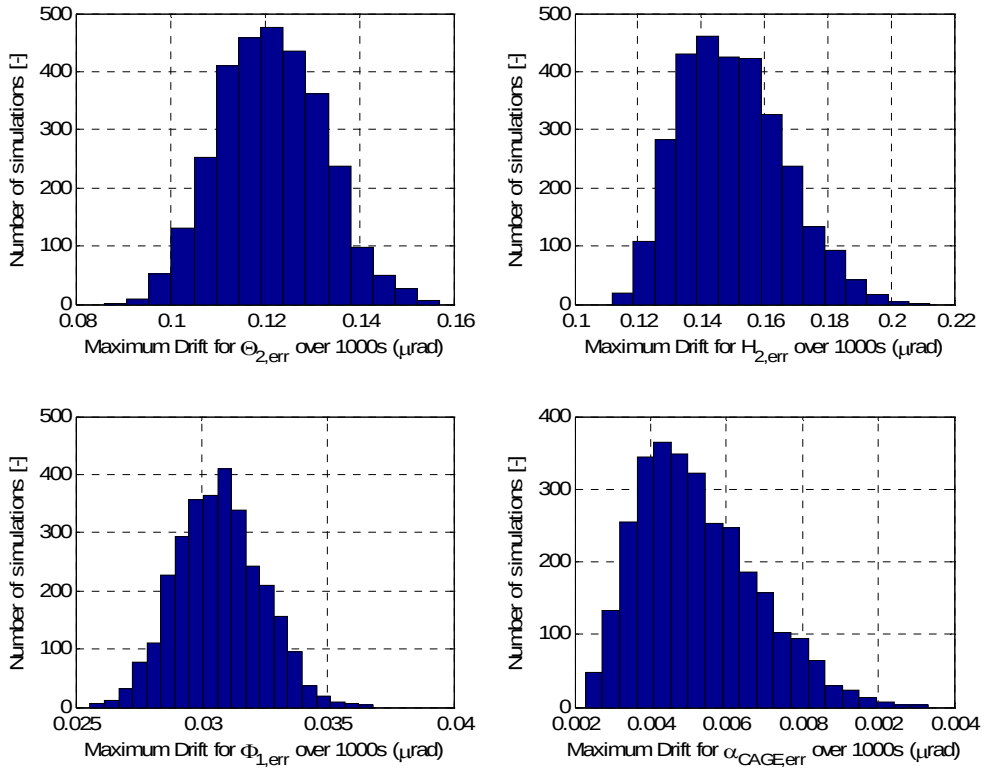

Figure A-40: Histograms of the number of simulations vs the long-term drift for the Kalman Filter 2

Error	Requirements (μrad)	Baseline (μrad)	Mean (μrad)	Standard Deviation (μrad)	$\frac{\text{Max-Min}}{\text{Baseline}} \times 100$
$\Theta_{2,err}$	-	0.1168	0.1214	0.0109	59.2 %
$H_{2,err}$	5	0.1338	0.1498	0.0163	75.2 %
$\Phi_{2,err}$	5	0.0308	0.0307	0.0017	36.4 %
$\alpha_{CAGE,err}$	1	0.0037	0.0046	0.0008	122.6 %

Table A-2: Statistics of the sensitivity analysis for the Kalman filter 2

Long-term drifts histograms and table of the Kalman filter 3 sensitivity towards model errors. Figure A-41 and Table A-3.

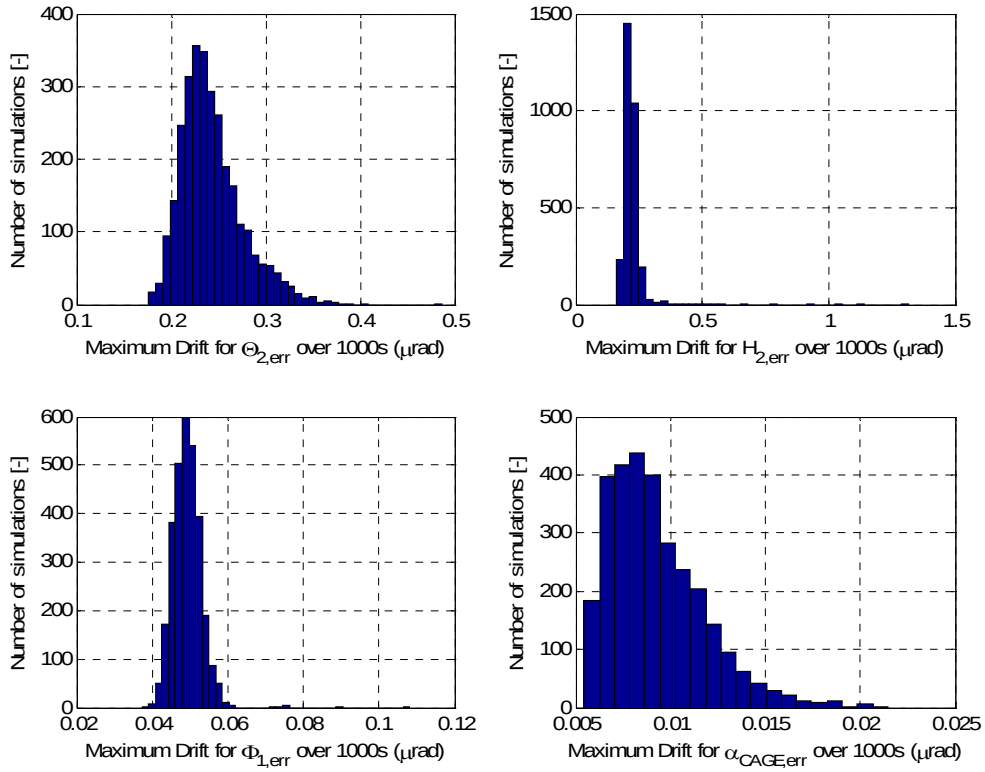

Figure A-41: Histograms of the number of simulations vs the long-term drift for the Kalman Filter 3

Error	Requirements (μrad)	Baseline (μrad)	Mean (μrad)	Standard Deviation (μrad)	$\frac{\text{Max-Min}}{\text{Baseline}} \times 100$
$\Theta_{2,err}$	-	0.2340	0.2433	0.0331	132.5 %
$H_{2,err}$	5	0.2084	0.2211	0.0488	554.7 %
$\Phi_{2,err}$	5	0.0490	0.0492	0.0039	144.5 %
$\alpha_{CAGE,err}$	1	0.0062	0.0093	0.0025	258.4 %

Table A-3: Statistics of the sensitivity analysis for the Kalman filter 2

Appendix B

Random Processes

B.1 Statistical Properties of Random Processes

A continuous-time random variable x(t) with an arbitrary distribution is usually characterized by the following statistical properties:

- **Mean**

$$\mu_x(t) = \bar{x} = E[x(t)] = \int_{-\infty}^{+\infty} x(t) f_x(x,t) dx(t)$$

- **Variance**

$$\sigma_x^2(t) = E[(x(t) - \mu_x(t))^2] = \int_{-\infty}^{+\infty} (x(t) - \mu_x(t))^2 f_x(x,t) dx(t)$$

- **Standard deviation**

$$\sigma_x(t) = \sqrt{\sigma_x^2(t)}$$

- **Mean square value**

$$\psi_x^2(t) = E[x^2(t)] = \int_{-\infty}^{+\infty} x^2(t) f_x(x,t) dx(t) = \mu_x^2(t) + \sigma_x^2(t)$$

- **Root mean square value**

$$RMS(t) = \psi_x(t) = \sqrt{\psi_x^2(t)} = \sqrt{\mu_x^2(t) + \sigma_x^2(t)}$$

- **Correlation function**

$$R_{xy}(t_1,t_2) = E[x(t_1)y(t_2)] = \int_{-\infty}^{+\infty}\int_{-\infty}^{+\infty} x(t_1)y(t_2)f_{xy}(x(t_1),y(t_2))dx(t_1)dy(t_2)$$

- **Auto-correlation function**

$$R_{xx}(t_1,t_2) = E[x(t_1)x(t_2)] = \int_{-\infty}^{+\infty}\int_{-\infty}^{+\infty} x(t_1)x(t_2)f_{xx}(x(t_1),x(t_2))dx(t_1)dx(t_2)$$

- **Covariance function**

$$Cov_{xx}(t_1,t_2) = E[(x(t_1)-\mu_x(t_1))(x(t_2)-\mu_x(t_2))]$$

where:

$f_x(x,t)$ Probability density function of the random variable x(t)

$f_{xy}(x(t_1),y(t_2))$ Joint probability density function of the random variable x(t) and y(t)

The Chebycheff Inequality demonstrates that, for every distribution, the $\pm 3\sigma$ interval around the mean value μ_x contains at least the 88.9 % of the distribution. If μ_x is anticipated to be small compared to σ or even zero, the RMS is close or equal to σ. Therefore, the expression RMS 1σ is used to indicate the conventional definition of the root mean square value, while the expression RMS 3σ is used to indicate

$$RMS_{3\sigma}(t) = \sqrt{\mu_x^2(t) + 3\sigma_x^2(t)}$$

When **x**(t) is a n-vector random process, the previous definitions can be applied to each component of the random process vector. In particular, the correlation function becomes the *correlation matrix*

$$R(t_1,t_2) = E[\mathbf{x}(t_1)\mathbf{x}^T(t_2)] = \begin{pmatrix} E[x_1(t_1)x_1(t_2)] & \cdots & E[x_1(t_1)x_n(t_2)] \\ \vdots & \ddots & \vdots \\ E[x_n(t_1)x_1(t_2)] & \cdots & E[x_n(t_1)x_n(t_2)] \end{pmatrix}$$

and, in perfect analogy, the covariance function becomes the *covariance matrix*. When the components of the **x**(t) vector are zero-mean random variables, the correlation and the covariance matrices coincide. Besides, when the components of the **x**(t) vector are

uncorrelated between them, the correlation matrix becomes a diagonal matrix whose elements are the auto-correlation functions of each vector component.

When x(t) is a stationary and ergodic random variable, its statistical properties are invariant with respect to translation in time and they can be computed for a time interval of length T as

$$\mu_x = \lim_{T\to\infty} \frac{1}{T} \int_0^T x(t)dt$$

$$\sigma_x^2 = \lim_{T\to\infty} \frac{1}{T} \int_0^T (x(t) - \mu_x)^2 dt$$

$$\psi_x^2 = \lim_{T\to\infty} \frac{1}{T} \int_0^T x^2(t)dt$$

Etcetera

All the previous definitions and considerations can be adapted to discrete-time random variables and vectors; e.g. the root mean square value for a discrete-time stationary ergodic random variable is given by

$$\psi_x = \lim_{N\to\infty} \sqrt{\frac{\sum_{i=1}^{N} x_i^2}{N}}$$

Obviously, T and N cannot be infinite, therefore a properly large time-interval length (T) or a properly large number of samples (N) have to be taken in consideration in order to obtain a good approximation of the desired statistics.

B.2 Power Spectral Density

When x(t) is a stationary random variable, it is defined the power spectral density function (PSD) $G_{xx}(f)$, which represents the rate of change of the mean square value with frequency

$$\psi_x^2 = \mu_x^2 + \sigma_x^2 = \int_0^\infty G_{xx}(f)df \qquad \text{(B.1)}$$

Considering a linear, time invariant, SISO system described by a *frequency response function* $H(j2\pi f)$, the relationship between the power spectral density of the system input x(t) and the power spectral density of the system output y(t) is given by

$$G_{yy}(f) = \left|H(j2\pi f)\right|^2 G_{xx}(f) \tag{B.2}$$

B.3 White Noise and Noise Shaping

A zero-mean white Gaussian noise is an uncorrelated random process with a Gaussian probability density function, zero-mean and a constant PSD over all frequencies

$$\mu_x = 0$$

$$G_{xx}(f) = G_{xx} \quad \forall f$$

$$R(t_1, t_2) = \mathrm{Cov}(t_1, t_2) = R(t_1)\delta(t_2 - t_1)$$

where $\delta(t_2 - t_1)$ is the *Dirac delta function.* In particular, a white noise with unitary power is characterized by

$$G_{xx} = 1 \tag{B.3}$$

A white noise is a mathematical abstraction, since it has an infinite mean square value (i.e. infinite power), but it is a useful theoretical approximation when the real noise disturbance has a correlation time that is very small relative to the natural bandwidth of the system.

A noise shape filter is a SISO or MIMO LTI system that, fed by one or more zero-mean white Gaussian noises, gives as output one or more zero-mean coloured (correlated) Gaussian noises. In the SISO case, indicating with $H(j2\pi f)$ the frequency response function of the shape filter, with x(t) the white noise of unitary power used as input and with y(t) the coloured noise obtained as output, it follows from Eq. (B.2) and Eq. (B.3) that

$$G_{yy}(f) = \left|H(j2\pi f)\right|^2 \tag{B.4}$$

B.4 Covariance Matrix

For the Kalman filter implementation, it is necessary to compute the elements of the covariance matrix of zero-mean white or coloured Gaussian random process vectors by means of the shape filter frequency response matrix. When the noise vector components are uncorrelated between them (as usually happens), the problem reduces to compute the variances of the vector components.

When the n-th noise component is generated by means of a single input shape filter (e.g. IS read-out noise, solar pressure noise, etc.) with given frequency response function $H(j2\pi f)$, the variance can be computed by combining Eq. (B.1) and Eq. (B.4) and by solving the resulting integral

$$\sigma_x^2 = \int_0^{f_{sample}} G_{xx}(f)\mathrm{d}f = \int_0^{f_{sample}} \left|H(j2\pi f)\right|^2 \mathrm{d}f \tag{B.5}$$

where f_{sample} is the simulation sampling rate (10 Hz). Sometimes it is useful to approximate the power spectrum with its constant high frequency value

$$G_{xx} \approx \lim_{f\to\infty} G_{xx}(f) = \lim_{f\to\infty} \left|H(j2\pi f)\right|^2 = \left|K_{H(j2\pi f)}\right|^2 \longrightarrow \sigma_x^2 \approx \left|K_{H(j2\pi f)}\right|^2 f_{sample}$$

where $K_{H(j2\pi f)}$ is the gain of the frequency response function.

When the n-th noise component is one or the only output of a multiple input shape filter (e.g. FEEP actuation noise), Eq. (B.5) is not valid. However, the variance of this noise component can be approximated with the following procedure. Indicating with $H_{ij}(j2\pi f)$ the frequency response function that relates the j-th white noise input I_j to the i-th coloured noise output O_i of the shape filter such that

$$O_i = \sum_{j=1}^{m} H_{ij}(j2\pi f)\cdot I_j$$

considering the following relationship between the inputs and the output variances

$$\sigma_{O_i}^2 = \sum_{j=1}^{m} \left(\frac{\partial O_i}{\partial I_j} \sigma_{I_j} \right)^2$$

and approximating the frequency response function with its gain, the variance of the noise component can be approximated by

$$\sigma^2_{o_i} \approx \sum_{j=1}^{m} \left|K_{ij}\right|^2 f_{sample}$$

Bibliography

Part I System-Level Introduction

[1] Ayre M., *"Spacecraft Design Requirement Specification"*, Requirements Specification, LISA-ASU-RS-4001, EADS Astrium GmbH, August 2005

[2] Barbagallo G., Stramaccioni D., *"Use of Spectral Analysis in Thermal Stability Verification"*, European Space Research and Technology Center, Noordwijk, 2001

[3] Bendat J. S., Piersol A. G., *"Random Data - Analysis and measurement Procedures"*, 3rd Edition, John Wiley & Sons, 2000

[4] Brandt N., *"Force and torque modelling and simulation"*, Technical Note, EADS Astrium GmbH, Friedrichshafen, September 2003

[5] Brandt N., *"Mathematical modelling of drag-free satellites"*, Technical Note, EADS Astrium GmbH, Friedrichshafen, September 2003

[6] Brandt N., *"Noise Generation and Data Analysis"*, Technical Note, EADS Astrium GmbH, Friedrichshafen, April 2003

[7] Gath P., *"Constellation Acquisition Control for LISA"*, Technical Note, LISA-ASD-TN-2003, EADS Astrium GmbH, September 2005

[8] Gath P., *"DFACS Design for LISA"*, Technical Note, LISA-ASD-TN-2002, EADS Astrium GmbH, April 2006

[9] Gath P., Fichter W., Kersten M., Schleicher A., *"Drag Free and Attitude Control System Design for the LISA Pathfinder Mission"*, Classical and Quantum Gravity 22, Institute of Physics publishing, 2005

[10] Gath P., Perkinson M.C., Stauss O., *"Coordinate System"*, Technical Note, LISA-ASD-TN-5003, EADS Astrium GmbH, September 2005

[11] Gath P., Weise D., Ayre M.C., *"Mission Design Description"*, Design Description, LISA-ASD-DD-5001, EADS Astrium GmbH, August 2006

[12] Gath P., *"Satellite Controller Design"*, Technical Note, EADS Astrium GmbH, September 2002

[13] Jörck H., *"End-to-End Simulation for LISA"*, Technical Note, LISA-ASD-TN-2001, EADS Astrium GmbH, September 2005

[14] Lange B., *"Experimental Gravitational Physics Using Drag-Free Satellites"*, http://www.dragfreesatellite.com

[15] Levenhagen J., *"Statistical Varriables for Equipment Specifications"*, Technical Note, EADS Astrium GmbH, Friedrichshafen, April 2003

[16] LISA Mission Formulation Team, *"Spacecraft Preliminary Design Description"*, Design description, LISA-ASU-DD-4001, EADS Astrium GmbH, April 2006

[17] LISA Science Team Information, *"LISA images"*, http://www.srl.caltech.edu/lisa/graphics/master.html

[18] Maghami P.G., Hyde T.T., Kim J., *"An acquisition control for the laser interferometer space antenna"*, Classical and Quantum Gravity 22 , S421-S428, Institute of Physics publishing, 2005

[19] Simulink, *"Simulink User Manual"*, Version 5, The MathWorks, 2002

[20] Stauss O., *"Payload Mechanical Design"*, Technical Note, LISA-ASD-TN-3006, EADS Astrium GmbH, April 2006

[21] Ziegler T., *"Controller Design for the LISA Pathfinder Spacecraft"*, Diploma Thesis, EADS Astrium GmbH, March 2004

Part II Kalman Filter Design

[22] Bar-Itzhack I.Y., Harman R.R., *"In-Space Calibration of a Skewed Gyro Quadruplet"*, Journal of Guidance, Control and Dynamics, Vol. 25, No. 5, 2002, pp.852-859

[23] Brown R.G., Hwang P.Y.C., *"Introduction To Random Signals and Applied Kalman Filter"*, Second Edition, J. Wiley and Sons, 1996

[24] Bryson A.E., Ho Y.C., *"Applied Optimal Control"*, Taylor and Francis,1987

[25] Chui C.K., Chen G., *"Kalman Filtering with Real Time Application"*, Springer-Verlag, 1987

[26] Gelb A., *"Applied Optimal Estimation"*, MIT Press, 1974

[27] Grewal M.S., Andrews A.P., *"Kalman Filtering: Theory and Practice, Using Matlab"*, Second Edition, J. Wiley and Sons, 2001

[28] Han B., Lin X., *"Adapt the Steady-State Kalman Gain Using the Normalized Autocorrelation of Innovations"*, IEEE Signal Processing Letters, Vol.12, No. 11, 2005, pp. 780-783

[29] Hide C., Moore T., Smith M., *"Adaptive Kalman Filtering for Low-cost INS/GPS"*, The Journal of Navigation, Vol. 56, 2003, pp.143-152

[30] Kalman R.E., *"A New Approach to Linear Filtering and Prediction Problems"*, Journal of Basic Engineering, March 1960, pp. 35-45

[31] Kalman R.E., Bucy R.S., *"New Results in Linear Filtering and Prediction Theory"*, Journal of Basic Engineering, March 1961, pp. 95-108

[32] Levenhagen J., *"ASG 62 Gyro-Stellar Estimator Description"*, Technical Note, EADS Astrium GmbH, Friedrichshafen, April 2006

[33] Levine W.S., *"The Control Handbook"*, CRC press and IEE Press, 1995

[34] Mehra R.K., *"Approaches to Adaptive Filtering"*, IEEE Transactions on Automatic Control, 1972, pp. 693-698

[35] Mengali G., *"Meccanica del Volo Spaziale"*, Edizioni Plus - Università di Pisa, Pisa, 2001

[36] Quarteroni A., Sacco R., Saleri F., *" Matematica Numerica"*, Spriger-Verlag, 2000

[37] Ribeiro M. I., *"Kalman and Extended Kalman Filters: Concept, Derivation and Properties"*, Institute for System and Robotics, Technical Report, February 2004

[38] Stearns S.D., David R.A., *"Signal Processing Alghoritm"*, Prentice-Hall, 1988

[39] Verrazzani L., *"Teoria dei Segnali"*, ETS Edizioni, 2002

[40] Welch G., Bishop G., *"An Introduction to the Kalman Filter"*, Technical Report, University of North Carolina at Chapel Hill, April 2004

[41] Wertz J. R., *"Spacecraft Attitude Determination and Control"*, Kluver Academic Publishers, 2002

[42] Yuanxi Y., Weiguang G., *"Comparison of Adaptive Factors in Kalman Filters on Navigation Results"*, The Journal of Navigation, Vol. 58, 2005, pp.471-478

[43] Zarchan P., Musoff H., *"Fundamentals of Kalman Filtering: A Practical Approach"*, Second Printing, AIAA, 2005